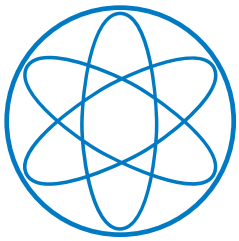

Physik Department

Development of a GEM-based TPC

for the

Measurement of In-Medium Signatures in Kaon Momenta in a Combined Setup at FOPI

PhD Thesis

by

Felix Valentin Böhmer

May 2015

Technische Universität München

Technische Universität München
Physik Department E18

Development of a GEM-based TPC
for the
Measurement of In-Medium Signatures in Kaon Momenta in a Combined Setup at FOPI

Felix Valentin Böhmer

Vollständiger Abdruck der von der Fakultät für Physik der Technischen Universität München zur Erlangung des akademischen Grades eines

Doktors der Naturwissenschaften

genehmigten Dissertation.

Vorsitzender:	Apl. Prof. Dr. Norbert Kaiser
Prüfer der Dissertation:	1. Univ.-Prof. Dr. Stephan Paul 2. Univ.-Prof. Dr. Norbert Herrmann, Ruprecht-Karls-Universität Heidelberg 3. Univ.-Prof. Dr. Peter Braun-Munzinger, Technische Universität Darmstadt (nur schriftliche Beurteilung)

Die Dissertation wurde am 28.05.2015 bei der Technischen Universität München eingereicht und durch die Fakultät für Physik am 21.09.2015 angenommen.

Dedicated to the people who stood by me through the times I spent in that weird bubble.

Abstract

In this work, the development of a novel type of tracking detector, a TPC with GEM-based gas amplification, is described. A TPC can be regarded as an almost ideal tracking detector, and devices of that kind have been widely used in particle physics in the past. Their small material budget allows the measurement of charged-particle trajectories in large volumes. At the same time, TPCs contribute to the identification of particles via the measurement of the specific energy loss along the path of flight. Their operation has so far been limited, however, to rather low rates by specifics of their technical implementation. It is discussed, how this important limitation can be overcome by the introduction of GEM foils into the detector design.

A large prototype of such a detector – constructed in 2010 – is presented, and its integration into the FOPI spectrometer at GSI during a two-weeks physics campaign in 2011 is described. The steps necessary for data reconstruction from the signals measured in this combined setup, as well as their implementation in software, are discussed. From the obtained data, key performance characterics of the device like the spatial tracking resolution, the momentum resolution and the performance of the specific-energy-loss reconstruction are evaluated. The convincing performance of the device has raised the interest of the particle-physics community. In cooperation with the ALICE collaboration, the ALICE TPC is currently being equipped with GEM technology in view of the upcoming luminosity upgrade of the LHC.

The second part of this work describes the extraction of physical properties from the 2011 data. Specifically, the production of strange hadrons in π-induced interactions at $1.7\,\mathrm{GeV}/c$ beam momentum is studied. Chiral perturbation theory in the $SU(3)$ flavour sector predicts the existence of a repulsive interaction between nucleons and kaons with $S = +1$. Signatures of this potential are studied in the momentum spectra of produced K^+ and K^0 for two different nuclear targets (C and Pb). For both charged and neutral kaons, a relative depletion of the phase space at small momenta is observed for the Pb system, qualitatively compatible with expectations. The results obtained in the K^0 channel are compared to predictions from transport calculations and earlier measurements.

Zusammenfassung

In dieser Dissertation wird die Entwicklung eines neuartigen Detektors zur Spurrekonstruktion, einer TPC mit GEM-basierter Gasverstärkung, beschrieben. Der Einsatz von TPCs in der Teilchenphysik ist weit verbreitet, denn Detektoren dieser Art können als nahezu ideale Spurdetektoren angesehen werden. Ihre geringe mittlere Dichte erlaubt die Abdeckung großer Volumina. Gleichzeitig können TPCs über eine Messung des spezifischen Energieverlusts von geladenen Teilchen beim Durchgang durch das aktive Detektormaterial zur Identifikation der Teilchenspezies beitragen. Allerdings war ihr Einsatz bisher durch einige Details ihrer technischen Realisierung auf Experimente mit niedrigen Reaktionsraten begrenzt. In dieser Arbeit wird erläutert, wie diese Einschränkung durch die Einbringung von GEM-Folien in die Konstruktion überwunden werden kann.

Ein großer Prototyp einer solchen GEM-TPC, der im Jahr 2010 fertiggestellt wurde, wird beschrieben. Im Jahr 2011 wurde der Detektor für eine zweiwöchige Strahlzeit in das FOPI Spektrometer (GSI) integriert. Die nötigen Schritte, um aus den gemessenen Signalen physikalische Größen zu extrahieren, sowie deren Implementierung in Software, werden erläutert. Die aufgezeichneten Daten erlauben die Charakterisierung wichtiger Leistungsdaten des Detektors, wie z.B. der Spurauflösung, des Beitrags zur Impulsauflösung und der Leistungsfähigkeit bezüglich der Messung des spezifischen Energieverlusts. Die überzeugenden Resultate dieser Studien haben u.A. dazu geführt, dass im Rahmen einer neuen Zusammenarbeit mit der ALICE Kollaboration die TPC des ALICE Detektors mit GEM-Technologie aufgerüstet wird. Dies ist notwendig, um vom aktuell durchgeführten Upgrade des LHC profitieren zu können.

Im zweiten Teil dieser Arbeit wird die Analyse der Daten aus dem Jahr 2011 im Hinblick auf ihren physikalischen Inhalt beschrieben. Konkret kann dabei die Produktion von Hadronen mit Strangeness in π-induzierten Reaktionen bei einem Strahlimpuls von $1.7\,\mathrm{GeV}/c$ studiert werden. Im Rahmen der chiralen Störungstheorie im $SU(3)$ flavour Sektor wird die Existenz einer repulsiven Wechselwirkung zwischen Nukleonen und Kaonen mit Strangeness $S = +1$ vorhergesagt. Die gemessenen Impulsverteilungen der mit unterschiedlichen Targets (C und Pb) produzierten K^+ und K^0 werden auf Signaturen dieser Wechselwirkung hin untersucht. Sowohl für neutrale wie auch für geladene Kaonen kann eine Entvölkerung des Phasenraumes bei kleinen Impulsen beobachtet werden, die im Falle des Bleitargets größer ausfällt. Diese Beobachtung ist mit den theoretischen Vorhersagen verträglich. Zuletzt werden die Ergebnisse im Falle der K^0 mit Vorhersagen aus Transportrechnungen sowie mit einer früheren Messung verglichen.

Contents

Terms & Abbreviations

ADC	analog-to-digital converter
BAR	BARrel scintillator array
BUU	*Boltzmann-Uehling-Uhlenbeck*
CCS	collision cross section
ChPT	chiral perturbation theory
CDC	central drift chamber
DAF	Deterministic Annealing Filter
DAQ	data aquisition
DOS	dipole oscillator strength
EAA	Elastic Arms Algorithm
FWHM	full width at half maximum
FVP	fermi virtual photon
FPGA	field-programmable gate array
GOR	*Gell-Mann-Oakes-Renner*
GEM	Gas Electron Multiplier
GOS	generalized oscillator strength
GPU	graphics processing unit
GSI	Gesellschaft für Schwerionenforschung
GUI	graphical user interface
HSD	Hadron-String Dynamics
IC	internal conversion

LHC	Large Hadron Collider
MC	Monte Carlo
MIP	minimum ionizing particle
MWPC	Multi-Wire Proportional Chamber
PAI	photo absorption ionisation
PANDA	Antiprotons at Darmstadt
PCB	printed circuit board
pdf	probability density function
PID	particle identification
POCA	point of closest approach
PSA	pulse shape analysis
QED	quantum electroynamics
QFT	quantum field theory
QCD	quantum chromodynamics
QMD	Quantum Molecular Dynamics
RPC	Resistive Plate Chamber
RMS	root mean square
SIS	Schwerionen-Synchrotron
STT	Straw Tube Tracker
TOF	time-of-flight
TPC	Time Projection Chamber
TUM	Technische Universität München

"Whether it's good or bad, it is sometimes very pleasant, too, to smash things."

Fyodor Dostoyevsky,
Notes from the Underground

Chapter 1

Introduction

How can one understand the structure of the universe at the smallest scales, of objects appearing indivisible and which are mysterious themselves? Indeed, one has to smash things. The starting point of what is called *particle physics* can be seen in the first scattering experiments conducted by Ernest Rutherford in the beginning of the 20^{th} century. In their famous gold-foil experiment, Rutherford, Geiger and Marsden concluded from the observed distribution of deflected α particles, which they detected with the help of a fluorescent screen, that the mass of atoms had to be concentrated in a surprisingly small volume.

Since then, scattering experiments have played a decisive role in establishing today's profound understanding of the structure of matter and the nature of the forces binding everything together (the *standard model* of physics). In the framework of quantum field theory (QFT), the standard model describes three of the four fundamental forces of nature: i) the electromagnetic force mediating between particles carrying electrical charge, ii) the weak force – historically first associated with the radioactive β decay – and iii) the strong force, which binds quarks into colour-neutral hadrons. Prime examples are protons and neutrons, which are the building blocks of the nuclei found in ordinary, atomic matter. The fourth force, gravity, remains an exception: So far, it has not been possible to integrate its theoretical description into the scheme of the standard model.

The quantum field theories of the standard model interpret the interaction of particles as the exchange of force quanta or *gauge bosons*. These are the massless photons in the case of the electromagnetic force, the massive $W^{\pm}$ and Z bosons for the weak interaction and the massless gluons for the strong interaction. The QFT of the electromagnetic interaction is named quantum electroynamics (QED), while the strong interaction is described by quantum chromodynamics (QCD). QED can be treated perturbatively, i.e. expanded in powers of its coupling constant, and is experimentally tested to an astounding precision. In the realm of hadrons, on the other hand, QCD mostly eludes this scheme due to the fact that the value of the strong coupling "constant" grows

for small energies.

The standard model is also intimately entangled with the concept of *symmetries*. It is formulated within the mathematical framework of group theory. The continuous symmetries obeyed by the individual interactions determine the structure of the force, and they translate into conserved quantities (*currents*) via *Noether's theorem*. A related concept of utmost importance is that of *spontaneously broken* or *hidden* symmetries, in which the symmetry is still respected by the theory of the interaction itself, but not by the ground state realised in nature. The mechanism of spontaneous breaking is used to explain the generation of i) the masses of the $W^{\pm}$ and Z gauge bosons in the unified theory of the electromagnetic and weak force, and ii) large fractions of the hadron masses in the picture of a spontaneous breakdown of the chiral symmetry of QCD.

For the first mechanism to work, the existence of another, scalar field had been postulated in the 1960s. Couplings to this *Higgs field* can also be understood to be responsible for giving the elementary fermions (including quarks) their masses, which cannot be explained otherwise by the standard model. The mass problem had been one of the most pressing and long-standing questions of particle physics. After the recent discovery of a boson which is believed to be an excitation of this scalar field in the ATLAS and CMS detectors at CERN, Peter Higgs and François Englert were awarded the Nobel Prize in Physics in 2013.

The second mechanism is directly related to this work. The spontaneous breaking of the chiral symmetry of QCD can be used to explain the large mass of hadrons when compared to the masses of their constituent quarks. Technically, the symmetry breakdown is introduced via the non-zero expectation value of the quark condensate, $\langle \bar{q}q \rangle$, the value of which is expected to change inside nuclear matter. The study of physical properties in dense environments (heavy-ion collisions) in order to improve the understanding of low- and mid-energy QCD is thus an active field of research. At the end of this thesis, an experimental signature of such *in-medium effects* in the interaction of strange mesons and nucleons will be investigated.

1.1 Tracking detectors

On the experimental side, in order to be able to resolve smaller and smaller structures, ever more powerful particle accelerators are required. Conservation laws of nature can be exploited to reconstruct physical processes from the collected collision debris. This task requires the precise determination of the defining properties of the produced particles, which are their energy/mass and their momentum. For charged particles, the latter is measured with so-called *tracking detectors*, providing a pictorial measurement of particle trajectories that are bent by an external magnetic field in order to allow the determina-

tion of the momenta. Considering once more the gold foil experiment, tracking detectors assume the role of Rutherford's simple fluorescent screen. In modern particle physics experiments, however, immense numbers of collision events need to be studied in the search for rare processes. This requires detectors capable of dealing with high-rate environments and a fully automated, computer-aided analysis of the measured signals.

While very different technologies are available for measuring the path of flight of particles, experiments conducted at high energies also entail the requirement of covering very large volumes for this task. The ATLAS detector at CERN, for instance, is more than 45 m long, measures ~ 25 m in diameter and weighs more than 7000 tons. A cost- and energy-efficient class of tracking detectors relies on the principle of *gas ionisation* by traversing charged particles. The most elegant such device is probably the Time Projection Chamber (TPC), which directly measures particle trajectories in one homogeneous, gas-filled volume. TPCs have been widely used in the past, but have been limited to rather low-rate experiments by specifics of their technical implementation.

In this work, the development of a new type of TPC is documented, which promises to overcome these rate limitations. A large prototype of the device has been sucessfully comissioned and tested, and its convincing performance has led to the currently ongoing upgrade of the world's largest TPC (operated inside the ALICE detector at CERN) with this technology.

1.2 Structure of this work

The first part of the present thesis describes the development and characterisation of a novel type of a gaseous tracking detector, a Gas Electron Multiplier (GEM)-based TPC. The focus of the author's work in this project has been the development of software algorithms required for data taking and analysis, and this circumstance will be reflected in the structure and contents of this thesis.

Chapter 2 will first discuss the concept of a classical TPC. In the course of this chapter, it will be shown how the employment of GEM foils can overcome the limitations of classical TPCs. Chapter 3 will introduce the reader to a large prototype of such a GEM-TPC, which was integrated into an already existing spectrometer and used for a dedicated physics data-taking campaign. The specifics of the setup will be detailed.

Chapter 4 will provide a detailed discussion of all algorithms that are required for a computer-aided analysis of the obtained data. This chapter will be first followed by a qualitative assessment of the combined data-reconstruction quality in Chapter 5, and then by a qualitative study of the performance of the GEM-TPC in Chapter 6.

The second part of this work will be concerned with the extraction of physical properties from the data taken. Specifically, the production of strange mesons (K^+ and K^0) and a possible signature of their in-medium modifications will be investigated. For this purpose, first an improved strategy for the identification of particles in the combined setup will be explored in Chapter 7. Finally, the reader will be made familiar with the theoretical background of the kaon-nucleon interaction in the framework of chiral perturbation theory (ChPT), before the specifics and results of the data analysis will be detailed in Chapter 8. The thesis will be concluded by a summary of the obtained results and future prospects in Chapter 9, which also contains an explicit listing of the author's personal contributions to the project.

Chapter 2

A GEM-based TPC

A Time Projection Chamber (TPC) [1] can be regarded as an almost ideal device for charged-particle tracking in large volumes. Detectors of this type have been successfully used as tracking devices in many particle-physics experiments, for example PEP-4 [2], TOPAZ [3], DELPHI [4], ALEPH [5], NA49 [6], STAR [7], CERES [8] and ALICE [9], listed in order of publication date.

Section 2.1 will introduce the reader to the general principle of operation of a TPC and its strengths and limitations as a large-volume tracking detector. This general discussion will be used to motivate GEM [10] foils as an advantageous alternative to the traditional Multi-Wire Proportional Chamber (MWPC)-based gas amplification scheme. The section will be concluded with a discussion of the main conceptual challenges of this approach.

In addition to its role as a tracking detector, a TPC can also provide information about the identity of a measured particle through the measurement of its specific energy loss. In order to establish a theoretical foundation for the associated performance analysis given later in this work (cf. Sec. 6.5), the underlying physical principles will be explored in depth in Sec. 2.2.

Finally, the arising concept of a GEM-TPC as a *continuously operating tracking pipeline* will be explored in Sec. 2.3. The ALICE TPC – which is currently being equipped with a GEM-based readout for the upcoming high-luminosity upgrade of the Large Hadron Collider (LHC) – will be presented as an example of such a device.

2.1 Tracking in large volumes: Basics of a TPC

The main purpose of a tracking detector is to provide spatial information about the path of flight of a particle. In the presence of an external magnetic bending field, this information can be used to infer the momentum of the detected particle. At the same time, the measurement should be performed with the minimal possible amount of interaction with the projectile.

The active material of a TPC is gaseous, and thus the previous requirement

is ideally realised in detectors of this type. Charged particles penetrating the active volume of the detector ionise gas molecules in collision events and thus leave behind a trace of electron-ion pairs on their path. The average number of created pairs n_p is proportional to the energy ΔE deposited in such ionisation events:

$$n_\mathrm{p} = \frac{\Delta E}{W} \quad . \tag{2.1}$$

W is treated as a phenomenological material constant specific to the choice of the detector gas and gives the energy needed to create a single electron-ion pair on average. Tabulated values for a wide range of detector gas mixtures exist. A detailed discussion of the ionisation processes on microscopic level follows in Sec. 2.2 of this chapter.

The trace of charges left by the traversing particle as imprint in the detector gas contains the spatial information about the particles' flight path and the energy loss it has suffered (cf. Eq. (2.1)). In order to access this information, the liberated charges need to be prevented from recombining and need to be extracted from the active volume. This is achieved by applying a well-defined, strong electric field, the *drift field* $\mathbf{E}_\mathrm{d}$.

Due to their much higher mobility compared to the left-behind ions, the ionisation electrons are the relevant carriers of information in the detection scheme. In the presence of the drift field they are accelerated along the field lines. At the same time, frequent collisions with the much heavier gas molecules randomise their movement, resulting in an effective "stop-and-go" fashion of motion. At atmospheric pressure, the average distance between collisions is much larger than the Compton wavelength, and the process can thus be described classically and macroscopically. In this picture one can expect the interactions of the gas molecules with the electrons and the acceleration by the external field in between collisions to establish a net, macroscopic *drift velocity* $\mathbf{v}_\mathrm{d}$. In the additional presence of an external magnetic field $\mathbf{B}$, the equation of motion can be written down as

$$m_\mathrm{e}\frac{\mathrm{d}}{\mathrm{d}t}\mathbf{v}_\mathrm{d} = e\mathbf{E}_\mathrm{d} + e(\mathbf{v}_\mathrm{d} \times \mathbf{B}) - K\mathbf{v}_\mathrm{d} \quad . \tag{2.2}$$

Due to historical reasons, Eq. (2.2) is commonly called the *Langevin* drift equation. The effect of the frequent collisions of the electron with gas molecules is absorbed in the form of a friction parameter K in the last term.

2.1.1 Diffusion

Let us further investigate the randomisation of the movement of the electron caused by these collisions, which occur on a time scale τ. Due to the statistical nature of this process, initially point-like charge clouds can be expected to expand over the course of their drift. In the absence of electromagnetic fields,

this process can be compared to the mechanism of *diffusion* of microscopic particles in a thermal system: Let us consider a point-like cloud of ionisation electrons at time $t = 0$ and at position $\mathbf{x} = (0,0,0)$ in thermal equilibrium with the detector gas (electron mass m_e, temperature T, average thermal kinetic energy of the individual charges $\varepsilon_\mathrm{t} = \frac{3}{2}k_\mathrm{B}T$). For $t \gg \tau$ the random Brownian motion will not have changed the expectation value $\mathrm{E}[\mathbf{x}] = (0,0,0)$. Microscopic diffusion theory predicts however an expansion of the charge cloud due to the large number of random collisions. More specifically, the width $\sigma(\mathbf{x})$ of the spatial profile – or, equivalently, the spatial probability density for a single particle – will grow in any of the spatial directions as in

$$\sigma_{x,y,z} = \sqrt{2D_\mathrm{t}t} \quad . \tag{2.3}$$

Here $D_\mathrm{t} = \mu k_\mathrm{B}T = \frac{2}{3}\mu\varepsilon_\mathrm{t}T$ is the *diffusion constant* and $\mu = e\frac{\tau}{m_\mathrm{e}}$ denotes the electron mobility. The subscript t emphasises the restriction to diffusion caused solely by thermal motion up to this point.

In the presence of a drift field $\mathbf{E}_\mathrm{d}$, one has to consider the additional contribution to the kinetic energy ε_E supplied by the field, $\varepsilon = \varepsilon_\mathrm{E} + \varepsilon_\mathrm{t}$. For typical field strengths found in drift detectors we have $\varepsilon_\mathrm{E} \gg \varepsilon_\mathrm{t}$. In this case – and with a constant equilibrium drift velocity $\mathbf{v}_\mathrm{d}$ over a drift distance L in the detector volume [1] –, one finds the relation

$$\sigma_{x,y,z} = \sqrt{2Dt} = \sqrt{\frac{4\varepsilon L}{3e|\mathbf{E}_\mathrm{d}|}} \tag{2.4}$$

for the diffusion-equivalent. From Eq. (2.4) we see that the variance is inversely proportional to the strength of the drift field, but at the same time grows linearly with the resulting average kinetic energy of the drifting electron. Against first intuition, the relation of ε_E and the strength of the drift field is not trivial and furthermore depends strongly on the choice of the detector gas. For a given $\mathbf{E}_\mathrm{d}$, "hot" gas mixtures show high electron energies and drift velocities, while "cold" mixtures have the advantage of a smaller diffusion. A pedagogical review of the matter can for example be found in Ref. [11].

So far, all spatial components of the expansion due to diffusion have been treated equally. In the presence of external fields, however, the situation becomes more complicated. Restricting the discussion to the scenario found in TPCs, $\mathbf{E}_\mathrm{d} \parallel \mathbf{B}$, it is sufficient to discriminate between the two diffusion components along ($D_\parallel$) and transverse ($D_\perp$) to the drift direction. Both electrostatic and magnetic forces lead to a difference between $D_\parallel$ and $D_\perp$ (*electric* and *magnetic anisotropy*). Most importantly, for strong magnetic fields one observes a considerable suppression of the diffusion transverse to the drift direction:

$$D_\perp(\mathbf{B} \neq 0) = D_\perp(0) \cdot \frac{1}{1 + \omega^2\tau^2} \quad . \tag{2.5}$$

[1] In comparison to typical drift times, the initial process of acceleration after ionisation – until the equilibrium value of $\mathbf{v}_\mathrm{d}$ is reached – can be assumed to be instantaneous.

As before, τ marks the average time scale between collisions of the electron with gas molecules, and $\omega = \frac{e}{m_e}|\mathbf{B}|$ is the cyclotron frequency of the electron. The result of Eq. (2.5) can be intuitively understood insofar as the arising Lorentz force dampens the instantaneous transverse motion after a collision, and thus the net expansion of the charge cloud.

Before continuing with the technical aspects of a TPC, it should be mentioned in this context that diffusion presents a theoretical limit to the spatial resolution of such a detector. Let us consider a point-like cloud [2] of N_{el} ionisation electrons. While the expectation value of the c.o.g. of the charge cloud is not changed by the drift, microscopic diffusion results in a spatial uncertainty of each electron position $\propto \sigma_{x,y,z}$. The resulting uncertainty of the measured c.o.g. thus goes with $\sigma_{x,y,z}/\sqrt{N_{\mathrm{el}}}$.

In practice, the situation is more complicated. In anticipation of the following sections, some additional considerations shall be shortly discussed. In a real detector, the position of a charge cloud can only be measured with a finite resolution, which is determined by the technical specifics of the detector, e.g. the effective structure size S on which such a measurement is performed. This presents the resolution limit as long as the spatial expansion due to diffusion is small in comparison (for example in the case of short electron drift). This fact will be picked up again in the discussion of the clustering algorithms in Sec. 4.3.

The above scenario of a measurement of an isolated charge cloud is of course academic: Instead, one actually measures the combined signals left by a traversing projectile along its trajectory. This changes the situation drastically, since S is usually much larger than the average distance between ionisation events. A measured signal will thus always consist of the contributions from multiple such events, which are additionally mixed by diffusion. It is thus clear that the impact of the structure size S on the final tracking resolution under the influence of diffusion is non-trivial. S can best be optimised in a microscopic simulation of the detector. The readout plane of the FOPI GEM-TPC (cf. Chapter 3) has been designed in this way.

Finally, there is an additional important effect that affects the spatial resolution: Uncorrected distortions of the drift field lead to deviations from the ideal, straight-line electron drift paths. Sources of such distortions are i) mechanical problems of the field-defining structure and ii) the buildup of a space charge from ionisation processes inside the active volume of the detector. Distortions resulting from the latter can easily reach values of 10^2 times the intrinsic spatial resolution of the detector. This topic will be discussed in the context of ion backflow in a GEM-based gas amplification scheme in Sec. 2.1.3.

[2] Already at this point an additional limitation to the spatial resolution is neglected: Electrons receiving a large energy transfer during primary ionisation may travel distances of the order of the intrinsic resolution of the detector and beyond ("*delta electrons*"). See the discussion of Sec. 2.2.2.

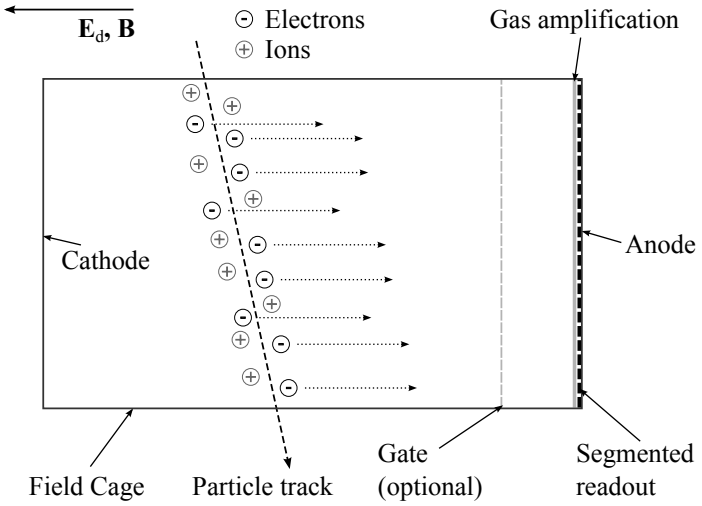

Figure 2.1: Principle of operation of a TPC: Traversing charged particles leave behind a trace of electron-ion pairs. A homogeneous electric drift field projects the electrons onto the detection plane, while the ions drift towards the cathode where they are absorbed. Before the electrons from ionisation events can be detected, they have to be amplified. Signal detection happens in a subsequent step using a segmented readout structure. An optional gating structure can be used to prevent ions created in the gas amplification process from entering the active volume (cf. Sec. 2.1.3). With knowledge of the drift velocity, the relative time information of the detected signals can be used to recover the shape of the track also along the drift direction. Reconstruction of the *global* position along this axis is only possible if external information is available, e.g. data from stationary tracking detectors or an event time supplied by a trigger system.

2.1.2 Technical implementation

The fundamental working principle of a TPC is to capture the three-dimensional imprint of the trajectory followed by a charged particle in the detector gas by *projecting* the charges onto a detection plane by means of – ideally – straight-line electron drift. The detection plane must be segmented so that the two-dimensional projection of the particle flight path can be measured with sufficient precision. Making use of the additional, relative *time* information of the individual signals allows one to recover the full dimensionality of the particle track. Figure 2.1 shows this concept schematically for the common case $\mathbf{E}_\mathrm{d} \parallel \mathbf{B}$ and a detector with rectangular cross section.

It is clear that any inhomogeneities of the drift field (and the drift velocity) will distort the obtained picture and diminish the quality of the extracted physical properties. With typical drift-path lengths being of the order of 1 m, a very high level of homogeneity and a precise knowledge of the actual field

topology are of central importance. The drift field itself is usually defined by an array of electrodes (*field cage*), uniformly degrading the potential between anode and cathode. A typical value for the drift field strength is $|\mathbf{E}_\mathrm{d}| \approx 10^2\,\mathrm{V\,cm^{-1}}$, already requiring considerable differences in the electric potential along the length of the field cage for larger chambers.

Another important issue is the choice of the detector gas. A basic wish list describing an ideal detector gas can be formulated as follows: i) a high electron drift velocity – ideally stable under moderate variations of $|\mathbf{E}|_\mathrm{d}$ – reduces the track occupancy of the detector, ii) a low electron diffusion leads to a high spatial resolution, iii) a low electron attachment prevents losses during drift, iv) a high primary ionisation (low W in Eq. (2.1)) benefits the spatial and energy resolution, v) a large radiation length limits multiple scattering of the projectile particle and vi) a stable operation with large gas gains at moderate field strengths facilitates the amplification process. It is obvious on first glance that the items from this list are partly in contradiction. Finding a sound compromise fulfilling all constraints of an experiment is an involved process. It is beyond the scope of this work to provide a fundamental discussion of this matter, instead the most important considerations shall be mentioned briefly in the following [3].

In order to allow gas amplification at moderate field strengths, the main component of the gas mixture is most commonly chosen to be a noble gas, as these lack additional channels of excitation that would act as an energy drain during the avalanche creation. Argon and Neon are affordable and common choices. Of these two, Argon has a twice as large ionisation rate but an almost three times shorter radiation length.

In a detector gas consisting only of a noble gas, precisely the aforementioned advantage would become a problem: the resulting abundance of ions would cause standing discharges in the vicinity of the anode. In addition, excited gas atoms in the avalanche emit photons. These are in the energy range of $E_\gamma \approx 10\,\mathrm{eV}$, which is comparable to the work function of electrodes in the vessel. Thus, as a secondary effect, additional electrons would be produced elsewhere in the active volume of the detector. The solution to these problems is the addition of a so-called *quenching gas*. These either inorganic or organic compounds feature additional rotational and vibrational modes of excitation over a wide energy range. Quenching gas molecules are able to efficiently neutralise ions of the main gas component by means of direct electron transfer and absorb photons before secondary reactions occur.

A large variety of quenching gases has been used in the past. The most widely used are Methane (CH_4), Ethane (C_2H_6), Isobutane (C_4H_{10}), dimethyl ether (C_2H_6O), CF_4 and CO_2. The choice of the quencher not only influences the fundamental properties of the detector gas, but also entails additional considerations. A technical, yet very important question connected to the selection

[3] Once again, the reader is referred to Ref. [11] for a discussion of gas properties.

of the quenching gas is that of *ageing*, e.g. chemical reactions between the detector gas and the mechanical structure leading to a change of the behaviour of the detector over time. Independent of the choice of the mixture, the detector gas has to be void of impurities to a high degree in order to prevent electron attachment during drift and thus a loss of primary ionisation charge.

2.1.3 Gas amplification and ion backflow: Motivation of a GEM-based TPC

Traditionally, gas amplification in TPCs has been realised with a grid of wires acting as the anode end of the drift region, similar to the setup of a MWPC with one field region extended to form the active volume of the TPC. The very large strength of the radial field in close vicinity of the wires leads to the creation of avalanches by incoming drift electrons. At the same time, the movement of the charge cloud in this field creates a signal on the respective wire that can be detected by the readout electronics. In the application of a TPC, the signals are instead picked up on the close-by cathode plane, which is segmented in order to provide two-dimensional positional information.

Unfortunately, just as many ions are created in the avalanche as electrons. While the latter get absorbed on the signal wire, the produced ions travel in the opposite direction into the active volume, where their presence distorts the drift field. This mechanism is called *ion backflow*. Since the ion drift velocity is several orders of magnitude smaller compared to that of the electrons, local distortions move only slowly towards the cathode. Thus, if the rate of ionising particles penetrating the active volume of the detector becomes larger than the average inverse ion drift time, a positive space charge will begin to accumulate in the active volume.

In MWPC-based TPCs it is possible to work around this problem by introducing a so-called *gate* in short distance of the amplification stage. This additional, electrically active structure allows to temporarily terminate the field lines of the drift field at the gate position. Such gating structures offer a charge opacity of $\mathcal{O}(10^{-4})$. If synchronised with a well-known time of the recorded physics event, the gate can be closed in time to absorb the back-drifting ions and prevent them from reaching the active volume above the gate. However, this strategy comes at the expense of leaving the detector blind while the gate is active. The typical time scale of a gate cycle limits the rate of an experiment employing a gated TPC to the kHz level. This fact presents a major limitation of this design and has rendered MWPC-based TPCs an ineligible choice for many modern particle-physics experiments.

The employment of GEM foils instead of wire grids for gas amplification offers the means to lift this limitation. GEM foils consist of a thin (usually $\approx 100\,\mu\text{m}$) sheet of insulating material (polyimide), clad in a conductive layer (Cu) on both sides. A regular pattern of holes (diameter and pitch $\mathcal{O}(100\,\mu\text{m})$)

penetrates all layers. Due to the small dimensions, already the application of moderate potential differences $\mathcal{O}(100\,\mathrm{V})$ between the two sides of the foil leads to field strengths sufficient for avalanche creation inside the holes. A close-up picture of a GEM foil is provided in Fig. 2.2.

Incoming drift electrons are guided into the region of the amplification field inside GEM holes by the drift field and the GEM field. On the side opposite to the incoming primary electron, the negative charge cloud is guided out of the hole using an extraction field $\mathbf{E}_\mathrm{e}$, where usually $|\mathbf{E}|_\mathrm{e} > |\mathbf{E}|_\mathrm{d}$. This asymmetric field configuration inside and outside of the holes gives rise to the crucial property of an *intrinsic* suppression of the backflow of amplification ions: Most of the field lines found inside the amplification region do not extend far into the active volume above the foil and terminate on the surface. Due to their low mobility, the ions originating from the amplification region closely follow field lines and thus have a large probability to get absorbed on the foil surface. On the other hand, the larger extraction field on the bottom side of the hole favours the extraction of the electrons. This effect is further enhanced by the much larger mobility of the electrons, which increases the probability of diffusion into the reach of the extraction field. Figure 2.3 shows the result of a microscopic simulation of the charge dynamics.

The *effective* gain G_eff of a GEM can be straight-forwardly written as the ratio of the number of amplification electrons arriving at the anode N_a^- and the number of primary ionisation electrons N_i^- arriving at the GEM:

$$G_\mathrm{eff} = \frac{N_\mathrm{a}^-}{N_\mathrm{i}^-} \quad . \tag{2.6}$$

G_eff is called "effective" because it already contains the losses caused by an imperfect electron collection efficiency $\varepsilon_\mathrm{coll}$ and extraction efficiency ε_ex of the foil, and is thus linked to the intrinsic gas gain G^* by

$$G_\mathrm{eff} = \varepsilon_\mathrm{coll} \cdot \varepsilon_\mathrm{ex} \cdot G^* \quad . \tag{2.7}$$

Neglecting any losses of charge in the detector gas, N_i^- is equal to the number of produced ions in primary ionisation N_i^+: $N_\mathrm{i}^- = N_\mathrm{i}^+ \equiv N_\mathrm{i}$.

The ion backflow can finally be defined as the ratio of the number of positive ions arriving at the cathode N_c^+ and the number of amplification electrons N_a^-,

$$IB = \frac{N_\mathrm{c}^+}{N_\mathrm{a}^-} \quad . \tag{2.8}$$

This definition of IB is convenient since it can be directly measured as the ratio of the cathode and the anode current, but other definitions exist in the literature. It is important to note that N_c^+ contains two contributions, the number of ions from primary ionisation N_i and the number of back-drifting ions from the amplification stage:

$$N_\mathrm{c}^+ = N_\mathrm{i} + \epsilon N_\mathrm{i} \quad . \tag{2.9}$$

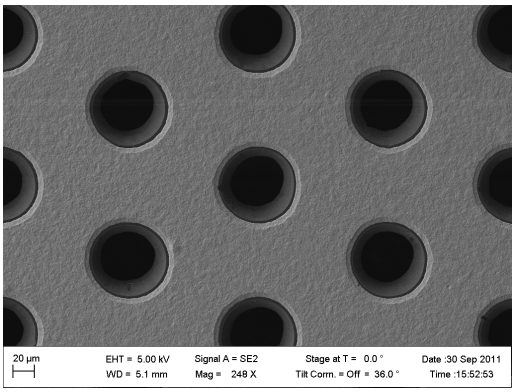

Figure 2.2: Closeup of a GEM foil used for a PixelGEM detector at the COMPASS experiment. The photograph has been provided by B. Ketzer [12].

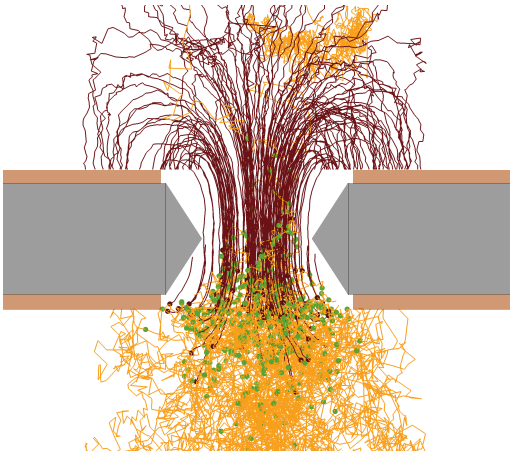

Figure 2.3: Microscopic simulation of two electrons entering a GEM hole, performed with the Garfield-/Magboltz [13] [14] software packages. Yellow lines show electron paths, brown lines those of ions, brown dots mark the positions where electron-ion pairs have been created and green dots those where excitations have occurred. The plot was taken from Ref. [15] and slightly modified.

The coefficient ϵ appearing in Eq. (2.9) thus gives the net number of ions leaking back from the amplification stage into the active volume per incoming primary ionisation electron. From Eqs. (2.6), (2.8) and (2.9) follows the relation

$$IB = \frac{1+\epsilon}{G_{\text{eff}}} \quad . \tag{2.10}$$

Under typical conditions present in a TPC, the ion backflow IB of a single GEM foil is $\mathcal{O}(1-10\,\%)$, and thus the offered suppression of ion leaking is still significantly weaker than what can be achieved with a gate.

Using more than one such foil in series in a *stack* can bring this number down to 1 % and below. It also allows to realise high values of G_{eff} of the combined stack at moderate individual GEM voltages [4]. The task of tuning the set of voltage settings of such a setup with respect to the resulting gain, stability, combined electron transparency and extraction (e.g. final energy res-

[4]The effective gain G_{eff} of the entire GEM stack is given as the product of the effective gains of the individual foils, $G_{\text{eff}} = \prod_i G^i_{\text{eff}}$.

olution) and backflow suppression quickly becomes complex. For the latter, additional effects like the geometrical alignment of the GEM holes of different layers play a decisive role. Finding an optimal trade-off between spatial as well as energy resolution, stability, and suppression of back-drifting ions has been a major effort during the design of the upgrade of the ALICE detector at the LHC [16],[17]. It has been shown necessary to employ different foil geometries within a stack of four GEMs in order to reach the design specifications of the upgraded ALICE detector.

Values of $IB \approx 1\,\%$ will still lead to a considerable accumulation of positive space charge in the active volume. However, the arising drift distortions can be expected to be mild enough that efficient track finding and fitting is still possible at moderate interaction rates. If a sufficiently accurate model of the space charge is available during these tasks, even larger distortions $\mathcal{O}(10\,\mathrm{cm})$ can still be handled. For the final ("offline") reconstruction of the data, however, an exact measurement of the actual space charge during data taking is mandatory in order to recover the native spatial resolution of the detector. Such a measurement of the space charge density requires a dedicated calibration system, and such systems have been realised ([18], [19]) in form of a high-precision array of laser beams being repeatedly fired inside the active volume. A detailed simulation study of the expected space charge, its influence on the tracking performance and a possible correction scheme for the case of the GEM-TPC for Antiprotons at Darmstadt (PANDA) has been performed and published ([15], Appendix A) by the author, using a value of $\epsilon = 4$ to characterise the backflow suppression of the GEM stack.

2.1.4 Advantages and challenges entailed by the employment of GEMs

From the general discussion of the preceding sections, the main strengths of *traditional*, MWPC-based TPCs can be summarised as follows: Like for other drift chambers, the low material budget of the gaseous active material allows the coverage of large volumes. The world's largest such detector, the cylindrical TPC of the ALICE detector at the LHC, covers a volume of little below $90\,\mathrm{m}^3$. Solid-state tracking detectors offer superior spatial resolution, but cannot be used to cover large volumes due to their high cost, the generally larger net material budget and the entailed amount of dissipated heat.

Considering the technicalities that play a role during the extraction of physical properties (see Chapter 4 for a discussion of reconstruction algorithms), another important advantage of TPCs is that they offer a large number of hits per track. This circumstance eases the task of track finding ("*pattern recognition*", cf. Sec. 4.4) considerably. Unlike wire chambers, TPCs provide space-point-like hits, and no ambiguities due to symmetries connected to drift-time measurements need to be resolved.

As the main limitation of traditional TPCs, the need of a gating structure has been identified in the previous discussion, along with the potential remedy of replacing the combination of a wire-based gas amplification and a gate by (a stack of) GEM foils. The introduction of GEMs does of course not alter the workings of a TPC from primary ionisation up to the amplification stage; However, one has to ask if the quality of the extracted information in terms of i) spatial resolution and ii) energy resolution may suffer.

The first question can safely be answered. The structure sizes of GEMs are comparable to those of MWPCs, and as such there is no additional, *a priori* limitation on the spatial resolution. The employment of GEMs as tracking detectors has been pioneered ([20],[21],[22]) at the COMPASS experiment [23] at CERN. Today, GEMs are routinely used in many other experiments and have shown to work reliably also in high-rate environments.

The remaining question regarding the expected energy resolution of a GEM-TPC is more delicate. In multi-GEM stacks already small, local variations of the spacing in between foils have a large influence on the transfer fields. This, in turn, modifies the collection and extraction coefficients, while leaving the intrinsic gain G^* unchanged (cf. Eq. (2.7)). The consequence are variations of the effective gain, which have been observed to be as large as 20 % [24]. It is clear that such variations need to be corrected for if one wishes to preserve a competitive energy resolution. An elegant method to directly measure the gain uniformity across the amplification plane even during data taking is the introduction of a suitable radioactive gas into the active volume. In Sec. 6.4 the results of such a measurement with a large GEM-TPC will be discussed. Using the obtained calibration values, the final performance regarding the measurement of the specific energy loss (see the following section) has been assessed and compared to expectation values derived from the past experience with traditional devices. The results of this study will be presented in Sec. 6.5 and have previously been published by the author [25].

2.2 Measuring the specific energy loss

Even though very little interaction of the projectile particle with the active volume is one of the defining characteristics of gas detectors, a TPC can nevertheless contribute to particle identification (PID) through the measurement of the specific energy loss ("$\mathrm{d}E/\mathrm{d}x$") along the particle trajectory. However, the correct interpretation of the experimental data is not trivial. Some of the implications are discussed briefly as the end of this section (an extensive review can be found in [26]).

A detailed analysis (published by the author in [25] and appended to this document in Appendix B) investigating the performance of the GEM-TPC for FOPI (see Chapter 3) with respect to the measurement of $\mathrm{d}E/\mathrm{d}x$ will be presented in Sec. 6.5. The utilisation of the obtained data in a global

approach towards PID will be demonstrated in Chapter 7. In order to provide a sufficiently general footing for this discussion, the most important physical concepts are explored in this section.

2.2.1 Mean energy loss: The Bethe formula

After the trajectory of a particle has been reconstructed and fitted with a mathematical model (cf. Sec. 4.5), further properties can be extracted from the hit data of such an identified particle *track*. The amplitude (charge) information along the particle trajectory can be used to infer the rate of energy loss per travelled distance through ionisation processes of the projectile particle while traversing the active volume. For heavy projectiles [5], this is the dominant channel of energy transfer in the momentum region the analysis of this work is concerned with.

In the microscopic picture, energy loss occurs in independent collisions [6] of the projectile particle with atoms in the medium, characterised by a mean free path length λ_{mf} in between consecutive events and described by Poissonian statistics. In each such collision the projectile loses energy according to the atomic properties of the medium. At the energies relevant for this discussion, hit nuclei remain intact and are not internally excited. Due to their much larger mass compared to the typical projectile, such elastic collisions can be neglected and the energy transfer is therefore dominated by collisions with shell electrons. The corresponding total collision cross section (CCS) σ is linked to the mean free path via

$$\lambda_{\mathrm{mf}} \propto \frac{1}{\sigma} \quad . \tag{2.11}$$

If enough energy is transferred to a shell electron, it is liberated from the atomic compound (*primary* ionisation). In addition, *secondary* ionisation occurs in ionisation processes induced by the liberated electrons or via metastable states of hit gas atoms (*Penning effect*). All liberated electrons contribute to the signal created in the detector by the traversing particle. The fact that these collision events and therefore the energy transfer are statistical processes has important consequences, especially for the understanding of energy loss fluctuations (discussed in Sec. 2.2.2).

In order to define a macroscopic observable we average over many such ionisation events and consider the total energy deposit ΔE over some travelled distance Δx. The underlying *mean* rate of energy loss through ionisation $\mathrm{d}E$

[5] Projectile mass much larger than the electron mass.
[6] Internal excitations of the projectile are ignored.

per travelled distance $\mathrm{d}x$ is well described by the Bethe equation [27] [7]

$$-\left\langle \frac{\mathrm{d}E}{\mathrm{d}x} \right\rangle_{\mathrm{B}} = \frac{Z\rho N_{\mathrm{A}}}{A} \cdot \frac{4\pi}{m_{\mathrm{e}}} \cdot \left(\frac{z\alpha\hbar}{\beta}\right)^2 \left[\ln \frac{2m_{\mathrm{e}}c^2\beta^2\gamma^2}{I} - \beta^2\right] \quad , \tag{2.12}$$

where

Z	atomic number of the medium,
ρ	density of the medium ($\mathrm{kg\,m^{-3}}$),
N_{A}	Avogadro's number ($\mathrm{mol^{-1}}$),
A	relative atomic mass of the medium ($\mathrm{g\,mol^{-1}}$),
m_{e}	electron mass ($\mathrm{eV}\,c^{-2}$),
z	charge multiplicity of projectile particle,
α	fine-structure constant,
$\hbar$	reduced Planck constant ($\mathrm{eV\,s}$),
c	velocity of light ($\mathrm{m\,s^{-1}}$),
β	particle velocity relative to c, $\beta = v/c$,
γ	Lorentz factor, $\gamma = 1/\sqrt{1-\beta^2}$,
I	mean excitation potential of the medium (eV).

Note that the energy loss rate as given by Eq. (2.12) depends only on the velocity β, not on the mass M of the projectile [8]. Combined with a measurement of its momentum $p_{\mathrm{p}} = \gamma M\beta c$ it is this fact that can be exploited for inferring the mass and hence identifying the projectile. For gas detectors operating at atmospheric pressure, Eq. (2.12) yields values for $\mathrm{d}E/\mathrm{d}x$ of the order of $1\,\mathrm{keV\,cm^{-1}}$, so that on relevant length scales Δx the rate of energy loss can be treated as small compared to typical projectile energies and thus

$$\langle \Delta E \rangle \simeq -\left\langle \frac{\mathrm{d}E}{\mathrm{d}x} \right\rangle_{\mathrm{B}} \Delta x \tag{2.13}$$

in good approximation.

It is worthwhile to take a detour and motivate Eq. (2.12) classically, as it helps to introduce some concepts important for the further discussion. Without loss of generality we assume the traversed material to consist of only one element [9]. Most generally, the energy loss can be decomposed as

$$-\langle \mathrm{d}E \rangle = \underbrace{\begin{pmatrix} \text{No. of } e^- \\ \text{per unit volume} \end{pmatrix}}_{(Z\rho N_{\mathrm{A}})/A} \times \begin{pmatrix} \text{Mean energy loss} \\ \text{in a single collision} \\ \text{and unit surface} \end{pmatrix} \times \mathrm{d}x \quad . \tag{2.14}$$

[7] The form given here already includes the approximation of Eq. (2.21), motivated by the following derivation. A formulation explicitly including the maximum energy transfer in a single collision can be found for example in Ref. [28].

[8] Actually, there is a subtle implicit dependency on the projectile mass M through the maximum energy transfer $\delta_{\max} \approx 2m_{\mathrm{e}}c^2\beta^2\gamma^2$ – cf. Eq. (2.21) – but this effect is negligible for projectile energies below $\sim 100\,\mathrm{GeV}$.

[9] For compound materials the physical principles are of course the same, but the individual contributions need to be properly weighted.

The first term provides the link to the macroscopic medium properties and is simply given by the density, the charge number and the atomic mass of the material. It has dimension of [length^{-3}]. The second term thus needs to have dimension [energy] [length^2] and is obtained by averaging over the collision cross section (CCS), $\sigma(E,\beta)$, differential in the transferred energy E. Thus we can write

$$-\left\langle \frac{\mathrm{d}E}{\mathrm{d}x} \right\rangle = \frac{Z\rho N_\mathrm{A}}{A} \cdot \int_0^\infty E' \, \frac{\mathrm{d}\sigma(E',\beta)}{\mathrm{d}E'} \, \mathrm{d}E' \quad . \tag{2.15}$$

To go any further from Eq. (2.15), a model for the CCS has to be chosen. The simplest of models – and the one used in the following to motivate Eq. (2.12) – is to regard the interaction of the projectile (carrying three-momentum $\mathbf{p}_\mathrm{p}$) with the medium as classical Coulomb scattering off *free* electrons. It is clear that this assumption can only be valid for energy transfers much larger than typical atomic binding energies, but it is nevertheless worthwhile to work it out. In the *rest frame of the projectile*, this scenario is equivalent to electron scattering off the heavier projectile particle: Taking into account spin effects but neglecting the recoil of the projectile, the kinematics are those of Mott scattering with

$$\left(\frac{\mathrm{d}\sigma}{\mathrm{d}\Omega} \right)_\mathrm{Mott} = \left(\frac{\mathrm{d}\sigma}{\mathrm{d}\Omega} \right)_\mathrm{R} \cdot \left(1 - \beta^2 \sin^2 \frac{\Theta}{2} \right) \quad , \tag{2.16}$$

where

$$\left(\frac{\mathrm{d}\sigma}{\mathrm{d}\Omega} \right)_\mathrm{R} = \left(\frac{z\alpha\hbar c}{2|\mathbf{p}||\mathbf{v}|} \right)^2 \cdot \frac{1}{\sin^4(\Theta/2)} \tag{2.17}$$

is the Rutherford cross section (differential in the solid angle Ω) for elastic scattering off the electromagnetic potential of a charge $z \cdot e$. In Eqs. (2.16) and (2.17) Θ denotes the deflection angle in the scattering plane, $\mathbf{p} = \hbar\mathbf{k} = \gamma m_\mathrm{e}\mathbf{v} = -\mathbf{p}_\mathrm{p}$ and $\mathbf{v}$ are three-momentum and velocity of the inbound electron (after scattering: $\mathbf{p}' = \hbar\mathbf{k}'$, $|\mathbf{p}'| = |\mathbf{p}|$).

For elastic scattering, the angle Θ is directly linked to the 3-momentum transfer $\mathbf{q} = \mathbf{p} - \mathbf{p}'$ via

$$\sin\left(\frac{\Theta}{2} \right) = \frac{|\mathbf{q}|}{2|\mathbf{p}|} \quad , \tag{2.18}$$

and from Eq. (2.16) follows the cross section differential in the transferred energy $E = \mathbf{q}^2/2m_\mathrm{e}$:

$$\left(\frac{\mathrm{d}\sigma}{\mathrm{d}E} \right)_\mathrm{Mott} = \frac{2\pi}{m_\mathrm{e}} \cdot \left(\frac{z\alpha\hbar}{E\beta} \right)^2 \left[1 - \frac{E}{2m_\mathrm{e}c^2} \left(1 - \beta^2 \right) \right] \quad . \tag{2.19}$$

Now the integral of Eq. (2.15),

$$\int_{\delta_\mathrm{min}}^{\delta_\mathrm{max}} E' \cdot \left(\frac{\mathrm{d}\sigma(E',\beta)}{\mathrm{d}E'} \right)_\mathrm{Mott} \mathrm{d}E' \quad , \tag{2.20}$$

has to be evaluated. It also has become definite: the upper bound is given by the kinematic limit of energy transfer for head-on collisions, specifically

$$\delta_{\max} = \frac{2m_e v^2\gamma^2}{1 + 2\gamma m_e/M + (m_e/M)^2} \overset{\gamma m_e \ll M}{\approx} 2m_e v^2\gamma^2 \quad , \tag{2.21}$$

where M is the mass of the projectile particle. In the scope of the classical free-electron scattering model used so far, the lower bound enters in Eq. (2.20) as a technical necessity due to the logarithmic divergence of the integral in the limit $E \to 0$. The usual physical line of argument is that $\delta_{\min}$ should mark the transition from i) the regime where the energy transfers are so small that electrons appear completely inert or only shell excitations are possible to ii) the scenario of quasi-free electrons above the ionisation threshold [10].

Assuming the identity

$$I \equiv \delta_{\min} \quad , \tag{2.22}$$

the argument of the logarithm appearing in Eq. (2.12) is in that scenario just the ratio of the maximum and the minimum energy transfer $\delta_{\max}/\delta_{\min}$ appearing as integration limits in Eq. (2.20). We will see in a moment that by assuming (2.22) we have overstepped the limits of the free electron model. I in Eq. (2.12) is called the *mean excitation energy*, and it is the only link to the atomic structure of the medium in Eq. (2.12). From the foregoing, one is tempted to take the experimentalist's point of view and regard I as a phenomenological material property absorbing all quantum-mechanical shell corrections of the target material that have been ignored so far in the scope of the free electron assumption. Tabulated values of I are available.

Performing the integral in Eq. (2.20) finally yields the functional form of Eq. (2.12), but there is still a factor 2 missing. While it is plausible that under the assumption of free, unbound electrons the obtained result should underestimate the mean rate of energy loss, recovering this factor in a classical framework is not straight forward. The remedy is of course a full quantum-mechanical description of the scattering problem, but this is not explicitly shown in this work (see, for example, Ref. [29]). Instead, the remainder of this section is concerned with outlining some key elements of such a quantum mechanical treatment that are useful for the further discussion.

When dropping the free-electron assumption and taking into account the bound atomic system in the description of the scattering process – in the first Born approximation of incoming and outgoing flat waves scattering off the Coulomb potential of the atom –, the Rutherford-like kinematics survive the transition to a quantum-mechanical description. In addition, however, the inelastic nature of scattering off the atomic shell manifests itself in atomic

[10] Another possible point of view is to regard the impact parameter b of the scattering process: for very large b (very low energy transfers) arguments of charge screening in the medium can be used to construct an equivalent cutoff.

matrix elements entering as additional form factors

$$F_n(\mathbf{q}) = \langle n| \sum_{i=1}^{Z} \exp(i\mathbf{q}\cdot\mathbf{r}_i/\hbar)|0\rangle \quad , \tag{2.23}$$

where the $\mathbf{r}_j$ denote the coordinates of individual shell electrons. The cross section for excitation into a specific atomic state $|n\rangle$ – be it discrete or a state in the continuum – is now proportional to $|F_n(\mathbf{q})|^2$. The form factors $F_n(\mathbf{q})$ thus give the conditional probability that the atom (in its ground state), receiving a momentum transfer $\mathbf{q}$, will find itself in the excited state $|n\rangle$ after the collision. In other words, they represent the additional degrees of freedom the atom has of converting a given momentum transfer $\mathbf{q}$ into shell excitations.

Lacking any preferred direction when averaging over many collisions we can simplify $F_n(\mathbf{q}) \to F_n(|\mathbf{q}|)$. The matrix elements can be related to the generalized oscillator strength (GOS) $f_n(|\mathbf{q}|)$ used in atomic physics as in

$$f_n(|\mathbf{q}|) = \frac{\hbar\omega_n}{E} \cdot |F_n(|\mathbf{q}|)|^2 \quad , \tag{2.24}$$

where $\hbar\omega_n$ is the excitation energy for the atomic state $|n\rangle$ above the ground state.

In addition, a relation between the mean excitation potential I in Eq. (2.12) and the $|F_n(\mathbf{q})|^2$ can be constructed (cf. [27], [30]):

$$Z \cdot \ln(I) \propto \sum_n f_n(0) \cdot \ln(\hbar\omega_n) \quad . \tag{2.25}$$

Again, $\hbar\omega_n$ is the energy necessary for the transition into the excited atomic state $|n\rangle$ and the sum runs over all possible such states. In principle Eq. (2.25) provides the possibility to obtain the mean excitation energy I from atomic theory. For all but the lightest elements this is of course yet again model-dependent, so the situation does not change much in terms of parameter reliance and I stays a phenomenological constant in practice.

This concludes the short detour taken to motivate the Bethe mean rate of energy loss. Additional corrections are available for Eq. (2.12), the most important being the so-called *density correction* $\delta(\beta)$ (an overview can be found in Ref. [31]). It takes into account screening effects caused by polarisation of the medium that become more and more important at higher projectile velocities due to the relativistic expansion of the electromagnetic field transverse to the direction of flight. The density correction can be derived using an oscillator model of the medium, but also effectively parametrised (cf. [32]). With this correction, Eq. (2.12) becomes

$$-\left\langle \frac{\mathrm{d}E}{\mathrm{d}x} \right\rangle_{\mathrm{B}} = \frac{Z\rho N_{\mathrm{A}}}{A} \cdot \frac{4\pi}{m_{\mathrm{e}}} \cdot \left(\frac{z\alpha\hbar}{\beta}\right)^2 \left[\ln\frac{2m_{\mathrm{e}}c^2\beta^2\gamma^2}{I} - \beta^2 - \delta(\beta)\right] \quad . \tag{2.26}$$

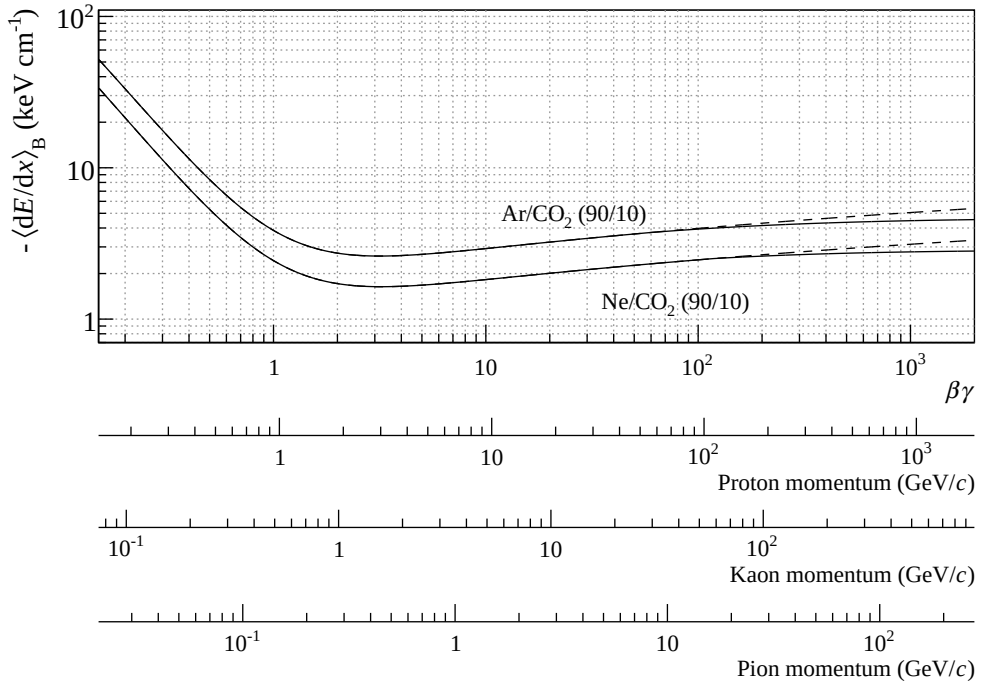

Figure 2.4: Bethe energy loss rate as a function of the projectile velocity according to Eq. (2.26) (solid lines) for two detector gas mixtures at atmospheric pressure. The molar mixture fractions are given in brackets. The dashed lines show the result without density correction according to Eq. (2.12). For computing the energy loss, the effective ionisation potential of the composite gas mixtures is calculated using the Bragg additivity rule (see for example [31]). The density correction is computed using Sternheimer's parametrisation [32] for the noble gas component.

Already, Eq. (2.26) describes experimental data for intermediate-Z materials within a few percent accuracy (cf. Ref. [28]) in the region $0.1 \lesssim \beta\gamma \lesssim 10^3$. Figure 2.4 shows the energy loss according to Eq. (2.26) as a function of the projectile velocity β for two common detector gas mixtures (which were both used during data taking with the FOPI GEM-TPC, cf. Chapter 3).

2.2.2 Fluctuations of the energy loss: Straggling functions

The discussion of Sec. 2.2 motivated the Bethe formula (2.26) describing the *mean* energy loss of fast, heavy particles in matter. The average nature of $\langle \mathrm{d}E/\mathrm{d}x \rangle_\mathrm{B}$ is explicit in Eq. (2.15). From an experimentalist's point of view – when measuring $\Delta E/\Delta x$ with a limited sample size – an important question is that of the fluctuations occurring around the average value $\langle \Delta E \rangle$. The distribution of ΔE around this mean value will turn out to be completely

defined by the CCS σ, so we shall turn our attention to the cross-section model on the single-collision level.

The fundamental starting point of a realistic model can be the discussion leading to Eq. (2.24): treating the scattering process quantum-mechanically, the atomic wave functions enter the cross-section model as a set of inelastic form factors $f_n(|\mathbf{q}|)$, containing the shell-excitation degrees of freedom. As remarked earlier, closed solutions for the atomic wave functions exist only for the lightest elements. For heavier atoms, effective models have to be used to parametrise the $f_n(|\mathbf{q}|)$. This fundamental approach of modelling the CCS is usually referred to as the *Bethe-Fano* model.

An important simplification of the above arises from the fact that in the limit of small momentum transfer $\mathbf{q}$ the GOS approaches the (optical) dipole oscillator strength (DOS) f_n:

$$\lim_{\mathbf{q}\to 0} f_n(|\mathbf{q}|) = f_n \quad , \tag{2.27}$$

where

$$f_n = \frac{\hbar\omega_n}{E} \cdot |\langle n| \sum_{j=1}^{Z} \mathbf{r}_j |0\rangle|^2 \quad . \tag{2.28}$$

The above can be immediately checked by performing a series expansion of the exponential in Eq. (2.23).

The f_n are proportional to the cross section for photo absorption as long as the photon wavelength exceeds the size of the atomic system, and are as such experimentally accessible. Thus, approximating the $f_n(|\mathbf{q}|) \approx f_n$ [11] opens the appealing possibility to model the CCS with experimental data. This method is commonly known as fermi virtual photon (FVP) or photo absorption ionisation (PAI) model [33] and widely used, e.g. for simulation purposes in particle physics (GEANT4, cf. [34]) or material science. Figure 2.5 shows a direct comparison of the Bethe-Fano and FVP/PAI models.

With sufficiently exact models for the CCS $\sigma(E,\beta)$ in place, we can move on to examine the fluctuations around the mean energy loss according to Eq. (2.13) on the microscopic level. In each collision, the probability to transfer a certain amount of energy follows $\mathrm{d}\sigma(E,\beta)/\mathrm{d}E$. The energy loss ΔE_{N_c} for exactly N_c collisions is hence distributed according to the N_c-fold convolution of $\sigma(E,\beta)$, $\widetilde{\sigma}_{N_\mathrm{c}}(E,\beta)$. It can be calculated iteratively as follows [26]:

$$\widetilde{\sigma}_{N_\mathrm{c}}(\Delta E,\beta) = \int_0^E \sigma(E',\beta) \cdot \widetilde{\sigma}_{N_\mathrm{c}-1}(E-E',\beta)\,\mathrm{d}E' \quad , \tag{2.29}$$

defining $\widetilde{\sigma}_0(\Delta E,\beta) = \delta(\Delta E)$ and $\widetilde{\sigma}_1(\Delta E,\beta) = \sigma(E,\beta)$.

[11] More correctly: f_n and a delta function, cf. Ref. [26] for details.

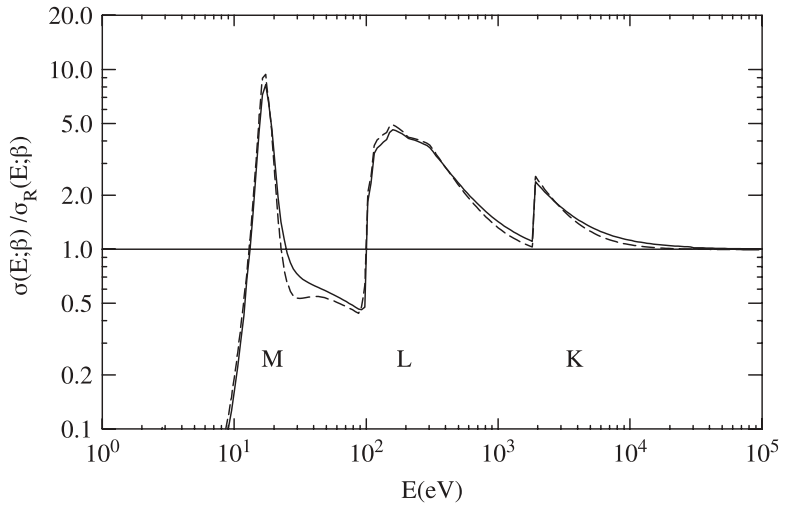

Figure 2.5: Comparison of the inelastic Bethe-Fano cross section (solid line) and the FVP/PAI cross section (dashed line) normalised to the Rutherford cross section (2.17). The calculations have been performed for single collisions of MIPs ($\beta\gamma = 4$) in Si. The figure was taken from Ref. [26] and slightly modified.

Furthermore, the number of collisions N_c in the slice of material of thickness Δx is distributed following Poissonian statistics,

$$P(N_\mathrm{c}; \Delta x, \lambda_\mathrm{mf}) = \frac{(\Delta x/\lambda_\mathrm{mf})^{N_\mathrm{c}}}{N_\mathrm{c}!} \cdot \exp(-\Delta x/\lambda_\mathrm{mf}) \quad , \tag{2.30}$$

which is in turn linked to the collision cross section (CCS) through the mean free path length $\lambda_\mathrm{mf} = \lambda_\mathrm{mf}(\beta)$ as given by Eq. (2.11).

Putting everything together, the total ionisation energy loss ΔE for a material slice of thickness Δx is distributed following the sum of all $\widetilde{\sigma}_{N_\mathrm{c}}(\Delta E,\beta)$ weighted by their Poissonian probability for having exactly N_c collisions:

$$f(\Delta E; \Delta x,\beta) = \sum_{N_\mathrm{c}=0}^{\infty} P(N_\mathrm{c}; \Delta x, \lambda_\mathrm{mf}(\beta)) \cdot \widetilde{\sigma}_{N_\mathrm{c}}(\Delta E,\beta) \quad . \tag{2.31}$$

The mean value $\langle \Delta E \rangle$ is given by Eq. (2.13). The distributions $f(\Delta E; \Delta x,\beta)$ are called *straggling functions* [12]. They are completely defined by $\sigma(E,\beta)$. From Eq. (2.31) one can expect the Poissonian contribution – with relative width $(1/\sqrt{\lambda_\mathrm{mf}})$ – to become more and more dominant for very small number of collisions N_c (thin absorbers).

An example for such a case of a very thin slice of material (1 µm of Si) is shown in Fig. 2.6a (solid line). The distinct peaks visible at small ΔE

[12]Following the notation proposed in Ref. [26] with $\Delta E \equiv \Delta$.

correspond to the convoluted cross sections $\widetilde{\sigma}_{N_c}(E,\beta)$ for $N_c = 1, 2, 3, \ldots$, each weighted by the Poissonian probability for N_c and summed up according to Eq. (2.31). Towards larger N_c – or ΔE, respectively – the structure in the straggling spectrum washes out. For $\Delta x = \mathcal{O}(1\,\mathrm{cm})$ and gaseous material we have $N_c \sim 30$ and can expect the peak structure from small N_c to vanish in the straggling distribution. Figure 2.6b shows such a case obtained for minimally-ionising particles with $\beta\gamma = 3.6$ traversing 1.2 cm of Ar (solid line, normalised). One observes an asymmetric, long-tailed distribution with a most probable value ΔE_{mp} clearly different from its mean value $\langle \Delta E \rangle$. Also shown in Fig. 2.6b is the cumulative straggling function $F(\Delta E) = \int_0^{\Delta E} f(\Delta E)$, which gives an indication of the large weight of the distribution tail outside the plotted scale, extending up to the kinematic limit $\delta_{\max} \approx 2m_e c^2\beta^2\gamma^2 \gg \langle \Delta E \rangle$. It should be noted that the tail towards very large energy transfer is also experimentally not accessible: High-energetic "*delta electrons*" might leave the detector, escape detection and/or correct association by the tracking algorithms, or – depending on track geometry – saturate the dynamic range of the readout electronics [13]. These effects can be regarded as an effective cutoff in the experimental treatment of Eq. (2.12). Accordingly modified models of the specific energy loss ("*restricted energy loss*") are available (see, for example, Ref. [11]), but are not further discussed in this work.

The dashed curves shown both in Figs. 2.6a and 2.6b follow the so-called *Landau function*, a name which is commonly misused as a synonym for the straggling functions $f(\Delta E; \Delta x, \beta)$ in the field of experimental particle physics. The Landau approach [35] aims to describe fluctuations in energy loss as well, but is derived specifically using the Rutherford cross section (2.17). It is thus clear that we cannot expect good agreement to straggling functions based on much more realistic CCS models for very small N_c (Fig. 2.6a). However, also in the case of larger N_c when the shell effects in the CCS are starting to be washed out in the final straggling function according to (2.31), Fig. 2.6b shows that the Landau function is distinctively more narrow than the calculated $f(\Delta E; \Delta x, \beta)$. The reason for this behaviour lies in the connection to the mean free path λ_{mf} and hence the number of collisions N_c as given by Eq. (2.11): the Rutherford cross section model underestimates (overestimates) λ_{mf} (N_c) as opposed to more realistic CCS models. For these, the Poissonian contribution to the straggling function via N_c with (relative width $= 1/\sqrt{N_c}$) leads to the observed broadening.

2.2.3 Experimental considerations

The basic connection to the actual measurement of the rate of energy loss of a detected particle is provided by Eq. (2.1). Under idealised conditions, all of the "created" charges reach the readout where they are amplified and finally

[13] Thus, they also present a limit to the spatial resolution.

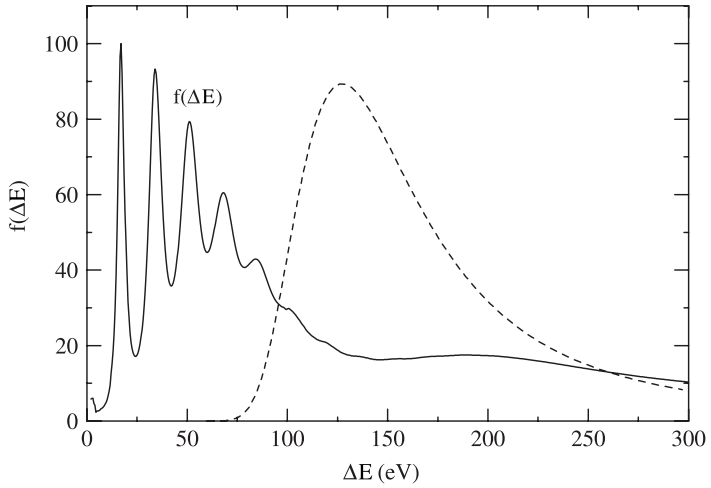

(a) 2 GeV protons, 1 µm Si. The mean value for the energy loss as obtained from Eq. (2.12) is $\langle \Delta E \rangle \sim 400\,\mathrm{eV}$.

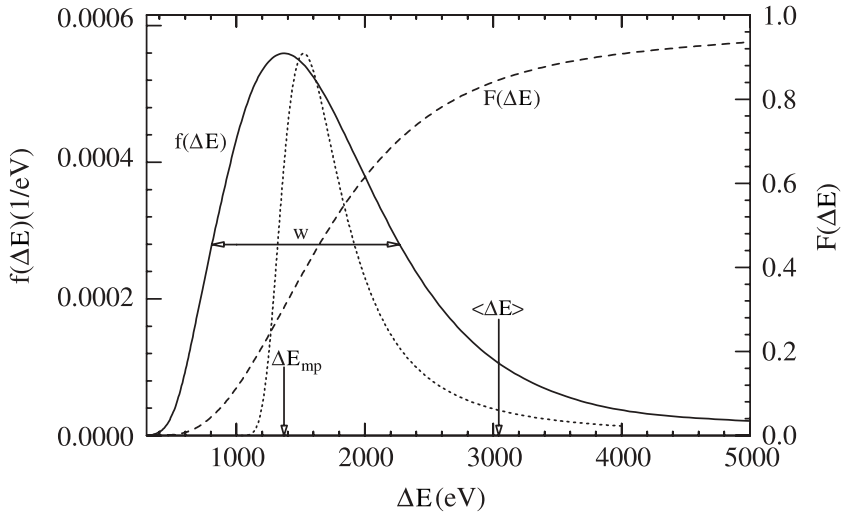

(b) Minimally-ionising particles, 1.2 cm Ar.

Figure 2.6: Calculated straggling functions for two different scenarios. The plots are taken from Ref. [26] and slightly modified in order to match the definitions as used in the text. Both straggling functions have been obtained with the photo absorption ionisation (PAI) model for the collision cross section.

measured as a signal current proportional to the initial energy deposit and we can write

$$\text{signal amplitude} \propto \Delta E \quad . \tag{2.32}$$

Several mechanisms degrade this proportionality:

- loss of charge carriers due to impurities of the detector gas,
- local variations or unstable gain during gas amplification,
- non-linearities of the readout electronics,
- threshold effects introduced by noise suppression.

As already discussed at the end of Sec. 2.1.1, the structure size of typical readout geometries used in traditional TPCs – as well as the FOPI GEM-TPC, described in the following chapters – is typically much larger than the free path length λ_{mf}, which is $\mathcal{O}(100\,\mu\mathrm{m})$. Under the additional influence of diffusion, the deposited charge is effectively spread out across the readout plane, leading to a loss of spatial information and an enhancement of the impact of undesirable threshold effects. Consequently, any attempt to recover the energy loss rate by measuring the straggling functions inevitably involves a macroscopic averaging over several measured hits: For each track, a set of amplitude/Δx pairs is available, where the readout structure size presents the lower limit to Δx.

The situation shown in Fig. 2.6b thus gives a good impression of what to expect. When approaching the task of identifying particles – e.g. assigning probabilities for different mass hypotheses to a measured particle track – one is ultimately interested in finding a single, stable estimator for the straggling function based on a limited sample size of measurements. Obviously, the mean value $\langle \Delta E \rangle$ of a distribution similar to the one shown in Fig. 2.6b is not a good estimator. Rather, one would like to extract the characteristic most probable value ΔE_{mp}, but this requires a full reconstruction of the underlying straggling distribution and becomes increasingly difficult and unstable with smaller sample sizes. Due to the long tails towards high energy deposits, this turns out to be problematic even for very large detectors. An alternative method of extracting a stable estimator for the specific energy loss is making use of the *truncated mean*, which will be discussed in Sec. 6.5.1.

2.3 Continuous operation: The TPC as *tracking pipeline*

In the previous sections, the employment of GEM foils instead of the classical MWPC-based gas amplification has been motivated as a solution that potentially makes TPCs an eligible choice also for high-rate experiments. The remaining chapters of this work will document the development of such a GEM-based TPC, as well as its successful participation in a physics campaign

as part of the FOPI spectrometer, however still operating at low interaction rates.

A very important future application of such a device operating in a high-rate environment is the ALICE TPC: After the LHC will return to operation in 2018, the ALICE detector will face Pb-Pb collisions at a rate of $\sim 50\,\mathrm{kHz}$. At such high rates, the average time in between collision events becomes smaller than the maximum electron drift time in the chamber ($\sim 100\,\mu\mathrm{s}$), and a gated operation is no longer possible. Instead, the chamber has to be read out *continuously* in the fashion of a *tracking pipeline*. Motivated by recent technological advancements such as the one documented in the work at hand, the ALICE collaboration took the decision to upgrade the – originally MWPC-based – TPC tracker with GEM technology in order to meet these requirements [16],[17].

The continuous operation of a GEM-TPC at such high interaction rates entails important consequences for the whole spectrometer. First of all, higher interaction rates directly translate into higher data rates for all detectors. As the system with the largest contribution to the data output of the combined spectrometer, the ALICE TPC will produce $\sim 1\,\mathrm{TB\,s^{-1}}$ of raw data in the physics environment after the upgrade of the LHC. It is obvious that such vast data rates cannot be persisted, and thus sophisticated real-time ("online") algorithms are required for the decision whether to keep or discard data [14]. In terms of algorithm performance and computing-power requirements, this alone is a serious challenge.

Secondly, these algorithms will have to operate stably under harsh conditions: Several thousands of tracks from multiple collision events with displaced primary vertices will be stored in the active volume of the TPC at any given time. Since the absolute drift distance belonging to the registered signals cannot be determined with TPC data alone (cf. Sec. 2.1.2), any real-time trigger decision is only possible in combination with information provided by the surrounding tracking systems. This has to be reflected in the layout and organisation of the data aquisition (DAQ) system.

Track distortions due to space-charge buildup present an additional challenge: In the discussion of Sec. 2.1.3 it has been stated that the suppression of ion backflow, provided intrinsically by GEMs, is several orders of magnitude lower than that offered by a classical gate. A certain level of back-drifting ions thus cannot be avoided, and distortions of the subsequent electron drift are inevitable. For ALICE, the expected displacements are of the order of 10 cm, and thus three orders of magnitude larger than the intrinsic spatial resolution of the detector. A high-precision measurement of the underlying distortion profile is thus required for the analysis of physics data, if the performance of the detector is to be maintained after the upgrade. It is, however, not sufficient to have such a model available after data taking, as already the

[14] This is already true for the LHC detectors prior to the upcoming upgrade, but the requirements become more critical.

real-time algorithms mentioned earlier have to work under these conditions. For ALICE, a two-stage strategy is foreseen [16]: During data taking, a coarse map of the space charge – updated every $\sim 10\,\mathrm{m}$ – will be used for correction of drift distortions, facilitating the work of the real-time algorithms. For the final analysis of physics data, a high-precision map must be used. It will be calculated using external tracking information in time windows of a few ms width.

Chapter 3

A large GEM-TPC for FOPI: The S339 experiment

In this chapter, a large GEM-TPC detector [36] will be introduced, which was built to serve as a proof of principle in the context of research and development [37] conducted for the future PANDA experiment. At the same time, it has been designed specifically to allow its integration into the FOPI spectrometer (located at the Gesellschaft für Schwerionenforschung (GSI), Darmstadt, Germany) for the evaluation of its performance. The construction of the device was finished towards the end of 2010. In 2011, the detector successfully participated in a two-weeks physics campaign at the FOPI experiment (π^- beam of 1.7 GeV/c momentum, impinging on a number of different nuclear targets; GSI experiment number S339). The data taken during this campaign presents the foundation of the performance and physics analysis to follow in the remaining chapters of this work.

Section 3.1 will introduce the reader to the specifications of the GEM-TPC hardware. The focus will rest on the characteristics that are conceptually critical for the extraction of physical properties: the material budget of the device, the GEM stack used for gas amplification and the structure and performance of the readout.

Section 3.2 will briefly introduce the FOPI spectrometer, which serves as the reference system in the evaluation of the performance of the GEM-TPC detector. The FOPI spectrometer had been used to investigate heavy ion collisions in the region of low temperature and moderate nuclear matter density at the Schwerionen-Synchrotron (SIS) accelerator [1] for more than two decades, before it was finally dismantled in 2013. It is thus treated as a self-consistent, complete system in the scope of this work. Consequently, only the most important technical features of the spectrometer will be listed in the following. In the same way, the data provided by FOPI and the its data-processing software are – *a priori* – treated as a final and complete, external input to the analysis

[1] German for "heavy-ion synchrotron".

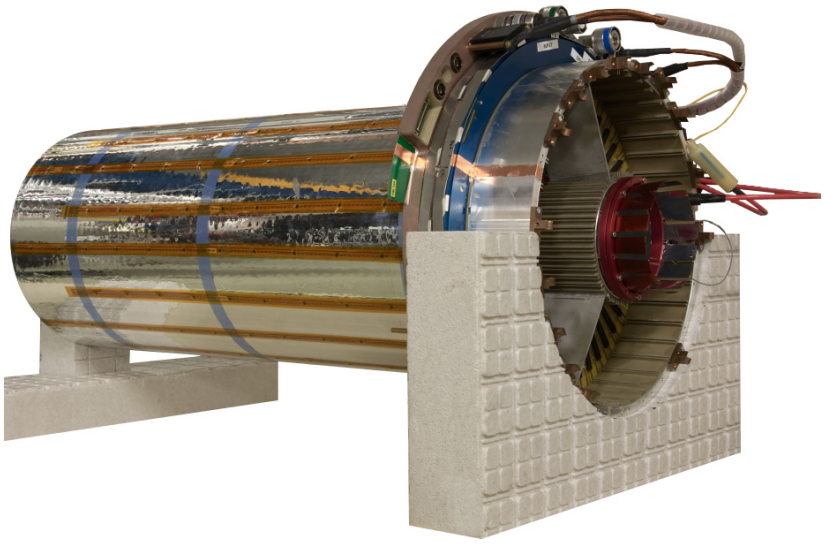

Figure 3.1: Photograph of the large GEM-TPC detector for the FOPI experiment, resting on a supporting structure. At the upstream end of the detector, the support flange for external connections, the holding structure for the readout electronics and the opening of the inner field cage cylinder are visible.

presented in the subsequent chapters. The limitations of this assumption will be discussed in Chapter 5.

3.1 The GEM-TPC detector

The construction of the GEM-TPC detector was completed in the end of 2010. Its combined gas- and field-cage vessel consists of two concentric cylinders and measures 727.8 mm in length. It has an outer (inner) diameter of 308.0 mm (104.0 mm), making it the detector with the largest active volume of its kind at the time. This choice of dimensions allowed the installation of the detector inside the inner bore of the central tracking detector of the FOPI spectrometer, as will be discussed in Sec. 3.2.

An extensive description of the design specifications of the GEM-TPC detector has already been provided elsewhere (cf. Refs. [36], [37]), and thus the discussion of technicalities will be kept to a minimum in this work. In the following, a brief overview over the key components will be provided, and the section will be closed with a list of all settings and parameters in effect during the 2011 beam time (Tab. 3.1). Figure 3.1 shows a picture of the detector, taken shortly before the integration into the FOPI setup.

3.1.1 Field cage

The mechanical structure of the GEM-TPC has been optimised aggressively towards a minimal material budget [38]. The supporting core (2 mm thickness) of the vessel (cylindrical walls and downstream end cap) is made of Rohacell^{TM}, thin layers of polyimide act as insulating material. The full composition of the field cage can be found in Tab. 1.11 of Ref. [37]. Figure 3.2 shows the average material budget X/X_0 in units of the respective radiation length of the GEM-TPC detector (including gas) in the r-z-plane cut. The numbers are computed using a detailed software model of the material distribution (cf. Fig. 3.5). For a large part of the acceptance, a value below 1 % is reached.

The drift field is formed by an array of 700 copper rings with 1.5 mm pitch along the symmetry axis of the detector. The potential of each strip is defined by a resistor chain. At a potential difference between cathode and anode of the field cage of $U_\mathrm{d} \approx 30\,\mathrm{kV}$, the design drift field strength of $E_z = 400\,\mathrm{V\,cm^{-1}}$ is reached. Due to mechanical damage of the field cage, suffered at the gas inlet during the commissioning phase, the field strength had to be reduced to a final value of $E_z = 234\,\mathrm{V\,cm^{-1}}$ during the physics campaign. This circumstance limited the available readout window of the detector to $\sim 75\,\%$ of its physical drift length (cf. Sec. 3.1.3 and Fig. 3.6). Additional problems were caused by short-circuited strips near the cathode, which lead to static distortions of the drift field. This topic will be revisited in Sec. 6.1.

3.1.2 Amplification stage

The basic principles of charge amplification and transport in a GEM have already been discussed in Sec. 2.1.3. Gas amplification in the FOPI GEM-TPC is realised with a stack of three identical GEM foils produced at CERN. Each foil is segmented into eight sectors, which are wired individually. This choice was made in order to reduce the risk of damaging the foils in case of a discharge. The foils have a thickness of 50 µm and a hole pitch of 140 µm.

Figure 3.3 provides a schematic view of the GEM stack. The positioning of the detector components is given in TPC detector coordinates (u,v,w), where u and v span the pad plane and w is anti-parallel to the drift direction [2]. The relation between the TPC coordinate frame and global spectrometer coordinates (x,y,z) will be covered in Sec. 4.7. The potential difference between the cathode and the field cage ring closest to the readout ("last strip") defines the drift field. The gain of each individual foil is determined by the field strength in the holes and thus controlled by the difference in potential between the two foil surfaces. The charge clouds exiting the amplification region present in the holes are guided towards the subsequent GEM layer by the transfer field, which is in turn defined by the voltage difference between the bottom and top

[2] If no external magnetic field is present or $\mathbf{E} \parallel \mathbf{B}$.

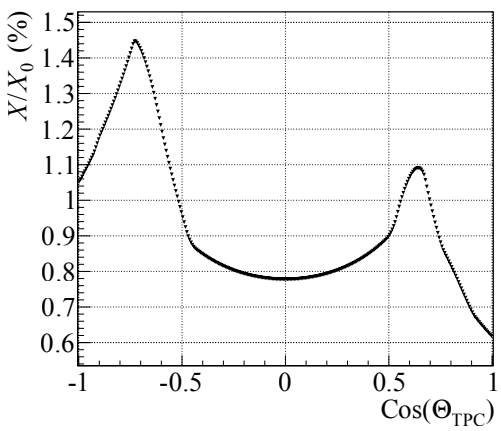

Figure 3.2: Material budget in units of the radiation length of the TPC vessel (including the detector gas) as a function of the scattering angle Θ_{TPC} (straight-line tracks originating from the nominal target position), and averaged over the azimuthal angle. The values are obtained from a realistic software model of the detector geometry (cf. Fig. 3.5).

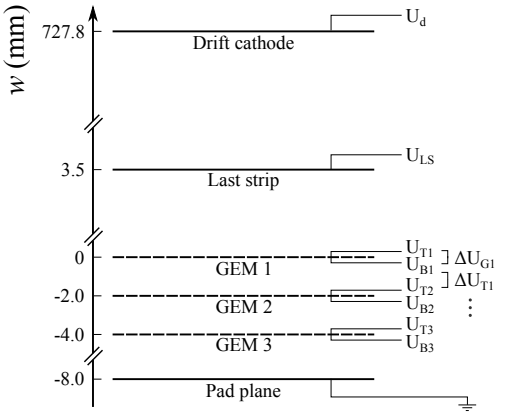

Figure 3.3: Schematic view of the GEM stack. The gain of each GEM i is determined by the potential difference between the top and bottom of the foil, $\Delta \mathrm{U}_{\mathrm{G}i} = \mathrm{U}_{\mathrm{T}i} - \mathrm{U}_{\mathrm{B}i}$. In between the amplification layers (and the pad plane), the charge clouds travel in *transfer fields* defined by $\Delta \mathrm{U}_{\mathrm{T}i} = \mathrm{U}_{\mathrm{B}i} - \mathrm{U}_{\mathrm{T}i+1}$ and the foil spacing. See Sec. 4.1.3 for the definition of the coordinate frame.

of the two neighbouring foils and the foil spacing.

The GEM settings used during the S339 experiment are given in Tab. 3.1. A direct measurement of the effective gain G_{eff} of the full stack will be presented in Sec. 6.4. The shown set of parameters has been adapted as a stable, conservative solution from earlier measurements performed with a smaller prototype detector [39], but has not been systematically optimised with respect to all observables, in particular the ion-backflow suppression.

3.1.3 Readout

A somewhat peculiar feature of the GEM-TPC detector for FOPI is the geometry of the readout plane. As shown in Fig. 3.4, the pickup electrodes ("pads") feature a hexagonal shape, resulting in a highly symmetric plane geometry. The pad plane consists of 10,254 identical such pads, the circumscribed circle of each has a radius of 1.5 mm. This pad size has been chosen based on results from simulation studies conducted for the PANDA TPC: It could be shown that reducing the pad size below this value does not further improve the spatial resolution of the detector, which is at this point already limited by diffusion (as discussed at the end of Sec. 2.1.1). However, a much higher magnetic field

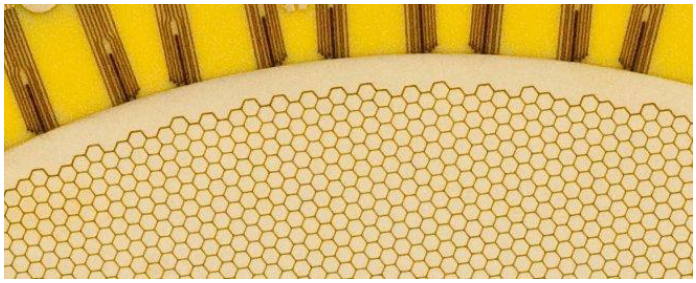

Figure 3.4: Detail of the readout plane of the FOPI GEM-TPC. Shown is the surface facing the inside of the detector vessel.

strength (2.0 T compared to 0.6 T in the FOPI setup) had been used in this study. The design of the pad plane is detailed in Ref. [40].

Signals on the pads are read out using the AFTER ASIC [41], which has originally been designed for the T2K experiment [42]. The AFTER chip features a (low-noise) charge preamplifier and a 511-cell analogue buffer per channel with adjustable sampling frequency and shaping time. Of the 72 channels of each chip, 64 are externally connected; Four of the remaining, unconnected channels are used for common-noise correction.

The AFTER units are mounted on double-sided, custom-made printed circuit boards (PCBs) in groups of four. In total, 42 such front-end cards are connected to the readout plane, each serving $64 \times 4 = 256$ pads. A recent, in-depth description of the AFTER ASIC and the front-end boards can be found in Ref. [43]. During data taking, the AFTER chips are continuously sampling the signals registered by the detector. Upon receiving an external trigger signal, the information stored in the analogue buffer is read out and digitised by 11-bit analog-to-digital converters (ADCs). Finally, baseline subtraction and zero suppression of the signals are performed using Virtex$^{\text{TM}}$-4 field-programmable gate arrays (FPGAs) mounted on GeSiCa [44] boards adopted from the COMPASS experiment [23], [45]. The combined noise performance of the entire readout chain has been evaluated to be below $700\,e^-$ equivalent charge at a sensitivity of $394\,e^-$ per ADC channel. Additional technical details concerning the electronics used for reading out the GEM-TPC detector can be found in Tab. 3.1 and Ref. [46]. The strategy used for combining the two data streams from the GEM-TPC and the rest of the FOPI spectrometer will be briefly introduced in Sec. 3.3.

The successful operation of a TPC crucially depends on the stability and homogeneity of the temperature distribution inside the active gas volume. The front-end boards carrying the AFTER chips present a localised, close-by source of heat, and their dissipated power (≈ 3 W per chip) thus needs to be cooled away efficiently. During data taking in the S339 setup, a water-based cooling system was used to keep the front-end cards at room temperature. The technical details of the cooling scheme can be found in Ref. [37].

Detector:	
Drift length	727.8 mm
Field cage inner ⌀	104.0 mm
Field cage outer ⌀	308.0 mm
Drift gas	Ar/CO_2 (90/10), 1 atm pressure
Drift field & velocity	$E_d = 234\,V\,cm^{-1}$, $v_d = 1.65 \cdot 10^{-3}\,cm\,ns^{-1}$
Effective gain G_{eff}	$\sim 1 \cdot 10^3$
GEM geometry	50 µm thickness
	140 µm pitch, 70 µm hole ⌀
Gaps between foils /	2 mm; 2 mm
last foil and readout	4 mm
ΔU_{G1}, ΔU_{G2}, ΔU_{G3}	324 V, 296 V, 259 V
ΔU_{T1}, ΔU_{T2}, ΔU_{T3}	604 V, 604 V, 1208 V
Readout granularity	10,254 hex. pads
Electronics:	
Type	AFTER ASIC / 11-bit ADC/ Virtex^{TM}-4 FPGA
Sampling clock	15.55 MHz
Buffer width	511 bins
Peaking time	$\approx$ 116 ns
Dynamic range	120 fC (11-bit ADC)
Sensitivity s	394 e^- per ADC channel
Mean noise σ_N	678 e^- (root mean square (RMS): 126 e^-)
Input capacitance	13 - 16 pF per pad
Threshold	4.5 σ_N (per channel)

Table 3.1: Key parameters of the GEM-TPC during the S339 experiment. For the definitions of the GEM voltages the reader is referred to Fig. 3.3.

3.2 The FOPI spectrometer

The aim of this section is to provide basic information on the detector systems of the FOPI spectrometer that are relevant for the analysis presented in this work. The FOPI spectrometer had been completed at GSI (Darmstadt, Germany) in a multi-stage process during the years of 1990 - 1995. In 2007, it was augmented with a new time-of-flight (TOF) system based on Resistive Plate Chambers (RPCs), offering an excellent TOF resolution of $\sigma_t < 100$ ps. Original descriptions of the spectrometer can be found in Refs. [47] and [48], a recent overview including the RPC is provided in Ref. [49]. FOPI was finally dismantled in 2013.

The FOPI spectrometer of 2011 is a detector system with close to 4π-solid-

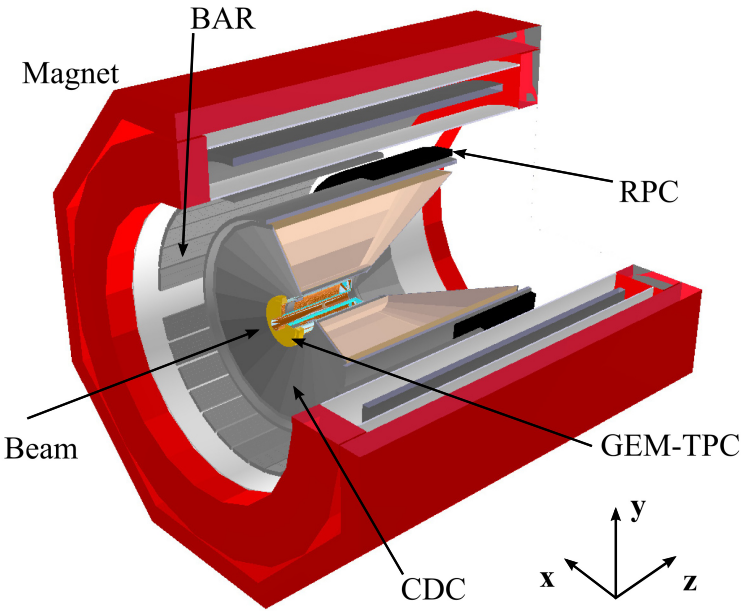

Figure 3.5: Software model of the FOPI spectrometer including the GEM-TPC. All active and passive detector components are included using their proper dimensions and material composition. This very information about the material distribution is also used during track fitting to model energy loss and uncertainties arising from multiple scattering, cf. Sec. 4.5.

angle acceptance. It operates in a 0.6 T solenoidal magnetic field for track bending, formed by a superconducting magnet. Figure 3.5 provides a three-dimensional model of the FOPI system, showing only the detector systems that will be used in the analysis presented in this work. Figure 3.6 provides a schematic of the cross section in the r-z plane.

For the data analysis to follow in the remaining chapters of this work, only a subset of the FOPI detectors is used: the central drift chamber (CDC) for tracking and the barrel scintillator array as well as the RPC system for particle identification using time-of-flight information [3]. An overview over the specifications of these systems is provided below, further details can be found in the original publications.

3.2.1 Tracking: The CDC

The FOPI spectrometer in the 2011 setup features two pictorial tracking systems: the central drift chamber (CDC) for particles with transverse momenta

[3] In contrast to the standard processing of FOPI data, the measurements from the TOF detectors are used as additional spatial hits in the track fits performed in a TPC-combined analysis. See Sec. 4.5.5 for details.

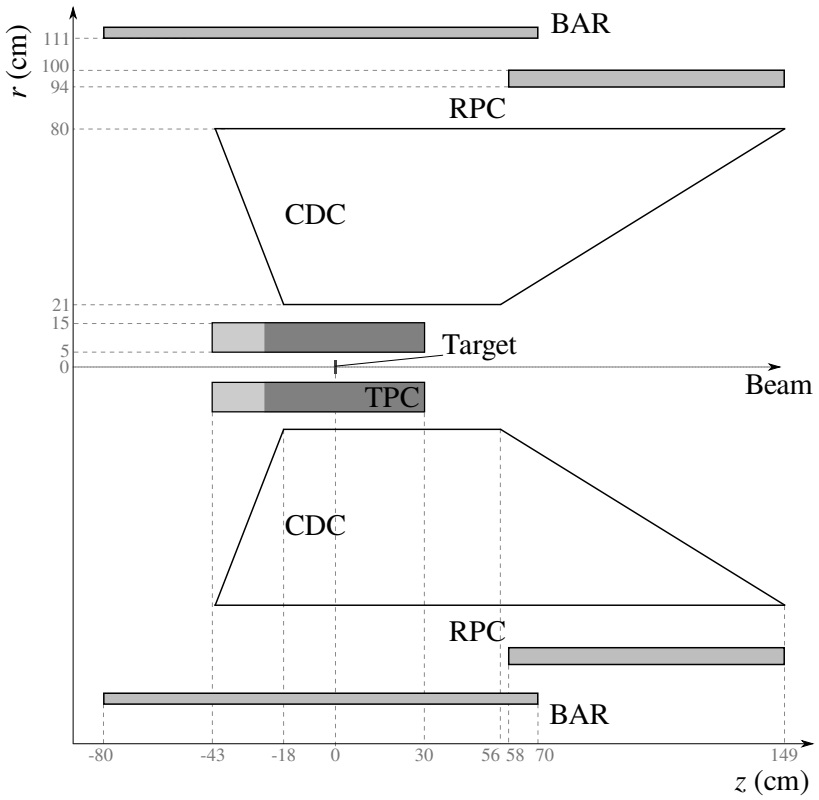

Figure 3.6: Cross section (schematic) of the TPC-augmented FOPI spectrometer, showing all detectors contributing to the analysis presented in this work. The effective readout window of the TPC (cf. Sec. 3.1.1) is additionally highlighted in darker colour. All given dimensions are rounded values.

of $\approx 20\,\mathrm{MeV}/c$ and above, and the Helitron covering the forward region. Only the first is relevant for the further analysis presented in this work.

The CDC (installed in 1992, description available in Ref. [47]) is a jet-drift-chamber detector with an inner (outer) radius of 21 cm (80 cm). In the azimuthal plane it is segmented into 16 identical sectors, each housing a planar array of a set of 60 sense wires and 61 potential wires, alternating along the array. Each of the wires is aligned parallel to the beam axis. Due to the peculiar shape of the detector in the r-z-cross section, their length varies considerably (between 86 and 190 cm). The geometrical design of a single CDC sector and the resulting electrical field configuration is shown in Fig. 3.7. The chamber is operated with a mixture of Ar, Isobutane and CH_4 at slightly above atmospheric pressure.

The drift velocity of electrons outside the gas amplification region of the wires is $v_\mathrm{d} \approx 40\,\mu\mathrm{m\,ns}^{-1}$ (drift field: $\approx 800\,\mathrm{V\,cm}^{-1}$). Once close enough to the wires, the arriving ionisation charges lead to the creation of avalanches, which induce signals on the sense wires. Using v_d and the measured drift time (plus

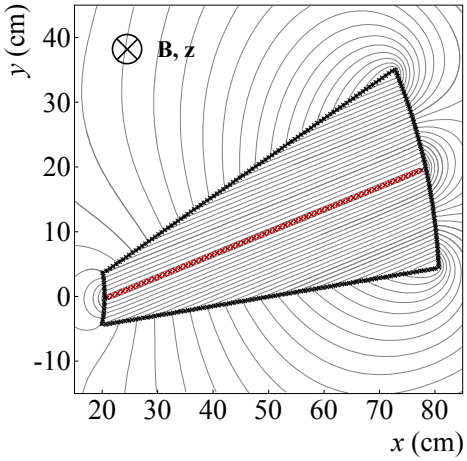

Figure 3.7: Geometrical layout of a CDC sector. Crosses mark potential wires, and red circles mark sense wires. Grey lines show surfaces of constant potential. The plot was taken from Ref. [50] and its labelling slightly modified, with the kind permission of Dr. M. Merschmeyer.

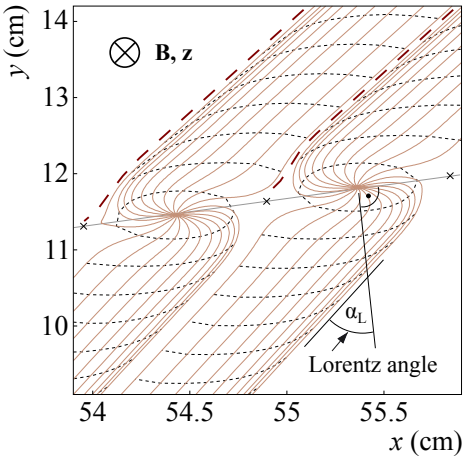

Figure 3.8: Due to the presence of the magnetic bending field, the drift direction is rotated away by an angle α_L compared to the situation at $\mathbf{B} = 0$. Brown lines show simulated drift paths and broken black lines show surfaces of equal drift time. The region in which all electrons will drift to one particular wire is called a *drift cell*. The broken red line highlights one such cell. The plot was taken from Ref. [50] and has been slightly modified.

a time offset t_0 of the readout electronics), the closest distance of the projectile particle to the wire can be determined. The functional relation between drift time and travelled distance $r_\mathrm{d}(t)$ needed for this calculation is assumed to be linear. Such a measurement of a distance leaves a left-right ambiguity with respect to the wire plane for the resulting tracks ("*mirror tracks*"). To be able to resolve this ambiguity, the wire planes are rotated out of the r-z plane by 8°. This breaking of azimuthal symmetry in the CDC detector geometry allows the rejection of mirror tracks using vertexing constraints during data processing by the FOPI software.

The exact values of the drift velocity v_d and the timing offset t_0 need to be determined in a dedicated calibration procedure. Apart from these, another quantity requires calibration: Due to the fact that the drift plane of the electrons in the CDC is aligned with the bending plane due to the magnetic field, the drift paths inside the CDC sectors are no longer perpendicular to the wire planes. Instead, they are effectively rotated away due to the Lorentz force by the *Lorentz angle* α_L. The situation is visualised in Fig. 3.8.

The parameters t_0, v_d and α_L are calibrated using tracks with large transverse momentum as part of the FOPI feature extraction procedure. In order to find the optimal settings, track offsets at sector boundaries are minimised. The values for t_0, v_d and α_L are *a priori* understood as external parameters of the TPC-combined feature extraction. It will be shown in Chapter 5, however, that this calibration does not yield optimal values.

Different values for the point resolution of the CDC have been cited in the past: While a first, synthetic measurement with laser beams yielded a point resolution in the azimuthal plane of $\sigma_{xy} \lesssim 300\,\mu\mathrm{m}$ [51], it has been stated to be "better than 500 µm" more recently [50]. The hit position along the wire direction is reconstructed using the fractional charge detected on both ends of the wire. The associated resolution is considerably worse and of the order of 10 cm. The actual values used for the combined feature extraction will be given in Sec. 4.5.5.

3.2.2 Time-of-flight systems: BAR and RPC

Originally, the barrel part of the FOPI TOF system consisted only of one array of 180 scintillator detectors, each 240 cm long and 3 cm wide. The scintillator modules were mounted at a radial distance of 111 cm with respect to the beam axis and covered the angular window $45° < \Theta_\mathrm{lab} < 140°$, Θ_lab denoting the scattering angle in the (FOPI) laboratory frame. The system was read out at both ends. The resulting time resolution has been quoted as 140-300 ps, which translates into a spatial resolution along the modules of $\sigma_z \approx 3\,\mathrm{cm}$ [47]. This system – or what remains of it in the S339 setup – will be referred to as BARrel scintillator array (BAR) from here on.

In order to improve its capability of kaon identification, the FOPI spectrometer was augmented with a multi-strip, multi-gap RPC barrel system in 2007. A detailed description of the system can be found in Ref. [52]. The upgrade made it necessary to shorten the original BAR detector and move it upstream. In the process, parts of the scintillator material were also replaced by a light guide (acrylic glass). As a consequence, the z-resolution of the BAR system has been reduced to $\sigma_z \approx 8\,\mathrm{cm}$. The new RPC system covers the polar region $38° < \Theta_\mathrm{lab} < 68°$. The design goal of a joint system time resolution (trigger and detector) of $\sigma_t < 100\,\mathrm{ps}$ could be met, and the spatial resolutions obtained in an evaluation with respect to tracks recorded in the CDC are quoted as $\sigma_\phi \approx 1.7\,\mathrm{mm}$ and $\sigma_z \approx 1.5\,\mathrm{cm}$ [52].

3.2.3 Magnetic field

The magnetic field for track bending in the FOPI setup is created by a superconducting Niobium Titanium/Copper solenoid magnet, cooled with liquid Helium. The design field strength is $B_z = 0.62\,\mathrm{T}$ at an electric current of

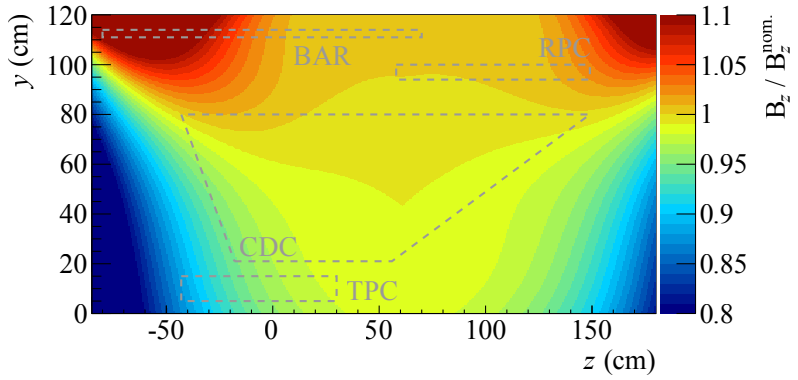

Figure 3.9: Variations of the z component of the magnetic bending field, normalised to the design field value.

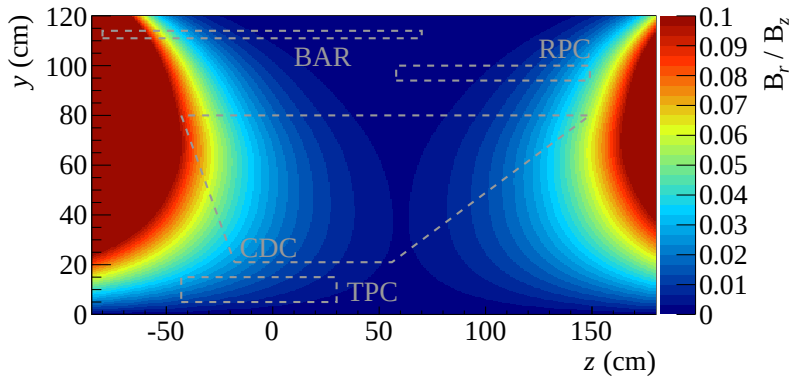

Figure 3.10: Level of inhomogeneity of the magnetic bending field. Drawn is the ratio of the field component in the r-ϕ plane and the component along the beam axis.

$I \simeq 720\,\mathrm{A}$ [47].

A spatial mapping of the magnetic field is available, obtained from earlier precision measurements of the field strength. Figures 3.9 and 3.10 show the spatial variations of the bending-field strength and the field homogeneity, together with the geometrical outlines of the FOPI detector systems.

As will be discussed in Chapter 4, the standard FOPI tracking routines assume the magnetic field to be constant across the volume covered by the CDC. From Fig. 3.9 it can be seen that this assumption is valid on the percent level, at least in the forward region. The situation changes when including the GEM-TPC as well as the spatial information provided by the BAR and RPC systems in the track fits of a combined analysis. In this case, the full spatial information of the field configuration has to be used. The fitting algorithms employed for this combined data processing will be discussed in Sec. 4.5.

Trigger ID:	Trigger condition:	Scaled:
9	PB & PLA>0	yes
10	PB & PLA>0 & RPC>0	no
11	PB & PLA>0 & BAR>0	no
12	PB & RPC>0 & BAR>0	no
13	PB & RPC>2	no
14	PB & RPC>0	yes
15	PB & BAR>0	yes

Table 3.2: Trigger conditions defined for the S339 setup. Trigger definitions with an ID < 9 in the numbering scheme refer to calibration settings and are omitted in the table. The abbreviation "PB" refers to "proper beam" and is defined by combined signals of the start detector and the beam halo veto detectors (see text). The stated values for the physics detectors (PLA, RPC, BAR) correspond to analogue thresholds. The PLA detector is a scintillator array in the forward region, that does not enter the analysis of this work.

3.2.4 Trigger system

The FOPI S339 start detector consists of a thin scintillator foil, located $\sim 2\,\mathrm{m}$ upstream of the target. Two additional scintillator arrays ("HALO" detectors) are arranged around the beam direction at $\sim 2\,\mathrm{m}$ and $\sim 20\,\mathrm{cm}$ upstream distance of the target, acting as a veto for incoming beam particles outside of the target region. When an incoming beam particle leaves a signal in the start detector and no signal is detected in the veto detectors, a start time can be defined by the trigger system, and the potential physics event is labelled as having "proper beam" conditions. A complete description of the trigger hardware can be found in Ref. [53].

For a positive trigger decision, signals in (one of) the FOPI physics detectors are required in addition. The trigger definitions used during the S339 setup are summarised in Tab. 3.2. For a trigger decision, the analogue signals of a given detector system are summed. The threshold values in Tab. 3.2 thus do not directly correspond to the number of detector hits that are later observed in the data, but a strong correlation between the two is observed. Three of the trigger conditions (9, 14, 15) had been downscaled during data taking, e.g. only a fraction of the these triggered events were actually forwarded to the DAQ systems. This was done in order to limit the final event rates, which was necessary in view of the rather long readout time of the AFTER chips of the GEM-TPC.

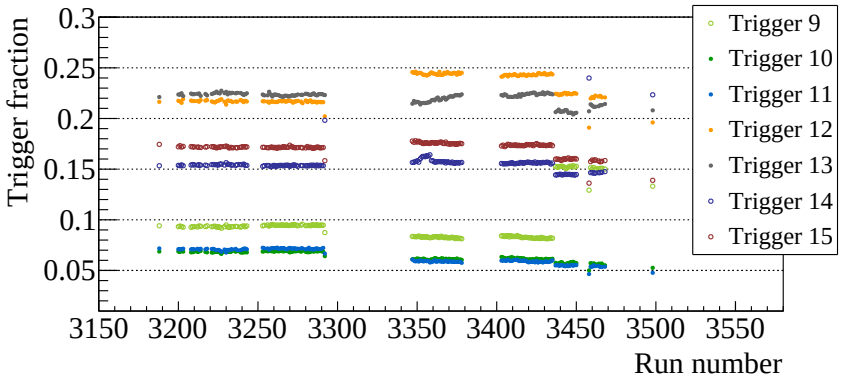

Figure 3.11: Observed fractions of the different trigger definitions (cf. Tab. 3.2) as a function of the run number.

3.2.5 Beam and target properties

The pions for the S339 experiment were produced by a primary $^{14}N^{7+}$ beam with an energy of $\sim$ 1.9 AGeV impinging on a production target made of beryllium. The extracted π^- beam reaching the FOPI experiment had a momentum of $1.70 \pm 0.03\,\mathrm{GeV}/c$ and an intensity of $\sim 9 \cdot 10^3\,\pi^-\,\mathrm{s}^{-1}$. This specific value of the beam momentum allows the production of $\Phi(1020)$ mesons close to threshold (centre-of-mass energy in the $\pi^- p$ system: $\sqrt{s} = 2.02\,\mathrm{GeV}$). An earlier measurement of pion-induced, in-medium production of strange matter in FOPI had been conducted at a beam momentum of $1.15\,\mathrm{GeV}/c$, and the S339 thus offers the possibility to repeat the measurement at a different beam energy. For a discussion of the obtained results, the reader is referred to Chapter 8.

During the S339 experiment, three different materials have been used as nuclear targets: C, Cu and Pb. The target discs measured $4.5 \times 4.5\,\mathrm{cm}$ in the plane perpendicular to the beam direction, but differed in thickness. From the full data set, only the data taken with the C and Pb targets are used in this work. Table 3.3 summarises the relevant target properties, including the total reaction-cross sections for pions at the appropriate momentum.

3.3 Combined DAQ

The term DAQ is commonly used to summarise the systems and strategies involved in collecting, synchronising and storing the data from the different detectors of an experiment during operation. An extensive description of the DAQ scheme employed by the FOPI experiment can for example be found in Ref. [50].

The electronic components involved in the signal extraction from the GEM-TPC have already been introduced in Sec. 3.1.3. Augmenting the FOPI spec-

Target:	d (mm):	ρ_t (g cm^{-3}):	σ_R (mb):
C	10	1.84	239.7 ± 2.8
Pb	5	11.35	1773.7 ± 41.1

Table 3.3: Properties of the targets employed during the S339 experiment. The thickness of the targets d along the beam direction, the corresponding mass density ρ_t as well as the total reaction-cross section σ_R for pions with 1.7 GeV/c incident momentum are listed. The latter is obtained from measured data using a π^- beam [54], and a linear interpolation in between the data points given therein is used.

trometer with the GEM-TPC detector required the synchronisation of the two DAQ schemes.

The data streams from the FOPI detector and the GEM-TPC were collected individually, stored in processor memory and transported via ethernet. In order to achieve a synchronisation of the data, additional hardware units had to be introduced to establish a communication between the two DAQ systems. The two streams were finally combined using a dedicated event-building machine and written to a common file. The data sets originating from the FOPI system and from the GEM-TPC are both appended by an unique event identifier in the process, allowing an unambiguous matching on the level of data reconstruction. Each file written out by the combined DAQ system contains $\mathcal{O}(100\,000)$ recorded events, corresponding to $\sim$ 1 hour of data taking ("one *run*").

The hardware aspects will not be detailed further in this work [4]. Instead, the matching on the level of particle track data of the two detector systems will be discussed in Sec. 4.6.

3.4 TPC online monitoring and decoding

For the purpose of real-time monitoring of the TPC data stream during data taking, a standalone computer software (*pandoraMon*) has been developed by the author. The program is written in the C++ programming language, and the graphical user interface (GUI) is modelled and implemented using the Qt™ framework (version 4.6.3). A screenshot of the program interface is shown in Fig. 3.12. For internal data handling, visualisation and persistence, the ROOT framework [56] is used, which is a standard choice in the particle-physics community.

In principle, ROOT provides its own GUI classes. These were, however, plagued by long-standing problems and generally outdated at the time the

[4] Another document, dealing with the specifics on the hardware level in greater detail, is currently in preparation [55].

development of the monitoring software was started. This unsatisfactory situation could be avoided by employing an additional software bridge: The Qt-ROOT software package, developed by Valeri Fine [57], allows to use graphical ROOT objects inside standalone Qt™ applications.

PandoraMon is designed in a modular fashion on the level of the program source code by means of abstraction. It is thus possible to quickly modify or add data containers for visualisation, which turned out to be an important advantage during the early commissioning of the GEM-TPC in the FOPI setup. Another central design choice was to enforce a human-readable format of all involved hardware mappings (cf. Sec. 3.3). This was achieved at the price of quite complex translation routines. In the final program, the only place where the actual setup of the readout electronics enters is an ASCII file containing one line for each connector of the readout plane (front-end card), specifying the mapping

`GESICA_ID` ← `ADC_ID` ← `ADC_PORT_ID` ← `CONNECTOR_ID`.

With the hardware mapping under control, a TPC provides space-point-like hit data that can be directly visualised. For this purpose, *pandoraMon* also features a real-time event display. An example event is shown in Fig. 3.13. Finally, the program is able to generate the output files for baseline subtraction from calibration data. Time stamps are automatically created specifying the validity range of the calibration files, which are then automatically used during the processing of physics data.

Since it is able to read the raw data produced by the GEM-TPC detector, the *pandoraMon* software was also used for the translation ("*decoding*") of this data into the binary objects that can serve as input for the final extraction of physical properties (discussed in the next chapter). For this purpose, a second executable is provided, which does not require user interaction and does not produce graphical output.

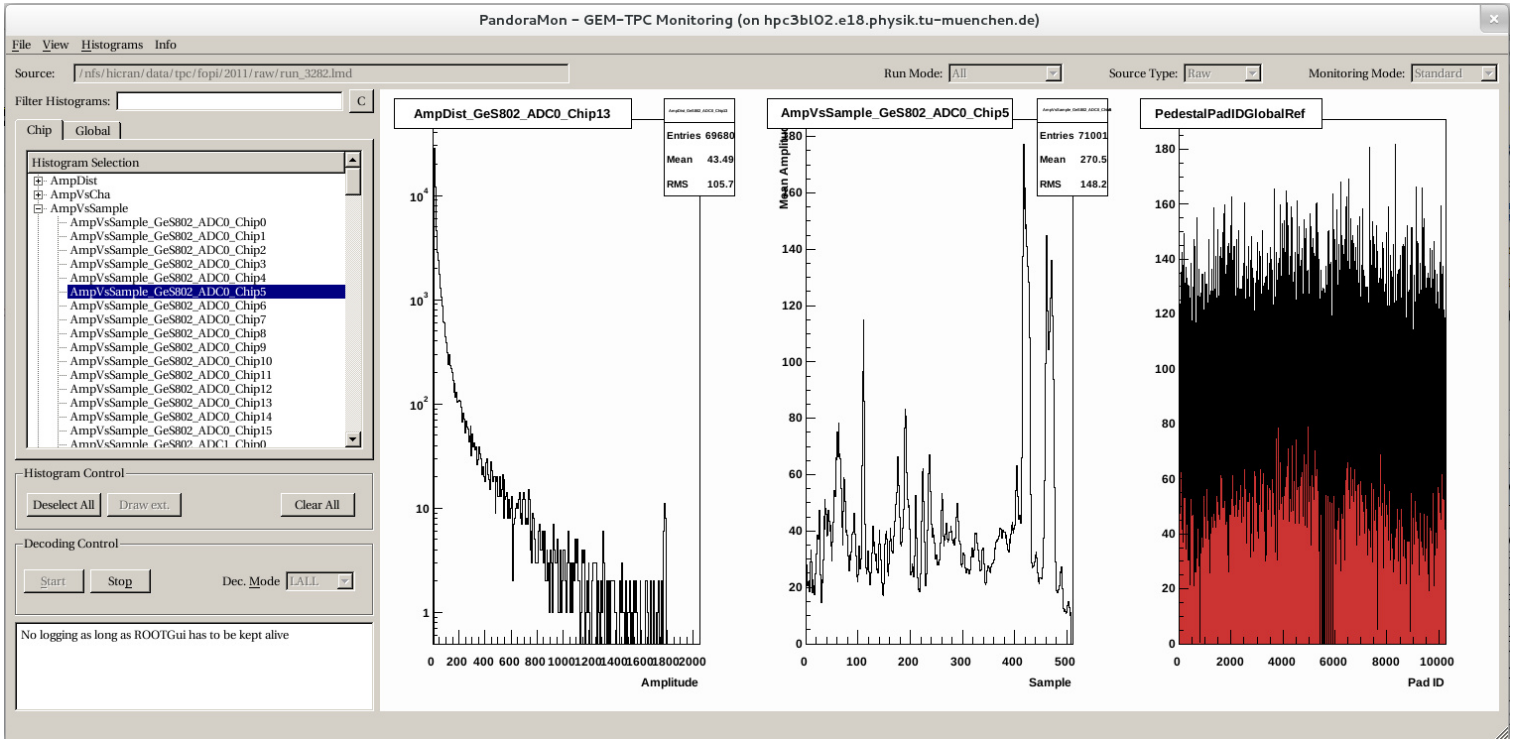

Figure 3.12: User interface of the *pandoraMon* online-monitoring software. The program can use a real-time data stream as well as persisted files as input. From a drop-down menu, a large variety of histograms – showing different aspects the accumulated data in real time – can be selected by the user. Search and filter functions for the quick navigation of the available data are available.

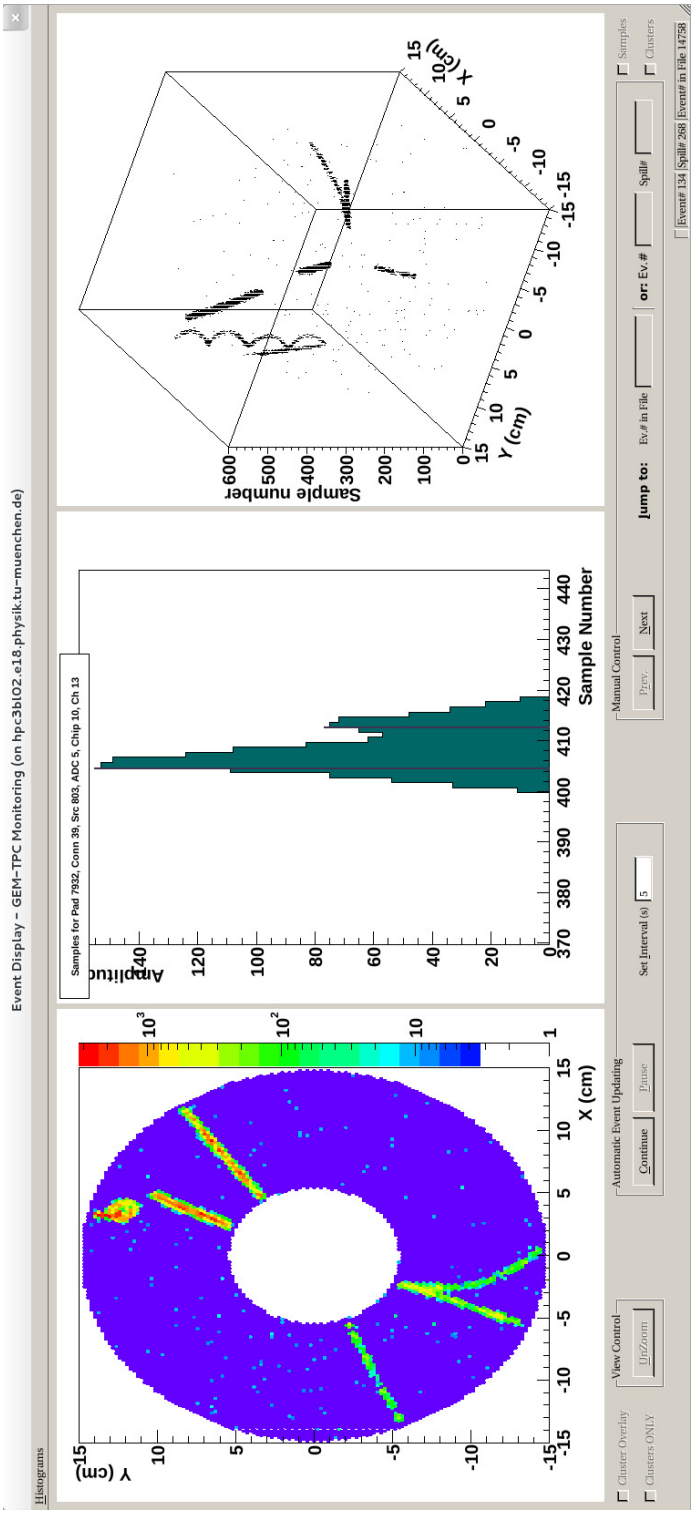

Figure 3.13: Event display of the *pandoraMon* monitoring software. The left panel shows the signal amplitudes registered by the pickup electrodes (pads) of the readout plane. Each pad can be clicked to show the time evolution of the signal in the middle panel, including the output of a simple pulse processing algorithm (cf. Sec. 4.2). The right panel shows the raw space-point information as function of the ASIC sample number/time bin in a rotatable view.

Chapter 4

Reconstruction algorithms

The processing of the recorded raw detector data in order to extract physical quantities is called *feature extraction* or simply data *reconstruction*. In this chapter, the algorithms used to perform this task on the data taken during the S339 experiment – as described in the previous chapter – will be introduced. It is important to note that the software introduced below is *not* part of the FOPI reconstruction software, which is described elsewhere (an extensive discussion can for example be found in Ref. [50]). Instead, it represents a stand-alone approach to perform feature extraction of the combined S339 setup starting with and based on GEM-TPC data. The results obtained from the standard FOPI reconstruction algorithms act as an external data source in this scheme. At the time this document is written, no complete description of the GEM-TPC feature extraction algorithms is available elsewhere. In this light and in anticipation of the physics analysis of Chapter 8, this chapter provides a rather detailed and sometimes also to some extent technical discussion.

In Sec. 4.1 the reader will be made familiar with the general organisation of the code. Sections 4.2 and 4.3 will be concerned with the transformation of raw signals recorded with the GEM-TPC into position measurements in three-dimensional space. Their association to particle-track candidates in the GEM-TPC volume will be covered in Sec. 4.4. The next step is the application of a mathematical model ("track fit") in order to extract physical properties, e.g. the particle momentum and charge. Section 4.5 will provide a detailed discussion of the algorithms used for this task, as well as their application for the reconstruction of decay vertices.

The subsequent sections will explain how the tracking information of the surrounding FOPI detectors is included into a combined feature extraction on S339 data. The method used for the matching of TPC and CDC tracks will be described in Sec. 4.6. Shifts between TPC and CDC tracks discovered during this step can be used to geometrically align both detectors. The technicalities of this procedure will be outlined in Sec. 4.7. The chapter will close with the discussion of an important limitation of the TPC-combined reconstruction in

Sec. 4.8, which is the lack of a combined software layer for the microscopic simulation of the detector response.

4.1 General structure

A GEM-based TPC as described in this work was originally considered as an option for the central tracking detector of the future PANDA experiment at the FAIR facility in Darmstadt, Germany. Consequently, the development of a microscopic software simulation has originally been embedded into the PANDA simulation framework, FairRoot [58]. As the name suggests, it is based on the widely used ROOT framework [56] developed at CERN.

In 2011, a decision was taken by parts of the PANDA collaboration in favour of the less challenging Straw Tube Tracker (STT) system as central tracking device. As a consequence, the TPC software has been branched out of the standard PANDA software and has been developed independently since. The commissioning of the first large GEM-TPC in FOPI presented an opportunity to test and refine the reconstruction algorithms developed so far on real interaction data.

The GEM-TPC simulation and reconstruction software is designed as a modular, object-oriented framework and is implemented in the C++ programming language. In a simplistic but instructive picture, all relevant physical objects (e.g. drifting electrons, signals induced on pads, clusters of hits, entire tracks, ...) are modelled as *objects in code*, and they all derive from ROOT's `TObject` [1] class. The most important advantage of this design choice is the access to the powerful data I/O facilities of the ROOT framework. The algorithms that generate/manipulate these objects and that take care of the dynamics arising between them are called *tasks* (derived from `TTask`).

The framework organises all this in an *event-based* way: For each event, all (generated) particle signatures are passed through the set of all selected tasks successively. The analogy to the case of real data is of course the detector data associated with a triggered event [2]. Technically, this structure allows to enable/disable or exchange tasks (algorithms) easily on a script-like software layer. Section 4.1.2 will provide an overview of the involved tasks for the reconstruction of real data. The simulation part of the software has already been described elsewhere ([59]) and will not be discussed in this work.

After the processed data has been stored, the final physics analysis is performed by scripts implemented in the Python programming language (through

[1] Entities appearing in `verbatim` style in this document refer to definitions in the source code or type qualifiers.

[2] This general design of the FairRoot framework is actually in contradiction with the "trigger-less" mode of operation envisaged for PANDA: The detector will become a continuous readout pipeline and the concept of an "event" breaks down. It will be interesting to see how FairRoot will be developed in the future in order to adapt to that paradigm.

the PyROOT interface provided by ROOT).

4.1.1 Conversion of FOPI data

Before proceeding with the discussion of the details of the implementation, the import of the data provided by the FOPI detectors into the combined reconstruction scheme should be explained. As mentioned earlier, the output of the native FOPI reconstruction software is taken as an external data source. The relevant results required for the combined analysis are the tracking and TOF information provided by the CDC, BAR and RPC detectors.

The FOPI feature-extraction software is implemented in the FORTRAN programming language, and the persisted data are thus initially incompatible with the GEM-TPC software. This problem is overcome by interfacing another piece of software with the FOPI reconstruction code, the sole purpose of which is to translate this output into entities that can be fed to the TPC algorithms. The objects that are finally written to disk and their data fields are summarised in Tab. 4.1. They will be shortly discussed in the following:

`CdcHit`s are the direct representations of single detector hits registered in the FOPI CDC. They are wire hits by nature, and thus represent the measurement of a drift radius. The inherent left-right ambiguity with respect to the CDC wire plane has already been resolved by the FOPI tracking algorithms, as described in Sec. 3.2.1. Using the additional position measurement along the wire direction, the two-dimensional wire hit can be promoted to a point in three-dimensional space.

A `CdcCircle` represents a collection of `CdcHit`s that have been identified to belong to a particle track by the FOPI CDC pattern recognition algorithm. From the subsequent track fit performed during the FOPI reconstruction, additional information like the particle's charge and momentum are available. The most important characteristic of the track-fitting algorithm has already made its way into the name of these objects: the track model in FOPI is a simple *circle*. Its parameters are obtained by a global χ^2 fit to the CDC hit data, and the geometrical nature of a helical arc is parametrised by an additional angle Θ_{CDC}, describing the circle's rotation out of the azimuthal plane. There is *no* treatment of energy loss, **B**-field inhomogeneities or curling / re-entering particles during any stage of the FOPI feature extraction.

In spite of their name, `BarrelTrack`s and `RpcTrack`s are the representations of single hits registered in the BAR and the RPC detectors [5]. The information about a possible spatial matching of these hits with CDC tracks is actually also already contained in the `CdcCircle` objects. The two containers hold information about the hit detector module and the measured TOF with respect to the recorded event time. They also contain the calculated particle velocity, which is the quantity relevant for particle identification. Clearly, it can only be inferred from the full particle track inside FOPI (and an assumption on

Entity:	Fields:	Type:	Description:
`CdcHit`	ArrayID	`int`	Position in the data array
	Wire_ID	`int`	Identifier of the hit wire
	WirePosXY	`floats`	Wire position and error
	Radius	`float`	Reconstructed drift radius of the wire hit and error
	DepCharge	`float`	Deposited charge
	PulseRL	`floats`	Pulse heights at the wire ends
	PositionXYZ*	`floats`	Conversion of the above into space-point coordinates (and errors) [3]
`CdcTrack`	Array_ID	`int`	Position in the data array
	Hits	`ints`	List of associated IDs of `CdcHits`
	NPoints	`int`	Number of points in track
	Momentum†	`float`	Total particle momentum
	Radius	`float`	Radius of the circular track model
	CentreXY	`floats`	Centre of the track circle
	Theta	`float`	Scattering angle [4]
	Z_0	`float`	Displacement along beam axis w.r.t. the c.o.g. of all tracks (*"vertex"*)
	Charge	`int`	Charge of the particle
	ELoss	`float`	Truncated mean estimator for the specific energy loss
	RPC_ID	`int`	Index of matched hit in the RPC
	BAR_ID	`int`	Index of matched hit in the BAR
`RpcTrack`	Array_ID	`int`	Position in the data array
	Position*	`floats`	Position and error
	TOF*	`float`	Time of flight (rel. to trigger) and error
	Velocity†	`float`	Particle velocity based on FOPI tracking
`BarTrack`	Array_ID	`int`	Position in the data array
	Position	`floats`	Position and error
	TOF*	`float`	Time of flight (rel. to trigger) and error
	Velocity†	`float`	Particle velocity based on FOPI tracking

Table 4.1: Data imported from the FOPI reconstruction software. Quantities marked with a dagger (†) are re-calculated during the combined analysis, and those marked with an asterisk (*) are found to require re-calibration (cf. Chapter 5).

the original vertex) at this point. Information on a how this quantity is recalculated during the TPC-combined feature extraction will be provided in Chapters 5 and 7.

4.1.2 The reconstruction chain

Figure 4.1 provides a schematic overview of how the combined processing of the combined data set taken during the S339 experiment is organised. Each box represents one logical step in the reconstruction scheme, but not necessarily a single *task* on the level of the software implementation. In the following, each step will be explained shortly, and the most important algorithms will be discussed in more detail in the subsequent sections. The order of execution in Fig. 4.1 is from top to bottom, and reconstruction steps appearing aligned horizontally are independent of each other and could thus be executed in parallel. The reconstruction chain can be conceptually divided into three main stages:

In the first stage, the input data from both the GEM-TPC and the surrounding FOPI spectrometer are read in and processed independently. As discussed in Sec. 4.1.1, the input data from the FOPI detectors consist already of the converted final results from the FOPI feature extraction routines. For the GEM-TPC, on the other hand, the most basic units of information entering are the digitised signal amplitudes (`TpcSample`s) sent out from the ADC boards. They contain the measured amplitude over threshold, the unique readout pad identifier and the ADC sample number. The samples belonging to a common signal pulse are recombined to `PadHit`s in the next step, during which the readout pad position and the timing information of the signal are also mapped into three-dimensional space. This procedure will be discussed in Sec. 4.2. In order to reduce the data throughput and increase the fitting performance, the `PadHit`s are further combined to so-called *clusters*. This task gains a special level of complexity due to the high degree of symmetry of the readout plane of the GEM-TPC detector, as will become clear in Sec. 4.3. Finally, the identified `TpcCluster`s are fed into the pattern recognition algorithm in order to associate them to track candidates (cf. Sec. 4.4).

After the spatially associated hit data are available from all contributing tracking systems, a mathematical model is applied to the track candidates in the second stage. All such track fits are performed using the GENFIT [60] track-fitting toolkit. The underlying principles and the mathematical foundations of the fitting algorithms will be presented in Sec. 4.5. Using the GENFIT framework requires a common interface (`GFTrack`s) in the software implementation, and consequently all hit data must first be converted into code objects compatible with GENFIT. This is done in dedicated initialisation tasks. Furthermore, in order to allow combined fits in the end, the space-point hits of the GEM-TPC need to be transformed from the TPC detector coordinate frame

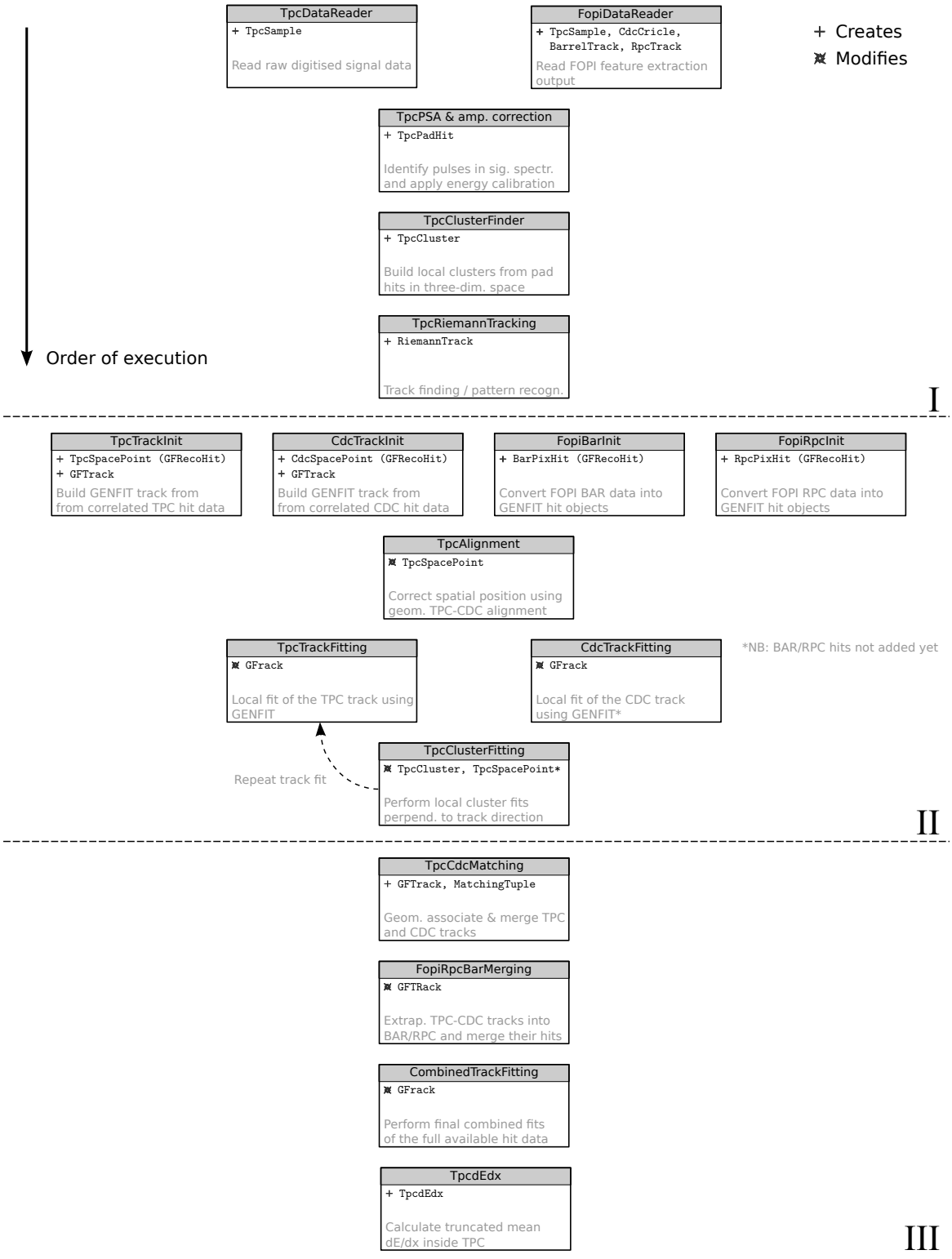

Figure 4.1: Overview of the logical steps performed during the GEM-TPC feature extraction, executed from top to bottom. Tasks appearing on the same level can be processed independently of each other. Details are discussed in the text.

into the global FOPI coordinate frame. The parameters of this transformation are obtained in an external geometrical alignment procedure, which will be shortly presented in Sec. 4.7. At this stage, it is possible to perform the first track fits, first working independently on TPC and CDC hits. The obtained fits in the TPC can in principle be used to refine the initial clustering, followed by another fit with the updated hit data.

In the final stage, all data from the GEM-TPC and the FOPI detectors are merged on track level, allowing combined fits and feature extraction at last. To this end, tracks from the TPC and the CDC are first proposed for merging based on a geometrical matching procedure, performed in the azimuthal plane only (cf. Sec. 4.6). The obtained pre-fits are then extrapolated into the FOPI TOF detectors. This is done to verify or break the already existing associations between these systems, as suggested by the FOPI reconstruction routines. The merged tracking information is now complete and a final track fit is performed. Using this highest-level result, the specific energy loss measured by the TPC is extracted as a final step (cf. Sec. 6.5).

4.1.3 Coordinate frames

Before turning to the specifics of the key algorithms, some introductory comments concerning the coordinate frames used during the reconstruction of the data are in order. The GEM-TPC is initially treated as an additional upgrade to the FOPI spectrometer, and it is thus reasonable to identify the global system of the combined reconstruction of both systems with the FOPI coordinate frame (x,y,z). In this frame, z runs along the beam axis, and x and y are aligned with the horizontal and vertical axis of the laboratory frame (cf. Fig. 3.5). The scattering angle in primary interactions is measured as the polar angle Θ_{lab}.

Irrespective of this choice, an independent coordinate frame (u,v,w) is used for the GEM-TPC, defined by the symmetries of the detector vessel: The w axis is chosen to be anti-parallel to the electron drift direction [6], u and v span the detection plane. This is the relevant coordinate frame for all reconstruction steps up to track finding in the TPC. The polar and azimuthal angles in this frame are Θ_{TPC} and Φ_{TPC}, respectively. Before track fits can be performed across detector boundaries, mechanical inaccuracies of the setup need to be corrected for by aligning the TPC coordinate frame with the global coordinate frame. The employed method and the parameters of this transformation will be discussed in Sec. 4.7.

[3] Quantity used for data modelling in the combined analysis; see Sec. 4.5.5

[4] Already containing RPC and BAR information if applicable.

[5] The author agrees that they are named rather unfortunately.

[6] The w and z axis are initially aligned sufficiently well so that $\mathbf{E} \parallel \mathbf{B}$ can be assumed.

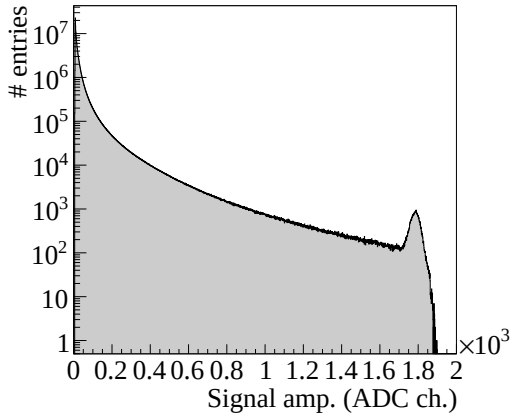

Figure 4.2: Amplitude spectrum of the time-sampled and digitised signals from $\approx 150\,000$ recorded physics events. The peak visible at the end of the spectrum is suspected to be caused by saturation effects of the pre-amplifier of the AFTER ASIC.

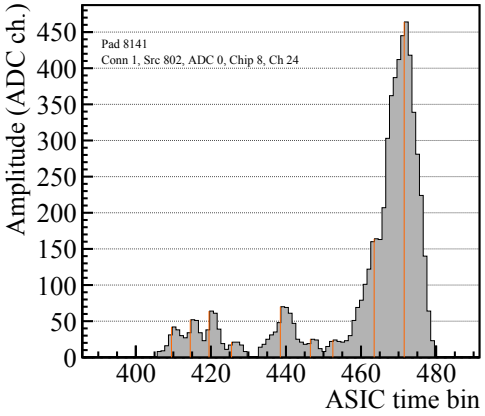

Figure 4.3: Example of the output of the PSA algorithm. Each merged pad hit is assigned a total, integral amplitude and a signal time – shown by vertical lines – according to Eq. (4.1). No tail cancellation or other corrections are performed. One time bin is 64.52 ns wide.

4.2 Pulse shape analysis and w-mapping

We begin the detailed discussion of the feature extraction algorithms with the reconstruction of spatial and timing information measured on pad level. It was already discussed in Sec. 2.1.1, that the signal induced on a single pad consists of contributions from multiple ionisation events, which are further mixed among each other by diffusion. It thus already represents an averaging in space and time. At the same time, it is the fundamental unit of information provided by the detector: The ensemble of all single-pad signals caused by one projectile particle determines the spatial tracking resolution (an evaluation based on the S339 data will be presented in Chapter 6). The goal of the pulse shape analysis (PSA) step is to recover from the signals the average spatial positions and the total associated deposited charge.

Under ideal conditions (cf. Sec. 2.2.3), the total charge registered on the pad is proportional to the contributing ionisation charge. The position information (u,v) in the detection plane can be directly obtained from the c.o.g. of the pickup electrodes. The average position along the drift axis (w), however, has to be inferred from the timing characteristics of the detected pulse.

The shape of the analogue signal is determined by the shaper response (cf. Sec. 3.1.3) to the arriving charge clouds after gas amplification. The exact/-analytic description of this response is unknown for the AFTER ASIC, but parametrisations of the measured response to synthetic input signals are avail-

able (see Ref. [43] and the primary references given therein). During the S339 physics run, the AFTER chips were operated at the fastest shaper setting (register configuration '0000'), corresponding to a signal peaking time of $\approx 116\,\mathrm{ns}$ [43]. The length of the signal shape is larger than the longitudinal expansion of the avalanche divided by the drift velocity in the last transfer field, and thus the AFTER signal shape can be expected to be roughly conserved during the superposition of the avalanche signals.

The time-sampled analogue signals stored in the ASIC buffer are digitised by an 11-bit ADC. These digitised amplitudes are the fundamental units of digital information recorded during the operation of the GEM-TPC, and thus the starting point of the feature extraction scheme discussed in this chapter. Figure 4.2 shows the amplitude spectrum of these data. The digitised signal shape of each pad is processed by a simple PSA algorithm that identifies the samples belonging to one "pulse" by means of a search for local minima. Each such pulse is called a *pad hit* and gets assigned a total signal charge and a signal time. The charge is calculated as the sum of all associated sample amplitudes, motivated by the fact that the time integral of the AFTER signal is proportional to the total deployed charge. The assigned time of the pad hit t_{ph} is given as the corresponding time t_{max} of the peak sample minus a constant offset t_{r} describing the effective rise time of the signal,

$$t_{\mathrm{ph}} = t_{\mathrm{max}} - t_{\mathrm{r}} \quad . \tag{4.1}$$

The effective rise time is obtained from simulations: $t_{\mathrm{r}} = 149.5\,\mathrm{ns}$. Figure 4.3 shows the result of the PSA algorithm on an example of an amplitude spectrum from physics data.

When pulses overlap in time as shown in Fig. 4.3, this simple algorithm will yield wrong individual pad hit amplitudes. In order to obtain correctly disentangled pulses, a subtraction of the tail leaking into the next, overlapping pulse would be required. Performing such a *tail cancellation* is only possible using a fit of the actual shape of each pulse identified by the PSA. The very low track density observed during the S339 experiment and the restriction of the data analysis to tracks entering the barrel detectors of FOPI ($\Theta_{\mathrm{lab}} > 20.6°$) led to the decision in favour of a simple and robust over a more involved PSA algorithm. The results of Sec. 6.5 can be seen as a confirmation of this ansatz.

With the start time t_{ph} known, each pad hit can finally be mapped into three-dimensional detector space. The pad hit position in the u-v plane is given by the c.o.g. of the corresponding pickup electrode. The coordinate along the drift axis is calculated using the drift velocity v_{d} in the gas,

$$w_{\mathrm{ph}} = v_{\mathrm{d}}(t_{\mathrm{ph}} + t_0) \quad , \tag{4.2}$$

where t_0 is a constant timing offset of the readout electronics. The drift velocity v_{d} is taken from simulation results at the correct drift field strength $|\mathbf{E}_{\mathrm{d}}|$, using

the MAGBOLTZ software package [14]. For selected runs [7], the simulation values were compared to direct measurements of v_{d}, and an agreement within the measurement uncertainties was observed [61].

Such measurements are also presented in Ref. [61] for the data taken during the S339 physics campaign, however with a larger systematic uncertainty attached. These data generally point towards a v_{d} smaller than the one obtained from simulation. This discrepancy will finally have to be resolved by extracting v_{d} from the alignment procedure (cf. Sec. 4.7), which is currently still being improved. Within the scope of this work, however, the values obtained from simulation are used (cf. Tab. 3.1).

4.2.1 Amplitude correction using Kr-calibration data

In Sec. 2.1.4, the correction of gain variations across the amplification plane has been identified as one of the major challenges arising when operating a TPC with a GEM-based readout. Using a method involving the introduction of radioactive Kr into the active volume of the GEM-TPC, a direct measurement of these effects has been obtained. The results from these dedicated measurements will be presented in Sec. 6.4.

From this analysis, a scaling factor for each pad is extracted (cf. Fig. 6.15) in order to correct for local gain variations. Applying this correction (according to Eq. (6.9)) to each pad hit amplitude presents the last step of the PSA scheme at this point of the feature extraction chain.

4.3 Clustering

In order to reduce the amount of data and facilitate track fitting, it is desirable to further condense the spatial information stored in the pad hits. For this purpose, an algorithm is used that locally and dynamically merges pad hits to so-called *clusters*. The procedure starts at local maxima in the pad-hit amplitude density and then adds neighbouring pad hits in three-dimensional space, i.e. next neighbours on the pad plane and hits sufficiently close along the drift direction (w). Whenever a local minimum in the amplitude density is found, a new cluster is started at the pad hit with the highest amplitude of the remaining, not yet associated candidates. As an additional advantage of the clustering step, isolated pad hits due to random electronic noise can be effectively suppressed even before track finding is attempted. This effect and the general distributions of the cluster sizes when operating on S339 data are shown in Fig. 4.4.

[7] These measurements have been performed on track data from cosmic particles during the commissioning phase at FOPI, before the field cage of the GEM-TPC was damaged (cf. Sec. 3.1.1). The higher drift field allowed the direct observation of the full drift window within one buffer length of the ASIC, and thus the drift velocity could be directly extracted.

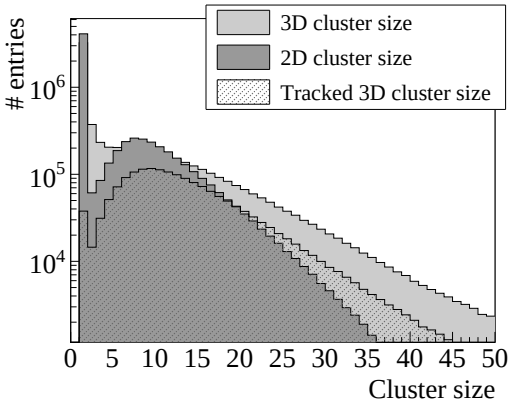

Figure 4.4: Cluster-size distributions before and after track identification of data from the S339 pion campaign. Compared are the sizes in all three dimensions and the sizes in the u-v projection. A strong suppression of small cluster sizes after track finding can be observed.

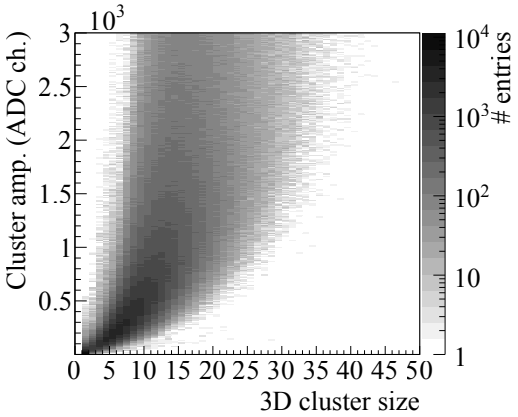

Figure 4.5: Correlation of the total cluster amplitude (cf. Eq. (4.3)) and the three-dimensional cluster size (after tracking).

The total amplitude A_{cl} of a cluster is simply given by the sum of the amplitudes a_k of the assigned pad hits $\{k\}$,

$$A_{\mathrm{cl}} = \sum_k a_k \quad . \tag{4.3}$$

Its position $\mathbf{u}_{\mathrm{cl}}$ in the (u,v,w) frame is calculated as the centre of gravity from the positions of the associated pad hits $\mathbf{u}_k$:

$$\mathbf{u}_{\mathrm{cl}} = \frac{1}{A_{\mathrm{cl}}} \sum_k a_k \mathbf{u}_k \quad . \tag{4.4}$$

The spatial uncertainty covariance $\mathbf{C}_{\mathrm{cl}}$ is constructed from the above as in

$$\mathbf{C}_{\mathrm{cl}} = f_{\mathrm{E}} \frac{1}{A_{\mathrm{cl}}} \sum_k \mathbf{u}_{\mathrm{cl}} \otimes \mathbf{u}_k \quad , \tag{4.5}$$

where $\mathbf{u}_{\mathrm{cl}} \otimes \mathbf{u}_k = \mathbf{u}_{\mathrm{cl}} \mathbf{u}_k^{\mathrm{T}}$ is the outer product. The quantities $\mathbf{u}_{\mathrm{cl}}$ and $\mathbf{C}_{\mathrm{cl}}$ represent the spatial information that is passed to the track-fitting algorithm [8] (cf. Sec. 4.5 and Tab. 4.3). When diagonalised, $\mathbf{C}_{\mathrm{cl}}$ contains the square of the measurement uncertainty along its eigenvectors on the diagonal elements. The

[8] For combined track fits in the S339 setup, an additional transformation into the global coordinate frame is required. See Sec. 4.7.

coefficient f_{E} appearing in the covariance enters as an additional scaling. It is required to absorb the arbitrary, absolute scale of the amplitude A_{cl}, which contains the characteristics of the readout electronics as well as the gas gain, and it has to be tuned with respect to the statistical observables of the track fit (cf. Tab. 4.3).

The clustering algorithm is optimised to avoid the creation of very small clusters as far as possible. If such clusters do get created – i.e. only one pad hit is available along any of the symmetry axis of the pad plane or along the time axis –, the above uncertainty has to be modified so that it reflects the limit of the measurement error σ_{lim} due to the finite detector structure size S. S is hereby determined by the pitch of the pad plane or the timing frequency of the ADC, respectively. In the u-v plane, the pad structure is approximated for this purpose by a rectangular distribution along any of its symmetry axis, and S is identified with the corresponding pad pitch. Along the w axis, S is simply taken to be the width (in time) of one ADC sample, multiplied by the drift velocity. This is a sound assumption, since the w position of a pad hit is obtained using only the information of a single ADC bin (cf. Eq. (4.2)). The covariance $\mathbf{C}_{\mathrm{cl}}$ is then altered in such a way that it reflects the measurement error along the respective axis to be

$$\sigma_{\mathrm{lim}} = \frac{S}{\sqrt{12}} \quad . \tag{4.6}$$

As long as the clusters do not become too large, the spatial information contained in the pad hits of a particle track is conserved during clustering (cf. Eq. (4.4)). The above definition of the spatial uncertainty $\mathbf{C}_{\mathrm{cl}}$, on the other hand, is more problematic. If one assumes that only the signals from the electrons created in a single ionisation event are measured in a cluster of pad hits, the measurement error would properly scale with the spatial expansion of the cluster (reflecting the effect of diffusion, cf. Sec. 2.1) and the inverse of $\sqrt{A_{\mathrm{cl}}}$ and thus $\sqrt{n_{\mathrm{p}}}$ (cf. Eq. (2.1)).

However, ionisation events in the gas occur on a length scale $\mathcal{O}(100\,\mu\mathrm{m})$, and their signals are thus already mixed on pad hit level (even in the absence of diffusion). Inevitably, any spatial correlation to primary ionisation events is lost, and cluster sizes and amplitudes will no longer show the scaling behaviour expected from diffusion theory applied to primary ionisation charge clouds. The connection of the cluster size and amplitude can be seen in Fig. 4.5, and the surviving correlations of the mean cluster error with the total cluster size and amplitude are shown in Figs. 4.6 and 4.7. In all these figures, only clusters associated to tracks are taken into account.

As an example for an even more problematic case let us consider a short-ranged δ-electron: If absorbed in a cluster containing otherwise "correct" positional information, the resulting centre of gravity $\mathbf{u}_{\mathrm{cl}}$ would be systematically biased, but, at the same time, a smaller error due to the additional amplitude would be assigned.

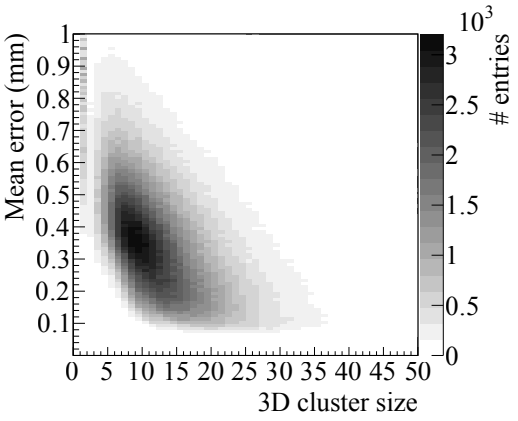

Figure 4.6: Scaling behaviour of the mean cluster error (RMS of the covariance eigenvalues) with the total cluster size.

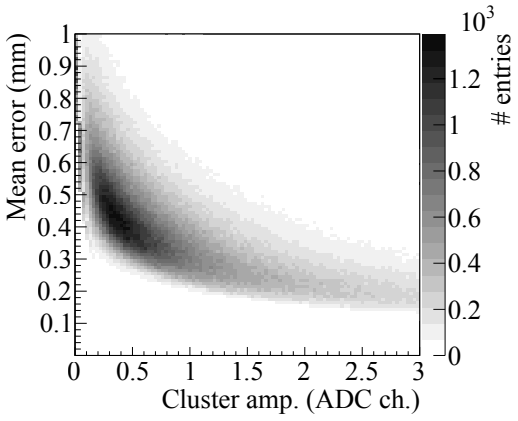

Figure 4.7: Scaling behaviour of the mean cluster error (RMS of the covariance eigenvalues) with the total cluster amplitude.

4.3.1 Outlook: Track-dependent clustering

Such issues could be avoided if the actual spatial distribution of the hit data *around the particle path* would be used to define the measurement uncertainty of a cluster. Its expansion is determined by the two diffusion components $D_{\parallel}$ and $D_{\perp}$ (cf. Sec. 2.1) – depending on the track geometry – and thus Gaussian in nature. If captured by a bi-variate Gaussian fit in the plane locally transverse to the track direction, the quality of the measurement can be probed: A larger diffusion will naturally lead to a larger observed width. If the total amplitude is kept constant, a larger drift length will therefore lead to larger relative fluctuations of the amplitude in between pad hits and thus larger uncertainties of the fit results. Outlying hits such as electronic noise or δ-electrons will in general not follow a normal distribution and thus degrade the fit quality and result in larger cluster errors. As an additional advantage, the dependence on the *absolute* value of the amplitude would vanish and no re-scaling would be required anymore.

The applicability of this method is being investigated by Martin E. Berger (Technische Universität München (TUM)) at the time this document is written. The foreseen technical implementation based on constructing planes perpendicular to the local track direction is very similar to the extraction of the specific energy loss data from GEM-TPC track fits, which will be discussed later in this work (cf. Sec. 6.5.1 and Fig. 6.16 for a visualisation of the procedure). Unfortunately, the required work could not be finished in time to enter the analysis presented in this work, and the quantities of Eqs. (4.3) - (4.5) are used instead.

4.4 Track finding / Pattern recognition

There are two possible approaches towards track identification (the much more general term "pattern recognition" is commonly used as a synonym in the particle-physics community) based on a collection of spatial measurements ("hits"): methods built on *global transformations* and those relying on *local correlation* of hits. Independent of that choice, the task is greatly facilitated by two key features of the track topology in TPCs: i) truly three-dimensional detector hits and ii) typically a large number of such hits per track. Especially the latter makes the problem in principle very suitable for global methods.

An example of a global approach is that of performing a so-called Hough transformation ([62], [63]) of the measurement points into a (discrete) parameter space. The goal is to transform the search for a pattern in the original image space into a search for maxima in the parameter space. A massively parallel algorithm for the search of helical tracks has been implemented by the author for execution on graphics processing units (GPUs) and is described in Ref. [64]. It was successfully used for the identification of high-energy tracks in a smaller prototype [43].

The focus during development of the GEM-TPC has, however, been lying on the continuous mode of operation (cf. Sec. 2.3). The inevitable residual drift distortions [9] and the high tack densities in that scenario call for a very robust algorithm. Global approaches tend to become unreliable faced with such challenges. In order to meet these requirements, a track-following algorithm based on local hit correlations has been developed, and will be presented in the following.

4.4.1 Riemann track finder

The track finding algorithm outlined in the following has been originally developed for the GEM-TPC option as central tracker of the PANDA experiment. Most of the work of implementing, testing and optimising the algorithm has been carried out by Johannes Rauch (TUM), initially under the author's supervision. A complete description of the algorithm and results on its performance are available in Ref. [65]. Here, only a brief overview shall be provided.

To put it simply, the software associates single TPC hits to tracks by testing for spatial proximity. This happens in two passes, each of which begins with the application of a different pre-sorting (radially and along the drift direction) of not yet associated hits. This step is followed by the actual track-building phase, in which the algorithm attempts to associate the sorted hits spatially and condenses them to a set of tracks candidates.

Initially, hits can only be tested against each other. After the first small track pieces ("tracklets") begin to form, the remaining free detector hits can

[9] A simulation study can be found in Ref. [15] and Appendix A.

additionally be tested against the underlying helical track assumption – allowing for track distortions up to a suitable degree. With growing size, the tracklets become more and more defined, and the cuts used in the hit-to-track association are dynamically tightened.

Testing the compatibility of a hit candidate with the "helicality" of a tracklet involves non-linear computations. To be exact, the compatibility of a point measured in the TPC readout plane $(u,v) = (r\cos\Phi_{\mathrm{TPC}}, r\sin\Phi_{\mathrm{TPC}})$ with the projection of the helix onto that plane (describing a circle or circular arc in good approximation) is tested by calculating the distance of the point to the latest circle assumption. In order to speed up this process, the algorithm employs a conformal mapping method that lends the procedure its name: The "Riemann transformation" is defined as

$$\begin{aligned} u' &= r\cos\Phi_{\mathrm{TPC}}/(1+r^2) \\ v' &= r\sin\Phi_{\mathrm{TPC}}/(1+r^2) \\ w' &= r^2/(1+r^2) \end{aligned} \tag{4.7}$$

and maps the measured point (u,v) to coordinates (u',v',w') on the surface of a sphere of radius 1, sitting on top of the origin of the readout plane. By construction, the transformation of Eqs. (4.7) guarantees that points describing a *circle* in the readout plane will be mapped onto the sphere surface in such a way, that they define a *plane* intersecting with this "Riemann sphere". This effectively transforms the non-linear hit-to-circle test into a linear computation – without any loss of precision – and thus significantly reduces execution time. The additional computations of Eqs. (4.7) only need to be performed only once for every TPC hit, while the number of hit-to-track comparisons is approximately (# of hits) × (# of tracks).

As stated before, the algorithm was originally designed and optimised for a GEM-TPC operating inside the PANDA experiment at its design luminosity of presently $2\cdot10^{32}\,\mathrm{cm}^{-2}\mathrm{s}^{-1}$. Figure 4.8 gives an impression of the track densities that are reached. In this scenario, approximately 4000 tracks would have been stored at any given time in the chamber (140 cm drift length). For the evaluation of the performance of the presented pattern recognition procedure, a signature channel ($\eta_c \to \phi\phi \to K^+K^-K^+K^-$) of the PANDA experiment has been simulated. The physics events have then been mixed with background events corresponding to the design luminosity and subjected to simulated drift distortions due to space charge accumulation [15]. It could be shown that the Riemann track finder described here performs very well in this challenging environment. Most importantly, the algorithm has proven to be virtually unaffected by simulated track distortions, and can thus be expected to perform well on prototype data.

This PANDA mixed-event scenario largely exceeds the requirements on pattern recognition presented by the data taken with the FOPI GEM-TPC. Similar simulations of the above channel without mixed-in background have

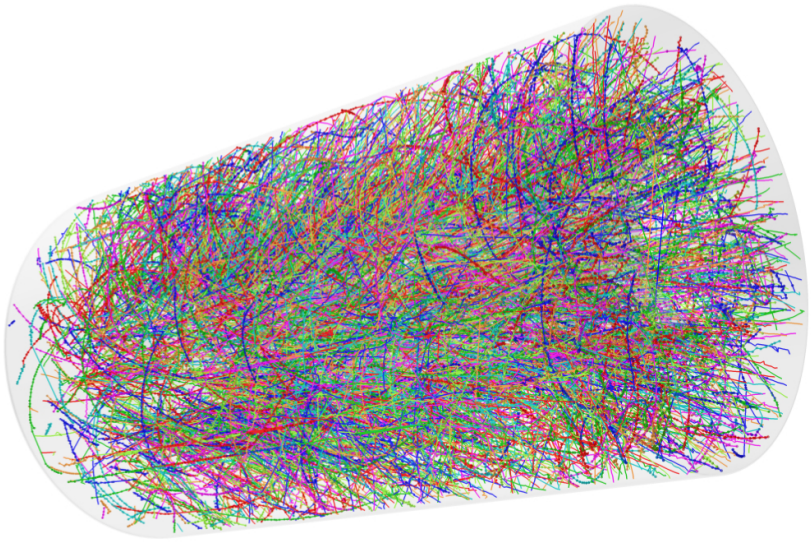

Figure 4.8: Snapshot of identified tracks after pattern recognition from simulated PANDA background. The plot has been kindly provided by J. Rauch, TUM.

resulted in track identification efficiencies and purities (1 − fraction of falsely correlated hits) of above 99 %. This is a scenario close to the requirements presented by the reconstruction of the FOPI GEM-TPC data in terms of the average track multiplicity per drift frame, and should thus yield reasonable expectations for the performance on real data. A combined evaluation of the performance of the pattern recognition and the track-matching algorithm will be presented in Sec. 4.6.

4.5 Track and vertex fitting – GENFIT

The purpose of this section is to give a detailed introduction into the technicalities of the track fitting algorithms used for feature extraction on the FOPI GEM-TPC data. The choice in favour of this rather in-depth discussion was taken because i) the fitting algorithms present the immediate bridge between detector data and physics results and ii) no documentation of the specifics of the FOPI GEM-TPC feature extraction are available elsewhere at the time. All results to be presented in the remainder of this work are based on fits performed with the track-fitting toolkit GENFIT [60] [10].

GENFIT emerged from within the GEM-TPC project during early software development in the context of PANDA, and has been developed by Christian Höppner and Sebastian Neubert. It was originally motivated by the wish to

[10] Whenever other methods are used for the purpose of comparison, it will be made clear in the text.

have a mathematically correct description of true space-point-like detector hit data, as provided by a TPC. In past experiments, approximations have been used by falling back to symmetry/geometry features of the individual detector systems. This can be seen as a symptom of a general fragmentation of the software used in high-energy particle physics: almost every experiment has its own, custom-made tracking software. In contrast, GENFIT was designed to be independent of the experimental setup, and is thus a candidate for becoming part of a code base shared among future experiments [11]. GENFIT has recently undergone a considerable amount of restructuring and improvement [66].

Following the implementation structure of the software package, the problem of track fitting can logically be separated into three independent building blocks: i) the *measurements* provided by the detector system(s), ii) *propagation* of the particles through material and magnetic fields (*track representations*) and iii) *fitting algorithms*. All of these elements will be introduced in the following, starting with and based on a general discussion of the default fitting algorithm (iii), the Kalman Filter. The mathematical framework presented there will then be used to introduce the propagation model (ii) of the track in Sec. 4.5.2. Finally, the modelling of data (i) from the FOPI tracking detectors will be discussed in Sec. 4.5.5.

4.5.1 The Kalman Filter

The Kalman Filter [67] is a *local*, recursive, linear least-squares fitting algorithm. Local in this context means that hit information is taken into account successively within an adaptive model, as opposed to a global fit of a single model to the entire hit ensemble at once. The circular track fit underlying `CdcCircle`s would be an example of a simple, global approach.

Let us return to the Kalman filter. Based on a serial stream of measurements k, the information about a system is to be determined with increasing precision. Within a chosen parametrisation of the system, its *state* at a given time can be represented by a vector of the model parameters $\mathbf{s} = (s_1, s_2, \ldots, s_N)$. A new measurement k is included by comparing it to a *prediction* $\widetilde{\mathbf{s}}_{k|k-1}$ of this model based on the information contained in the measurements so far, followed by a corresponding *update* of the state taking into account the new information. For any practical application, the measurements are affected by independent uncertainties $\mathbf{V}_k$. These are not required to be Gaussian in the framework of the Kalman filter, but are assumed to be in the following.

The recurring pattern of *predictions* and *updates* makes it an ideal (and widely used) candidate for real-time applications, for example in trajectory control and dynamic positioning (GPS). If new measurements do not have to

[11] Apart from the GEM-TPC project, it is currently being used by the PANDA and Belle-II collaborations.

be incorporated in real time, the incremental, "discrete" nature of the Kalman Filter and its extensions can still be a valuable feature, for example in pattern recognition schemes but also in the task of off-line track fitting we are concerned with here. The following, slightly technical discussion aims to demonstrate this.

Let $\mathbf{s}_{k-1}$ be the true model state at the time measurement k is considered. The following discussion assumes a perfectly known, *linear* evolution $\mathbf{F}$ of the state, described by the matrix equation [12]

$$\mathbf{s}_k = \mathbf{F}_k \mathbf{s}_{k-1} \quad . \tag{4.8}$$

Here $\mathbf{F}_k$ is the model for the transition between the two discrete states $k-1$ and k. Let $\widetilde{\mathbf{s}}_{k-1|k-1}$ be the last available state prediction and $\mathbf{C}_{k-1|k-1}$ the associated uncertainty covariance. Then the *a priori prediction* of the state relevant for including measurement k can be written in terms of the last available prediction as

$$\widetilde{\mathbf{s}}_{k|k-1} = \mathbf{F}_k \widetilde{\mathbf{s}}_{k-1|k-1} \quad . \tag{4.9}$$

Similarly, for the covariance of the state we have

$$\mathbf{C}_{k|k-1} = \mathbf{F}_k \mathbf{C}_{k-1|k-1} \mathbf{F}_k^{\mathrm{T}} + \mathbf{N}_k \quad , \tag{4.10}$$

where $\mathbf{N}_k$ describes intrinsic noise of the state transition model.

The next logical step is to incorporate the new measurement $\mathbf{m}_k$ [13] into the state. For doing so, we need to transform the state prediction into the space of $\mathbf{m}_k$. Let this transformation be defined by the matrix $\mathbf{H}_k$, then the measurement residual is given by

$$\mathbf{r}_k = \mathbf{m}_k - \mathbf{H}_k \widetilde{\mathbf{s}}_{k|k-1} \quad . \tag{4.11}$$

The effective residual covariance is given by the sum of the measurement uncertainty $\mathbf{V}_k$ and the covariance of the predicted state in the measurement space (Gaussian error propagation):

$$\mathbf{R}_k = \mathbf{H}\mathbf{C}_{k|k-1} \mathbf{H}_k^{\mathrm{T}} + \mathbf{V}_k \quad . \tag{4.12}$$

Now the crucial *update* of the state takes place: Most generally, the new *a posteriori* state containing the additional information of $\mathbf{m}_k$ can be written as

$$\widetilde{\mathbf{s}}_{k|k} = \widetilde{\mathbf{s}}_{k|k-1} + \mathbf{K}_k \mathbf{r}_k \quad . \tag{4.13}$$

The quantity $\mathbf{K}_k$ is called the *Kalman gain*. In Eq. (4.13) it appears as the relative weight of the measurement, and it must therefore be a function of $\mathbf{V}_k^{-1}$

[12] Some generalisations that have no relevance for the task of track fitting are omitted.

[13] The measurement is sometimes called *innovation* in this context, emphasising the incorporation of new information.

and the accumulated state uncertainty $\mathbf{C}_{k|k-1}$. If $\mathbf{K}_k = 0$, the new measurement is ignored and the state remains unchanged. For $\mathbf{K}_k \neq 0$ the state will be pulled towards $\mathbf{H}_k^{-1}\mathbf{m}_k$.

There is an important relation between $\mathbf{K}_k$ and the not yet discussed covariance of the posterior estimate $\mathbf{C}_{k|k}$: If the model is considered to be accurate, $\mathbf{C}_{k|k}$ can generally be given in terms of the true state $\mathbf{s}_k$ as

$$\mathbf{C}_{k|k} = \mathrm{cov}(\mathbf{s}_k - \widetilde{\mathbf{s}}_{k|k}) \quad . \tag{4.14}$$

Some algebra using the previous results leads to the expression ("Joseph form")

$$\mathbf{C}_{k|k} = (\mathbf{1} - \mathbf{K}_k\mathbf{H}_k)\mathbf{C}_{k|k-1}(\mathbf{1} - \mathbf{K}_k\mathbf{H}_k)^{\mathrm{T}} + \mathbf{K}_k\mathbf{V}_k\mathbf{K}_k^{\mathrm{T}} \quad , \tag{4.15}$$

$\mathbf{1}$ representing the unit matrix of corresponding dimensionality. Minimising the trace of $\mathbf{C}_{k|k}$ with respect to $\mathbf{K}_k$ yields

$$\hat{\mathbf{K}}_k = \mathbf{C}_{k|k-1}\mathbf{H}_k^{\mathrm{T}}\mathbf{R}_k^{-1} = \mathbf{C}_{k|k-1}\mathbf{H}_k^{\mathrm{T}}(\mathbf{H}\mathbf{C}_{k|k-1}\mathbf{H}_k^{\mathrm{T}} + \mathbf{V}_k)^{-1} \quad . \tag{4.16}$$

$\hat{\mathbf{K}}_k$ is called the *optimal Kalman gain*.

Two key features become evident at this point: First, when using the optimal gain $\hat{\mathbf{K}}_k$ the Kalman Filter is guaranteed to return a least-squares estimator for the state $\mathbf{s}$, since the minimisation of the trace $\mathrm{Tr}(\mathbf{C}_{k|k})$ is equivalent to minimising the expectation value of the square of the error $E(|\mathbf{s}_k - \widetilde{\mathbf{s}}_{k|k}|^2)$. This also means, however, that due to this quadratic nature the filter will be vulnerable to outlying noise. An extension of the filter aiming to attenuate this problem will be discussed in Sec. 4.5.3. Second, if the measurement uncertainties are Gaussian and uncorrelated, the least-square estimator is equal to the weighted average. Inserting the optimal gain into Eq. (4.13) yields

$$\widetilde{\mathbf{s}}_{k|k} = \widetilde{\mathbf{s}}_{k|k-1} + \mathbf{C}_{k|k-1}\mathbf{H}_k^{\mathrm{T}}\mathbf{R}_k^{-1}\mathbf{r}_k \tag{4.17}$$

and the nature of a *"weighted mean"* during the state increment is directly observed.

The final loose end is the choice of the initial state $\widetilde{\mathbf{s}}_{0|0}$ and its covariance $\mathbf{C}_{0,0}$, introducing an inevitable bias into the fit. This bias can be limited by performing multiple passes of the Kalman Filter, scaling the state covariance in between with a large factor (cf. Ref. [60]).

4.5.2 Track representation & Extended Kalman Filter

After this general introduction it is time to establish the connection to the problem of particle-track fitting. It is clear that the state parameters are to be identified with the physical properties of the detected particle. Each $\mathbf{m}_k$ will be the response of a detector system at a defined point in space, with their absolute uncertainties characterised by covariances $\mathbf{V}_k$. The evolution $\mathbf{F}$ must

then be a model for predicting the particle trajectory in between measurements (equation of motion).

This immediately leads to an important generalisation: The evolution model $\mathbf{F}$ has so far been restricted to be *linear*, but the propagation of a particle with mass M through a magnetic field $\mathbf{B} \neq 0$ and the detector material – described by the mass density $\rho(\mathbf{x})$ – certainly requires a non-linear model $f^{\mathrm{r}}(\mathbf{s}; \mathbf{B}(\mathbf{x}), \rho(\mathbf{x}))$ [14]. The three-momentum $\mathbf{p}$, charge q and mass M of the particle are encoded in the track parameters $\mathbf{s}$, $\mathbf{x}$ denotes the spatial coordinates. The index r is motivated by the analogy of the propagation model to the *track representation* in the implementation of GENFIT. For all purposes in the following, GENFIT's implementation of f^{r} based on a Runge-Kutta extrapolation algorithm (`RKTrackRep`) is used. The underlying Runge-Kutta solver for the equation of motion of charged particles was in turn taken over from the GEANT3 [68] software.

The non-linear track propagation model can be built into the Kalman Filter scheme in a straight-forward manner. The state prediction of Eq. 4.8 becomes

$$\mathbf{s}_k = f^{\mathrm{r}}(\mathbf{s}_{k-1}) \tag{4.18}$$

and Eq. (4.9) is modified accordingly. The prediction of the covariance (4.10), on the other hand, requires a linearisation of the transformation:

$$\mathbf{C}_{k|k-1} = \mathbf{J}_k \mathbf{C}_{k-1|k-1} \mathbf{J}_k^{\mathrm{T}} + \mathbf{N}_k \quad , \tag{4.19}$$

where $\mathbf{J}$ is the Jacobian of f^{r} defined at the point of the extrapolation. This modified algorithm incorporating a non-linear evolution mode is called *extended Kalman Filter*.

The model noise $\mathbf{N}$ now also gains a physical meaning: It contains the track extrapolation uncertainties due to multiple scattering and energy-loss fluctuations in the material. The non-zero mean of the energy loss in the detector material must already be accounted for in f^{r}.

At this point it has become clear why a local fitting approach has important advantages over a global track fit. The estimates $\widetilde{\mathbf{s}}$ will closely follow the particle trajectory, so local information like material distributions or inhomogeneities of the magnetic field can be taken into account accurately. This not only improves the propagation of the state, but even more so that of its error, since no long-range models for the correlations of the accumulated model uncertainties need to be constructed.

4.5.3 The Deterministic Annealing Filter

So far, it has been assumed that the task of track finding is performed in an ideal way and that it has no influence on the track fitter. In reality, this is

[14] The coordinates $\mathbf{x}$ are defined in a general coordinate frame in this context.

not the case: Uncorrelated hits from electronic noise as well as hits belonging to other, close-by particle tracks will be picked up by the pattern recognition algorithm(s) and falsely assigned to a given track.

The Kalman Filter as presented in the previous sections has no way of disregarding such polluting hits. On the contrary, large residuals will heavily bias the fit or – in the worst case – cause it to diverge (cf. the discussion below Eq. 4.16). A powerful extension of the Kalman Filter that offers protection against outlying hits, the Deterministic Annealing Filter (DAF), has been proposed by Frühwirth and Strandlie [69]. The basic idea is to give each hit in the track an assignment probability so that Eq. (4.13) becomes

$$\widetilde{\mathbf{s}}_{k|k} = \widetilde{\mathbf{s}}_{k|k-1} + \mathbf{K}_k \sum_{i=1}^{n_k} p_k^i \mathbf{r}_k \quad . \tag{4.20}$$

In addition, the formulation of the Kalman gain $\mathbf{K}_k$ and the state covariance $\mathbf{C}_{k|k}$ have to be modified to accommodate for the factors p_k^i (see Ref. [69] for details).

The sum in Eq. (4.20) runs over all competing hits relevant for the state transition $k-1 \to k$, and $\sum_{i=1}^{n_k} p_k^i = p_k$. In the application of particle-track fitting this corresponds, for example, to multiple, competing hits from the same planar detector or unresolved left-right ambiguities in wire hits. For a detector capable of providing truly three-dimensional space-point hits – like a TPC – we always have $n_k = 1$ and each measurement is assigned the weight p_k.

The filtering scheme now adds another layer of recursiveness: Assuming an initial choice for the p_k^i, a standard (extended) Kalman Filter fit of the track is performed, working with effective measurement errors $p_k^i \mathbf{r}_k$ (cf. Eq. 4.13). Subsequently, a backwards fit is performed using the same p_k^i. From both predictions – for each k – a weighted mean $\widetilde{\mathbf{s}}_k^*$ of the state can be computed based on all measurements *excluding* k. This procedure is called *smoothing*, and $\widetilde{\mathbf{s}}_k^*$ is called the *smoothed state* (with covariance $\mathbf{C}_k^*$). From this information the p_k^i are recalculated. An optional cut-off c on the p_k^i can be defined, below which hits are completely excluded from the fit. How this scheme is iterated and controlled will be discussed in the following.

First, we turn to the question how the p_k^i are modelled and recalculated. A possible and intuitive choice is to assume that the hits truly belonging to a track are normally distributed around the smoothed state prediction $\mathbf{H}_k \widetilde{\mathbf{s}}_k^*$ according to their measurement uncertainty $\mathbf{V}_k^i$ [15]:

$$p_k^i \propto \mathcal{N}(\mathbf{m}_k^i; \mathbf{H}_k \widetilde{\mathbf{s}}_k^*, \mathbf{V}_k^i) \quad . \tag{4.21}$$

[15] The choice of $\mathbf{V}_k^i$ for the distribution width instead of $\mathbf{R}_k^i$ as in Eq. (4.12) (with $\mathbf{C}_k \to \mathbf{C}_k^*$) can be motivated conceptually (cf. Ref. [70]). Intuitively, it is also clear that one can assume $\mathbf{H}_k \mathbf{C}_k^* \mathbf{H}_k^{\mathrm{T}} \ll \mathbf{V}_k^i$ for a sufficiently large number of measurements per track.

Fitter:	Prob. cutoff:	Annealing factors:	Term. parameter
`GFDaf`	$c = 0.01$	$\alpha_1 = 100$ $\alpha_2 = 31.62$ $\alpha_3 = 10$ $\alpha_4 = 3.162$ $\alpha_5 = 1$ $\alpha_6 = 0.3162$ $\alpha_{7,\ldots,10} = 0.1$	$\Omega = 10^{-3}$

Table 4.2: Parameters used with the GENFIT DAF implementation.

Here $\mathcal{N}(\mathbf{m}_k^i; \mathbf{H}_k\widetilde{\mathbf{s}}_k^*, \mathbf{V}_k^i)$ is a multivariate Gaussian distribution with mean $\mathbf{H}_k\widetilde{\mathbf{s}}_k^*$ and covariance $\mathbf{V}_k^i$. The assumption of normally distributed p_k^i is the one realised in the GENFIT implementation of the DAF (`GFDaf`).

In order to control the strictness of the outlier rejection (*"annealing"*), another parameter is required. Properly normalised, the final expression for computing the assignment weights p_k^i reads

$$p_k^i = \frac{\mathcal{N}(\mathbf{m}_k^i; \mathbf{H}_k\widetilde{\mathbf{s}}_k^*, \alpha\mathbf{V}_k^i)}{c(\alpha) + \sum_{k,i}\mathcal{N}(\mathbf{m}_k^i; \mathbf{H}_k\widetilde{\mathbf{s}}_k^*, \alpha\mathbf{V}_k^i)} \quad . \tag{4.22}$$

The additional parameter α appearing in Eq. (4.22) is the *annealing factor*. It simply scales the width of the assumed distribution. The optional cutoff $c(\alpha)$ appears in the denominator to ensure proper normalisation. For $\alpha \to 0$, the cumulative distribution function of the Gaussian approaches a step function, and the distribution of the p_k^i will strongly peak close to 0 and 1. Thus, α controls how strictly outlying hits will "freeze out" in the fit. When dealing with actual ambiguities [16], a hard freeze-out (α close to 0) is required, but in general a softer weighting scheme is desirable [69]. In the case of combined track fits in the S339 setup, however, the DAF offers protection mainly against outlying hits due to field distortions close to the field cage walls of the TPC and yet unresolved systematic problems introduced by the FOPI CDC (cf. Sec. 5.1). In this scenario, a small final value of α yields the best results.

During the fit, the annealing factor α is decreased step-wise. After reaching the last setting for α, the stability of the p_k^i in between iterations is monitored. The procedure is terminated either after ten iterations or earlier, if the absolute changes Δp_k^i fall below a fixed value Ω, e.g. $\Delta p_k^i < \Omega \,\forall\, k,i$. It shows improved fit results when compared to the standard Kalman Filter implementation (a qualitative impression is provided by Fig. 4.9) and is thus the standard method for feature extraction used in the scope of the analysis presented in this work. Table 4.2 summarises the parameters used.

[16] An example of such an ambiguous case are drift-time measurements from a wire detector (left-right ambiguity with respect to the wire in the detector plane).

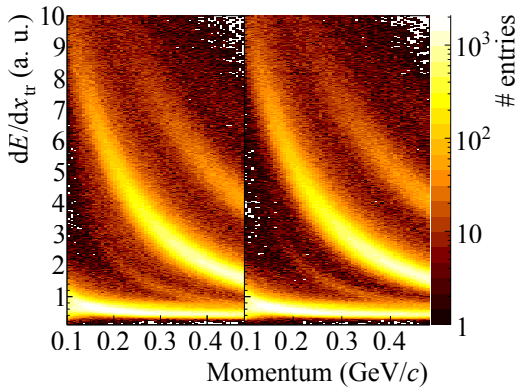

Figure 4.9: Comparison of spectra of the specific energy loss ($\mathrm{d}E/\mathrm{d}x$) vs. the particle momentum obtained with the standard Kalman Filter (left) and the DAF implementation (right) of GENFIT. The values on the ordinate are equal for both methods, only the recovered momentum depends on the fitting algorithm. For a discussion of the specific energy loss performance, see Sec. 6.5.

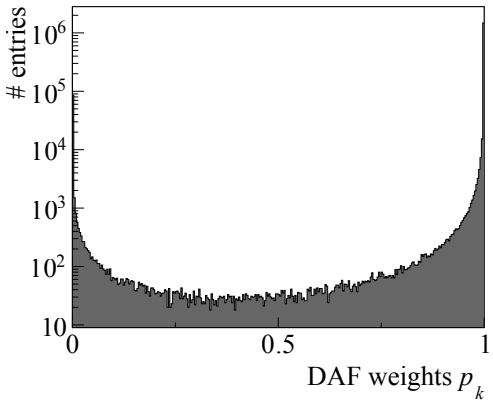

Figure 4.10: Distribution of weighting factors according to Eq. (4.22) in combined TPC-CDC fits. The parameters used result in a very "hard" spectrum, e.g. the dominant fraction of the hits is either rejected ($p_k = 0$) or accepted in the with its original uncertainty ($p_k = 1$).

As a final remark, the term "temperature" sometimes used in the literature for α has its origins in the correspondence of the DAF to the Elastic Arms Algorithm (EAA) [71]. Here, the (global) minimisation is performed in the context of a thermodynamical Boltzmann model, which lends the governing parameter the meaning of a temperature.

4.5.4 Vertex fitting: GFRave

Electrically neutral particles cannot be observed directly in tracking detectors, but they can be indirectly measured in their decays by tracking the charged daughter particles. In an exclusive measurement, and if all decay products carry electrical charge, the spatial positions, three-momenta and masses of the decay products can be used to infer the identity and kinematic properties of the parent particle at its decay vertex. GENFIT provides an interface ("GFRave") to the stand-alone vertex-fitting framework RAVE [72], which ships with implementations of numerous algorithms for vertex reconstruction. The simplest of these is that of a classical Kalman Filter is and discussed in the following.

It is instructive to consider the analogies to the previous discussion of a

Kalman Filter used for track fitting. The system state to be recovered is now the vertex position $\mathbf{v}$. The measurements k to be considered are the tracks selected for the vertex candidate, each parametrised by a set of parameters $\mathbf{s}_k$ (the former state of the *track* fit), which contain the three-momentum $\mathbf{p}_k$ of the track. Let the covariance associated with the $\mathbf{s}_k$ be $\mathbf{V}_k = \mathbf{G}_k^{-1}$. The track equation of motion (e.g. the *track representation* $f_k(\mathbf{s})$) can be linearised and written in the form

$$f_k(\mathbf{v}, \mathbf{p}_k) \approx \mathbf{A}_k \mathbf{v} + \mathbf{B}_k \mathbf{p}_k + \mathbf{C}_{k,0} \quad , \tag{4.23}$$

with $\mathbf{A}_k = [\delta f_k / \delta \mathbf{v}]$, $\mathbf{B}_k = [\delta f_k / \delta \mathbf{p}_k]$ and $\mathbf{C}_{k,0}$ a constant offset depending of the point of linearisation. From this separated formulation, update equations for both $\mathbf{v}$ and $\mathbf{p}$ and their respective covariances can be obtained. After including all tracks into the filter, least-square estimates for $\mathbf{v}$ and $\mathbf{p}$ are available. For a complete derivation, the reader is pointed to Ref. [73].

There are no free parameters entering [17] this classical Kalman Filter scheme, and consequently no tuning of the vertex fitter is required. This is a serious advantage. Numerous adaptive methods exist for the task of vertex fitting, but they require more care by the user. These algorithms become beneficial when large track densities or cascaded decays lead to wrong assignment of tracks to the vertex candidates ("track outliers"). The low charged particle multiplicities (< 2 on average) during the S339 experiment present a much simpler environment. Another source of such "track noise" is faulty pattern recognition (ghost tracks, track splitting), but these issues are largely suppressed by requiring matching between TPC and CDC tracks (cf. Sec. 4.6) in the analysis discussed in this work. For these reasons, all vertex fits in the following are performed using the "kalman" option of RAVE.

4.5.5 Modelling of FOPI data in GENFIT

The tracking data of the S339 experiment are modelled in C++ objects that are derived from GENFIT's hit implementations. These objects contain the underlying geometry the spatial hit information is defined in and the uncertainty of the measurement. The last missing connection to the previously discussed fitting scheme is the matrix $\mathbf{H}$ (cf. Eqs. (4.11) and (4.12)): It encodes the projection of the state onto the measurement plane and is defined for each detector hit.

For the S339 data, two classes of detector hits are required: *space-point hits* and *pixel hits*. The latter are straight forward to understand and implement: The measurement plane is defined by the physical detector geometry, and the matrix $\mathbf{H}$ is identical for every hit belonging to the same detector module. The measured position and its uncertainty are given by the c.o.g. of the sensitive

[17] As long as the choice of the expansion point in Eq. (4.23) is reasonable.

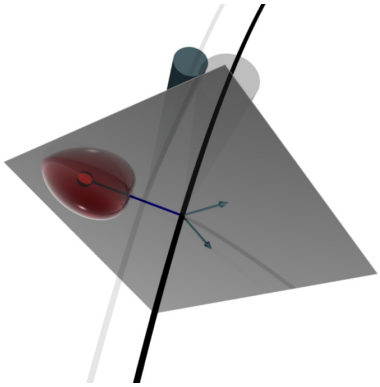

Figure 4.11: Virtual detector plane for a three-dimensional space-point hit. The plane is spanned perpendicularly to the track such that it contains the hit (shown as red dot with attached covariance ellipsoid). The track prediction (Black) and the updated state (light Gray) are also visualised. The corresponding state uncertainties are depicted as cones in the extrapolation plane.

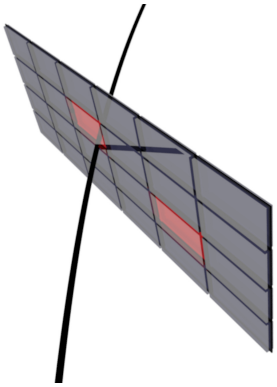

Figure 4.12: Example of a fixed detector plane in an array of pixel detectors. True hits and noise hits are treated equally in a generic Kalman Filter implementation. They can be made to compete within a probabilistic model. An example of such an implementation is the DAF.

element that provided a signal, and the pitch of the detector structure. In this case of a shared detector plane, however, noise hits picked up by the pattern recognition directly compete with track hits within the same prediction and update step. It has been described in Sec. 4.5.3, how an adaptive algorithm like the DAF is perfectly suited for such a situation (cf. Eq. (4.20), $n_k \neq 1$).

Space-point hits are a bit trickier, as no physical plane of measurement exists in that case. However, the information that a three-dimensional hit can contribute to a track fit *is* two-dimensional: The component of the measurement that projects onto the direction of the track has no influence on the fit, as is evident in Eq. (4.11). This circumstance is exploited in GENFIT by the concept of so-called *virtual detector planes*, which are constructed dynamically for each space-point hit during the fitting procedure. Based on the hit position and the *local* information provided by the corresponding prediction of the track state, a plane perpendicular to the track and containing the hit is constructed [18]. The concept is visualised schematically in Fig. 4.11. The projection matrix $\mathbf{H}$ needed for the update must be computed dynamically for each measurement. The simpler case of planar pixel hits with a fixed detector plane is shown in Fig. 4.12.

The data of four different detectors have to be modelled for the analysis

[18] This can be seen as another advantage of a *local* fitting scheme.

Detector:	Hit type:	Errors:
TPC	Space-point hit	*dynamic*; $f_{\mathrm{E}} = 10.0$
CDC	Space-point hit	$\sigma_{x,y} = 350\,\mu\mathrm{m}$, $\sigma_z = 10\,\mathrm{cm}$
BAR	Pixel hit	$\sigma_\Phi = 0.9\,\mathrm{cm}$, $\sigma_z = 8.0\,\mathrm{cm}$
RPC	Pixel hit	$\sigma_\Phi = 0.2\,\mathrm{cm}$, $\sigma_z = 1.5\,\mathrm{cm}$

Table 4.3: Overview of the hit information used for GENFIT fits on S339 data. The values for the FOPI detectors are taken over from the discussion of Chapter 3. The uncertainties of TPC hits are defined dynamically during clustering (cf Sec. 4.3). The quantity f_{E} is defined in Eq. (4.5).

presented in this work: The TPC and the CDC provide three-dimensional space-point hits, and hits from both the BAR and the RPC are modelled as two-dimensional pixel hits. The positions of the latter two are given by the centre of gravity of the respective detector modules. CDC positions in the x-y plane are initially calculated from the measured drift radii and after the rejection of mirror tracks, as explained in Sec. 3.2.1. The hit position along the wire direction is obtained from a measurement of the fractional charge at both ends of the wires. In anticipation of the findings presented in Chapter 5, the heuristic corrections summarised in Sec. 5.4 are applied after importing the original FOPI hit data from CDC and RPC. The calculation of cluster positions in the TPC has been explained in Sec. 4.3.

This leaves the question of the hit uncertainties. The values for the RPC and BAR detectors have already been summarised in Sec. 3.2.2. The uncertainty of the CDC hits is initially set inside the FOPI routines and is derived from the distance of each hit w.r.t. the circular track fit. This definition is obviously not a suitable choice for a re-fit of these data, since it would bias the fit towards the (wrong) assumption of a circular track. On top of that, one has to respect additional systematic effects present in the CDC system (discussion to follow in Sec. 5.1). The situation can be pragmatically cured by assigning *constant* errors instead, and this is the strategy pursued in the combined analysis: The CDC hit uncertainty in the x-y plane is set to a value of $350\,\mu\mathrm{m}$ and $10\,\mathrm{cm}$ along the wire direction, respectively. For the TPC, once again, the spatial covariances of individual clusters are determined dynamically according to Eq. 4.5. All numerical values are summarised in Tab. 4.3.

Finally, the mass distribution $\rho(\mathbf{x})$ of the detector setup and the magnetic field $\mathbf{B}(\mathbf{x})$ are required for track fitting (cf. Sec. 4.5.2). The software implementation of the material is modelled using the geometry package of ROOT (`TGeo` classes), and is visualised in Fig. 3.5. The magnetic field is modelled as a three-dimensional vector field according to the field map of Sec. 3.2.3.

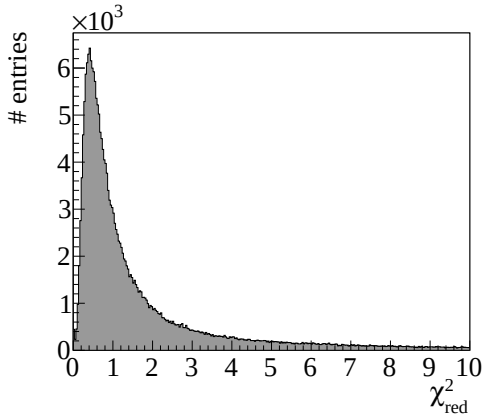

Figure 4.13: Reduced χ^2 distribution of TPC track fits.

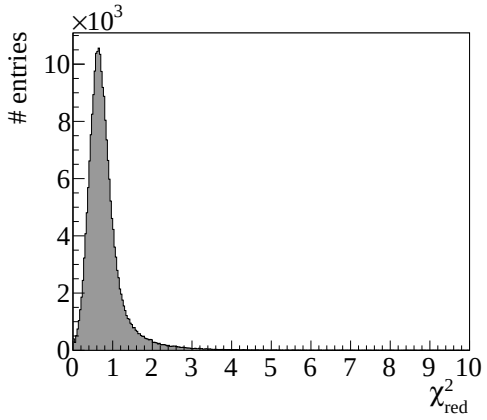

Figure 4.14: Reduced χ^2 distribution of combined fits in the TPC-CDC system.

4.5.6 Performance

Without being able to resort to to a quantitative cross check with results obtained from simulations (cf. Sec. 4.8), the consistency of the parameters passed to the track-fitting algorithms can still be checked qualitatively. A suitable measure of the goodness of the track fits can be constructed from the sum of the weighted, squared residuals

$$\chi^2 = \sum_k \frac{|\mathbf{r}|_k^2}{\sigma_k^2} \quad . \tag{4.24}$$

Here, $\mathbf{r}$ denotes the observed residual between the track fit and the detector hit, σ is the measurement uncertainty put into the model and the sum runs over all hits contributing to a track. If the measurement uncertainties are well described and under the assumption that they are normally distributed, the value of χ^2 should be equal to the degrees of freedom D of the performed fit.

It is convenient to normalise the above quantity by dividing out the model complexity D:

$$\chi^2_{\text{red}} = \frac{\chi^2}{D} \quad . \tag{4.25}$$

The quantity χ^2_{red} is called "reduced χ^2". As a rule of thumb, if χ^2_{red} is close to 1, the assumed measurement uncertainties σ give a good description of the observed variations around the mean of the obtained fit.

Figures 4.13 and 4.14 show the distributions of χ^2_{red} for track fits performed in the TPC alone and in the combined system of TPC and CDC, respectively. The dynamic calculation of TPC cluster uncertainties and the associated problems (cf. Sec. 4.3) lead to a very broad distribution in the first case. A long tail towards large values of χ^2_{red} can be observed, suggesting cases of largely

underestimated cluster errors or mis-interpreted correlations. In the case of combined track fits, a much more narrow distribution with a mean value close to 1 is observed. What is of course missing in this picture is the case representing track fits in the CDC alone. In Chapter 5 the reader will learn that CDC tracks are still to some extent globally shifted with respect to TPC tracks due to shortcomings of the CDC calibration (cf. Sec. 3.2.1). In that light, the value for the CDC hit uncertainties given in Tab. 4.3 are currently engineered in such a way as to yield a reasonable fit performance in *combined* track fits, which are – after all – the final objects used for the extraction of physical properties. In track fits performed in the CDC system alone, which are not affected by a translation of the entire track, the errors are currently observed to be generally overestimated. As soon as the remaining systematical effects are under control, the optimisation of the values of Tab. 4.3 has to be revisited.

4.6 Matching of FOPI and GEM-TPC tracks

After individual track fits for the TPC and the surrounding FOPI detectors are available, these can be matched and candidates for combined track fitting can be constructed. The CDC track candidates, as written out by the FOPI reconstruction routines, already contain the pairing information with respect to matched hits in the BAR or RPC detector (if applicable). What remains to be done in the scope of the TPC-combined analysis is the matching of these tracks with tracks measured with the GEM-TPC.

In view of the low charged-track multiplicity per event, it is sufficient to perform this matching in the azimuthal projection. From a technical point of view, the circular track model for CDC tracks as obtained directly from the FOPI reconstruction are used for this track comparison, instead of the computationally more costly extrapolations of GENFIT tracks. From the available matching criteria, two have emerged as the optimal choice: i) the azimuthal residual of the outermost hit in the TPC track and the innermost hit in the CDC track and ii) the angular residual of the tangent to both tracks at the intersection point. For the former a residual $< 15°$ is required, and for the latter an angular change $< 10°$.

In order to define an efficiency of this procedure without the possibility of refraining to information from simulations (see Sec. 4.8), the following scheme is applied: Starting from tracks found in the CDC, the fraction of successfully matched tracks in the TPC is studied as a function of the polar angle Θ_{lab}. In order to reject noise tracks and track fragments due to problems with the CDC pattern recognition algorithm, a minimum number of 45 hits per CDC track is required. The obtained efficiency can be regarded as the *combined* efficiency of the TPC pattern recognition (cf. Sec. 4.4) and the matching procedure itself. Its evolution with the polar laboratory angle is shown in Fig. 4.15. Tracks with ambiguous matches are not considered in the above study.

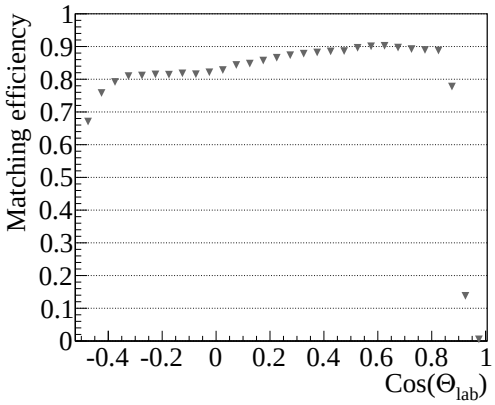

Figure 4.15: Combined efficiency of the track-matching routine and the TPC pattern recognition, based on CDC tracks. For every CDC track with more than 45 hits, the successful matching with a TPC track is checked. The polar angle of the CDC track is used for the abscissa.

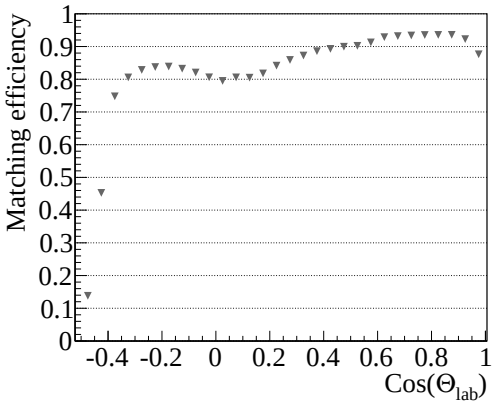

Figure 4.16: Combined efficiency of the track-matching routine and the CDC pattern recognition, based on TPC tracks. The latter are selected using the criterion shown in Fig. 4.17. The polar angle of the TPC track is used for the abscissa.

Complementary information can be obtained when reversing this scheme and studying the efficiency when matching CDC tracks based on valid TPC tracks. The definition of a quality cut for the latter is done differently than for CDC tracks: In view of the dynamic nature of hit clustering (cf. Sec. 4.3) and the superior spatial resolution along the z axis, the point of exit of a TPC track is used as a criterion. The spatial distribution in the r-z plane of the last point of TPC tracks is shown in Fig. 4.17. For the efficiency calculation, only tracks that exit the TPC on the radially outwards wall of the vessel are considered. The result is again a combined efficiency, this time of the matching procedure and the CDC pattern recognition. It is shown as a function of the polar laboratory angle in Fig. 4.16.

4.7 Alignment for combined track fits

Two separate coordinate frames have been defined in Sec. 4.1.3: the global laboratory coordinate frame (x,y,z) of the FOPI spectrometer and the coordinate frame defined by the physical vessel of the TPC, (u,v,w). Inevitable tolerances and imperfections involved in the mechanical mounting of the TPC introduce unknown shifts and rotations between the two. In order to perform combined track fits in this setup, the space points measured in the GEM-TPC need to be transformed into the global frame first.

An external procedure is used to determine the unknown parameters of this

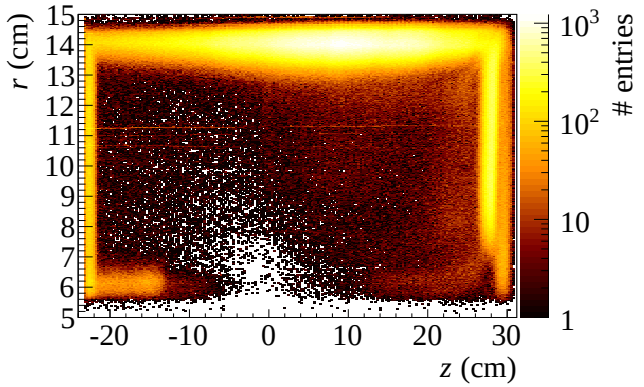

Figure 4.17: Position of the last point of $\sim 3 \cdot 10^7$ TPC tracks in the r-z plane. For the efficiency, only tracks exiting the vessel on the radially outwards border are taken into account. These are selected by fitting a Gaussian to exit peak of the radial profile and rejecting tracks outside a window of $\pm 2\sigma$ around the mean value (14.0 cm).

transformation. The tracking data available from the FOPI detectors represent the reference in this context: The algorithm uses track fits performed with GENFIT on FOPI data and extrapolates these tracks into the TPC volume. Such extrapolations are natively provided by GENFIT and make use of the same propagation model that is already part of track fitting (*track representations*, cf. Sec. 4.5.2). *A priori*, the coordinate frame of the TPC is assumed to be equal with the global one. By comparing the extrapolation to the cluster positions $\mathbf{u}^i_{\mathrm{cl}}$ of the matched TPC track, one obtains a set of residuals

$$\mathbf{r}_i = \xi_i - \mathbf{u}^i_{\mathrm{cl}} \quad , \tag{4.26}$$

where ξ_i denotes the point of closest approach (POCA) w.r.t. the position of cluster i found during the extrapolation. All quantities in Eq. (4.26) are defined in the (u,v,w) frame.

When defining a geometrical transformation $\mathcal{A} : (u,v,w) \rightarrow (x,y,z)$ – controlled by a set of parameters $\{a_i\}$ – the task of aligning the two coordinate frames can be transformed into the problem of finding the set of parameters $\{a^*_i\}$ that minimises the sum of squared residuals $\sum_i \mathbf{r}^2_i$. The actual minimisation in this parameter space is performed using the MINUIT [74] implementation shipped with ROOT. In order to achieve a sufficient coverage of the detector acceptance, the residual data need to be collected for a very large number ($\mathcal{O}(10^5)$) of tracks.

The full transformation can be decomposed into a translation and a rotation, executed in that order. The translation is trivially determined by a vector $\boldsymbol{\tau}$. The rotational degrees of freedom of the alignment transformation are described using three Tait-Bryan angles Ψ_x, $\Psi_{y'}$ and $\Psi_{z''}$. Applied in this order, the angles give the rotation about the x axis, the new y axis after the

Par.:	τ_x	τ_y	τ_z	Ψ_x	$\Psi_{y'}$	$\Psi_{z''}$
Val.:	$6.05 \cdot 10^{-2}$	$-1.63 \cdot 10^{-1}$	$-4.34 \cdot 10^{2}$	$1.18 \cdot 10^{-1}$	$4.73 \cdot 10^{-2}$	1.52

Table 4.4: Parameters of the alignment transformation as used during the analysis of the data taken during the S339 experiment. For the definition of the quantities, the reader is referred to the text of Sec. 4.7. The units are (cm) for the translation parameters and (deg.) for the rotations. It is important to note that these values determine the final alignment transformation, *after* the corrections discussed in Chapter 5 have been applied.

first rotation, and the new z axis after both rotations. In view of the numerical stability of the minimisation step, this choice of parametrisation is well-suited for the observed magnitude and distribution of mis-alignments. The set of values used for the data analysis in this work is summarised in Tab. 4.4. Once they are obtained, the position $\mathbf{u}_{\mathrm{cl}}$ and covariance $\mathbf{C}_{\mathrm{cl}}$ of every reconstructed cluster in the GEM-TPC can be transformed into the global coordinate frame by applying the transformation $\mathcal{A}$.

As an important upgrade of the current alignment scheme, it is foreseen to incorporate the drift velocity v_{d} in the GEM-TPC into the model as a free parameter. This feature is currently being implemented, and will be presented alongside additional information on the alignment procedure in Ref. [55] (currently in preparation).

4.8 The problem of a missing Monte Carlo simulation layer

The chapter is concluded by the discussion of an important limitation of the TPC-combined feature extraction of FOPI data: The lack of combined simulations for efficiency and acceptance corrections.

Most generally, the task of a microscopic simulation of the physics performance of a detector system can be divided into three logical steps: i) the randomised generation of particles entering the detector volume, ii) the transport of the particle through the detector material and iii) the modelling of the active response of the different detector systems to the passage of the particles. Stand-alone software packages implementing all of these steps exist for both the GEM-TPC and the FOPI spectrometer.

For the combined spectrometer, however, the situation is different. The generation of particles (i) does not depend on the detector setup and shall not concern us further. A model of the geometry and material distribution of the combined setup (ii) exists, as was shown in Sec. 3.2 and Fig. 3.5. The discussion of Sec. 4.5.2 showed how this is also a requirement for the task of track fitting. Regarding point (iii), however, there is no software available to simulate the

propagation of particles through the *combined*, TPC-augmented FOPI setup, taking into account the response of all detector systems. The development of a combined software package, merging the two simulation frameworks existing for FOPI and for the GEM-TPC into one self-consistent scheme, has simply not been possible due to manpower and time constraints.

This fact has two important implications. On the level of algorithm development for feature extraction, the lack of such a combined detector simulation prevents us from assessing algorithm performances in an unbiased way. Most importantly, in the context of a physics analysis, realistic corrections of the efficiency and the acceptance of the spectrometer are not available, rendering a measurement of absolute quantities impossible. Due to this fact, the physics results presented in Chapter 8 of this work are all relative measurements, where such effects can be expected to cancel out in good approximation.

Chapter 5

Quality of the combined feature extraction

As stated earlier, the data obtained from the standard FOPI reconstruction software are initially regarded as complete and self-consistent. After the previous introduction of the tools necessary for performing a combined feature extraction with the GEM-TPC in the S339 setup, the validity of this statement will be explored qualitatively in this chapter. For this purpose, some key figures of merit obtained from feature-extracted data are compared between the standard FOPI reconstruction routines and the TPC-combined analysis. Unfortunately, several rather severe problems can be identified in the process.

Section 5.1 is concerned with systematic problems found in the FOPI CDC, and a heuristic approach of mitigating these effects will be outlined. Section 5.2 is dedicated to the FOPI RPC. Here, the TPC-combined analysis reveals a deliberate, systematic modification of RPC positions introduced in the standard FOPI reconstruction scheme. An alternate approach is required in order to benefit from the additional tracking information provided by the TPC, which will be explored in the discussion. Following this survey, the impact of incorporating GEM-TPC data on the TOF performance of the augmented FOPI spectrometer is studied in Sec. 5.3. Finally, the implications of these findings in view of the data analysis presented later in this work will be summarised in Sec. 5.4.

5.1 Systematic effects found in the FOPI CDC

During the development of the combined reconstruction algorithms it became apparent early on that the performance of the combined track fits in the TPC-CDC system is not as expected.

The clearest evidence of these problems was found during the optimisation of the alignment parameters (cf. Sec. 4.7): Figures 5.1 and 5.3 visualise information extracted from the extrapolation residuals – as defined in Eq. (4.26) –

after the alignment procedure has converged. Specifically, Fig. 5.1 shows the residual distance in the azimuthal plane as a function of the cluster position in the TPC along the radial direction. The same information can be studied resolved as a function of the azimuthal coordinate of the reference track from the CDC, which is shown in Fig. 5.3.

The interpretation of these observations is not straight forward. Let us begin with Fig. 5.1: The observed preferred direction of the residuals implies a relative tilt between TPC and CDC tracks for both charge signs, which is clearly unphysical: No global transformation of either of the two systems as a whole can create this pattern. Therefore, a systematic detector effect in the TPC-CDC system must be at work. Considering the high level of symmetry of the TPC detector vessel and readout structure (cf. Sec. 3.1, specifically Fig. 3.4), a conceptual problem related to the physical structure of the TPC seems unlikely. Another possible explanation on the TPC side could be distortions of the drift field. However, a study of such distortions, using high-momentum cosmic tracks, revealed only relatively small deviations in close vicinity of the field cage walls [75]. In this light, the source of the effect has to be suspected to lie within the CDC detector. Indeed, the asymmetric shape of the CDC sector geometry, specifically the rotation of the wire plane out of the radial direction (cf. Fig. 3.7), is a likely source for a breakdown of the azimuthal symmetry of the system.

A plausible scenario from a technical point of view is a an incorrect description of the wire plane position in the FOPI reconstruction code. In the following, the possibility of a parallel translation along the wire plane normal vector is explored, which would result in a corresponding shift of CDC tracks. Due to the relatively small inclination angle of the wire planes, this would also in good approximation represent a parallel shift w.r.t. to the matched TPC tracks. Under that hypothesis, the alignment algorithm would attempt to minimise the squared residual distances generated by this offset by *rotating* TPC tracks around the beam axis, following the direction of this shift. The combination of these two transformations thus provides a qualitative explanation of the observed pattern and the change of sign in the residuals along the TPC tracks. Figure 5.2 provides a schematic visualisation of the transformation hypothesis.

In order to disentangle the two effects, one can first attempt to manually remove the undesired rotation introduced by the alignment scheme. Indeed, for a manual rotation of $\sim -0.95°$, the spectrum of Fig. 5.1 becomes flat along r and shows a constant offset of $\sim 1.80\,\mathrm{mm}$ in the residual distances. This value can then be used to cancel the suspected wire-plane shift on CDC hit level *before* combined track fits are performed. Exactly this heuristic strategy is enforced on the S339 data in the context of this work.

Let us move on to Fig. 5.3. It shows the same data as Fig. 5.1, but this time as a function of the azimuthal angle, which is taken at the point where

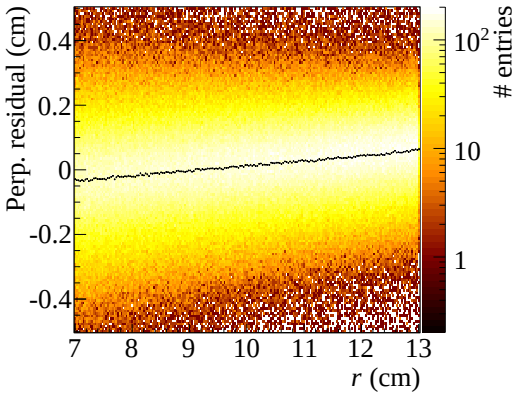

Figure 5.1: Extrapolation residuals (distance in the azimuthal plane) observed after alignment has initially converged, shown as a function of the cluster position along r. The sign is given by the change in the azimuthal angle between the aligned clusters $\mathcal{A}(\mathbf{u}_{\mathrm{cl}}) = \mathbf{x}_{\mathrm{cl}}$ and the POCA ξ, $\mathrm{sgn}(\Phi_{\mathrm{cl}} - \Phi_{\xi})$. The black points mark the mean and its error along the ordinate. TPC clusters close to the field cage walls (within 2 cm distance) are omitted during alignment in order to prevent potential distortions of the drift field from entering the procedure. The data have been kindly provided by S. Dørheim, TUM.

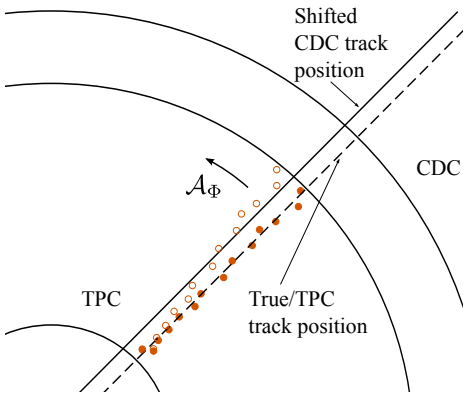

Figure 5.2: Schematic explanation of the effect introduced by a wrong description of the CDC wire plane position: A shift of the wire plane position results in a CDC track (solid straight line) that is equally shifted w.r.t. to the true track position measured by the TPC (solid circles, dashed line). When minimising relative residuals, the alignment procedure attempts to compensate this effect by introducing a global rotation $\mathcal{A}_\Phi$ of the TPC, resulting in transformed cluster positions (hollow circles).

the reference track penetrates the inner wall of the CDC. A distinct, periodic pattern is observed, which is correlated with the segmentation of the CDC into 16 sectors. The investigation of this effect [55] has revealed that the structure is correlated with the timing offset t_0, which is not optimally determined by the FOPI calibration procedure (cf. Sec. 3.2.1). As evidence supporting this interpretation, the same data is shown in Fig. 5.4 after the value of t_0 has been manually changed. While the periodic pattern is still visible, the situation is clearly improved by the introduction of this manual shift.

5.1.1 Summary and implications

In the foregoing, clear evidence of systematic problems in the FOPI CDC has been presented. The plausibility of the hypothesis of i) an effective shift of the

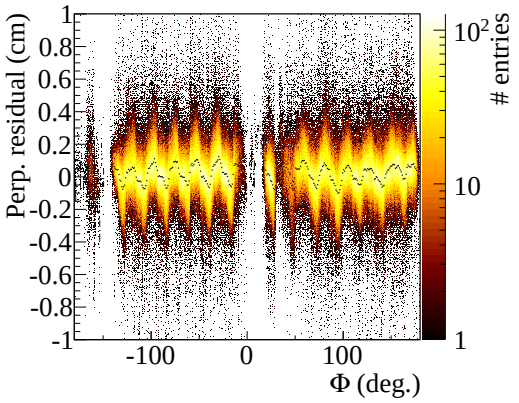

Figure 5.3: Extrapolation residuals (distance in the azimuthal plane) in the TPC after the initial alignment as a function of the azimuthal angle Φ of the penetration point of the CDC reference track. The data have been kindly provided by S. Dørheim, TUM.

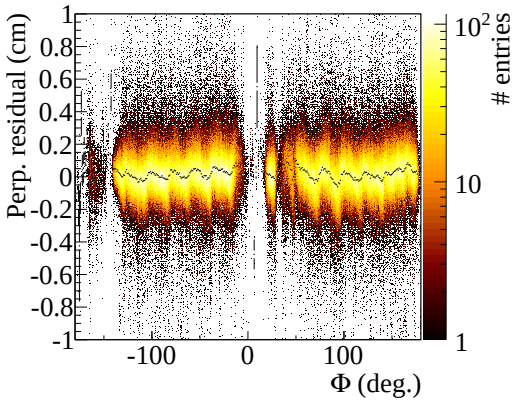

Figure 5.4: Same data as in Fig. 5.3, after introducing a manual change of the CDC readout-time offset t_0 (cf. Sec. 3.2.1) by $\sim 8\,\mathrm{ns}$. The data have been kindly provided by S. Dørheim, TUM.

CDC wire planes w.r.t. their nominal positions and ii) a wrong calibration of the time offset t_0 of the CDC readout electronics has been demonstrated.

However, the "correct" values of the wire plane positions and the timing offsets t_0 could so far only be obtained heuristically. In both cases, a systematic optimisation of the parameters is required to arrive at the theoretical performance of combined tracking that can be expected from the intrinsic spatial resolution of the TPC and the CDC. Such a quantitative optimisation is not available at the time this document is written, but will be provided in the future [55].

Even though the situation could already be improved considerably by using this heuristic "re-calibration", the remaining systematic effects still turn out to be larger than the intrinsic resolution of the CDC. In anticipation of Chapter 7, an important example where this situation can be observed is the spectrum of the specific energy loss measured in the CDC as a function of the particle momentum: Figure 5.5 shows a comparison of such $\mathrm{d}E/\mathrm{d}x$ spectra obtained both with the momentum calculated with the native CDC (circle) fits and TPC-combined fits performed with GENFIT. Clearly, the spectrum is more washed out in the latter case, especially in the low-momentum region.

The reason the systematic problems with the CDC remain unnoticed in the scheme of the standard FOPI feature extraction lies in the fact that spatial information external to the CDC (reconstructed vertices, hits registered in the BAR or RPC detectors) *never enters directly* into the track fit. The calculation of the momentum in the x-y plane is thus transparent to a translation of the

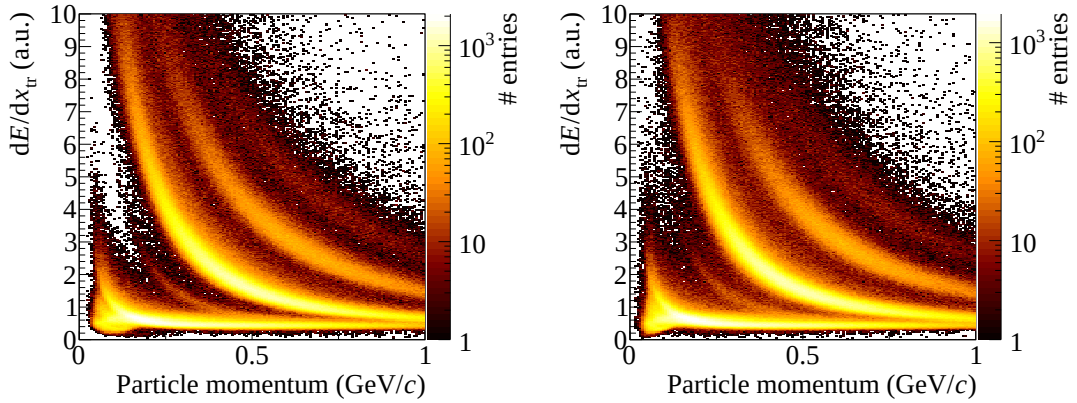

(a) Native CDC circle fits.

(b) TPC-combined fits.

Figure 5.5: CDC $\mathrm{d}E/\mathrm{d}x$ as a function of the particle momentum from $\sim 2.1{\cdot}10^6$ matched tracks. Compared are the situations where the momentum is taken (a) from native CDC circle fits ("Momentum" of `CdcTrack`s, cf. Tab. 4.1) and (b) from TPC combined track fits performed with GENFIT, after the heuristic corrections as discussed in Sec. 5.1 has been applied. The data on the ordinate is identical in both pictures ("Eloss" of `CdcTrack`s, cf. Tab. 4.1).

CDC track as a whole. Both a wrong position of the wire planes and an incorrect calibration of the timing offset t_0 lead to such a translation [1]. When external tracking information *is* taken into account – in the case of the TOF detectors – it is only propagated into the polar angle of the `CdcTrack` (cf. Tab. 4.1 and the attached discussion). Here, another important peculiarity of the FOPI feature extraction enters the picture, which will be discussed in the following section.

5.2 A change of paradigm in the treatment of the FOPI RPC

The liberal philosophy of the FOPI feature extraction concerning *absolute* position information manifests itself in another important systematic effect that was discovered during the TPC-combined feature extraction of the S339 data.

In addition to the effects in the x-y plane that have been discussed in the previous section, the CDC also shows variations of the average, global position along the wire axis (z) of reconstructed tracks in between the individual sectors. These can be measured by comparing the position measurements provided by the CDC with track fits performed in the TPC-RPC system. The relative

[1] The CDC drift-time relation $r_\mathrm{d}(t)$ is assumed to be linear during the FOPI feature extraction, cf. Sec. 3.2.1.

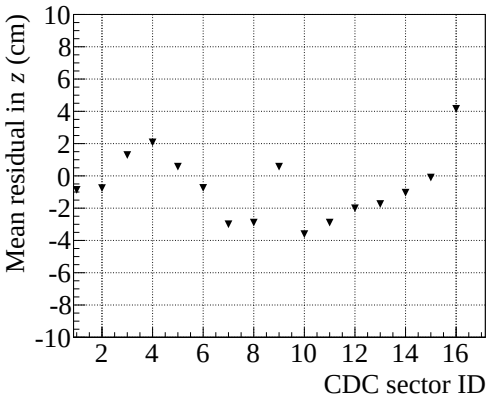

Figure 5.6: Relative shifts between CDC tracks and TPC-RPC tracks along the z axis as a function of the CDC sector number. For each sector, the data point corresponds to the mean value of all singe-wire residual data (an example is shown in Fig. 5.7).

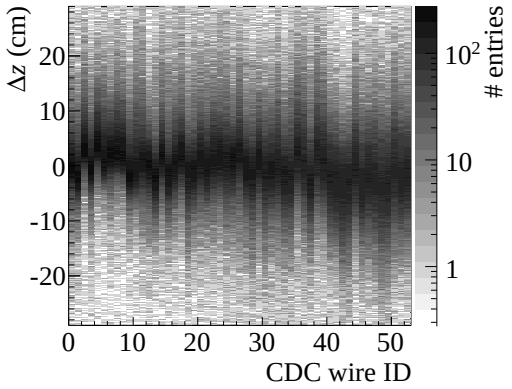

Figure 5.7: CDC hit residuals along the wire direction (z) with respect to the corresponding GENFIT track fit, when only hits from the TPC and the RPC are taken into account. Shown is a representative example of one sector.

variations in between sectors when averaging over all wires of each sector are observed to be of the order of several cm (cf. Fig. 5.6). Figure 5.7 shows the same data resolved on the single-wire level, in the example of one sector.

Even though the point-resolution of the CDC along the beam axis is one order of magnitude below that of the RPC (cf. Tab. 4.3), the strategy that is pursued in the original FOPI reconstruction software is to compensate these variations by introducing Φ-dependent *shifts of RPC modules* along the z axis. As expected from Fig. 5.6, the resulting, modified positions of the RPC modules are distributed asymmetrically and show fluctuations about the mean value of several cm (RMS of the distribution $\sim 2.8\,\mathrm{cm}$).

It can be argued that this approach restores consistency of the tracking information within the CDC-RPC system, in the sense of an effectively improved momentum resolution. However, it also represents a deliberate deterioration of the global determination of the particle trajectory along the beam direction. Most importantly, it renders these modified tracks incompatible with the external hit information provided by the GEM-TPC. Unfortunately, a proper calibration of the CDC positions w.r.t. the nominal RPC module positions is not foreseen in the FOPI reconstruction software. In view of the superior z resolution of the GEM-TPC, the most favourable strategy for a TPC-combined tracking is thus to force the RPC modules back to their nominal position in order to have the maximal amount of globally correct spatial information available for the final track fits. This is the approach that is taken for the data

analysis presented in this work [2].

In this situation, a calibration of the CDC on single-wire level can be attempted using the data shown in Figs. 5.6 and 5.7. Such a calibration is biased in the sense that it is restricted to the RPC acceptance and averages over any potential z-dependence of the systematics in the CDC. It however represents a valid strategy to homogenise the available tracking information, making use of the positional information provided by the TPC. Following this approach, CDC hits are re-positioned along the wire direction before they enter the combined track fits. It will be shown in Sec. 6.3 that these steps lead to a greatly improved momentum resolution for tracks penetrating the RPC detector for the TPC-combined analysis, when compared to the standard FOPI approach.

5.3 Impact on the TOF performance

In the previous section it has been shown that the strategy of the standard FOPI feature extraction is to optimise the momentum resolution at the expense of a loss of absolute positioning information. For both the CDC and RPC systems, alternate calibration methods for the TPC-combined reconstruction have been presented. In this section, the impact of this new strategy is explored further.

A simple check of the track fitting performance is the quality with which the beam spot can be reconstructed, extrapolating combined track fits back into the target plane. In Fig. 5.8, this is shown for tracks reaching the RPC detector. The impact of including the TPC data in the track fit is dramatic: If only FOPI tracking information is used – even when including the additional hit provided by the RPC –, the quality of the track fit is limited by the poor resolution of the CDC along the beam axis. In addition, the distribution still shows systematic effects. After including the hit information provided by the TPC, however, the beam spot can be clearly resolved within the boundaries of the target disc.

Such an improvement of the global positioning information should directly translate into the performance of TOF measurements, as these involve the total flight distance of the particle. For the purpose of PID, one is interested in clean reference data samples describing the detector response to different particle species. In the example of the RPC, the quality of the TPC-combined track fits allows a simple background rejection by means of a geometric cut on the beam spot (visualised as dashed Gray line in Fig. 5.8b).

Figure 5.9 shows the spectrum of the reconstructed particle velocity – from a TOF measurement in the RPC – as a function of the particle momentum.

[2] This also made a re-calibration of the RPC timing information on the level of the FOPI data reconstruction necessary. This was kindly performed by Prof. Norbert Herrmann, Heidelberg.

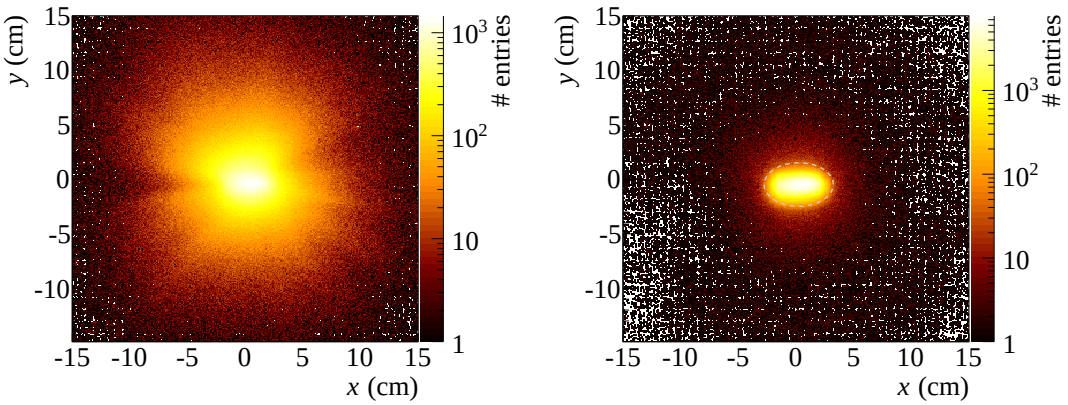

Figure 5.8: Back-extrapolation of GENFIT track fits containing a hit in the RPC into the target plane ($z = 0$). Compared are (a) tracks only defined in the CDC-RPC system and (b) tracks also including hit information from the GEM-TPC. The dashed outline drawn in (b) corresponds to a cut used for background rejection, as discussed in the text.

The spectra as obtained from the standard FOPI feature extraction and from the full TPC-combined reconstruction are compared. In the latter case, the travelled distance of the particle is obtained from the combined GENFIT track fit. A clear improvement is observed not only in the resolution, but also in the compatibility of the data with the physical expectation. In addition, reconstruction artefacts visible in the original data are largely removed by the improved treatment.

As opposed to the situation found earlier regarding CDC $\mathrm{d}E/\mathrm{d}x$ performance (cf. Fig. 5.5), the velocity extraction from RPC tracks represents a case where the performance of the TPC-combined feature extraction is clearly superior to the standard FOPI method. Two effects contribute to this improvement: i) the RPC covers the forward region of the phase space. Here, the good z resolution of the TPC and the incorporation of the additional RPC hit in the track fit outweigh the systematic problems in the x-y plane (cf. Sec. 5.1) in the determination of the particle momentum; This will be explicitly shown in a quantitative analysis in Sec. 6.3. Furthermore, ii) the travelled distance has to be estimated from the circle fit and a target vertex assumption during the standard FOPI reconstruction, but is obtained directly and with a higher precision from GENFIT track fits. As described in Sec. 4.5.2, the latter take into account the complete, re-calibrated set of spatial information, the description of the detector material and the magnetic field map.

Both these arguments can be expected to lose significance when considering tracks reaching the FOPI BAR array. Figure 5.10 shows extrapolations of BAR tracks into the target plane, analogue to Fig. 5.8. Also here, a considerable

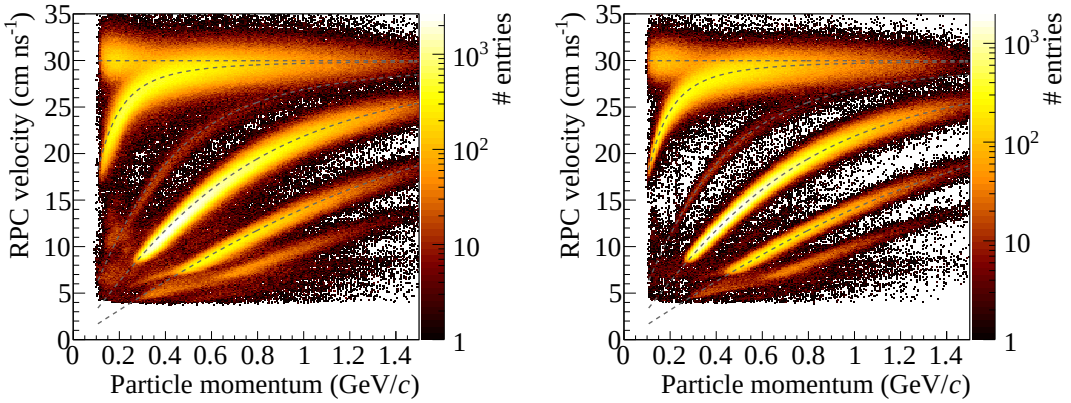

(a) Original FOPI RPC velocity vs. CDC momentum spectrum.

(b) Recalculation performed with the GEM-TPC present.

Figure 5.9: Distribution of the particle velocity v obtained from the RPC TOF measurement as a function of the momentum $|\mathbf{p}|$. Compared are the cases of (a) the standard FOPI reconstruction without any modifications ("Momentum" of the `CdcTrack` and "Velocity" of the `RpcTrack`, see Tab. 4.1) and (b) the TPC-combined feature extraction. For (b), the geometric cut indicated in Fig. 5.8b has been used for background suppression, reducing the statistics by $\sim 35\,\%$. In both plots the relation $v = |\mathbf{p}|/\gamma m$ is indicated as dashed lines for the individual particle masses.

improvement of the recovered image of the beam spot can be observed, which can be attributed to the improved determination of the track position along the beam axis. This does, however, not translate into an improved momentum resolution: Fig. 5.11 shows no qualitative improvement of the resulting TOF data for the TPC-combined analysis. On the contrary, while the overall resolution of the reconstruction seems to be comparable for both methods, a systematic shift away from the physical expectation is observed in the case of the TPC-combined extraction.

The additional hit in the BAR detector, that is taken into account in the combined analysis, has an uncertainty equal or larger compared to the CDC hits (cf. Sec. 3.2.2 and Tab. 4.3), and is thus of little help in the compensation of the systematic effects present in the TPC-CDC system. Most importantly, for tracks within the acceptance of the BAR detector, the transverse component of the momentum can be expected to be the dominant one. The situation is thus similar to the one found in the CDC $\mathrm{d}E/\mathrm{d}x$ data in the low-momentum region, where the systematic effects of the CDC in the azimuthal plane dominated the picture.

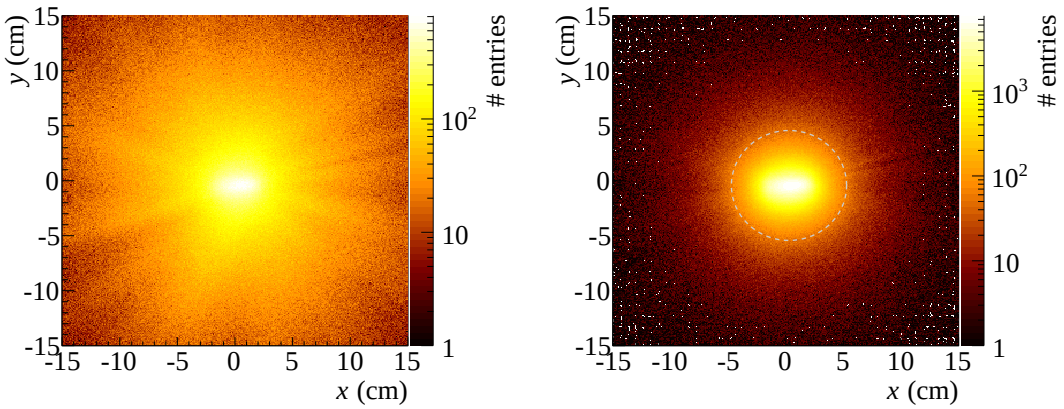

Figure 5.10: Back-extrapolation of GENFIT track fits into the target plane ($z = 0$). Compared are (a) tracks only defined in the CDC-BAR system and (b) tracks also including hit information from the GEM-TPC. The dashed outline in (b) corresponds to a cut used for background rejection, as already discussed in the context on Fig. 5.8b.

5.4 Summary & Conclusions

Before continuing with quantitative studies of the performance of the GEM-TPC in the FOPI setup in the following chapter, the findings of the previous sections shall be summarised: For the CDC, a heuristic model has been presented in Sec. 5.1 that can provide an explanation of the origin of the observed systematic shifts w.r.t. the tracking information supplied by the GEM-TPC. In addition, problems with the calibration of the timing characteristics of the CDC readout have been observed. In the discussion of the FOPI RPC in Sec. 5.2, artificial shifts of the RPC modules introduced in the FOPI feature extraction scheme have been identified as being incompatible with a TPC-combined analysis.

The following modifications are made to the feature-extracted data as provided by the FOPI reconstruction software, before being passed to the combined feature extraction algorithms presented in Chapter 4:

- Based on a heuristic model of track distortions, a shift of the CDC wire planes by 1.8 mm is enforced.
- The time offset of the CDC readout (cf. Sec. 3.2.1) is manually re-calibrated, based on residual information w.r.t. TPC tracks.
- The positions of the RPC modules, that are artificially shifted in the FOPI feature extraction, are forced to their nominal value.
- Based on reference tracks defined in this globally correct TPC-RPC system, hits measured by the CDC are re-calibrated along the beam direction on single-wire level.

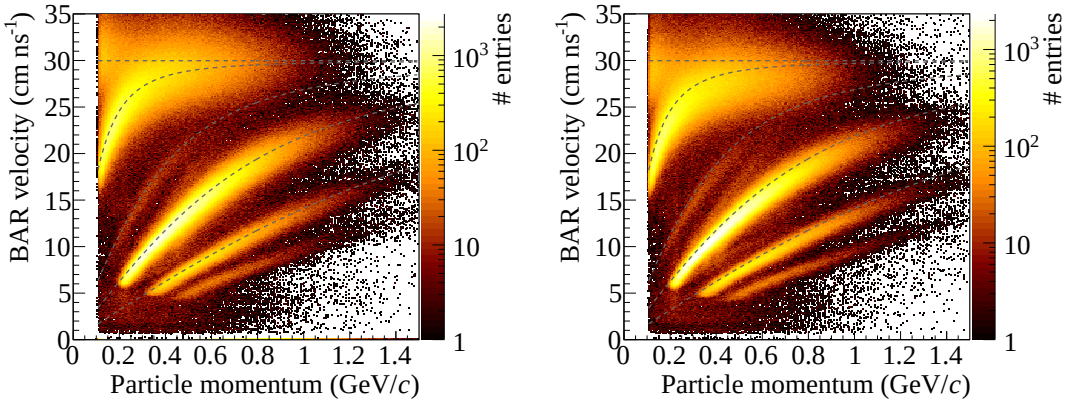

(a) Original FOPI BAR velocity vs. CDC momentum spectrum.

(b) Recalculation performed with the GEM-TPC present.

Figure 5.11: Distribution of the particle velocity v obtained from the BAR TOF measurement as a function of the momentum $|\mathbf{p}|$. Compared are the cases of (a) the standard FOPI reconstruction without any modifications and (b) the TPC-combined feature extraction. In both plots the relation $v = |\mathbf{p}|/\gamma m$ is indicated as dashed lines for the individual particle masses.

After implementing these corrections, the discussion of the TOF performance of the TPC-augmented FOPI spectrometer has revealed that we have to distinguish between *two distinct classes of tracks* for the further analysis: tracks with and tracks without a hit in the RPC. For the latter, the heuristic corrections performed on CDC data are not yet sufficient to fully compensate the influence of the observed systematic effects. It has been shown that the momentum resolution in the TPC-CDC system (low momentum region in Fig. 5.5) is actually deteriorated by the addition of TPC data. This situation is not significantly improved for tracks reaching the BAR detector.

For tracks that do leave a hit in the RPC system, the situation is reversed: The combination of a growing importance of the longitudinal component of the particle momentum in combination with the excellent resolution of the TPC along that direction outweighs the problems in the azimuthal plane. As an additional check of consistency, the data of Fig. 5.5 are shown again in Fig. 5.12, this time limited to tracks reaching the RPC (which are also included in Fig. 5.5). An improvement in the case of the TPC-combined analysis can be observed, growing with the magnitude of the particle momentum. This is consistent with the previous arguments. Again, the reader is referred to Sec. 6.3, where a quantitative analysis of the momentum resolution in the TPC-CDC-RPC system will be provided.

The main implication of these observations concerns the identification of particles, which will be discussed in Chapter 7. Especially for low-momentum tracks that only enter the TPC and CDC detectors, the separation power is

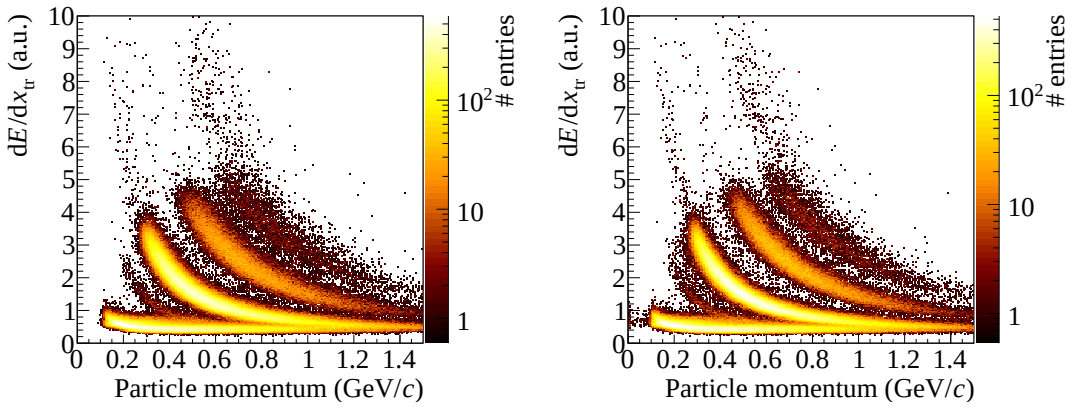

(a) Native CDC circle fits.

(b) TPC-combined fits.

Figure 5.12: CDC $\mathrm{d}E/\mathrm{d}x$ as a function of the particle momentum. From the data set shown in Fig. 5.5, only tracks entering the RPC are selected.

actually *lowered* by the incorporation of TPC data. This is a rather unfortunate situation, as precisely in this domain the GEM-TPC could potentially help to identify charged particles. In anticipation of the discussion of Chapters 7 and 8, this limitation translates into the requirement of having two separate PID strategies for the momentum region above and below $200\,\mathrm{MeV}/c$.

A more precise, *quantitative* correction of all the systematic effects discussed in this chapter could possibly be achieved in the framework of alignment (cf. Sec. 4.7), if properly integrated into one consistent mathematical model. This is currently being attempted [55], but, unfortunately, could not be completed in time for the analysis presented in this work.

5.4.1 Data stability over time

For the sake of completeness, it should also be noted in the context of this chapter that during the evaluation of the TPC-combined analysis rather large variations over time could be observed in the specific energy loss measured by the CDC. As this is however not directly related to the incorporation of GEM-TPC data, these findings will be discussed in the context of the PID strategy in Sec. 7.3.2.

Chapter 6

Performance of the GEM-TPC in FOPI

The purpose of this chapter is to provide an overview over the key performance characteristics of the FOPI GEM-TPC. With the data taken during the 2011 physics campaign at the FOPI spectrometer at GSI, many of the most important performance aspects can be studied: high-momentum cosmic tracks from the commissioning phase provide a straight-forward tool to benchmark the raw spatial hit-to-track resolution of the detector and to map out static drift distortions caused by imperfections of the field cage (Sec. 6.1). Based on the π-beam data, track-to-track resolution can be studied in particle-decay events (Sec. 6.2). After performing combined track fits including the tracking data from the surrounding FOPI detectors, the contribution of the GEM-TPC to the momentum reconstruction of the full setup can be quantified (Sec. 6.3). Data from dedicated calibration runs with radioactive Krypton gas allow the evaluation of the energy resolution of the GEM-TPC and of pad-wise gain variations (and their correction) across the amplification plane (both will be presented in Sec. 6.4). Finally, following the preparatory discussion of Sec. 2.2, the capabilities of measuring the specific energy loss of traversing charged particles can be put to the test and benchmarked against predictions (Sec. 6.5).

Of the results to be presented in this chapter, one has not been obtained directly by the author: The thorough analysis of the Krypton data for the correction of gain fluctuations in the GEM stack (Sec. 6.4) has been carried out by Roman Schmitz (HISKP, Universität Bonn, publication in preparation). In order to provide a consistent and complete picture of the performance of the FOPI GEM-TPC, his results will also shortly be discussed in this chapter and marked accordingly in the manuscript.

6.1 Spatial (hit-to-track) resolution and drift field inhomogeneities

In this section, the basic considerations of quantifying the spatial resolution of a TPC on the level of single "hits" are explored. The principles behind the deposition of charge and the following extraction of spatial tracking information from the active volume of a TPC have already been detailed in Sec. 2.1. Diffusion during electron drift was identified as a fundamental limitation in terms of the achievable spatial resolution. Even under idealised conditions, diffusion prevents the measurement of the individual charge clouds that are created during primary and secondary ionisation processes.

Additional limits are introduced by the technical realisation of the detector (cf. Sec. 2.1.2): The structure size S of the readout scheme – given by the pad size in the detection plane and the timing resolution of the electronics – presents the lower limit to the accuracy with which a point-like charge cloud can be measured, even in the absence of diffusion; Distortions of the drift field translate into systematic, spatial offsets of the measured signals; Finally, noise introduced by the readout electronics leads to (randomly distributed) fake hits, further degrading the performance.

In order to study the spatial uncertainty of single detector hits, a reference is required. Preferably, this would be supplied by high-precision external tracking detectors. In the FOPI setup, no such data are available – the GEM-TPC itself offers the best spatial resolution, as will be shown in the further discussion of this chapter. In this scenario, the best available reference is in principle given by *combined* track fits of TPC, CDC and BAR or RPC. The qualitative discussion of Chapter 5 has shown, however, that remaining systematic problems of the CDC are still larger than the theoretical spatial resolution of the TPC and the CDC. In this situation, it appears of little worth to quantify the single-hit spatial resolution of the TPC using such reference tracks. Alternatively, one can restrict the reference to the reconstructed track in the TPC alone. In order to extract hit-to-track residuals in an unbiased way, the hit in question then has to be excluded from the track fit. In general, the residual $\mathbf{r}$ of a hit at position $\mathbf{x}$ with respect to a track is given as

$$\mathbf{r} = \mathbf{c} - \mathbf{x} \tag{6.1}$$

with $\mathbf{c}$ being the POCA of the hit and the track.

However, the definition of a "hit" in the GEM-TPC is already not straight forward: At this point, the technicalities on the software side (feature extraction) introduce a certain level of arbitrariness into the discussion. As detailed in Chapter 4, the recovered and digitised signals on single-pad level (*pad hits*, cf. Sec. 4.2) are further combined to *clusters* before the information is passed on to the tracking algorithms. As shown in Sec. 4.3, the clustering procedure is a quite dynamical process. In the case of no clustering, the lower limit of the

single-hit resolution is reached. Increasing cluster sizes will naturally reduce the effective number of hits and their spatial fluctuations around the track trajectory, however at the price of decreasing the sensitivity to localised or non-linear track features (e.g. curvature, vertices, kinks).

Such studies of the single-hit resolution have already been performed outside the context of this work, and are not repeated here. Figures 1.93 and 1.94 of Ref. [37] show the single-hit resolution obtained from cosmic tracks during the commissioning phase at the FOPI setup [1]. A spatial resolution of $\mathcal{O}(300\,\mu\text{m})$ is observed along all spatial directions, which furthermore shows a dependence on the drift length compatible with the expectations from diffusion. It shall be pointed out again that these numbers already include the results of the clustering algorithm, and are as such to some extent arbitrary. From the same data, distortions introduced by imperfections of the field cage have been mapped out [75]. In this work, a qualitative agreement between the observed drift distortions and simulation results could be shown. The simulation was based on a detailed description of the field cage electrostatics and calculations performed with the algorithm described in Ref. [15]. However, the author did not arrive at a quantitative model that would allow a correction of such distortions on the level of feature extraction, and the observed distortions thus enter the analysis of this thesis uncorrected. Their effect is however to some extend mitigated by the rejection of outlying hits provided by the DAF (cf. Sec. 4.5.3).

The gist of the previous arguments is that for the extraction of physical particle properties, the definition of the entire *track* is the determining factor. The parameters of the clustering algorithms thus have to be optimised in terms of the final *tracking* resolution. Here, concepts like computational performance and noise reduction are in competition with the preservation of local spatial information on the level of the clustering algorithm. A quantitative evaluation of the tracking performance of the GEM-TPC will be provided in the next section. Single-hit studies, on the other hand, are an important tool for the study of *local* detector effects, as discussed above.

6.2 Vertex (track-to-track) resolution

Another way of obtaining a reference point in space for resolution studies is by reconstructing particle-decay events inside the active volume of the TPC. In the simplest case, such a reference can be obtained from the decay of a neutral particle into two oppositely charged tracks. Under the assumption that systematic effects of the detector cancel out over the phase space of the decay, the recovered vertex positions will on average agree with the true origin of the track pairs.

[1] These measurements have been performed at a drift field strength of $|\mathbf{E}_\text{d}| = 360\,\text{V}\,\text{cm}^{-1}$.

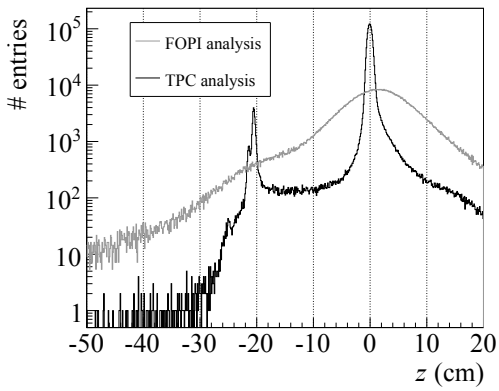

Figure 6.1: Raw distribution of the POCA of $\pi^+\pi^-$ pairs reconstructed from the carbon target runs along the beam axis, for the native FOPI reconstruction (Gray) and including the GEM-TPC hit information (Black). The target disc (thickness: 1.0 cm) is located at $z = 0$.

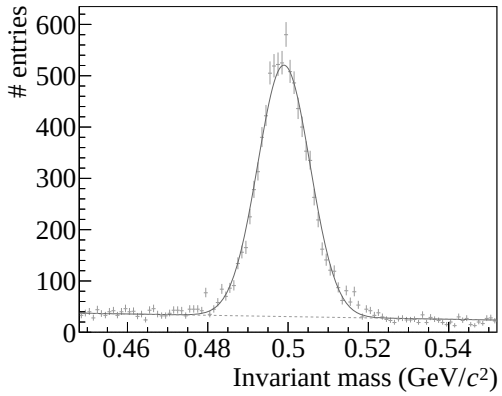

Figure 6.2: Invariant mass spectrum of selected K^0_s candidates. The spectrum shape is captured using a likelihood fit with a composite model consisting of a Gaussian and a first-order polynomial. The contribution of the linear background in a $\pm 3\sigma$ mass window around the peak position is 6.6 %.

In the analysis of the FOPI GEM-TPC data, vertices are reconstructed based on pairs of tracks consisting of combined FOPI hit data using the GFRave interface (cf. Sec. 4.5.4). The result of such a constrained fit under the assumption of a common point of origin consists of a vertex position $\mathbf{v}$ and the modified momenta $\mathbf{p}_{1,2}$ of the participating tracks. Spatial residuals $\mathbf{r}_{1,2}$ can be defined after computing the points of closest approach $\mathbf{c}_{1,2}$ of the two *original, unmodified tracks* with respect to $\mathbf{v}$ as

$$\mathbf{r}_{1,2} = \mathbf{c}_{1,2} - \mathbf{v} \quad . \tag{6.2}$$

In this way the spatial tracking resolution can be studied on *track-to-track* level.

The signature used in the following is the decay of the short-lived weak eigenstate of the neutral kaon into two charged pions:

$$K^0_s \rightarrow \pi^+\pi^- \quad . \tag{6.3}$$

We start out with a qualitative assessment: taking the set of *all* possible $\pi^+\pi^-$ pairs – without attempting to limit the selection to the actual K^0_s decays – the obtained vertex positions of the pion pairs are expected to be distributed mostly according to the geometrical overlap of the beam and the target material [2]. While there is no physics to be learned from this integral spectrum of

[2]This is only true for primarily produced π. Most of the actual K^0_s from K^0 production

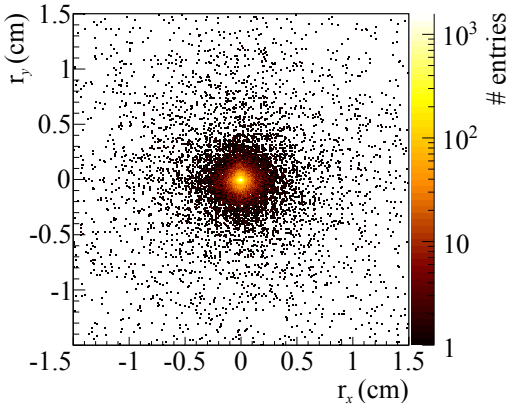

Figure 6.3: Vertexing residuals (azimuthal pane) from GENFIT/GFRave fits of tracks leaving a hit in each of the TPC, CDC and RPC detectors.

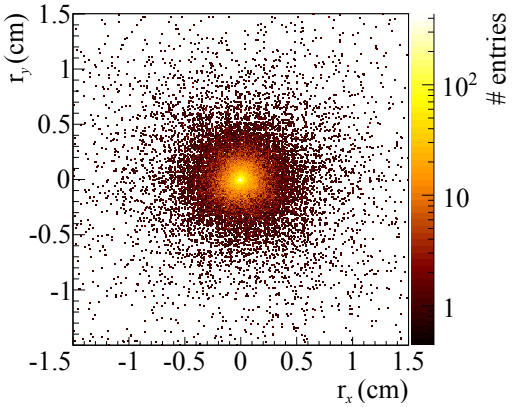

Figure 6.4: Vertexing residuals (azimuthal plane) from CDC tracks (standard FOPI reconstruction, circular track fits plus polar angle) when compared to the vertex information imported from the TPC-combined analysis.

$\pi^+\pi^-$ vertices, one can immediately get an impression of the improvement of the vertexing-performance when adding the GEM-TPC tracking information to the analysis. Figure 6.1 shows the reconstructed vertex positions along the beam axis both with and without using GEM-TPC information. The tracking performance along the beam axis is improved drastically by the presence of the GEM-TPC. The target disc at $z = 0$ is clearly resolved, as well as additional structures at the end of the beam line at $z \approx -21\,\mathrm{cm}$ and $z \approx -22\,\mathrm{cm}$. These are believed to correspond to an inefficient veto detector and the beam pipe window (cf. Sec. 3.2.4).

In the next step, in order to get more quantitative, the selection of the $\pi^+\pi^-$ pairs is now restricted to genuine K^0_s decays. This is achieved by selecting only vertices that were reconstructed *outside* of the target material. Details of this identification follow in the context of the dedicated analysis of this channel, presented in Sec. 8.5. In the K^0_s case the definitions leading to Eq. (6.2) are adapted by changing the labels for the two charged pions: $(1, 2) \rightarrow (+, -)$. From the two momenta $\mathbf{p}_{+,-}$ and using the pion mass $m_{\pi^\pm} = 139.570\,\mathrm{MeV}/c^2$, the four-momentum of the parent particle $p_{\pi^+\pi^-} = (E_+ + E_-, \mathbf{p}_+ + \mathbf{p}_-)$ can be constructed. The corresponding distribution of the invariant mass is shown in Fig. 6.2. The surviving background is due to fake K^0_s candidates.

The invariant $\pi^+\pi^-$ mass is now utilised further to put an additional constraint on the set of vertices that are to be taken into account for the resolu-

at the S339 beam energy decay within a few cm and will be hidden in this distribution to a large extent. For details see Sec. 8.5.

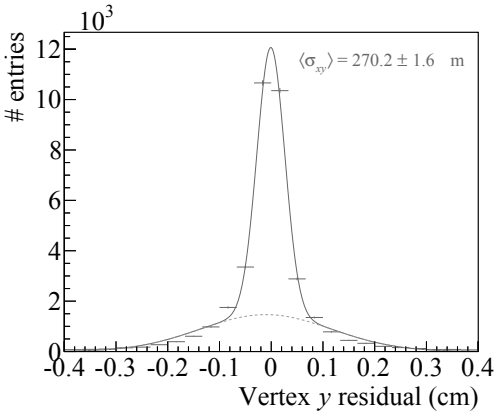

Figure 6.5: y-projection of the bivariate Gaussian likelihood fit performed in the x-y plane. The given mean resolution corresponds to the mean value of the semi-axes of the central Gaussian covariance ellipsoid.

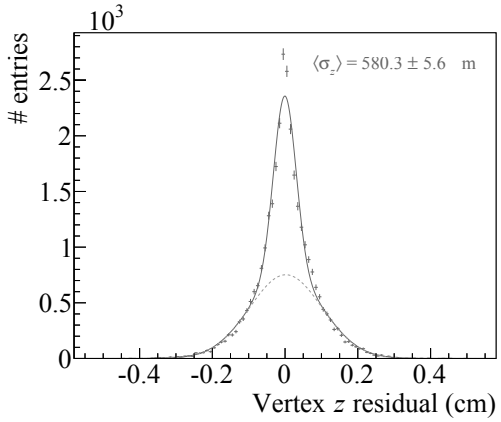

Figure 6.6: Vertex residual profile along the beam axis (z) with the result of the likelihood fit. The value for the resolution is calculated as the weighted mean of the two Gaussian components of the fit function.

tion extraction: Only reconstructed vertices that fall into a $\pm 3\sigma$ mass window around the peak position are considered. Figure 6.3 shows the obtained distribution of both residuals $\mathbf{r}_{+,-}$ of the surviving 40,700 K^0_s candidates in the projection onto the azimuthal plane.

For comparison, the procedure is repeated using only FOPI tracking information (circle fits, cf. Sec. 4.1.1) for the residual calculation according to

$$\mathbf{r}^\mathrm{F}_{+,-} = \mathbf{c}^\mathrm{F}_{+,-} - \mathbf{v} \quad , \tag{6.4}$$

where $\mathbf{v}$ is the *same* as in Eq. (6.2) – acquired using GENFIT tracks including GEM-TPC hits – and taken as the *true* vertex position. The projection of all $\mathbf{r}^\mathrm{F}$ in the x-y plane is plotted in Fig. 6.4. Again, the improvement when taking into account GEM-TPC hit information is clearly visible, but less dramatic as observed along the beam direction. It should be noted, however, that this comparison is somewhat theoretical, since such a clean selection of K^0_s candidates for FOPI CDC tracks was only possible using the GEM-TPC hit data in Eq. (6.4). Once again, the reader is referred to Sec. 8.5 for details of the K^0_s identification.

The distribution shown in Fig. 6.3 can be well described using a bivariate Gaussian model. A one-dimensional projection of the data and this fit is shown in Fig. 6.5. One observes a well-defined central peak sitting on a small background which is sufficiently well modelled using another Gaussian component. The integral fraction of the Gaussian background contribution amounts to 6.1%, which is in fairly good agreement with the integral background fraction (6.6 %) in the $\pm 3\sigma$ mass window used earlier for the K^0_s candidate selection

(Fig. 6.2). It thus seems reasonable to ignore the background contribution in the extraction of the vertexing resolution in the x-y plane. From the fit, an average central width of $\langle\sigma_{xy}\rangle = 270.2 \pm 1.6\,\mu\text{m}$ is obtained. Systematic uncertainties due to the imperfect description of the data by the fit are expected to exceed the statistical uncertainty, but are not investigated further.

Finally, the z-component of the residual distribution remains to be studied. It exhibits a non-Gaussian shape and is shown in Fig. 6.6. A likely source of this more washed-out structure is a wrong drift velocity used during data reconstruction. Once the drift velocity will be directly obtained from the alignment procedure (cf. Sec. 4.7), it would be worthwhile to re-visit this study. In order to extract a number for the resolution, the distribution is yet again modelled with a composite two-Gaussian density. However, the previous argument of well-separated "signal" and "background" contributions cannot be applied in this case. An upper limit estimate for the z-vertexing resolution of the detector setup can be given as the weighted mean of the Gaussian widths from the fit: $\langle\sigma_z\rangle = 580.3 \pm 5.6\,\mu\text{m}$. As before, only statistical uncertainties of the fit parameters are considered.

Owing to the short range of the studied K^0_s, the above results are to be understood as a measurement at $z \approx 0$ which corresponds to a drift length in the GEM-TPC of $\approx 45\,\text{cm}$ (cf. Fig. 3.6). In summary, it has been demonstrated that the GEM-TPC dominates the spatial tracking resolution of the S339 setup.

6.3 Momentum resolution

Neglecting the impact of multiple scattering, the curvature uncertainty δk due to the finite statistical sample and the single-measurement resolution can generally be estimated (see Ref. [28]) using

$$\delta k = \frac{\delta x}{L^2} \cdot \sqrt{\frac{720}{N_\text{h} + 4}} \quad , \tag{6.5}$$

where

δx	absolute spatial uncertainty of the detector hits perpendicular to the trajectory,
L	length of the track in the bending plane projection,
N_h	number of hits participating in the track fit.

Compared to the main FOPI tracking detector, the GEM-TPC is a small device. For the FOPI magnetic field and for tracks lying in the x-y plane, $|\mathbf{p}| = 500\,\text{MeV}/c$, $L = 10\,\text{cm}$, $N_\text{h} = 20$ and $\delta x = 300\,\mu\text{m}$ (motivated by the previous sections), Eq. (6.5) translates into a relative resolution for the reconstructed momentum of $\delta|\mathbf{p}|/|\mathbf{p}| \sim 45\,\%$, if only the GEM-TPC track

data were to be considered. It is thus clearly not of great value to study the momentum resolution of the TPC alone. However, considering the vastly improved tracking resolution along the beam direction in the TPC-combined setup (cf. Fig. 6.1), it is certainly interesting to investigate the impact of the TPC on the final momentum resolution of the entire spectrometer.

For this determination, a reference measurement of the particle momentum is required. The most accurate measurement available in the FOPI setup is the particle travel time measured by the RPC (cf. Sec. 3.2.2). From the corresponding particle velocity v and using

$$|\mathbf{p}| = \gamma m v \tag{6.6}$$

the reference value $|\mathbf{p}|_{\mathrm{ref}}$ is directly obtained. In the following, the momentum reconstruction performance is compared between i) standalone FOPI feature extraction and ii) a re-analysis using also the matched TPC information and the extraction tools and algorithms described in Chapter 4.

Apart from the requirement of a matched hit in the RPC, for this study the track selection is constrained to protons only, since these can be identified rather easily over a wide momentum range (see the discussion in Chapter 7). The particle velocity is calculated using the TOF value and the full, combined track fit based on the spatial hit information from TPC, CDC and RPC (cf. Sec. 5.3). For the computation of the reference value given by Eq. (6.6), a proton mass of $m_{\mathrm{p}} = 938.272\,\mathrm{MeV}/c^2$ is used.

In order to study the performance as a function of the momentum, the reconstructed momenta are organised into bins of the reference momentum, each of which is $25\,\mathrm{MeV}/c$ wide. The study is limited by the RPC phase-space acceptance to the range $350 < |\mathbf{p}|_{\mathrm{ref}} < 800\,\mathrm{MeV}/c$. Figure 6.7 shows the distribution of the differences of the recovered momenta with respect to $|\mathbf{p}|_{\mathrm{ref}}$ from both reconstruction scenarios in the example of one such bin. The properties of the spectra are captured using likelihood fits with a two-component Gaussian model. The second Gaussian component of the fit function improves the modelling of the tails of the spectra, but the central component is dominant with a contribution to the fit of well above 90 % over the full momentum range (Fig. 6.8). All values extracted from the fits in the following correspond to the weighted mean from both contributions.

The results of this study are shown as a function of the particle momentum in Figs. 6.9 and 6.10. In Fig. 6.9, a systematic shift of the mean of the reconstructed momenta with respect to $|\mathbf{p}|_{\mathrm{ref}}$ of $\sim 20\,\mathrm{MeV}/c$ in the case of the standalone FOPI reconstruction is observed. In contrast, the momentum recovered from the TPC-combined analysis is in good agreement with the reference value.

Figure 6.10 compares the relative resolution that is obtained from the widths of the distributions for both reconstruction scenarios. Both data sets follow the same general trend and show only a weak dependence on the particle

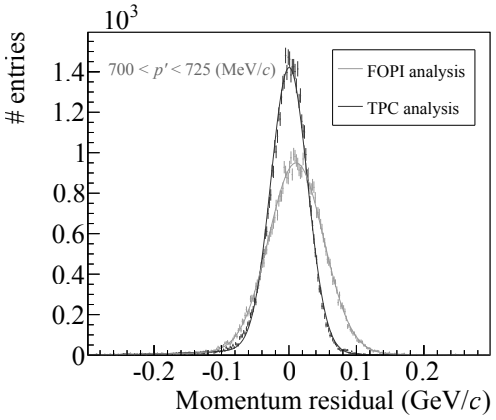

Figure 6.7: Residual distribution of the reconstructed momentum $|\mathbf{p}|'$ relative to the reference momentum from the FOPI RPC time-of-flight measurement, $|\mathbf{p}|' - |\mathbf{p}|_{\mathrm{ref}}$. The distributions are fitted using the sum of two Gaussians $f_{\mathrm{c}} \cdot G_{\mathrm{a}}(\mu_{\mathrm{a}},\sigma_{\mathrm{a}}) + (f_{\mathrm{c}} - 1) \cdot G_{\mathrm{b}}(\mu_{\mathrm{b}},\sigma_{\mathrm{b}})$.

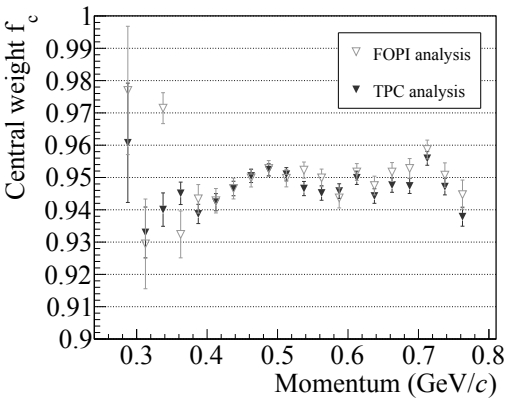

Figure 6.8: Relative weight of the central component f_{c} of the fit function as function of the particle momentum. The value corresponds to the fraction of the norm of the fit function.

momentum. Again, the values obtained with from the TPC-combined data are drastically improved (29 % - 34 %) in comparison to the native FOPI analysis, and are found to be well below 5 % over the studied momentum range.

The reason for the improved resolution can be traced back to the systematic effects in the combined CDC-RPC system, which have been discussed in Sec. 5.2: When forcing the RPC module positions to the default value and applying the corrections for CDC hits (cf. Fig. 5.7), combined fits in the TPC-CDC-RPC system greatly benefit from the globally correct and consistent set of information. The source of the wrong absolute value of the momentum extracted from the standard FOPI reconstruction, however, could ultimately not be determined: Also the artificially shifted RPC modules had been distributed around the correct mean position, and the RPC positions thus cannot explain a global offset. Other known shortcomings of the momentum extraction as performed in the native FOPI reconstruction are i) the missing treatment of energy loss (circle fits), ii) the assumption of a constant magnetic field and iii) the systematic shifts CDC tracks in the azimuthal plane (cf. Sec 5.1). The first should result in too *small* values of the momentum, and the neglected energy loss is also of a different magnitude. It thus cannot provide a valid explanation. The effects of the latter items would have to be studied in dedicated simulations. Such an evaluation is, however, not part of this work.

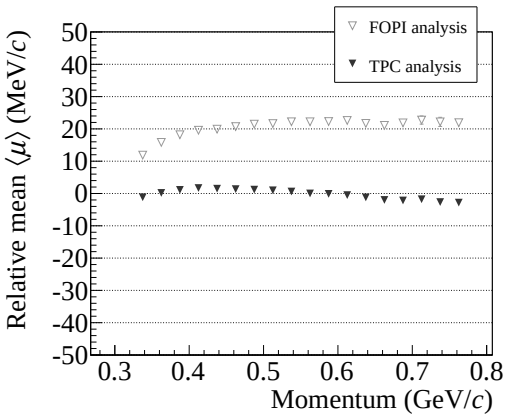

Figure 6.9: Mean values of the momentum residual spectra. Shown are the weighted means $\mu = f_c \cdot \mu_a + (1 - f_c) \cdot \mu_b$. Error bars reflecting the statistical uncertainty of the fit results are drawn, but smaller than the data points.

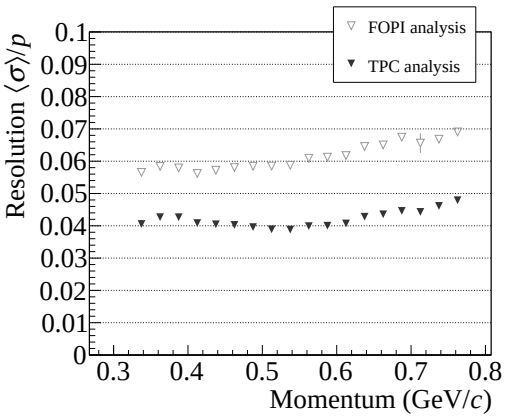

Figure 6.10: Relative resolutions σ/p as a function of the particle momentum, where $\sigma = f_c \cdot \sigma_a + (1 - f_c) \cdot \sigma_b$. Error bars reflecting the statistical uncertainty of the fit results are drawn, but smaller than the data points.

6.4 Gain calibration & energy resolution

A widely used method for the energy calibration of gaseous detectors is the introduction of the meta-stable, isomeric state $^{83m}_{36}$Kr of Krypton into the active volume of the detector. The method is attractive mainly because it does not require any physical invasion of the detector and allows full coverage of its active volume. The reconstruction of the well-known decay spectrum of $^{83m}_{36}$Kr allows the calibration of the absolute effective gain as well as a study of gain variations over the amplification stage. As discussed in Sec. 2.1.4, such variations are of particular interest for gas-amplification systems realised with a stack of GEM foils.

For this purpose a $^{83}_{37}$Rb source (2.5 MBq activity, produced at HISKP, Bonn) was installed during the 2011 setup at FOPI into the gas system of the GEM-TPC in a separated, parallel pathway [37]. $^{83}_{37}$Rb decays (via electron capture, lifetime $\tau = 124\,\mathrm{d}$) predominantly into the desired meta-stable state of Kr, which features an excitation energy of 41.6 keV. Switching the gas supply to the pathway containing the Rb source feeds the produced $^{83m}_{36}$Kr into the active detector volume for calibration purposes.

The meta-stable state further decays (energy of the transition $E_{tr} = 32.2\,\mathrm{keV}$, lifetime $\tau = 2.64\,\mathrm{h}$) into a short-lived state at 9.4 keV, which finally undergoes another transition into the ground state ($\tau = 212\,\mathrm{ns}$). A simplified sketch of the decay scheme is given in Fig. 6.11 [3]. The crucial property of these last two

[3] Here, only the decay channels relevant for the calibration are considered.

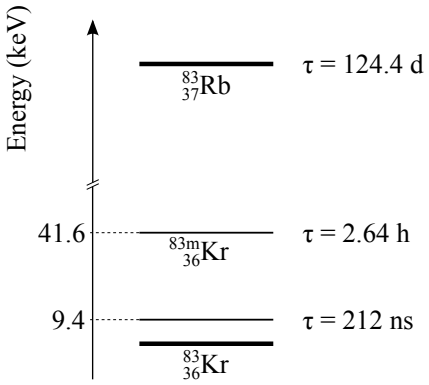

Figure 6.11: Simplified energy level scheme of the transition $^{83}_{37}\mathrm{Rb} \rightarrow {}^{83}_{36}\mathrm{Kr}$. The level at 41.6 keV above the ground state corresponds to the long-lived isomeric state introduced into the detector.

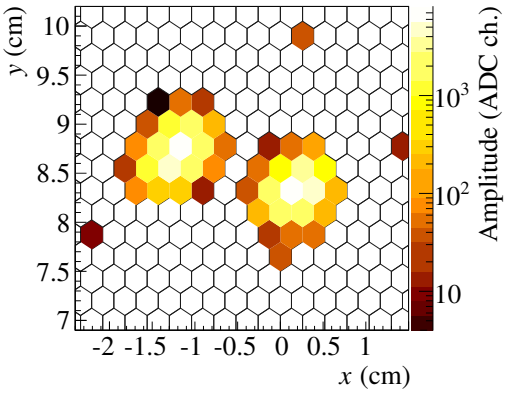

Figure 6.12: Signals from two close-by $^{83m}_{36}\mathrm{Kr}$ decays as recorded on the GEM-TPC pad plane. Pads with an amplitude below threshold are shown only by their outlines.

processes for the purpose of calibration is that both occur predominantly via internal conversion (IC), producing a short-ranged electron carrying the net energy E_e. Transitions via gamma emission only occur rarely in comparison (0.5 ‰ and 5 % of the cases, respectively, cf. Ref. [76]).

The net energy carried away by the conversion electron is given by the transition energy minus the binding energy of the electron prior to emission:

$$E_\mathrm{e} = E_\mathrm{tr} - E_\mathrm{b} \quad . \tag{6.7}$$

The following de-excitation of the electron shell can occur either through emission of an X-ray γ or (an) Auger electron(s), the latter being the dominant mechanism. For the 9.4 keV transition, only the weakly bound outer shell (L, M, N) electrons are viable carriers ($E_\mathrm{b} < 1.92\,\mathrm{keV}$, cf. Ref. [77]). Outer electrons are also predominantly involved in the 32.2 keV IC transition, but the higher transition energy additionally allows inner-shell electrons with $E_\mathrm{b} > 10\,\mathrm{keV}$ to participate.

The emitted conversion electrons are stopped quickly in the gas, transferring the energy E_e in ionisation processes. If the following shell de-excitation occurs through Auger emission, the full transition energy E_tr is thus stored in the detector gas. The short mean range of the involved e^- leads to spatially confined clouds of ionisation charge that can be reconstructed easily. Figure 6.12 shows an example of typical signal patterns from such decays, recorded with a random trigger.

Neglecting threshold effects, the measured total amplitude A_Kr (ADC chan-

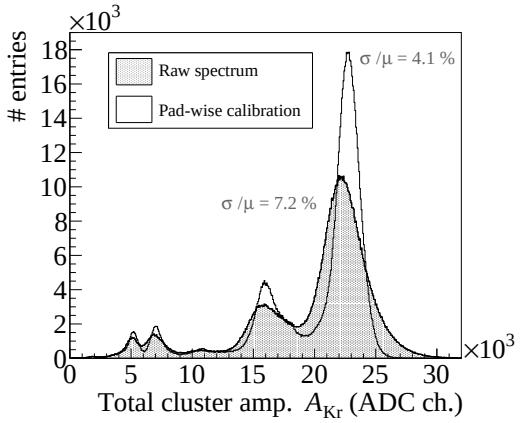

Figure 6.13: Spectrum of the reconstructed, total Kr cluster amplitude w/ and w/o pad-wise gain calibration, taken at 83 % nominal GEM voltage. The shown data was supplied by Roman Schmitz, HISKP, Universität Bonn. The pad-wise calibration is discussed in Sec. 6.4.1.

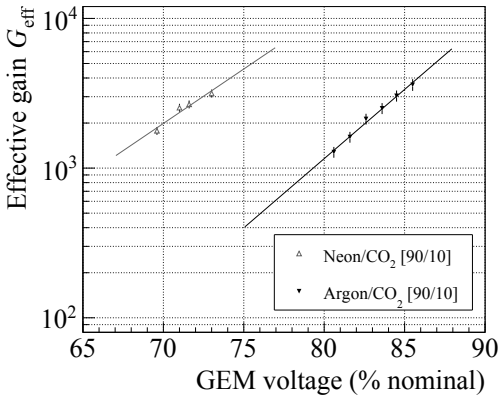

Figure 6.14: Effective gain G_{eff} of the FOPI GEM-TPC from the Kr data analysis as function of GEM voltage setting (nominal voltage: 400 V, cf. Sec. 3.1.2) for two different gas mixtures. The shown data was supplied by Roman Schmitz, HISKP, Universität Bonn.

nels) of such a localised Kr cluster Eq. (2.32) becomes

$$A_{\text{Kr}} = \frac{E_{\text{tr}}}{W} \cdot \frac{G_{\text{eff}}}{s} \quad , \tag{6.8}$$

with

W	mean ionisation energy of the gas mixture (eV/e^-, cf. Eq. (2.1)),
G_{eff}	effective gain,
s	single-channel sensitivity of the readout chain (e^-/ADC ch.).

With W and s known (cf. Tab. 3.1), reconstructing the full energy deposit of Kr-decay events allows i) the global calibration of the effective detector gain and ii) the study of pad-wise gain variations from a large statistical sample. The following results from the analysis ([78]) of the Kr calibration data have been provided by Roman Schmitz, HISKP, Universität Bonn.

The shaded distribution in Fig. 6.13 shows the raw spectrum of the total Kr-cluster amplitude according to Eq. (6.8). The structure can be understood as follows: the dominant peak at the largest cluster amplitudes corresponds to the full 41.6 keV excitation energy of the meta-stable Kr state. In this case both core transitions occurred via IC and the associated shell de-excitations via Auger emission, thus the full energy is dumped into the detector gas; The second-largest peak at $A_{\text{Kr}} \approx 17 \cdot 10^3$ ADC ch. actually has two contributions: i) the 9.4 keV-to-ground-state transition occurs via γ emission ($\approx 5\,\%$ of all

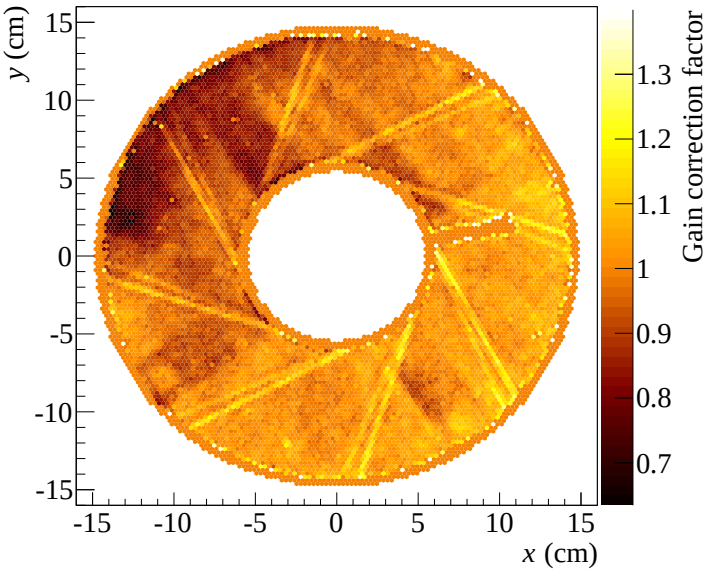

Figure 6.15: Visualisation of the pad-wise, relative gain correction factors. The RMS of the underlying distribution is 0.086. Pads with insufficient or no data (e.g. pads close to the field cage walls, broken channels) are set to the nominal setting 1. The shown data was provided by Roman Schmitz, HISKP, Universität Bonn.

cases) and only the IC / Auger e^- of the 32.2 keV transition are measured, and ii) the first IC involves a K-shell electron ($\approx 13\,\%$ of all cases) and $E_\mathrm{e} = 19.5\,\mathrm{keV}$ together with the IC / Auger electrons from the 9.4 keV transition are measured; The peak at $A_\mathrm{Kr} \approx 7 \cdot 10^3$ ADC ch. is linked to the former K-shell IC and corresponds to the conversion of the associated 12.7 keV X-ray elsewhere in the detector; The last visible structure is the 9.4 keV peak, originating from the conversion of an escaped 9.4 keV photon.

From the amplitude data, the global gain is fixed via Eq. (6.8). Figure 6.14 shows the gain as a function of the GEM voltage for the two gas mixtures used in the FOPI GEM-TPC. This can be compared to Fig. 1.75 of Ref. [37], which shows a gain measurement of the GEM stack in an external test setup. The extraction from the Kr data offers a more direct measurement, since the GEM stack is operated in the actual detector environment.

6.4.1 Application for pad-wise amplitude correction

The large amount of available $^{83m}_{36}$Kr data also allows the study of gain variations in between the individual readout channels. After carefully analysing the shifts of the recorded spectra for individual channels [78], each readout pad k can be assigned a gain correction factor g_k^c, so that the recorded, raw

amplitude a'_k of each *pad hit* (cf. Sec. 4.2.1) can be corrected:

$$a_k = g_k^{\mathrm{c}} \cdot a'_k \quad . \tag{6.9}$$

Figure 6.15 provides a visualisation of the obtained correction factors for all readout pads. The most striking features are the iris-shaped lines following the segmentation borders of the (last two) GEM foils (cf. Sec. 3.1.2), where the effective gain is lower ($g_k^c > 1$). In addition, a darker, cross-shaped pattern is visible, most likely caused by stress applied by the mounting structure of the GEM stack. In these regions of larger foil tension, an increase in effective gain is observed ($g_k^c < 1$).

The correction of the pad hit amplitudes a_k, according to Eq. (6.9) and the data shown in Fig. 6.15, is performed for all reconstruction results shown in this work. The effect of this correction can be seen most directly in the Kr decay spectrum of Fig. 6.13 (open distribution): pad-wise calibration enhances the energy resolution of the detector by more than 40 %.

6.5 Specific-energy-loss performance

In Sec. 2.2, the physical principles behind the energy loss which particles suffer through the ionisation of gas atoms were detailed. The *mean* rate of energy loss $\langle \mathrm{d}E \rangle$ per travelled distance $\mathrm{d}x$ is given by the Bethe equation Eq. (2.26) – already including the density effect in this formulation. For convenience it is repeated here:

$$-\left\langle \frac{\mathrm{d}E}{\mathrm{d}x} \right\rangle_{\mathrm{B}} = \frac{Z\rho N_{\mathrm{A}}}{A} \cdot \frac{4\pi}{m_{\mathrm{e}}} \cdot \left(\frac{z\alpha\hbar}{\beta} \right)^2 \left[\ln \frac{2m_{\mathrm{e}}c^2\beta^2\gamma^2}{I} - \beta^2 - \delta(\beta) \right] \quad . \tag{6.10}$$

Equation (2.13) links the above rate to macroscopic measurements of $\Delta E/\Delta x$ under the assumption that ΔE is negligible compared to the total kinetic energy of the particle. Due to the statistical nature of the underlying scattering processes, however, $\Delta E/\Delta x$ is expected to fluctuate around the mean value given by Eq. (6.10). This aspect has already been addressed in Sec. 2.2.2, and it was found that the distributions describing these fluctuations ("straggling functions") are largely asymmetric and long-tailed for measurement parameters typical for a TPC (cf. Fig. 2.6b).

The crucial property of Eq. (6.10) is that it depends only on the velocity β of the projectile. This means that for a given momentum of the projectile particle the mean energy loss separates for different particle species. If the resolution with which the energy loss of a detected particle can be reconstructed is sufficient, this fact can be used to identify the particle species.

Before discussing the contribution of the GEM-TPC to particle identification (PID) in the full FOPI setup in Chapter 7, this section is concerned with

the benchmarking of the "dE/dx" measurement [4] performance of the detector. As a final remark before proceeding, the reader is pointed to Ref. [25], where the results of this study have already been published by the author [5]. Since the initial publication, however, the feature extraction quality could be further improved. The most recent results are presented in the following.

6.5.1 Extraction method

The fundamental unit of information about the deposited energy due to ionisation "dE" is given – via Eq. (2.1) – by the corrected amplitude a_k (cf. Sec. 6.4.1) of a single *pad hit*. As discussed in Sec. 2.2.3, the proportionality of such an amplitude measurement to the actual energy deposit is threatened by detector effects (and further complicated by diffusion). The most important such effect is due to gain fluctuations in the GEM stack. It was shown in the previous section, how this can be corrected on single-pad level.

Information about the travelled path length ("dx"), on the other hand, has to be inferred on the level of final feature extraction (particle tracks). Here, it is common practice to fall back to structural features of the readout stage (e.g. "pad rows") for a (simplified) definition of Δx. This has the disadvantage of mixing contributions from different straggling shapes, which are a function of Δx. Due to the high degree of symmetry of the FOPI-TPC pad plane, we are not tempted to introduce such simplifications. Instead, the energy loss information is obtained directly from the full, *combined* track fit.

Using this information, the available amplitude data can be sampled along the actual particle path: All *pad hits* within a *fixed* step length Δx are collected by walking along the obtained track fit in three-dimensional space. For the i-th step, this is realised by constructing planes P_i and P_{i+1}, both perpendicular to the track and defined in such a way, that the path along the track between them has the length Δx. The set of all pad hits Ω_i, lying between P_i and P_{i+1}, are combined to one measurement $A_i/\Delta x$, where

$$A_i = \sum_{k \in \Omega_i} a_k \quad . \tag{6.11}$$

The procedure is visualised in Fig. 6.16.

Similar to Eq. (6.8), the amplitudes A_i can now be related to the actual energy loss ΔE_i in the corresponding gas volume [6]. Since absolute values are of no concern in the following discussion, the statement

$$A \propto \Delta E \tag{6.12}$$

[4] The rate dE/dx is never measured, but is connected to macroscopic measurements of $\Delta E/\Delta x$ via Eq. (2.13) in good approximation.

[5] The publication is also appended to this document, cf. Appendix B.

[6] In the direction perpendicular to the track, the effective volume is limited by the hit-to-track association performed during pattern recognition, cf. Sec. 4.4.

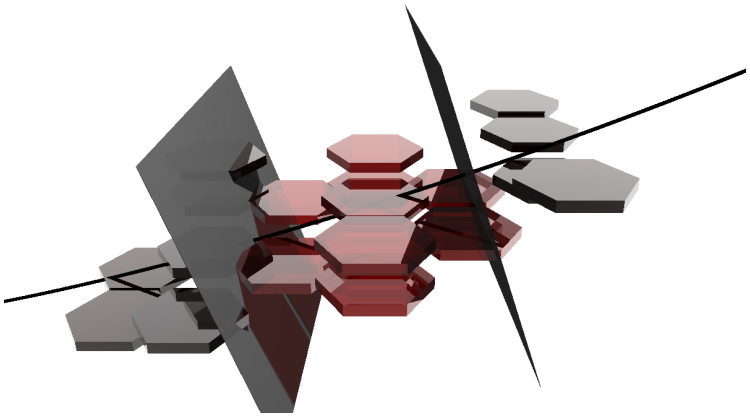

Figure 6.16: Sampling procedure for the amplitude/Δx extraction. Hexagonal slabs represent single measured pad hits, their displacement out of the measurement plane corresponds to the different hit times. All hits located in between two adjacent planes – perpendicular to the track fit and distributed with a fixed step length Δx along the particle trajectory – are combined into a single measurement. For this selection, only the centre of gravity of the hexagons is taken into account.

shall suffice to treat the extracted amplitudes as the actual energy loss ΔE. The extracted pairs of $A_i/\Delta x_i$ for each particle track can then be regarded as a measurement of the straggling spectrum $f(\Delta E; \Delta x, \beta)$.

For infinitely large sample sizes per track, the moments of the measured straggling functions would exhibit an uncertainty only due to the energy resolution of the detector. In reality, they are subject to statistical fluctuations, and this effect is enhanced by the non-trivial shape of $f(\Delta E; \Delta x, \beta)$. The widths and separation of the measured distributions define the capability to discriminate between particle species.

Truncated mean

At the end of the general discussion of energy loss in Sec. 2.2.3, the technique of extracting the "truncated mean" from such measured straggling spectra was introduced. It was motivated as a necessary alternative to reconstructing the exact, asymmetric shape of the straggling spectra $f(\Delta E; \Delta x, \beta)$ in the scenario of small sample sizes, which is the situation we find for FOPI GEM-TPC energy-loss data.

The basic idea is to reduce the statistical uncertainties affecting the recovered straggling spectra by truncating the tail of the energy-loss straggling spectrum and then take the simple mean $\langle \Delta E \rangle_{\mathrm{tr}}$ of the *remaining* distribution as a stable – nevertheless biased – estimator. Instead of the actual mean energy loss $\langle \Delta E \rangle$ expected from the Bethe energy loss rate of Eq. (6.10), the truncated values will be much closer to the most probable value ΔE_{mp} of the

straggling distribution (cf. Fig. 2.6b). In the application of particle identification we are ultimately interested in, this should not lead to worry: in the end, only differences between particle species will matter. In practice, it can be the case that in addition to cutting away a fraction t_{high} of the highest values also a truncation on the other end of the spectrum (by a fraction t_{low}) helps to improve the final performance.

Expected resolution

Before moving on to a quantitative study of the obtained energy-loss spectra and resolutions, it is helpful to introduce a detector-independent model for the resolution of energy-loss measurements with gas detectors. In their work on charged-particle identification, Allison and Cobb [33] gave a phenomenological parametrisation of the expected resolution R (in % FWHM) of gas detectors as a function of the available size N_{s} of the $\Delta E/\Delta x$ sample, Δx (in cm) and the gas pressure P (in atm):

$$R(N_{\mathrm{s}}, \Delta x, P) = 0.96 \cdot N_{\mathrm{s}}^{-0.46} \cdot (\Delta x \cdot P)^{-0.32} \quad . \tag{6.13}$$

This result is based on the analysis of data from multiple experiments, all of them using Ar-based detectors and operational parameters corresponding to a sample-size range of roughly $50 \lesssim N_{\mathrm{s}} \lesssim 300$. It is also mentioned that for a truncated-mean analysis a slightly modified exponent for the sample size leads to a better description of the data:

$$R_{\mathrm{tm}}(N_{\mathrm{s}}, \Delta x, P) = 0.96 \cdot N_{\mathrm{s}}^{-0.43} \cdot (\Delta x \cdot P)^{-0.32} \quad . \tag{6.14}$$

In the form of Eq. (6.14), this parametrisation is commonly used as a benchmark for the energy resolution of gas detectors. It should be stressed, however, that the result from Allison and Cobb is based on data with significantly larger sample sizes than those appearing in the analysis of the GEM-TPC data ($\mathcal{O}(100)$ as opposed to ~ 20). In the following discussion it will become clear that asymmetries of the recovered samples of $\Delta E/\Delta x$ data play an important role in the case of FOPI GEM-TPC data. It is thus *a priori* not clear how well Eq. (6.14) can be extrapolated into that regime in order to use it as a benchmark.

6.5.2 Remaining asymmetries: A Monte Carlo study

The truncation method helps to attenuate the effect of statistical fluctuations by reducing the asymmetry of the underlying distribution, but the efficiency of the truncation is itself limited: for very small sets of $(\Delta E, \Delta x)$ pairs per track – or for very short track lengths, equivalently – the probability that pairs from the high-energy tail survive the truncation grows. In that case, parts of the original asymmetry will bleed into the distributions of $\langle \Delta E \rangle_{\mathrm{tr}}$.

The link between $\Delta E/\Delta x$ sample size and the remaining asymmetry has been investigated in a data-driven Monte Carlo study. For this purpose, a clean sample of proton tracks from a narrow momentum window was isolated from the data using FOPI's most powerful PID system, the RPC (cf. Chapter 7). From this raw spectrum – prior to any truncation – a certain number N' of $\Delta E/\Delta x$ measurements is drawn, simulating a track of length $l = N'\Delta x$. The extracted sets are then truncated and the obtained spectra are studied as a function of N'.

The truncated proton $\Delta E/\Delta x_{\mathrm{tr}}$ spectrum shows the expected dominant Gaussian component, but – as already conjectured – it also exhibits an asymmetry, growing with smaller sample size N'. In order to quantify this effect, a parametrisation is required that is able to capture this general shape. A well-suited choice is the convolution $C_{\mathrm{EG}}(\epsilon;\mu,\sigma,\tau) = E(\epsilon;\tau) \otimes G(\epsilon;\mu,\sigma)$ of an exponential decay function $E(\epsilon;\tau)$ and a Gaussian distribution $G(\epsilon;\mu,\sigma)$. Here τ is the decay constant, μ and σ are the Gaussian mean and standard deviation, respectively.

$C_{\mathrm{EG}}(\epsilon;\mu,\sigma,\tau)$ has the analytic form

$$\begin{aligned} C_{\mathrm{EG}}(\epsilon;\mu,\sigma,\tau) = \frac{\tau}{2} \cdot \exp\left[\frac{\tau}{2}\left(2\mu + \tau\sigma^2 - 2\epsilon\right)\right] \\ \cdot \operatorname{erfc}\left(\frac{\mu + \tau\sigma^2 - \epsilon}{\sqrt{2}\sigma}\right) \quad , \end{aligned} \tag{6.15}$$

where $\operatorname{erfc}(\epsilon;\mu,\sigma,\tau)$ is the complementary error function. Properly normalised, $C_{\mathrm{EG}}(\epsilon;\mu,\sigma,\tau)$ can be regarded as the probability density function (pdf) of the detector response ϵ to protons, $p_{\mathrm{tpc}}(\epsilon|\mathrm{proton})$, which in the present case is the specific energy loss measured by the GEM-TPC. This probabilistic interpretation can be used to combine measurements (from multiple detectors) in the attempt to identify the unknown particle species, as will be discussed in Chapter 7.

The variance of C_{EG} is $\sigma^2 + 1/\tau^2$. In the limit $\tau \to \infty$, the exponential component vanishes and a normal distribution is recovered, so the ratio $\sigma/\sqrt{\sigma^2 + 1/\tau^2}$ is a straight-forward measure of the asymmetry. Figure 6.17 shows this ratio as a function of N'. It slowly approaches 1 for large sample sizes (track lengths) [7]. In the region relevant for GEM-TPC data (Gray area), however, the asymmetry is already quite large. Also shown are the obtained "resolutions" both in terms of the full width at half maximum (FWHM) and simply by taking the standard deviation of the Gaussian component from Eq. (6.15).

Finally, the solid black lines in Fig. 6.17 represent the phenomenological prediction by Allison and Cobb [33], also for both the FWHM and – under

[7] For real, correlated track data the straggling function never becomes purely Gaussian: The requirement of identically distributed random variables in the central limit theorem is not met, since the particle loses energy along its path (Eq. (2.13) is only an approximation).

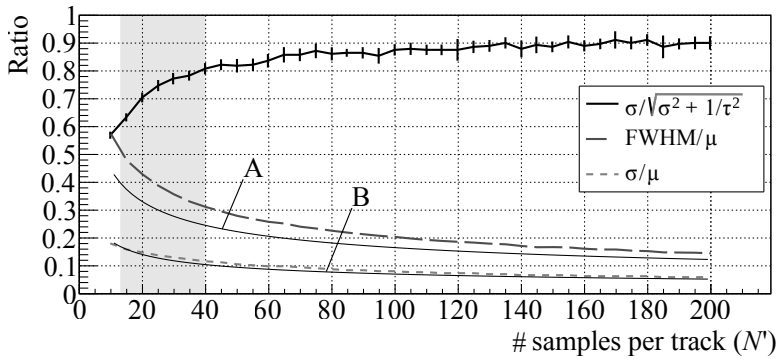

Figure 6.17: Monte Carlo study of obtained resolutions according to fits using Eq. (6.15) as a function of the number N' of $\Delta E/\Delta x$ measurements (before truncation). A step length of $\Delta x = 0.5\,\mathrm{cm}$ and a truncation of the 5 % (25 %) lowest (highest) measurements were used. The two broken lines show the obtained resolutions in terms of FWHM and Gaussian σ extracted from the fit. The corresponding asymmetry $\sigma/\sqrt{\sigma^2 + 1/\tau^2}$ is also drawn. The two solid black lines A and B show the external parametrisation by Allison and Cobb: Line A corresponds directly to Eq. (6.14), line B is scaled down by factor of 1/2.35, representing a Gaussian assumption. The Gray area marks the relevant window for actual FOPI GEM-TPC data when using this step length.

the assumption of a Gaussian shape – σ. The agreement of the latter with the Gaussian resolution component extracted from the data is quite remarkable, but it should be stressed again that Eq. (6.13) was originally parametrised using measurements in the regime $N' \approx 100$.

In summary, the results of the presented Monte Carlo study suggest a strong agreement between the energy-loss resolutions obtained with the FOPI GEM-TPC and the "prediction" provided by Eq. (6.14). The asymmetries of the truncated energy-loss spectra can be understood as arising from statistical fluctuations and can be fully absorbed in form of the single parameter τ. Figure 6.17 can provide additional justification for an extrapolation of the obtained resolution values to larger GEM-TPCs.

6.5.3 Experimental results

Figure 6.18 shows the specific-energy-loss spectrum of the GEM-TPC as a function of the particle momentum, separated by the sign of the particle charge. The discrimination between "$\Delta E/\Delta x$" and "$\mathrm{d}E/\mathrm{d}x$" is dropped from here on out, respecting common practice [8].

In order to extract a value for the "$\mathrm{d}E/\mathrm{d}x$ resolution" of the detector, the data is divided into bins of the particle momentum with a common width

[8] Equation (2.13) is understood to hold.

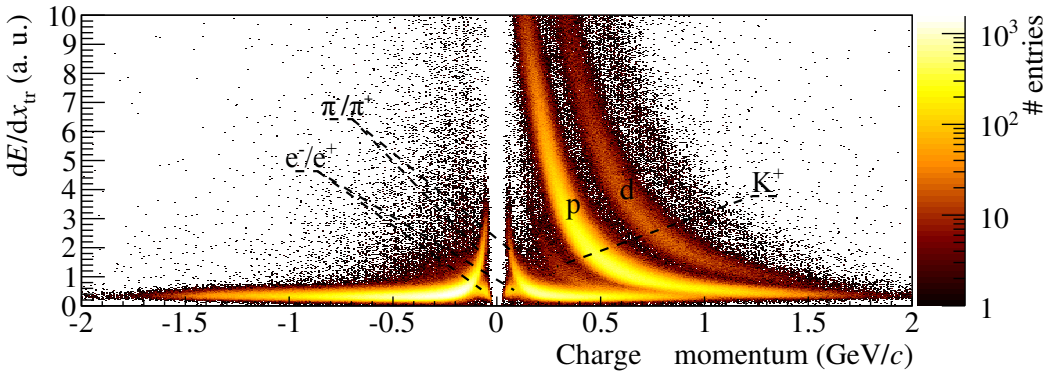

Figure 6.18: Spectrum of obtained $\mathrm{d}E/\mathrm{d}x_{\mathrm{tr}}$ values from the GEM-TPC as function of the particle charge×momentum (GENFIT fit of combined FOPI tracking information). $2.1{\cdot}10^6$ tracks from the π data have entered the analysis. The GEM stack was operated at 81 % of the nominal voltage in a $\mathrm{Ar/CO_2}$ [90/10] gas mixture.

of 25 MeV/c, now no longer separating between different signs of the particle charge. The peaks of the resulting projections are captured (binned maximum likelihood fits) by a composite model constructed from Eq. (6.15),

$$\mathcal{M}(\epsilon) = \sum_x w_x \, C^x_{\mathrm{EG}}(\epsilon; \mu_x, \sigma_x, \tau_x) \quad , \tag{6.16}$$

where the index x runs over an appropriate selection of particle species and the coefficients w_x give the corresponding statistical weight. Figure 6.19 shows two selected bins, demonstrating the quality of the fit.

From these spectra in narrow momentum bins, the resolution of the $\mathrm{d}E/\mathrm{d}x_{\mathrm{tr}}$ measurement can be extracted. Due to the nature of the fit function Eq. (6.15), it can be formulated in terms of the Gaussian σ or the full width at half maximum (FWHM) of the peak. The result of this evaluation is shown in Fig. 6.20 as function of the particle momentum.

Considering once more Fig. 6.18, it is clear that by organising the underlying data set in momentum bins of finite width, the slope of the Bethe-energy-loss curves will lead to an additional broadening of the binned spectra. This is especially true for low momenta. Another glance at Fig. 6.19 reveals, however, that this effect seems to be very efficiently described by the exponential contribution to the fit function. It is thus clear that the exponential component serves to absorb two effects: i) the truncation remnants of the high-energy tail of the straggling spectra as discussed in Sec. 6.5.2, and ii) the contribution of the Bethe slope picked up during the binning of the data in momentum space.

In this light it appears reasonable to regard the Gaussian component – governed by the parameters μ and σ of Eq. (6.15) – as the best-suited figure of merit. Figure 6.17 can be used – to some extent – to judge the validity of

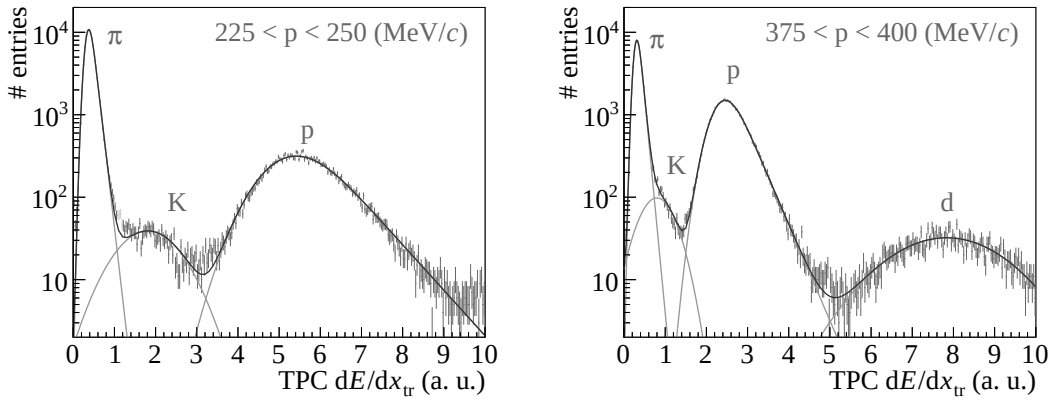

(a) $225 < p < 250\,\mathrm{MeV}/c$. (b) $375 < p < 400\,\mathrm{MeV}/c$.

Figure 6.19: GEM-TPC specific energy loss measured in two different ranges of the particle momentum. The spectra are fitted with the composite model given in Eq. (6.16).

this approach.

Choice of parameters & selection cuts applied

The free parameters of the presented extraction method are the step length Δx during amplitude sampling (cf. Fig. 6.16) and the truncation limits t_{low}, t_{high}. The most solid lever arm for their optimisation is the relative peak width of the resulting $\mathrm{d}E/\mathrm{d}x_{\mathrm{tr}}$ spectra for a given particle. Using protons as reference species, the optimal settings were found to be a truncation of the lowest 5 % and the highest 25 % of the collected samples, while for the step length a choice of $\Delta x = 0.5\,\mathrm{cm}$ gives the best results [9]. In addition, two cuts are applied during extraction of TPC $\Delta E/\Delta x$ data:

- the number of $\Delta A/\Delta x$ samples per track must be equal or larger than 13.
- for the radial position r_{pad} of the centre of gravity of the pad hit we require $6.0\,\mathrm{cm} < r_{\mathrm{pad}} < 14.0\,\mathrm{cm}$.

For the motivation and discussion of both cut choices the reader is referred to Sec. 4.3 of Ref. [25].

Impact of the pad-wise gain calibration

Finally, the effect of the pad-wise calibration of the effective detector gain (cf. Sec. 6.4.1) on the specific-energy- loss performance is studied. Figure 6.21 provides a direct comparison of results obtained with and without gain calibration on pad level for otherwise identical reconstruction parameters. A relative

[9] See Fig. 13 of Ref. [25].

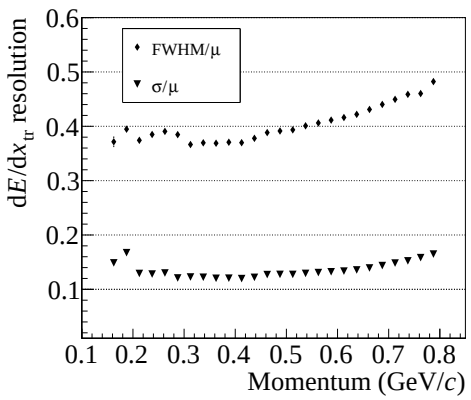

Figure 6.20: Resolutions for the proton peak obtained from the truncated specific-energy-loss data of Fig. 6.18 in momentum bins. Values for both the FWHM and σ corresponding to the Gaussian component of the fit (cf. Eq. (6.15)) are shown. Statistical errors of the fit parameters are drawn but small, systematical errors arising from the model selection are not studied.

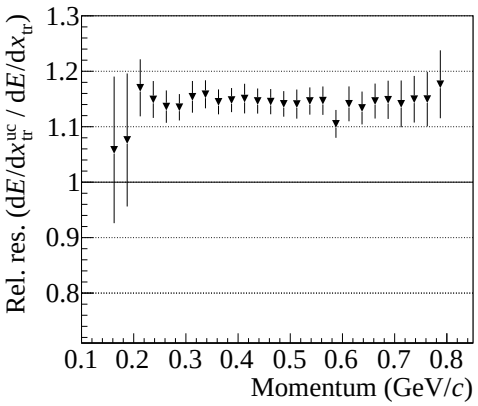

Figure 6.21: Direct comparison of the $\mathrm{d}E/\mathrm{d}x_{\mathrm{tr}}$ resolution (FWHM) without pad hit amplitude correction ("uc") to the corrected scenario. The weighted average of the resolution degradation is 14.3 %. The error bars correspond to the propagated statistical uncertainties of the fit parameters.

improvement of 14.3 % on the final resolutions is observed. A comparison to the 40 % improvement seen in the raw energy resolution (cf. Fig. 6.13) reveals that the dominating effects limiting the specific-energy-loss performance are of conceptual nature, e.g. given by the limitations faced when reconstructing the moments of straggling spectra (truncated mean analysis).

Chapter 7

A new approach towards combined PID in FOPI

In the past, FOPI data has been analysed using hard cuts in selected spectra of detector response data in order to identify particle species. While trivial to implement, this approach does not make optimal use of the complete set of PID-relevant information contained in the data. It is also especially vulnerable to background in the spectra, detector systematics and reconstruction artefacts.

In Sec. 6.5, a method to extract the resolution of a measurement of the specific energy loss ("$\mathrm{d}E/\mathrm{d}x$") in the FOPI GEM-TPC has been presented. While spectra of the $\mathrm{d}E/\mathrm{d}x$ data in bins of the particle momentum show distinguishable peaks for different particle species, the level of separation certainly does not allow to perform hard cuts on the particle identity. However, it could be shown that the peaks generated by different particle species can be accurately described by a suitable mathematical model $\mathcal{M}$ (c.f. Eq. (6.15)). Fits of the model to the data provide a probabilistic description of the measured detector response.

It is the purpose of this chapter to demonstrate how this technique can be extended to other detectors of the FOPI setup, and how the complete set of information from all participating detector systems can be merged into one probabilistic, albeit phenomenological approach towards combined PID. However, this approach currently cannot be used for small particle momenta, where remaining problems with the FOPI CDC unfortunately still dominate the picture (as discussed in Chapter 5). As a consequence, the discussion in this chapter will be limited to the momentum region above $200\,\mathrm{MeV}/c$.

The methods discussed in the following are – to the knowledge of the author – the first such attempt on FOPI data. In Sec. 7.1, the data sets used for the characterisation of the detector response of the participating systems will be presented. This will be followed by an overview over all performed fits in bins of the particle momentum (Sec. 7.2). Section 7.3 will introduce the mathematical

tool used for combining the obtained descriptions of the detector response into one probabilistic model for the purpose of PID. In the course of this discussion, also the issue of the stability over time of the detector response spectra will be addressed. Finally, some details of the usage and implementation of the procedure on the level of software code will be provided in Sec. 7.4.

7.1 Detector data used for PID

The systems contributing to particle identification in the TPC-augmented FOPI spectrometer are (cf. Chapter 3):

- The GEM-TPC, measuring the specific energy loss of traversing particles. Due to its comparably small size, the GEM-TPC is not expected to play a dominant role in the task of particle identification in the full FOPI setup. As demonstrated in Sec. 6.5, the GEM-TPC offers a $\mathrm{d}E/\mathrm{d}x$ resolution of $\sim 15\,\%$.
- The FOPI CDC, which also contributes to PID with a measurement of the specific energy loss.
- The FOPI RPC, providing a measurement of the TOF of traversing particles w.r.t. to the event time. The resulting timing resolution combined with the FOPI trigger system (cf. Sec. 3.2.4) is below $\sim 100\,\mathrm{ps}$, and it will be shown that the RPC provides the most valuable data for combined PID for particles reaching its acceptance.
- The FOPI BAR, also providing information of the particles' TOF.

When performing combined track fits (cf. Chapter 4), all of the above information is extracted concurrently with the momentum $|\mathbf{p}|$ of the particle, which thus represents the common parameter of the PID scheme. In the following, an overview of the data sets used for each of these systems will be provided. The analysis of the data revealed that the spectra show variations over time, especially in the case of the GEM-TPC and the CDC. In order to arrive at clean samples for the treatment in a combined scheme of PID, individual reference subsets of the full available data have to be chosen for these two systems. The topic of stability over time and the entailed necessity of an additional calibration outside of the reference ranges will be covered in Sec. 7.3.2.

7.1.1 TPC: $\mathrm{d}E/\mathrm{d}x$

A detailed discussion of the extraction of (truncated) specific energy loss information from TPC data has already been provided in Sec. 6.5. Since the PID scheme does not distinguish between positively and negatively charged particles, the combined data of Fig. 6.18 for both charges are shown again as a function of the particle momentum in Fig. 7.1.

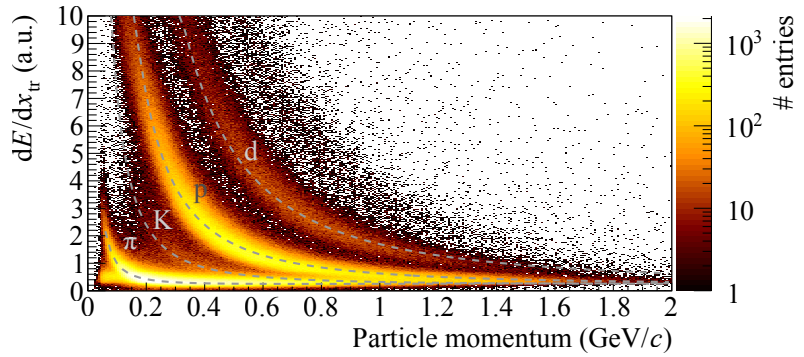

Figure 7.1: Specific energy loss from a truncated mean analysis of TPC data, drawn as function of the particle momentum. Shown is the reference sample ($\sim 2.1 \times 10^6$ tracks) from the (carbon target) runs 3280-3292. The dashed lines show phenomenological parametrisations of the Bethe energy loss for different particle species (defined on an arbitrary scale), which have been optimised to describe the detector data.

7.1.2 CDC: dE/dx

The information on the specific energy loss taken over from the FOPI feature extraction already represents the result of a truncated mean analysis. It is plotted as a function of the particle momentum in Fig. 7.2. Owing to the larger dimensions of the CDC, the resolution on the energy axis is superior compared to to the CDC.

Some additional remarks are in order at this point: First of all, it was shown in Sec. 5.1 that remaining systematic problems in the FOPI CDC data lead to a deterioration of the tracking performance in combined track fits in the TPC-CDC system, especially in the low-momentum region. This translates into an inferior separation between different particle species in Fig. 7.2 when compared to the same spectrum obtained directly from the FOPI reconstruction values (cf. the comparison of Fig 5.5). For a combined treatment of PID-relevant data, however, the particle momentum has to be obtained from combined fits. Most noticeably, this results in a shift of the spectrum along the momentum axis (cf. Sec. 6.3) towards smaller momenta.

Secondly, the extracted values of "dE/dx" naturally depend on the assumption of the particle trajectory. Consequently, there is a subtle inconsistency introduced when combining the specific energy loss value obtained from the FOPI feature extraction with the momentum value extracted from a TPC-combined track fit. In principle, one could also perform a re-calculation of the $\Delta E/\Delta x$ spectra of each track, taking into account the particle trajectory determined in the combined fit. The possible gain of this approach is, however, currently outweighed by the remaining imperfections of the CDC system.

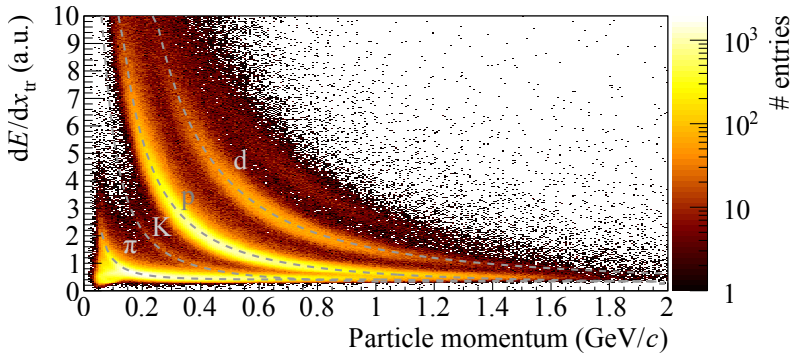

Figure 7.2: Specific energy loss measured by the FOPI CDC as a function of the particle momentum. The value on the ordinate ("Eloss" of `CdcTracks`, cf. Tab. 4.1) is obtained directly from the FOPI reconstruction and already represents a truncated mean analysis. Shown is the reference sample of $\sim 2.3 \times 10^6$ tracks from the (lead target) runs 3415-3430.

7.1.3 RPC: Time of flight

In contrast to the situation found in the CDC system, the comparison performed in Sec. 5.3 revealed that the extraction of TOF information from RPC data represents an example where the combined feature extraction with GEM-TPC tracking data is beneficial to the final performance. As described there, the particle velocity is re-calculated using the information of the travelled distance that is directly obtained from GENFIT track fits. The data of Fig. 5.9b is shown again in Fig. 7.3, this time in an extended momentum range.

7.1.4 BAR: Time of flight

The summary of the data contributing to the combined PID scheme is completed by the FOPI BAR. The data shown in Fig. 5.11b is reproduced in Fig. 7.4.

7.2 Fits in bins of the particle momentum

After the discussion of the basic extraction of the PID-relevant data for the different detector systems, attention will now turn to a quantitative treatment. In Sec. 6.5 it has been demonstrated how the detector response of the GEM-TPC for a given momentum region – in terms of the measured $\mathrm{d}E/\mathrm{d}x$ signature – can be described using a suitable mathematical model $\mathcal{M}$, in which every peak of the spectra is described by a convolution of an exponential decay function and a Gaussian (cf. Eqs. (6.15) and (6.16)). Let us now investigate how this method carries over to the other detector systems.

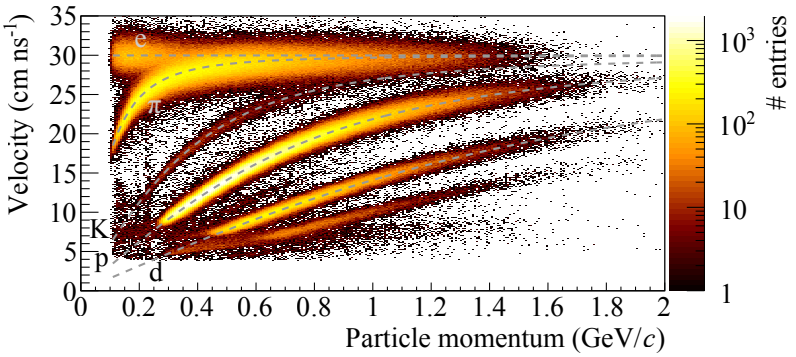

Figure 7.3: Reconstructed particle velocity from the TOF measurement provided by the RPC, plotted as a function of the particle momentum $|\mathbf{p}|$. The velocity v is obtained from the RPC TOF information provided by the FOPI feature extraction ("TOF" of `RpcTracks`, cf. Tab. 4.1) and the particle trajectory from the combined track fit. The dashed lines show the expected velocity $v = |\mathbf{p}|/\gamma m$ for electrons, pions, kaons, protons and deuterons.

Figures 7.5 to 7.8 show binned, maximum likelihood fits of the composite model $\mathcal{M}$ to the detector response data of all previously listed systems. The fits are performed in bins of the particle momentum (25 MeV/c width) in the range 200 MeV/c < $|\mathbf{p}|$ < 800 MeV/c. As stated previously, the particle momentum is treated as a common parameter, and the uncertainty of the momentum measurement is not propagated into the fits. The starting values of the fit parameters are chosen based on the functional expectation for each particle species (dashed lines in Figs. 7.1 to 7.4). None of the fit parameters are constrained during the fits [1]. The main application of the combined PID procedure in the context of the physics analysis of Chapter 8 will be the identification of kaons, and thus the kaon contributions of the composite fits are additionally highlighted.

Some additional comments are in order concerning the fitting technicalities. Inevitably, background due to imperfections of the detector hardware and the reconstruction methods enters the response spectra, deteriorating the quality of the fit. Since no Monte Carlo (MC) model of such background is available (cf. the discussion of Sec. 4.8), the mathematical description of the detector response remains purely phenomenological. A proper description of the background can thus only be achieved by increasing the complexity of the fit model. Ultimately, however, one is interested in a clean separation between different particle species based on the fits shown in Figs. 7.5 to 7.8. Therefore, the decision is taken to *exclude* certain areas of the response data in order to achieve

[1] Due to the largely different statistical content of the individual peaks, fit stability is an issue and the choice of the right starting values and optimisation ranges requires careful tuning.

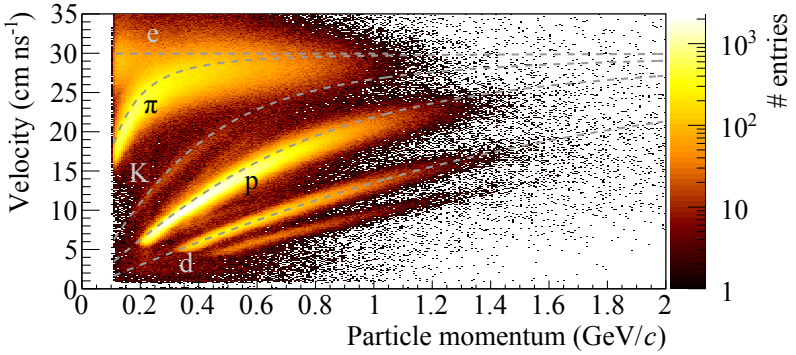

Figure 7.4: Reconstructed particle velocity from the TOF measurement provided by the BAR, drawn as a function of the particle momentum. The velocity is obtained from the BAR TOF information provided by the FOPI feature extraction ("TOF" of `RpcTrack`s, cf. Tab. 4.1) and the particle trajectory from the combined track fit. The dashed lines show the expected velocity $v = |\mathbf{p}|/\gamma m$ for electrons, pions, kaons, protons and deuterons.

the best possible description of the physically motivated peaks. The excluded areas are drawn in lighter colour in Figs. 7.5 to 7.8. This approach minimises the probability of mis-identifying particles at the cost of an inevitable loss of efficiency in the areas that are not described by the fits. Special care has to be taken in the case of the kaons: Their small statistical weight makes them especially vulnerable to an overlap from the model description of the much more abundant neighbouring particles, protons and pions.

7.3 The fractional likelihood method

Finally, a mathematical model is required for a combined, probabilistic treatment of the available set of information. As discussed in Sec. 6.5, after individual normalisation, each particle component C^x_{EG} of the combined model (6.16) can be understood as the (phenomenological) probability density function (pdf) $p_k(\epsilon_k|x)$ in terms of the expected detector response ϵ_k of detector k, under the assumption a particle of species x left the signal.

For the purpose of particle identification, however, one would like to ask the reversed question: What is the probability for species x, *given the measured detector response* ϵ_k. This probability is however not directly defined by the available data. Still, evaluating the functional shape $p_k(\epsilon_k|x)$ at the measured ϵ_k can be expected to give some sort of *likelihood* $l^x_k(\epsilon_k)$ of having observed particle x.

The goal is now to construct a normalised quantity from these likelihoods that can be used as a handle to separate different particle species, taking into account the full set of information $\boldsymbol{\epsilon}$ from *all* contributing detectors $\{k\}$.

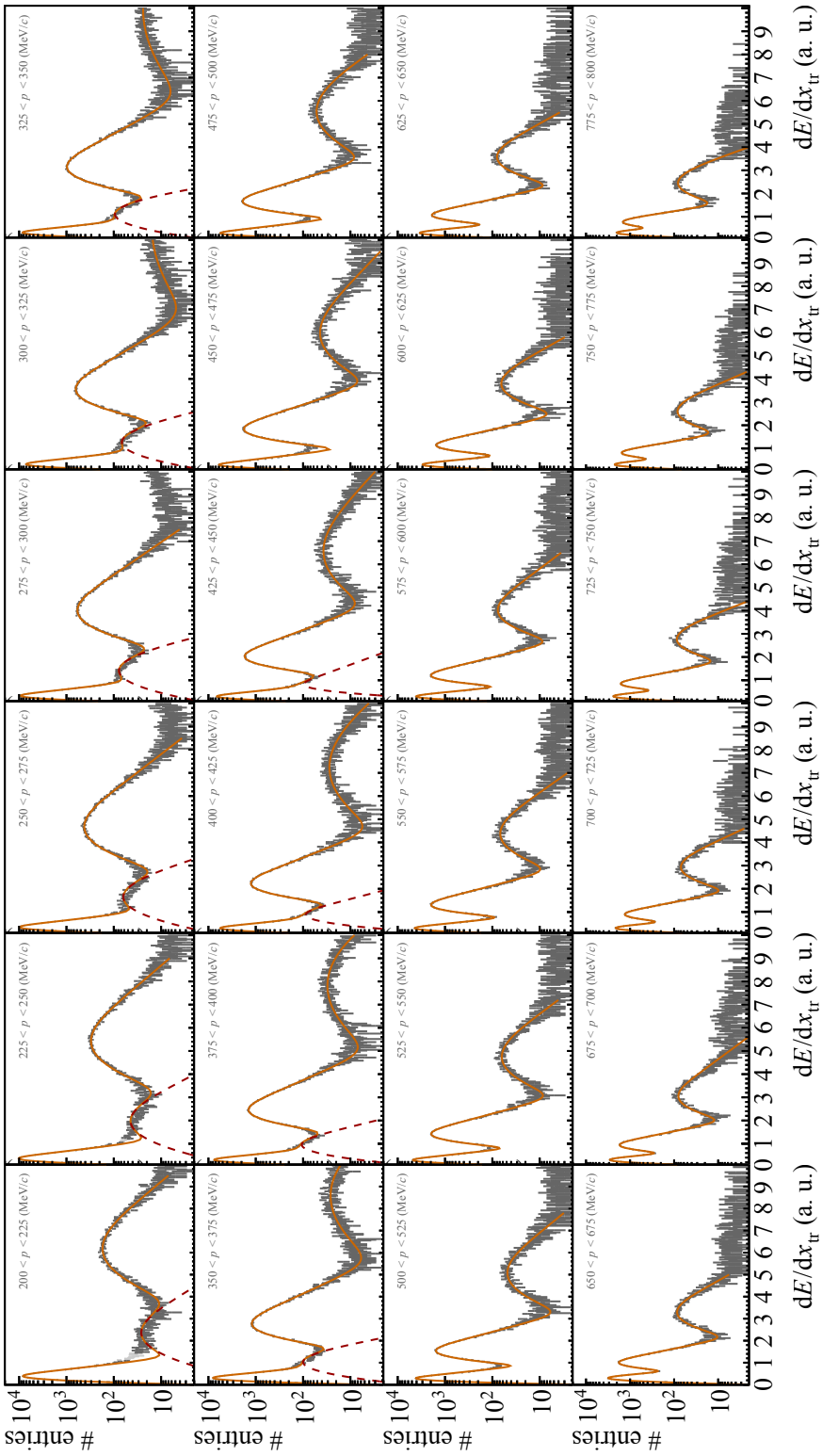

Figure 7.5: TPC $\mathrm{d}E/\mathrm{d}x$ data of Fig. 7.1 in 25 MeV/c-wide momentum bins. The full composite model is shown as orange solid line, its kaon component as broken red line where applicable. Data points appearing in lighter colour have been excluded from the fit (see discussion in the text).

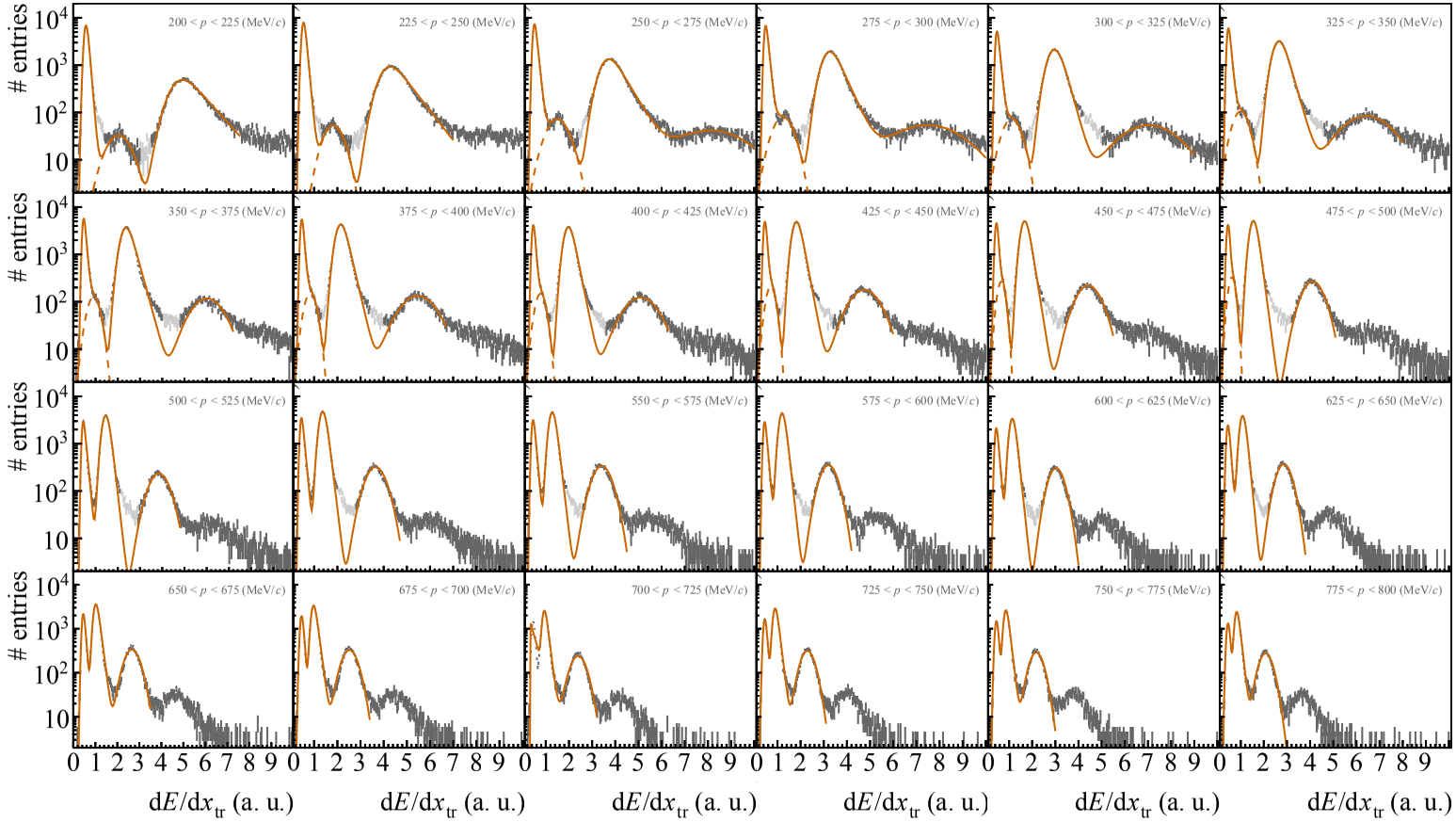

Figure 7.6: CDC $\mathrm{d}E/\mathrm{d}x$ data of Fig. 7.2 in 25 MeV/c-wide momentum bins. The full composite model is shown as orange solid line, its kaon component as broken red line where applicable. Data points appearing in lighter colour have been excluded from the fit (see discussion in the text).

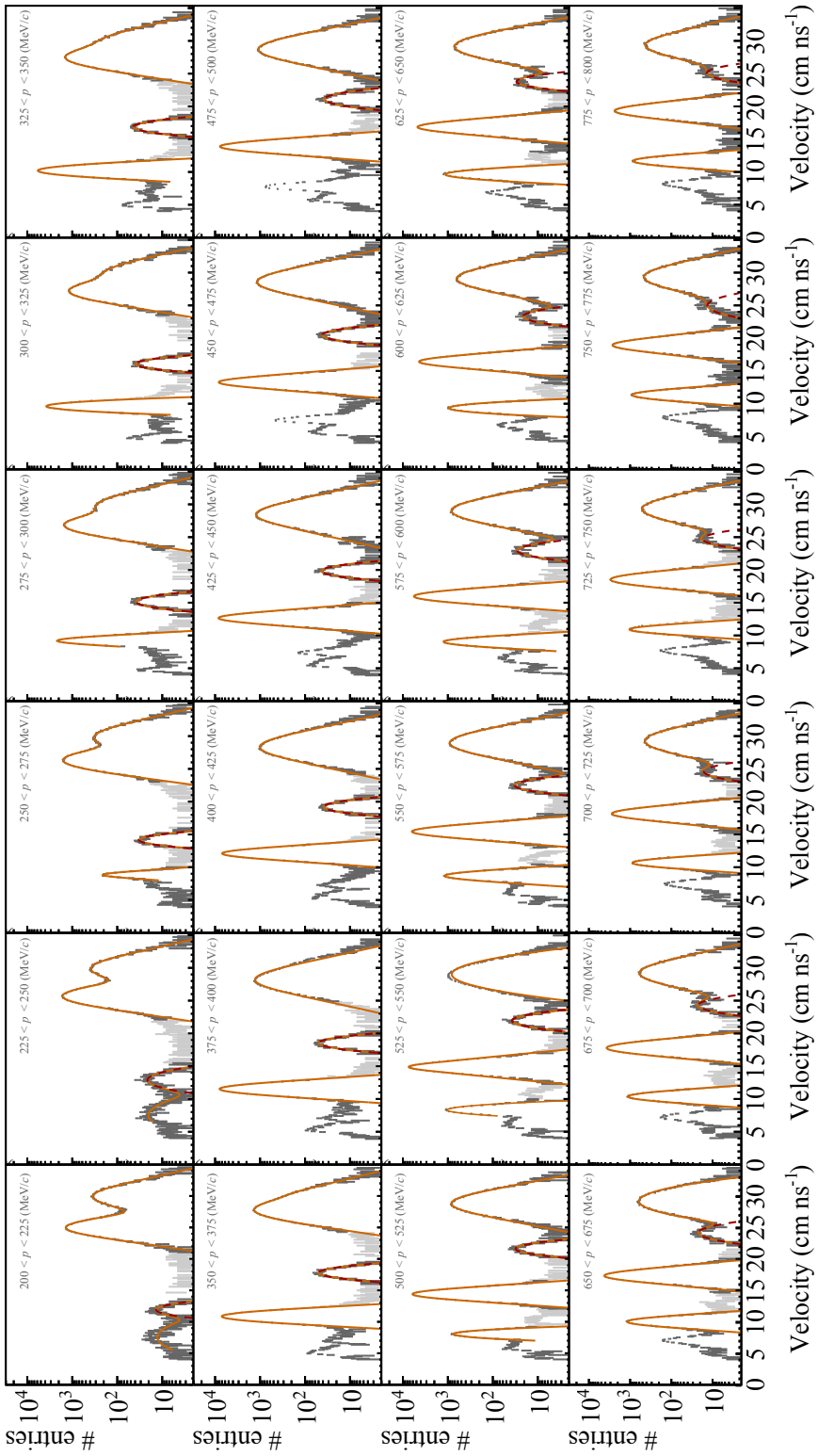

Figure 7.7: RPC velocity data of Fig. 7.3 in momentum bins of 25 MeV/c width. The full composite model is shown as orange solid line, its kaon component as broken red line where applicable. Data points appearing in lighter colour have been excluded from the fit (see discussion in the text).

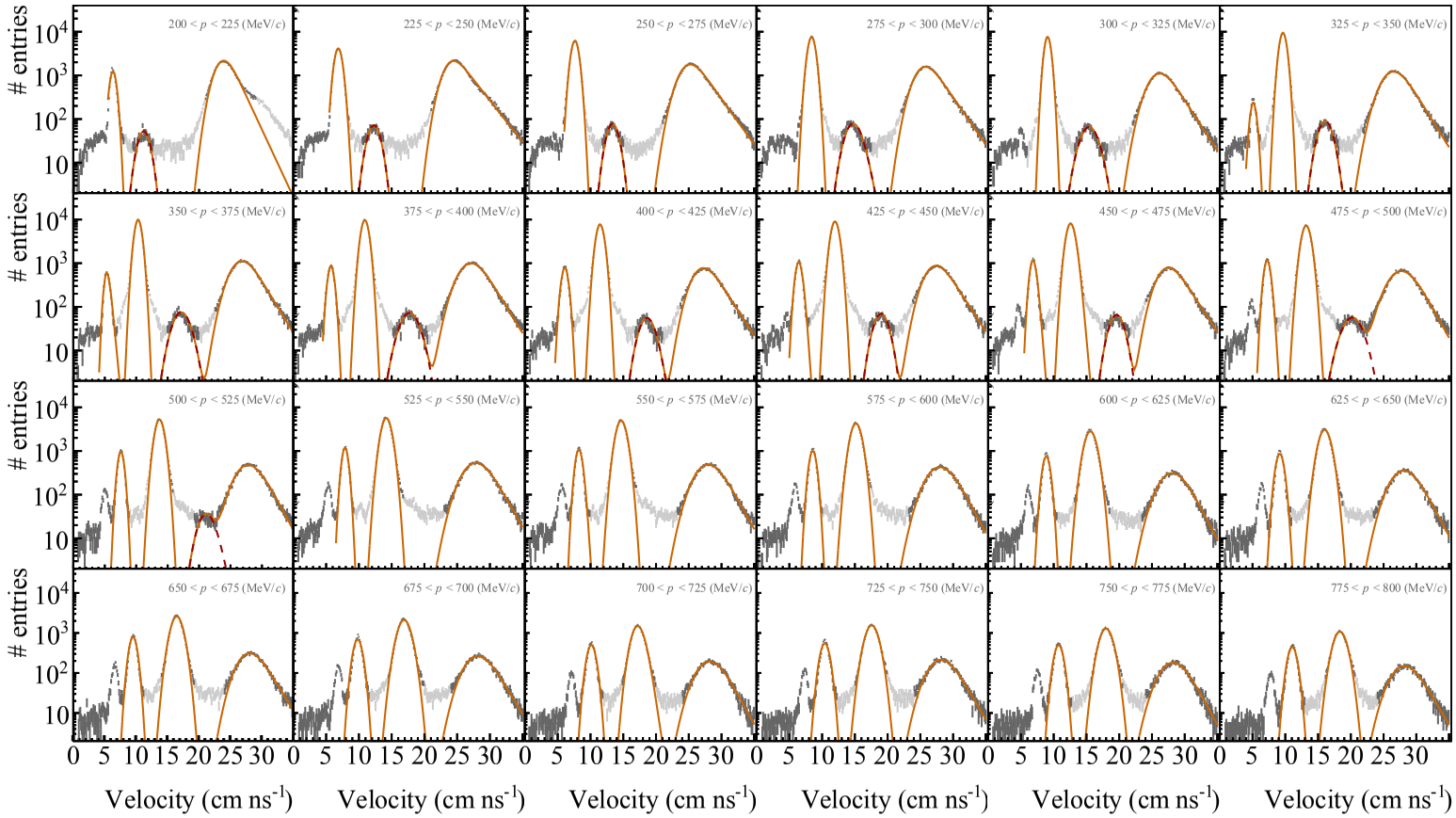

Figure 7.8: BAR velocity data of Fig. 7.4 in momentum bins of 25 MeV/c width. The full composite model is shown as orange solid line, its kaon component as broken red line where applicable. Data points appearing in lighter colour have been excluded from the fit (see discussion in the text).

A standard method is to construct the so-called *fractional likelihood* $\mathcal{L}(\boldsymbol{\epsilon})^x_Y$, evaluating the (combined) likelihood of a certain particle hypothesis x *relative to a (set of) contestant hypothesis/hypotheses* $Y = \{y\}$:

$$\mathcal{L}(\boldsymbol{\epsilon})^x_Y = \frac{\prod_k f^k_x \cdot l^x_k(\epsilon_k)}{\prod_k f^k_x \cdot l^x_k(\epsilon_k) + \sum_{y \in Y} \prod_k f^k_y \cdot l^y_k(\epsilon_k)} \quad . \tag{7.1}$$

Equation (7.1) gives an answer – in form of a number $\in$ [0,1] by construction – to the question how likely it is that the observed set of detector response data $\boldsymbol{\epsilon}$ was generated by a particle of species x, in comparison to the contesting hypotheses Y. The index k in Eq. (7.1) runs over all detectors that contributed to the PID measurement for the particle track in question, while the sum in the denominator runs over all particle species in the set Y. It can be seen how the set of available information $\boldsymbol{\epsilon}$ from all detectors is combined by forming products of the respective likelihoods: Only if all individual likelihoods $l^x_k(\epsilon_k)$ are in agreement ("overlap") in the sense of a compatible particle hypothesis, the product will be non-zero. The coefficients f appearing in Eq. (7.1) additionally give an initial weight to each particle hypothesis. It is only plausible that they should describe the *a priori* probability that any given charged particle measured in the detector is a member of that species, thus re-introducing the information lost during individual normalisation of the model components C_{EG} (the coefficients w_x in Eq. (6.16)). Formally, Eq. (7.1) has the appearance of a "*Bayesian likelihood*", with the weighting factors f entering as prior probabilities.

For the final decision on a particle hypothesis, still a cut is required on the value returned by Eq. (7.1). The difference to the conventional method of introducing hard cuts in single detector response spectra is that the fractional likelihood method properly takes into account all available information relevant for PID, as well as the shape of the respective distributions and the quality with which they are measured.

7.3.1 Particle fractions / Prior probabilities

The next question is how to obtain the particle weights f. Ideally, f^k_x should resemble the absolute probability that any of the particles that left a signal in detector k is of type x. In principle, this information is contained in the detector response, specifically in the weights w of the individual components of the fit (cf. Eq. (6.16)). However, this is only true if the fit perfectly captures the data. Background from reconstruction artefacts, and the related choice of excluding parts of the data, will obviously have an effect on the retrieved weights, and its magnitude will be different for each system (consider, for instance, the large amount of background and artefacts in the BAR data). Moreover, the RPC is the only detector capable of resolving the (large) contribution from

electrons bleeding into the "pion peak", and this only in the low-momentum region (cf. Fig. 7.7).

A convenient and pragmatic alternative, that is not biased by these technical problems, is to retrieve the weights from simulation. For this purpose, a large sample of MC data is generated at S339 conditions, using the GiBUU (cf. Sec. 8.3.1) particle generator. From this data, all relevant charged particles that reach the acceptance of the TPC are collected, taking into account target effects and the software model of the TPC material. The relative particle fractions are obtained by simple counting of the particles entering the acceptance of the TPC. In view of the initially discussed problems, it is also a reasonable approach to use these MC priors for *all* detector systems: $f_x^k \equiv f_x \,\forall\, k$. In doing so, Eq. (7.1) can be simplified to

$$\mathcal{L}(\boldsymbol{\epsilon})_Y^x = \frac{f_x \prod\limits_k l_k^x(\epsilon_k)}{f_x \prod\limits_k l_k^x(\epsilon_k) + \sum\limits_{y \in Y} f_y \prod\limits_k l_k^y(\epsilon_k)} \quad . \tag{7.2}$$

Figure 7.9 shows the particle fractions f as obtained from the MC data in the example of the carbon target. As a crude check of consistency, they are compared to the proton weights w_{proton} obtained directly from the fitted TPC detector response. A reasonably good agreement with the MC values is observed. It should be noted that the absolute precision of the prior probabilities is not expected to have a significant impact on the final quality of particle separation: As long as the order of magnitude of the priors is correct, the distribution of the fractional likelihood values is mostly determined by the shape and the overlap of the response distributions. This will be demonstrated in an application on S339 data for the purpose of kaon identification in Sec. 8.4.

7.3.2 Stability of PID data over time

Figures 7.1 and 7.2 only show a small subset of the available data for the GEM-TPC and the FOPI CDC. As remarked earlier, this restriction was introduced after relatively large variations over time of the specific energy loss spectra had been observed in the data. Figure 7.10 shows the time evolution of the position of the proton and pion peaks in the $\mathrm{d}E/\mathrm{d}x$ spectra for both detectors. The plot covers all data recorded with the carbon and lead targets during the S339 experiment. The highlighted areas (orange boxes) mark the reference regions corresponding to the data shown in Figs. 7.1 and 7.2 [2].

The variations over time are observed to be of the order of 20 % for the TPC and 10 % for the CDC. For both the BAR and the RPC system, the

[2] In the case of the TPC, this also corresponds to the data set that entered the analysis of Ref. [25] and Sec. 6.5.3.

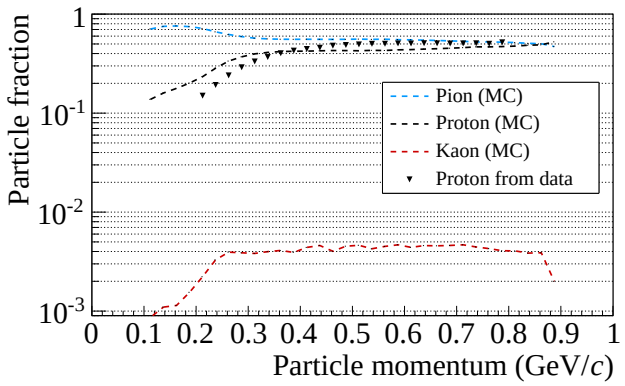

Figure 7.9: Statistical weight of different charged particles entering the TPC acceptance, according to GiBUU MC simulations. Shown is the example of the carbon target. Also drawn is the experimental proton fraction w_{proton}, extracted from the fit of the response model $\mathcal{M}$ (cf. Eq. (6.16)) to the TPC $\mathrm{d}E/\mathrm{d}x$ reference data set.

variations are small ($\mathcal{O}(1\,\%)$) and do not require further attention. While fluctuations over time of un-calibrated data had been anticipated in the case of the TPC, it was somewhat surprising to find a similar situation for the CDC data, which had initially been regarded to be consistently equalised already on the level of the FOPI feature extraction. In general, the variations show a clear correlation between the CDC and TPC systems, which strongly suggests changes of the environmental conditions (air pressure, temperature) to be the underlying cause. The sharp drop visible in the carbon data of the TPC corresponds to a period in which the chamber had been operated at a lower voltage setting of the GEM stack. It will be demonstrated in the following section, how the data shown in Fig. 7.10 are used for a calibration of the PID data outside the reference ranges in the software implementation of the combined PID scheme.

7.4 Software implementation

The defining quantities of the combined PID scheme according to Eq. (7.2) are the likelihoods $l_k^x(\epsilon_k)$ and the prior weights of the contributing particle species f. The likelihoods are evaluated from the functional form of the detector response pdfs C_{EG}^x, which are in turn obtained from maximum-likelihood fits of the composite model $\mathcal{M}$ (6.16) to the detector response data (cf. Figs. 7.5 to 7.8). The fits are performed using the RooFit [79] data modelling toolkit. RooFit internally treats the model components C_{EG}^x already as correctly normalised probability densities (`RooAbsPdf`). These objects are once obtained for all momentum bins from the reference data sets – or the full available data

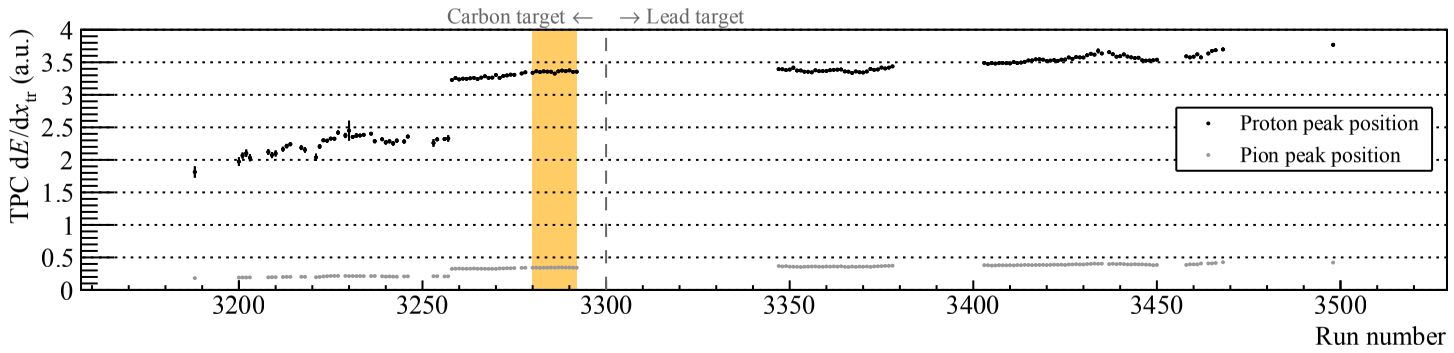

(a)

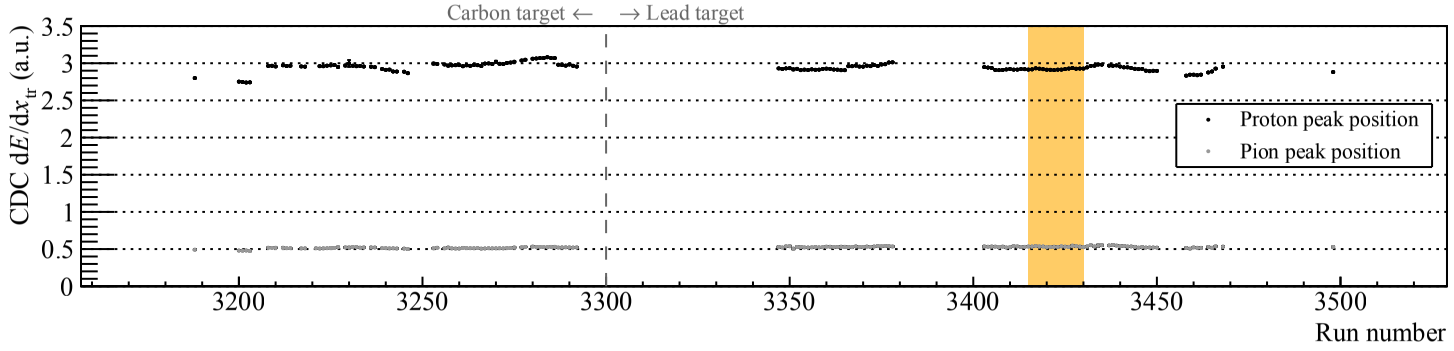

(b)

Figure 7.10: Variations of the proton and pion peak positions in the $\mathrm{d}E/\mathrm{d}x$ data from (a) TPC and (b) CDC. The values are extracted using a Gaussian χ^2 fits in the momentum range $300 < |\mathbf{p}| < 350\,\mathrm{MeV}/c$. Error bars corresponding to the statistical uncertainty of the extracted fit parameters are drawn, but are mostly smaller than the data points. The orange areas mark the data regions used for calibration in the scope of the combined PID scheme. The sharp drop visible in the TPC data for run numbers $\lesssim 3260$ corresponds to a period in which the detector had been operated at a lower gain.

in the case of the RPC and BAR detectors – and stored on disc for the subsequent physics analysis. As discussed in Sec. 7.3.1, the prior probabilities f are taken from MC simulations and stored separately.

The performance-critical code of the PID model is implemented in the `C++` programming language and integrated into the common feature extraction framework: Equation (7.2) itself is implemented in a central code object, called the `FopiPidHub`. This entity is also responsible for the management of all fit data and takes care of the entailed bookkeeping. On the level of the analysis of the feature-extracted data, each track is associated with a measurement of its momentum and a selection of PID-relevant information, which is collected in a `FopiPidInfo` data container.

This leaves the question of how to deal with the previously discussed variations over time of the PID-relevant data. First, the data of Fig. 7.10 are passed to the `FopiPidHub` instance, along with the definition of the reference intervals. These are defined in regions in which the data points only show little movement (cf. Fig. 7.10). In these regions, a weighted mean of both the pion and the proton peak is calculated. Under the assumption of a perfect proportionality of the readout electronics, these two points define the calibration base, and a linear re-calibration of the detector response outside of the reference regions can be performed.

The code snippet shown in Fig. 7.11 scripts demonstrates the usage of the `FopiPidHub` in the example of a track leaving hits in the TPC, CDC and RPC detectors: In lines 2-18, all relevant global information is passed to the `FopiPidHub` for its initialisation. These are the files containing the detector response fits (lines 2-6), the file containing the prior probabilities (line 8), and the data describing the variations over time for TPC and CDC along with the definitions of the reference intervals (lines 10-16). When looping over individual track fits, the PID-relevant data are collected inside a `FopiPidInfo` object (lines 23-34). When passed to the hub instance (line 37-38), the measured $\mathrm{d}E/\mathrm{d}x$ information of TPC and CDC is internally re-calibrated *before* the likelihoods are evaluated, as described above. Finally, a value for the fractional likelihood, according to Eq. (7.2), is returned. This value can then be used for a decision on the particle hypothesis.

7.5 Discussion & Outlook

In this chapter, a probabilistic approach towards the identification of particles in the S339 setup has been presented. In addition to the GEM-TPC, the data from three FOPI detector systems are combined into one normalised quantity, using a phenomenological, probabilistic description of the detector response spectra in bins of the particle momentum.

Before continuing with an application of this scheme in a physics analysis of the S339 data, some additional comments are in order: The spectra of

```
#Initialisation:
hub = FopiPidHub()
hub.setDetProbFile("tpc",tpcPidFile)
hub.setDetProbFile("cdc",cdcPidFile)
hub.setDetProbFile("rpc",rpcPidFile)
hub.setDetProbFile("bar",barPidFile)

hub.setUseMCFractions(fractionsFile)

hub.setCalibrationFile("tpc", calibrationFile,
                       "tpcCalPion", "tpcCalProton",
                       3280, 3292)

hub.setCalibrationFile("cdc", calibrationFile,
                       "cdcCalPion", "cdcCalProton",
                       3415, 3430)

hub.init()

#loop over combined track fits:
for track in tracks :
   #extract magnitude of the momentum from combined fit:
   mom = track.getCardinalRep().getMom().Mag()

   #after obtaining PID information:
   #dedxTPC: (truncated mean) dE/dx measured in the TPC
   #dedxCDC: (truncated mean) dE/dx measured in the CDC
   #rpcVel : velocity calculated from the RPC TOF
   #         and the track fit
   #runNr  : Run number of the analysed data

   pidData = FopiPidInfo(runNr)
   pidData.setRpcVel(rpcVel)
   pidData.setTpcdEdx(dedxTPC)
   pidData.setCdcdEdx(dedxCDC)

   #get frac. likelihood value for kaons vs. pions, protons
   fracLi = hub.getFracLikelihood("kaon","proton","pion",
                                  mom,pidData,True)

   if fracLi > CUT :
       #proceed under kaon assumption
       #...
```

Figure 7.11: Code snippet from a data analysis script (written in the Python programming language) used for kaon identification.

Figs. 7.5 to 7.8 all show clear peaks belonging to different particle species, but also – in varying magnitude – contributions from general background and reconstruction artefacts. It can be seen that the RPC is the FOPI system that clearly provides the best separation of particle species, free of overlaps in a large momentum range. In contrast to that, the spectra of the BAR detector display the largest amount of reconstruction problems (level of background compared to the central peak widths), and wide ranges of its response data have to be excluded for the fits to converge at all. The spectra of the CDC and TPC, on the other hand, demonstrate that the contribution to PID from these systems is mostly limited by their intrinsic $\mathrm{d}E/\mathrm{d}x$ resolution.

A general trend of degradation is observed towards smaller momenta. This has two reasons: The first is a feature of the method itself and arises from the projection of the original response spectra onto the momentum axis. By doing so, the generally larger slope of the bands in that region leads to an additional broadening of the spectra (cf. Figs. 7.1 to 7.4). This problem can be overcome by normalising the spectra w.r.t. a single hypothesis before slicing along the momentum axis, however at the expense of making the fits of the remaining peaks more difficult. This method has proven to be slightly beneficial in the important case of kaon identification; The corresponding spectra are not explicitly shown in this work, however. When aiming to maximise the purity of the identification, an alternate strategy is to restrict the track sample to particles that left a signal in the RPC. The analysis of charged kaons in the next chapter is performed this way.

The second source of this trend are the remaining problems in the TPC-CDC system, as discussed in Chapter 5. It will be interesting to see how much the PID scheme presented in this chapter can be improved once these issues are resolved, and whether its applicability can then be extended to smaller momenta.

Chapter 8

Analysis: Pion-induced strangeness production

The S339 physics run served as an excellent opportunity to study the performance of the GEM-TPC detector under realistic conditions. In the full setup and using the tools presented in the previous chapters of this work, it is also possible to perform a physics analysis of the data set in a TPC-combined analysis. In this chapter, the obtained results will be presented.

Section 8.1 will provide a short overview over the motivations for performing strangeness physics at intermediate energies, specifically the experimental production of kaons. This introduction will be followed by an overview over the production channels during the S339 experiment.

In Sec. 8.2, the theoretical background of chiral symmetry breaking will be presented, and the reader will be introduced to an effective theory based on ChPT that describes the interactions of kaons and nucleons in a mean-field approximation. The goal is to work out a model for the modification of the properties of kaons, when embedded in nuclear matter, on a level that allows the interpretation of experimental observables.

Section 8.3 will introduce the strategy of the measurements which will be presented in the sections to follow. A short introduction to the so-called hadronic *transport models* will be given, which are required to establish a link between theory and experiment.

Finally, Secs. 8.4 and 8.5 will provide an in-depth discussion of the physics analysis performed on the S339 pion-beam data: The measurement of the relative effect of the target material on the momentum distribution of produced K^+ (Sec. 8.4) and K^0 (Sec. 8.5).

8.1 Motivation

Over the last decades, the study of strange particles produced in nuclear collisions has gained a lot of interest [80], [81]. Since strangeness is strictly con-

served by the strong interaction, strange particles emerging from the hadronisation of the initially produced $\bar{s}s$ pairs can easily leave the collision zone: Their strange quarks act as a protection against re-absorption in strong-interaction processes.

Under S339 conditions, the strange hadrons produced are hyperons with a single strange quark (Λ^0, Σ^-, Σ^0, Σ^+) and kaons (K^-,K^0, $\bar{K^0}$, K^+). From this set, the K^0 and K^+ play a special role in the context of the previous argument: Their $\bar{s}$ quark also prevents strangeness-exchange reactions with nucleons of the sort

$$\begin{pmatrix} K^- \\ \bar{K}^0 \end{pmatrix} N \longleftrightarrow \pi\, Y \quad , \tag{8.1}$$

where Y denotes a hyperon taking part in the exchange. This fact translates into a mean free path of $\approx$ 7 fm in nuclear matter for K^+ and K^0, which makes them an excellent probe for the investigation of the dynamics of nuclear collisions. As an example, the (sub-threshold) production of K^+ has been a key asset in the experimental exploration of the equation of state of nuclear matter above the nuclear saturation density ρ_0.

Apart from the study of the bulk dynamics in nuclear collisions, also the fundamental nature of the K-N interaction and the modification of the physical properties of the kaons themselves – when embedded in nuclear matter – are of great interest. The phenomena connected to the latter are commonly referred to as *in-medium effects*. An experimental signature of these effects is the modification of the energy-momentum relation of kaons that are produced inside nuclear matter. Sections 8.3 and beyond will discuss the strategy and results of such a measurement performed on the S339 data.

An appropriate framework for a theoretical treatment at low energies is that of ChPT. Employing effective models based on ChPT in the $SU(3)$ flavour sector allows a theoretical description of the kaon-nucleon potential in a *mean-field* picture, at least in the case of K^+ and K^0. The obtained interpretation of in-medium effects for kaons is linked to the non-vanishing expectation value of the chiral quark condensate $\langle \bar{q}q \rangle$, which spontaneously breaks the chiral symmetry of QCD. A short introduction to the theoretical background will be given in Sec. 8.2.

8.1.1 Pion-induced kaon production at FOPI

At the S339 beam momentum of 1.7 GeV/c, kaons (K^+, K^0) are primarily produced in binary collisions with target nucleons (p, n). Anti-kaons are not explicitly analysed in this work.

For K^+, the most important production channels are

$$\begin{aligned} \pi^- p \longrightarrow & \Sigma^- K^+ \\ & \Lambda^0 \pi^- K^+ \end{aligned} \tag{8.2}$$

and

$$\pi^- n \longrightarrow \Sigma^- \pi^- K^+ \quad . \tag{8.3}$$

For K^0, these are

$$\begin{aligned} \pi^- p \longrightarrow & \Lambda^0 K^0 \\ & \Lambda^0 \pi^0 K^0 \\ & \Sigma^0 K^0 \\ & \Sigma^+ \pi^- K^0 \end{aligned} \tag{8.4}$$

and

$$\begin{aligned} \pi^- n \longrightarrow & \Sigma^- K^0 \\ & \Sigma^- \pi^0 K^0 \quad . \end{aligned} \tag{8.5}$$

It should be noted that the fermi motion of the nucleons can provide additional centre-of-mass energy, and can thus effectively lower the production thresholds. In addition, the production dynamics could be altered by the transitional formation of resonances. An acceptance-corrected measurement of the inclusive K^0-production cross section in $\pi^- A$ collisions (1.15 GeV/c pion momentum) has been performed with the FOPI apparatus by Benabderrahmane *et al.* [82], showing a clear elevation of K^0 yields when compared to the elementary cross sections. This study was performed for five different nuclear targets, and the extracted cross sections were found to follow a power law of the mass number A of the target material,

$$\sigma(\pi^- A \longrightarrow K^0 + X) \propto A^b \quad , \tag{8.6}$$

with $b = 0.67 \pm 0.03$. This result can be seen as evidence that kaon production in π-A reactions at 1.15 GeV/c pion momentum occurs on the surface of the nucleus (radius $R \propto A^{1/3}$).

In heavy-ion collisions, short-lived nucleon resonances populate the hot/-dense region of the collision, providing an additional energy reservoir for the production of kaons. This feature can be used in their deliberate sub-threshold production, as they are guaranteed to originate from the dense region of the collision in that scenario.

8.2 Introduction: Chiral symmetry (breaking) and effective theories

With the goal of motivating the theoretical footing of the kaon-nucleon potential, this section undertakes a short tour through the key theoretical concepts

of chiral symmetry breaking. An extensive and very useful pedagogical review can be found in Ref. [83]. The discussion will first be restricted to only two quark flavours, u and d. Natural units ($\hbar = c = 1$) are used throughout this section.

In the limit of vanishing quark masses, the QCD Lagrangian

$$\mathcal{L} = i\bar{q}\partial_\mu\gamma^\mu q + \mathcal{L}_{\text{glue}} = i\bar{q}_{\text{L}}\partial_\mu\gamma^\mu q_{\text{L}} + i\bar{q}_{\text{R}}\partial_\mu\gamma^\mu q_{\text{R}} + \mathcal{L}_{\text{glue}} \tag{8.7}$$

is invariant under independent, unitary (flavour-) rotations of the left-handed and right-handed quark fields $q = (u,d)^{\text{T}}$. The symmetry group is $U(2)_{\text{L}} \times U(2)_{\text{R}}$, which can be decomposed into $SU(2)_{\text{L}} \times SU(2)_{\text{R}} \times U(1)_{\text{V}} \times U(1)_{\text{A}}$. The singlet components are not of interest in the following discussion. The remaining symmetry, $SU(2)_{\text{L}} \times SU(2)_{\text{R}}$, leads to two conserved currents via *Noether's theorem*, a *vector* current V_μ and an *axial-vector* current A_μ. This property is what is commonly referred to as *chiral symmetry*.

Allowing a mass term

$$\mathcal{L}_{\text{M}} = -m_{\text{q}}\bar{q}q \tag{8.8}$$

to enter in Eq. (8.7) explicitly breaks the symmetry associated with the axial-vector current A_μ. For simplicity, we assume $m_{\text{q}} \approx m_{\text{u,d}}$. When composing mesons from the quark fields, it can be seen that the broken symmetry transformation corresponds to a mixing of meson states, which would be degenerate in the fully symmetric case. Since the bare quark masses are small ($m_{\text{q}} = \mathcal{O}(1\,\text{MeV})$), one would also expect a relatively small effect on the degeneracy of the meson states introduced by this breaking of symmetry. However, the mass differences in the experimentally observed meson spectrum are large ($\mathcal{O}(100\,\text{MeV})$) and of the same order as the meson masses themselves.

At the same time, evidence exists that A_μ, in fact, *is* largely conserved (PCAC and *Goldberger-Treiman* relations), as one would also initially expect from the smallness of m_{q}. Both of these seemingly contradictory observations can be explained – in addition to the explicit breaking introduced by $m_{\text{q}} \neq 0$ – by allowing the axial-vector symmetry to be *spontaneously broken*. This means that the symmetry is realised in the Lagrangian, but not in the ground state (the "vacuum"), which gains a finite expectation value. Commonly used analogies are those of a ferromagnet or a classical "Mexican-hat" potential. In the meson picture and in the example of the π and the σ fields – which are mixed by the axial symmetry transformation –, the σ has the quantum numbers of the vacuum and thus gains a mass. For the σ, this is equivalent to the statement

$$\langle\bar{q}q\rangle \neq 0 \quad , \tag{8.9}$$

i.e. the scalar quark condensate $\langle\bar{q}q\rangle$ becomes finite. The π fields, on the other hand, play the role of *Goldstone bosons* of the spontaneous breaking and remain massless. Thus, the scenario of a spontaneous breakdown of the axial-vector symmetry combined with the explicit breaking introduced by the finite

quark masses is in conceptual agreement with the structure of the observed meson mass spectrum.

The aspects of chiral symmetry and its breaking can be used to relate the fundamental level of quarks to the observable spectrum of hadrons. Before discussing the application of an effective, chiral theory in the following section, a few important such relations shall be introduced. The first is the so-called *Gell-Mann-Oakes-Renner* (GOR) relation [84], which for pions reads

$$m_\pi^2 f_\pi^2 = -\frac{m_u + m_d}{2} \langle 0|\bar{u}u + \bar{d}d|0\rangle \quad . \tag{8.10}$$

The quantity f_π is the pion decay constant, which can be extracted from experiment (weak decay of the pion) [1]. The significance of Eq. (8.10) is that it explicitly shows the generation of the pion mass m_π from both the explicit breaking by the bare quark masses and the spontaneous breaking related to the quark condensate $\langle\bar{q}q\rangle$. It thus also directly translates a possible variation of the latter into a modification of the pion mass. Indeed, it is conjectured (see, e.g., Refs. [85] and [86]) that the expectation value (8.9) shrinks with growing energy and/or density (*chiral restoration*). Finding experimental evidence for such *in-medium effects* is an active field of research.

Another quantity that will re-appear in Sec. 8.2.1 is the so-called *pion-nucleon sigma term*

$$\Sigma_{\pi N} = \frac{m_u + m_d}{2} \langle N|\bar{u}u + \bar{d}d|N\rangle \quad , \tag{8.11}$$

where $|N\rangle$ are nucleon states. Both Eqs. (8.10) and (8.11) can be motivated ([83]) within the scope of the *linear sigma model* due to Gell-Mann and Lévy [87]. There, the quantity $\Sigma_{\pi N} \simeq 45\,\mathrm{MeV}$ emerges as the contribution of the explicit symmetry breaking to the nucleon mass.

All of the above can be expanded to the $SU(3)$ flavour sector, i.e. also including strange quarks. In doing so, the full pseudoscalar meson octet appears in the role of Goldstone bosons. Strange quarks are, however, considerably heavier than u and d, and the argument of a relatively "small" explicit breaking becomes to some extent questionable. The discussion will now proceed with an effective, chiral model in the $SU(3)$ flavour sector, ultimately leading to a quasi-particle description of kaons in nuclear matter, including a prediction of the in-medium modifications of the kaon properties.

8.2.1 ChPT and the kaon-nucleon potential

QCD cannot be treated perturbatively at small energies due to the scaling behaviour of the strong coupling constant: Quarks (and gluons) are confined into

[1] Different normalisations of f_π exist in the literature, differing by a factor $\sqrt{2}$. The value given in Ref. [28] is $f_\pi \simeq 130\,\mathrm{MeV}$.

colour-neutral hadrons. Motivated by the smallness of the explicit breaking of chiral symmetry (at least in the light-quark sector), one can instead formulate an effective theory that respects chiral symmetry in the degrees of freedom of hadrons instead of quarks. The dynamics at low energies are dominated by the lightest available hadrons (for example the pions in the $SU(2)$ flavour sector), and thus scattering amplitudes (S-matrix elements) can be expanded in powers of their momentum, as long as the latter is small compared to the expansion scale $\Lambda_\chi \sim 1\,\mathrm{GeV}$. *A priori*, the infinite set of all possible operators respecting chiral symmetry is allowed to enter the theory. By defining a suitable power counting strategy, one can arrive at a consistent, perturbative scheme with a finite set of terms at a given order. These considerations are the basis of ChPT. An important limitation of this scheme is that it cannot be used to describe resonances, as these represent singularities in the scattering amplitudes.

The application of ChPT to the $SU(3)$ flavour sector – now in the degrees of freedom of baryons and the pseudoscalar meson octet – was first accomplished by Kaplan and Nelson [88], [89]. The obtained expression for the ChPT Lagrangian is lengthy and of no significance for the following discussion, as we are only interested in the interactions of kaons and nucleons. With this restriction, the Lagrangian can be significantly simplified.

The result is an effective model describing kaons in the nuclear medium, which shall serve as the entry point of the following discussion. The manuscript will closely follow the line of argument found in Ref. [80], however in less detail. Dropping everything but the kaon and nucleon fields [2] – $K = (K^+, K^0)^\mathrm{T}$, $\bar{K} = (K^-, \bar{K}^0)$, $N = (p, n)^\mathrm{T}$ and $\bar{N} = (\bar{p}, \bar{n})$ – leads to to the Lagrangian

$$\begin{aligned}\mathcal{L}_\mathrm{eff} =& \bar{N}(i\gamma^\mu\partial_\mu - m_N)N + \partial^\mu\bar{K}\partial_\mu K - \left(m_K^2 - \frac{\Sigma_{KN}}{f_\pi^2}\bar{N}N\right)\bar{K}K \\ & - i\frac{3}{8f_\pi^2}\bar{N}\gamma^\mu N\bar{K}\partial_\mu K \quad .\end{aligned} \tag{8.12}$$

The parameters of Eq. (8.12) are the kaon and nucleon mass $m_{K,N}$, the kaon-nucleon sigma term Σ_{KN}, and the pion decay constant f_π. The quantity Σ_{KN} is the analogue to the one given in Eq. (8.11), but experimentally not as well established. It is currently believed to have a value $\Sigma_{KN} \simeq 400\,\mathrm{MeV}$ [80]. The Lagrangian (8.12) contains two terms that couple kaon and nucleon fields: a scalar interaction term, which is attractive for both K and $\bar{K}$, and a vector interaction term, which is repulsive for K and attractive for $\bar{K}$.

The Klein-Gordon equation for the kaon fields $\Phi_{K^\pm}(x)$ can be extracted from the above Lagrangian via the Euler-Lagrange equation. In order to arrive at a manageable theory, this step is performed in the *mean-field approximation*:

[2] The mass of the nucleon is already $\mathcal{O}(\Lambda_\chi)$, but at low energies the kinetic energy of the nucleon enters the dynamics, not its mass.

Factorising terms pair-wise in the field degrees of freedom and identifying $j_\mu = \langle \bar{N}\gamma_\mu N\rangle$ (nucleon current) and $\rho_\mathrm{s} = \langle \bar{N}N\rangle$ (scalar nucleon density) leads to

$$\left[\partial_\mu\partial^\mu \pm i\frac{3}{8f_\pi^2}j_\mu\partial^\mu + \left(m_K^2 - \frac{\Sigma_{KN}}{f_\pi^2}\rho_\mathrm{s}\right)\right]\Phi_{K^\pm}(x) = 0 \quad . \tag{8.13}$$

The coupling of the kaon and nucleon fields has thus been transformed into a coupling to mean nucleon densities and currents. Defining the vector potential

$$V_\mu = \frac{3}{4f_\pi^2}j_\mu \quad , \tag{8.14}$$

the above Klein-Gordon equation can be re-written introducing an *effective*, *in-medium* kaon mass m_K^*,

$$\left[(\partial_\mu \pm iV_\mu)^2 + {m_K^*}^2\right]\Phi_{K^\pm}(x) = 0 \quad , \tag{8.15}$$

where

$$m_K^* = \sqrt{m_K^2 - \frac{\Sigma_{KN}}{f_\pi^2}\rho_\mathrm{s} + V_\mu V^\mu} \quad . \tag{8.16}$$

In this picture, kaons and anti-kaons experience an equal shift of their effective mass when embedded in nuclear matter. Introducing one last effective quantity,

$$k_\mu^* = k_\mu \mp V_\mu \tag{8.17}$$

completes the quasi-particle picture. The energy-momentum relation now reads

$$E(\mathbf{k}) = \sqrt{\mathbf{k}^{*2} + {m_K^*}^2} \pm V_0 \quad . \tag{8.18}$$

Equations (8.16) - (8.18) allow the interpretation of an effective kaon-nucleon *potential* to be responsible for the shift in kaon mass and energy, and it turns out to be repulsive for kaons and attractive for anti-kaons. The density dependence of both the kaon energy and mass is shown in Fig. 8.1. This mean-field potential contains a contribution connected to the scalar nucleon density and one connected to the nucleon current. Like in the GOR relation (8.10), a link between meson masses and the chiral condensate – entering as ρ_s in the mean-field picture – has been established. Indeed, it can be shown [80] that the scaling behaviour (8.16) of the kaon mass with the scalar nuclear density ρ_s is compatible with the picture of chiral restoration, using a GOR relation for kaons.

The above predictions for the K^+-N potential are in agreement with results extracted from the scattering length measured in elastic K^+-N scattering. For the K^-, the picture is considerably more complicated, since resonances play an important role. As remarked earlier, the framework of ChPT is not applicable in such a situation, and the systematical uncertainties of theoretical predictions

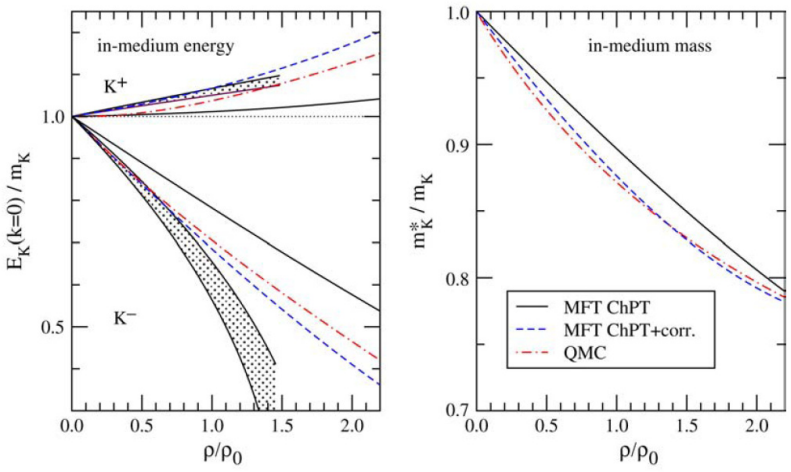

Figure 8.1: Density dependence of the energy (left) and mass (right) of kaons in (infinite) nuclear matter from theory and experiment. The black lines correspond to calculations performed in the effective ChPT model as presented in Sec. 8.2.1 ("MFT ChPT"). The coloured lines represent results obtained from more involved models. The shaded bands mark experimental data obtained from K^+-nucleon scattering and kaonic atoms (K^-). The figure was taken from Ref. [80]; additional information can be found therein.

are large. However, firm experimental data are available from the study of kaonic atoms (cf. Fig. 8.1). Since the analysis of the S339 data is restricted to K^+ and K^0, the properties of the interactions of anti-kaons and nucleons will not be discussed further in this work. The reader is referred to the literature – for example the reviews found in Refs. [80] and [81] – for a discussion of the considerations connected to anti-kaons.

8.3 Measurement: Kaon momentum spectra

In the previous section, we arrived at an effective, mean-field model for the kaon (K^+, K^0) mass and energy inside the nuclear medium. The density-dependent energy shift that kaons experience in this picture can be attributed to an effective, repulsive K-N potential. Within the assumptions of this model it follows that a kaon, produced inside the nuclear medium at $\rho > 0$, feels the relative shift of its mass-shell energy as a momentum kick [3] upon leaving the nucleus. Thus, a measurement of the momentum distribution of kaons is potentially sensitive to such in-medium modifications of the kaon energy.

The information that can be extracted from a detected kaon corresponds, however, to the integral in time and space of the entire interaction dynamics

[3] Assuming that, when interacting with the mean field, the recoil dynamics are similar to the case of classical scattering off the nucleus as a whole.

of the kaon and the nucleus. This includes the mean-field interaction as well as further re-scattering off nucleons: Outside of the mean-field picture, kaons produced in heavy nuclei will, on average, travel farther through the nuclear medium than kaons produced in lighter systems. This translates into a different probability for an additional energy transfer in elastic collisions. Consequently, in order to establish a link between experimental results and the theoretical properties of the mean-field interaction, a model is required describing the *transport* dynamics of the kaon in nuclear matter. Such models do exist and will be shortly discussed in the following section. They are mandatory for the quantitative interpretation of experimental results. Such an interpretation, however, will not be part of this work.

In Sec. 4.8, the implications of the lack of a combined detector simulation scheme in the S339 setup were discussed. Since no model of the detector acceptance and the efficiency of the combined reconstruction is available, absolute particle yields cannot be measured. This issue is reflected in the measurement presented in this chapter insofar as that the recovered kaon momentum spectra are investigated only in a relative fashion, i.e. only the *ratio* of the spectra obtained from different nuclear targets is considered. Since the acceptance of the spectrometer and the efficiency of the reconstruction are multiplicative corrections for a given cell of phase space, their effect can be assumed to cancel in such a measurement [4].

Measurements of this kind have already been performed in the past, both for proton- [90] and pion-induced reactions [82]. In this work, the measured momentum spectra for K^+ and K^0 produced in a carbon and a lead target will be compared. Even though generally occurring on the surface of the nucleus, kaon production in the C nucleus can still be expected to happen at a smaller average density compared to the Pb system. Thus, based on the previous results, one would expect to see an increased de-population in the phase-space region of small kaon momentum for the Pb system when compared to the C system. At the same time, however, elastic re-scattering off nucleons will change the picture, which will play a more important role in the Pb system. A careful study with transport models will be required for the final interpretation of the data.

8.3.1 Transport models

There are basically two different approaches to the modelling of nuclear collisions on a microscopic level: models based on solving the *Boltzmann-Uehling-Uhlenbeck* (BUU) transport equation and methods based on Quantum Molecular Dynamics (QMD). The purpose of this section is to provide a very basic

[4] This is a valid approximation as long as the compared data generally populate the same region of phase space and/or the variations of the efficiency/acceptance across the relevant area of phase space are small.

introduction of the two and motivate a future study of transport model parameters based on the results of this work. More in-depth information can, for example, be found in Refs. [91], [92], [93] and [94].

The BUU transport equation describes the time evolution of a single-particle phase-space density under the influence of a mean field parametrisation. The general idea of BUU transport models is to propagate the particles partaking in the nuclear collision by solving the transport equation using MC models and statistical ensembles of point-like test particles. The evolution explicitly models two-particle collisions under the constraint of momentum conservation. Pauli-blocking is taken into account in the sense that the evolution into the same phase-space cell is forbidden. Apart from this, particles are propagated according to classical mechanics in the assumed mean-field model.

QMD models take a different approach. Here, particles are modelled as wave packets with a finite size in phase space, and the collision partners are composed as products of these single-particle wave functions. The approach thus resembles a quantum-mechanical n-body collision, however with the important restriction that the composite wave functions are stable in time and are usually not anti-symmetrised. The interaction potential is again a model-dependent parametrisation in order to arrive at a manageable implementation, but could also be included as derived from first principles.

Transport models are a powerful tool to simulate nuclear collisions, and they are *required* to relate final-state observations to elements of the underlying theory. However, they also contain important idealisations and feature numerous parameters. Apart from the parameters of the models themselves, many physical quantities that enter the calculations are poorly known. For instance, collision probabilities and particle productions are modelled using cross sections of elementary processes, of which some are experimentally unknown and have to be modelled using theoretical predictions. In their recent review paper on strangeness production in nuclear collisions [81], Hartnack et al. state on the matter of transport models that "*[...] the results published in the literature are not always comparable among each other as they are coming from different program versions*" (p. 121). Providing additional input from experimental data is thus of great importance to further improve the predictive power of these models. In this spirit, the results to follow in the remaining sections of this work could help to confirm or improve the parametrisations of the kaon-nucleon interactions and correlated assumptions within the transport models.

8.4 Analysis I: Charged kaons

Due to the conservation of strangeness in strong interactions, strange mesons can decay only weakly after they have been produced. The mean lifetime of charged kaons is $\tau = 1.24 \cdot 10^{-8}\,\mathrm{s}$, and they can thus be considered as stable

particles on the length scale of the FOPI tracking detector coverage. As no further (vertexing) constraints can be applied during the reconstruction of K^+, their extraction from data critically depends on the performance of the PID scheme. As discussed in Chapters 5 and 7, the applicability of the combined, probabilistic PID scheme is currently limited by remaining issues in the CDC system.

The discussion shall thus first be restricted to the case $|\mathbf{p}| > 200\,\mathrm{MeV}/c$, where the full PID-relevant information of all detectors can be used to obtain a fractional likelihood according to Eq. (7.2). An alternate approach for $|\mathbf{p}| < 200\,\mathrm{MeV}/c$ will be discussed in the context of the final result in Sec. 8.4.2. Given this current restriction of the particle momentum, the track selection can also be limited to particles leaving signals in the TPC, CDC and RPC detectors. This choice ensures an optimal purity of the obtained kaon sample [5], as the RPC clearly offers the best separation between different particle species (cf. Sec. 7.5).

The spectrum of the obtained likelihood values $\mathcal{L}^K_{\pi,p}$ is shown in Fig. 8.2. The observed distribution nicely demonstrates the power of the fractional likelihood method: Combining the information from all participating detector systems, a clear separation between values against (peak at 0) and in favour of the kaon hypothesis (peak at 1) is observed, while ambiguous situations are comparably rare and evenly distributed. The suggestive shape of the distribution facilitates the choice of the final selection cut, which is set to a value of 0.8 for the following analysis.

An additional confirmation of the procedure is provided by Fig. 8.3, where the distribution of the specific energy loss of particles fulfilling the requirement $\mathcal{L}^K_{\pi,p} > 0.8$ is shown. When compared to the full spectrum (cf. Fig. 7.2), a convincing selection of the kaon band is observed. The remaining background is negligible in comparison. This result can be considered as a proof of principle of the PID method as described in Chapter 7.

From the selected particles, one directly obtains the sought-after kaon momentum distributions $n(|\mathbf{p}|)$ for both targets, from which the final ratio can be extracted. Before proceeding, however, the normalisation of the data needs to be discussed.

8.4.1 Data sample & Normalisation

In order to avoid normalisation problems with downscaled trigger settings, only events triggered by the definitions 10-13 (cf. Sec. 3.2.4) enter the analysis. Furthermore, Fig. 3.11 shows a sudden change of the trigger fractions for run numbers > 3435, coinciding with a changed setting for one of the scaled

[5] Actually, allowing *all* particle tracks to enter the analysis only marginally changes the final result, but considerably complicates the discussion of systematical effects to follow at the end of this section.

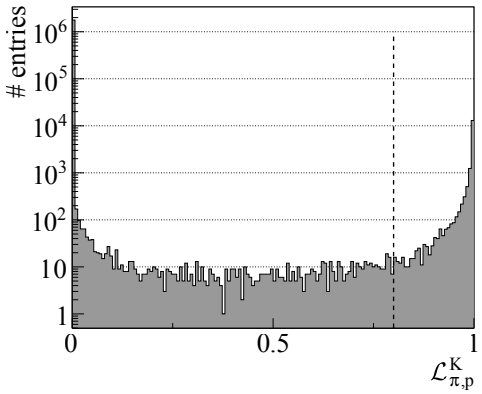

Figure 8.2: Distribution of the kaon PID likelihood according to Eq. (7.2) in the combined TPC-CDC-RPC system. The dashed line marks the selection cut used for the further analysis.

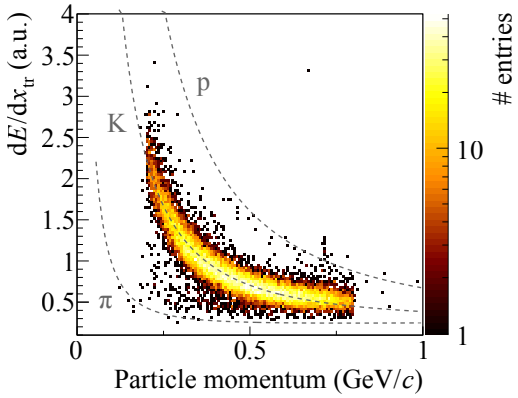

Figure 8.3: Specific-energy-loss spectrum measured by the CDC, plotted vs. the momentum for particles with positive charge. Only particles fulfilling $\mathcal{L}^{K}_{\pi,p} > 0.8$ (cf. Fig. 8.2) enter. The reader is pointed to Fig. 7.2 for a direct comparison with the full spectrum.

triggers. Currently, the motivation for this change and its effect on the absolute trigger efficiency are unknown. The data recorded after this change are thus excluded from the analysis. The resulting number of accepted events N^{tr} is $5.55 \cdot 10^6$ for the carbon target and $4.08 \cdot 10^6$ for the lead target, respectively. Apart from this global selection and the requirement of a successful match between TPC and CDC tracks (cf. Sec. 4.6), *no further cuts are applied on the data*.

The measurement observable $\mathcal{R}$ is defined as the ratio of the kaon production cross-sections σ_{K} for the lead and carbon targets:

$$\mathcal{R}(\mathrm{Pb/C}) \coloneqq \frac{\sigma_{\mathrm{K}}^{\mathrm{Pb}}}{\sigma_{\mathrm{K}}^{\mathrm{C}}} \quad . \tag{8.19}$$

Within the data set obtained for one target, the quantity σ_{K} can be expressed in terms of the total cross section for pion-induced reactions σ_{R}, i.e. the process $\pi^- A \longrightarrow X$, which is available from experiment at the relevant energies (cf. Tab. 3.3):

$$\frac{\sigma_{\mathrm{K}}}{\sigma_{\mathrm{R}}} = \frac{N_{\mathrm{K}}}{N_{\mathrm{tr}}} \quad . \tag{8.20}$$

Here, N_{K} and N_{tr} are the total number of reconstructed kaons and triggered events, respectively. Equation (8.20) contains the assumption that the spectrometer acceptance and trigger effects cancel out in the ratio. Using this

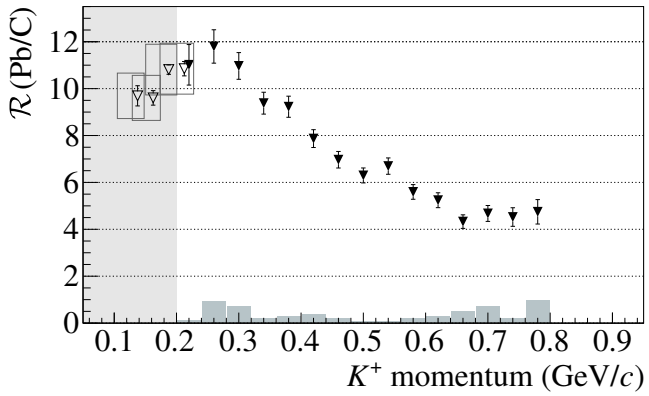

Figure 8.4: Ratio of the production cross-sections for K^+ as defined in Eq. (8.21), shown as a function of the kaon momentum. In the region above $200\,\mathrm{MeV}/c$, kaons are identified using the fractional likelihood method (full data points). The shown error bars are of statistical nature. The grey bars show the absolute changes in the final ratio when the width of the fits to the kaon peak in the RPC detector response data (cf. Fig. 7.7) is scaled up by a factor of 2. Below $|\mathbf{p}| < 200\,\mathrm{MeV}/c$, kaons are counted directly in spectra of $\mathrm{d}E/\mathrm{d}x$ measured in the CDC (see discussion in the text). The region in which this alternate approach is used is highlighted.

relation, Eq. (8.19) can be written as

$$\mathcal{R}(\mathrm{Pb/C}) = \frac{N_\mathrm{K}^\mathrm{Pb} \cdot \sigma_\mathrm{R}^\mathrm{Pb} \cdot N_\mathrm{tr}^\mathrm{C}}{N_\mathrm{K}^\mathrm{C} \cdot \sigma_\mathrm{R}^\mathrm{C} \cdot N_\mathrm{tr}^\mathrm{Pb}} \quad . \tag{8.21}$$

Calculating the ratio in bins of the kaon momentum, $N_\mathrm{K}(|\mathbf{p}|) \equiv n(|\mathbf{p}|)$, $\mathcal{R}(\mathrm{Pb/C})$ becomes sensitive to effects of the kaon-nucleon potential.

8.4.2 K^+: Result and discussion

The ratio $\mathcal{R}(\mathrm{Pb/C})$ is finally shown in Fig. 8.4. The full data points above $200\,\mathrm{MeV}/c$ momentum show the results of the analysis using the full probabilistic PID method, as discussed above and presented in Figs. 8.2 and 8.3. Below a value of $|\mathbf{p}| \sim 250\,\mathrm{MeV}/c$, a drop in the ratio is observed, which is in qualitative agreement with the expected depletion of this phase-space region for kaons produced in the heavier lead nucleus.

Unfortunately, this signature is located at the lower end of the available data range. It is thus attempted to continue the measurement towards smaller momenta, using an alternate approach: The best available information on the particle identity in this region – on the level of a single detector system – is given by the specific energy loss measured by the CDC. In order to avoid the problem of a deteriorated momentum resolution in this region (discussed in

Chapter 5), the *original* data from the standard FOPI reconstruction are used ("Eloss" and "Momentum" of `CdcTrack`s, cf. Tab. 4.1) instead. In momentum-binned spectra, the kaon peak and the neighbouring data range are fitted with a suitable model, yielding a direct counting of the observed kaons. The values for $\mathcal{R}$(Pb/C) obtained using this technique are drawn as hollow points in Fig. 8.4. The results of Chapter 5 and Sec. 6.3 have shown, however, that the native FOPI momentum and the momentum obtained from combined fits are not compatible. This fact is visualised by the associated boxes in Fig. 8.4: Using the observed differences between the two values for the momentum in the appropriate region, the systematic uncertainty along the momentum axis is composed from the i) most probable value ("offset") and ii) the RMS of the underlying distribution. Along the ordinate, the systematic uncertainty of the alternate method – given by the selection of the fit model – is approximated as 20 % of the absolute value of $\mathcal{R}$(Pb/C). One additional point at 225 MeV/c is calculated using this method in order to check the compatibility with the standard approach. The region in which the alternate method is used is highlighted in Fig. 8.4.

The systematic uncertainty above that region is dominated by the probabilistic PID scheme. Here, one has to distinguish between two contributions: i) a possible momentum-dependent efficiency of the method and ii) surviving, non-kaonic background. The first is a multiplicative effect and cancels out completely, since the PID scheme is parametrised as a function of the momentum only (cf. Chapter 7) [6]. Already from Fig. 8.3, the contribution from remaining background can be expected to be very small. In order to quantify this effect nonetheless, the calculation of $\mathcal{R}$(Pb/C) is repeated after the widths of the fits to the kaon peak in the dominant system for PID, the RPC, have been scaled up by a factor of 2. This represents a crude, but very conservative quantification of the possible impact from remaining background due to misidentified particles. The absolute differences in $\mathcal{R}$(Pb/C) w.r.t. the original calculation are visualised as grey bars in Fig. 8.3. Considering Fig. 7.7, the trends show the expected behaviour.

It has been stated in the introduction of Sec. 8.3, that unaccounted-for effects due to the acceptance of the spectrometer are assumed to cancel in a ratio measurement such as the one presented in Fig. 8.4. A quantitative approximation of the validity of this assumption can be obtained in the scope of an analogue analysis performed for K^0 (cf. Sec. 8.5.4). A further source for systematic effects are changes of the trigger efficiency or the beam intensity over time. These would, however, only propagate into the global normalisation and not into the shape of the observed ratio. Recent calculations of the cross sections from the observed trigger rates [95] limit the impact of such effects to the percent level.

[6] Likewise, potential effects due to the general efficiency of the reconstruction algorithms are assumed to cancel in the final result.

8.5 Analysis II: Neutral kaons

As in the case of K^+ presented earlier, the study of neutral kaons can be used to investigate the repulsive kaon-nucleon interaction. As an important conceptual advantage, however, there is no mixed-in contribution from the Coulomb interaction with the protons of the nucleus.

The weak interaction, responsible for the decay of the produced K^0, differentiates between two eigenstates with definite lifetimes τ: the K^0_S (*short*, $c\tau = 2.68\,\mathrm{cm}$) and the K^0_L (*long*, $c\tau = 15.34\,\mathrm{m}$). Due to this large difference in the decay length, neutral kaon decays observed inside the FOPI spectrometer can be expected to be those of the K^0_S type. The dominant decay mode is

$$K^0_S \longrightarrow \pi^+\pi^- \tag{8.22}$$

with a branching ratio of $69.20 \pm 0.05\,\%$ [28]. This is the signature channel used in this analysis. The second-widest channel is the decay into neutral pions, $K^0_S \longrightarrow \pi^0\pi^0$ (branching ratio: $30.690 \pm 0.05\,\%$ [28]), which is irrelevant for this measurement. All other decay modes, including the *CP*-violating decays into three pions, are strongly suppressed.

Before going into details, the analysis strategy shall be shortly outlined: K^0_S-decay vertices are reconstructed from assumed $\pi^+\pi^-$ pairs. The K^0_S candidates are then organised in bins of their laboratory momentum. In each bin, the recovered $\pi^+\pi^-$ invariant mass spectrum is analysed in order to distinguish the K^0_S signal from remaining background from fake K^0_S candidates. The contents of the background-subtracted signal represent a direct counting of detected K^0_S, and thus directly translate into the K^0_S momentum spectrum across the momentum bins. The spectrometer acceptance / reconstruction efficiency as well as the PID efficiency enters multiplicatively and is, once again, assumed to cancel in the ratio of the momentum distributions measured with different targets. An additional, *target-dependent* efficiency factor enters the measurement due to the different dimensions of the target in combination with a geometrical cut on the decay vertex. Section 8.5.2 will explore this effect and provide a strategy for its correction.

8.5.1 Reconstruction of K^0_S

From the available data, all possible $\pi^+\pi^-$ pairs are used for the reconstruction of K^0_S. All tracks that could at least be matched between the TPC and CDC detectors are considered. Apart from this requirement and the selection of pions discussed below, no explicit cuts are applied during the analysis.

For each pair, a vertex fit using the `GFRave` interface (cf. Sec. 4.5.4) is performed, for which the mass of the pion candidates is set to $m_\pi = 139.570\,\mathrm{MeV}/c^2$. The result is a least-squares fit of the vertex position $\mathbf{v}$ and the four-momentum p^μ of the K^0_S candidate.

For the pion identification itself, the following PID scheme is used: Above $|\mathbf{p}| = 200\,\mathrm{MeV}/c$, pions are identified using the probabilistic PID method ($\mathcal{L}^{\pi}_{K,p} > 0.4$) for all particles leaving a signal in at least the TPC and the CDC. Below this momentum threshold, all particles with a CDC $\mathrm{d}E/\mathrm{d}x < 3.0\,\mathrm{a.u.}$ are taken into account (cf. Fig. 7.2). Background due to fake K^0_S decays can be expected to be dominated by uncorrelated $\pi^+\pi^-$ pairs and mis-identified electron tracks. The former problem is independent of the identification strategy, and the latter cannot be resolved with the available PID information (cf. Chapter 7). Due to the additional constraints entailed by the reconstruction of a common vertex (and a mass), the PID selection criteria can be chosen to be less stringent than in the K^+ case.

8.5.2 Vertex constraints and target geometry

With a decay length of $c\tau = 2.68\,\mathrm{cm}$, a large fraction of the K^0_S decays occur outside of the target volume. This situation can be exploited to suppress background generated by (fake) $\pi^+\pi^-$ pairs from interactions inside the primary interaction volume, i.e. the geometrical overlap of the target disc with the beam profile, by requiring a vertex position outside of this region. Prior to the installation of the GEM-TPC inside the FOPI setup, such a cut could only be performed in the x-y plane. The suppression of background during the selection of K^0_S for the measurements presented in Ref. [82] was performed this way.

In Sec. 6.2, it was shown how the introduction of the GEM-TPC into the analysis significantly improves the vertex resolution, especially along the beam direction. With the achieved resolution of approximately 500 µm, it becomes possible to perform an anti-cut on the target disc using only the positional vertex information along this axis. This method has the advantage that it does not depend on the shape and stability of the beam profile. The construction of the target cut c_t for background rejection – using only the measured vertex positions along the z axis – is explained in Fig. 8.5, which shows a smaller range of the data already presented in Fig. 6.1.

Large values of c_t allow an efficient suppression of the background. This can be seen when comparing the invariant mass spectrum shown in Fig. 8.6, which has been obtained with a cut value $c_t = 8\,\mathrm{mm}$, with the one shown earlier in Fig. 6.2 ($c_t = 15\,\mathrm{mm}$). The corresponding phase space distributions ($c_t = 15\,\mathrm{mm}$) for both targets for the same cut value are presented in Fig. 8.7. Figure 8.7b shows signs of a de-population of the phase space at small momentum, which would be the expected signature of a larger mean-field interaction in the Pb system. It will become clear shortly, however, that the phase-space distribution has already been biased by the introduction of c_t.

Since the average decay length of the K^0_S is a function of its momentum, imposing such a geometrical selection on the set of vertices affects the momentum

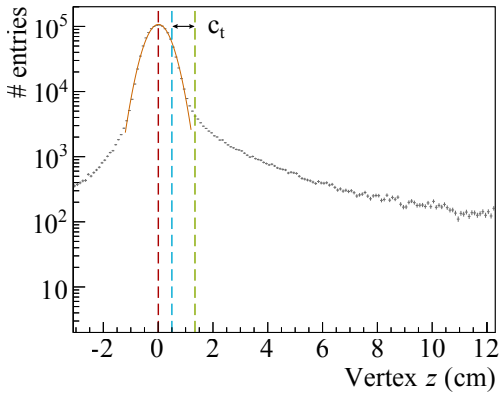

Figure 8.5: Distribution of $\pi^+\pi^-$ vertices along the beam axis for the carbon target. The target position (centre) is obtained from a Gaussian fit to the central peak region (red dashed line). Adding half the target thickness (blue dashed line), all vertices less than the cut value c_t downstream of the target surface are rejected (green dashed line). The plot shows the example of $c_t = 8\,\text{mm}$.

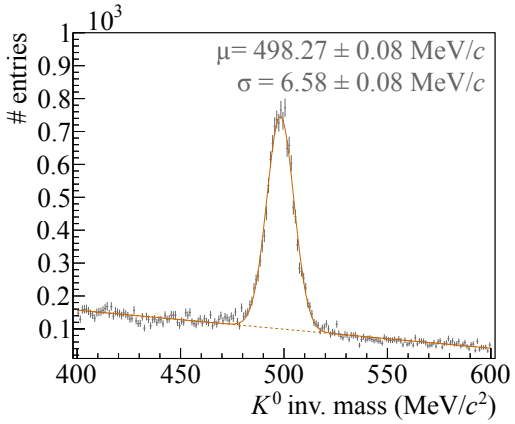

Figure 8.6: Invariant mass spectrum of K^0_S candidates for a vertex cut value of $c_t = 8\,\text{mm}$. The data are fitted with a composite model consisting of a Gaussian signal and a linear background. The fit results for the signal parameters and their statistical errors are shown in the plot. The reconstructed mass of the K^0 is in very good agreement with the current world average of $497.61 \pm 0.022\,\text{MeV}/c^2$ [28].

distribution of the accepted kaon candidates. This fact poses a direct threat to the analysis of the K^0 momentum spectrum. For a cut defined along the beam direction, this effect is further complicated by the different thicknesses of the targets that were used during the S339 experiment (cf. Tab. 3.3). The projection of the spatial distribution of the decay vertices onto the beam axis is given by the convolution of their production distribution inside the target, their decay length distribution and the distribution of the polar emission angle Θ_{lab} of the kaons.

In order to eliminate this bias, a dedicated MC model of the underlying effects has been developed. The situation described above is mimicked in the MC model by the following steps: i) The production coordinate of the K^0 along the z axis inside the target disc is randomly drawn in accordance with the corresponding pion interaction length; ii) A random momentum $|\mathbf{p}| \in [0,1]\,(\text{GeV}/c)$ is obtained from a uniform distribution; iii) The polar angle of the kaon momentum vector is uniformly randomised, $\cos(\Theta_{\text{lab}}) \in [0,1]$; iv) The decay length of the K^0_S is drawn from the appropriate distribution $\propto \exp(-\beta\gamma c\tau)$, and with that the z coordinate of the decay is obtained; v) The vertex resolution of the combined setup along the z axis is modelled by applying

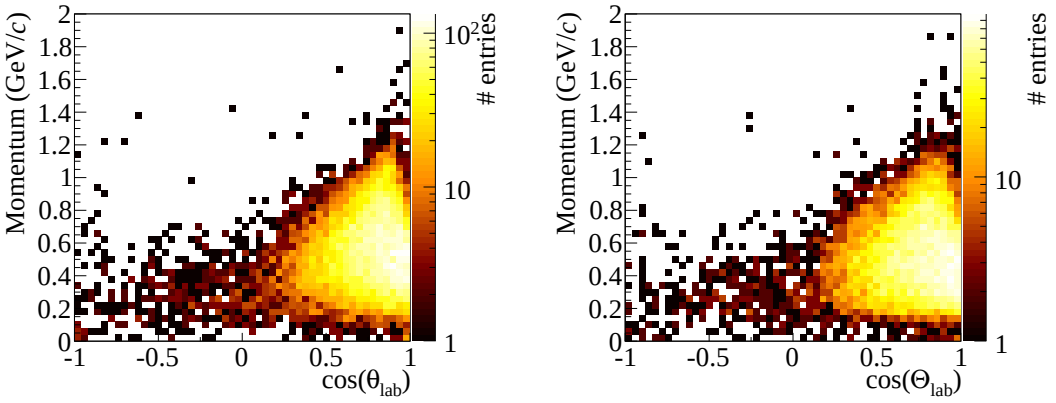

(a) (b)

Figure 8.7: Phase-space distributions of the reconstructed K^0_S candidates from the carbon (a) and lead (b) targets, obtained with a target cut $c_t = 8\,\mathrm{mm}$. Only K^0_S that fall into mass window of $\pm 20\,\mathrm{MeV}/c^2$ around the reconstructed mean mass enter the plot.

a Gaussian smearing with $\sigma_z = 580\,\mu\mathrm{m}$ (cf. Fig. 6.6). Interactions of the kaons with the target material after production are not taken into account, and the target discs are assumed to be perfectly perpendicular to the beam axis.

The purpose of this procedure – which is to be repeated for every choice of the cutoff value c_t and for each target – is to obtain a map of the theoretical reconstruction efficiency Γ in the space of the polar angle Θ_lab and the kaon momentum $|\mathbf{p}|$. The efficiency Γ gives the statistical fraction of K^0_S produced in the phase space cell ($|\mathbf{p}|$,Θ_lab) that survived the vertexing cut c_t.

The results obtained from the MC study are shown in Figs. 8.8 and 8.9. The former shows the projection of the simulated K^0_S decay vertex positions onto the beam axis as an intermediate step. The distributions are clearly different for the C and the Pb target. The second figure shows the ratio of the efficiencies Γ for both targets and for a given choice of c_t as a function the phase space. For each choice of c_t and for each target, $2 \cdot 10^8$ K^0_S have been simulated.

8.5.3 Data sample & Normalisation

As in the case of charged kaons (cf. Sec. 8.4.2), it can be argued that effects due to the reconstruction algorithms and the PID scheme present multiplicative corrections that are equal for both targets and can thus be expected to cancel in the ratio of the momentum spectra. The suppression $1/\Gamma$ has been identified as an additional effect connected to the geometrical vertex selection, and needs to be corrected for. For each momentum bin, the correction is given by the ratio of the efficiencies Γ, integrated over the polar angle in the respective

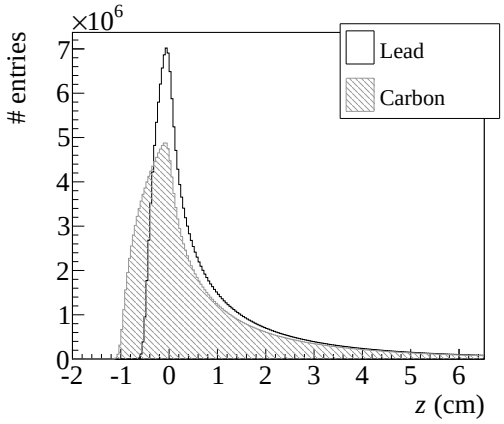

Figure 8.8: Spectrum of the z component of the K^0_S decay vertices based on a MC model of the target geometry, as described in Sec. 8.5.2. The origin of the z axis is defined to coincide with the target surface in this study, not its centre of gravity. Since the finite vertex resolution is included in the simulation, the distributions do not immediately drop to zero at the upstream end of the target disc.

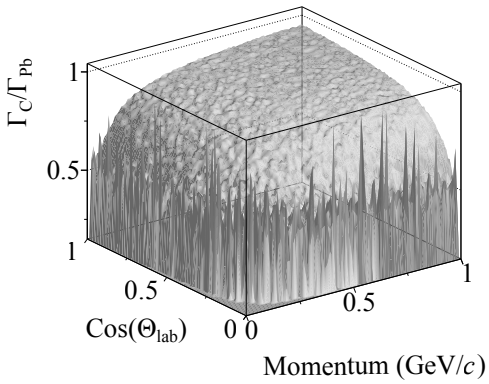

Figure 8.9: Ratio of the reconstruction efficiency Γ for the carbon and lead targets and for a vertex cut value of $c_t = 4\,\mathrm{mm}$. Due to the larger dimensions of the C target (cf. Fig. 8.8), the efficiency Γ is lower than for the Pb target. The fluctuations visible at the end of the distribution are of statistical nature, as Γ drops to zero for both targets. Since only the integral over the polar angle axis enters the final analysis, they can be ignored.

momentum range. Also here, an identical population of the phase space for both target samples is implicitly assumed.

Apart from this correction, the global normalisation of the momentum ratio is identical to the one discussed in the context of the charged kaons (cf. Sec. 8.4.1, Eq. (8.21)). The same holds true for the event sample that enters the analysis. Note that the restriction to particles penetrating the RPC is dropped and *all* tracks – if successfully matched between the CDC and TPC – are taken into account.

8.5.4 K^0: Result and discussion

The final ratio of the momentum spectra $\mathcal{R}(\mathrm{Pb/C})$ for reconstructed K^0_S is presented in Fig. 8.10. The error bars are of statistical nature, and correspond to the propagated uncertainty of the integral of the signal peak, as obtained from fits of the invariant-mass spectrum (cf. Fig. 8.6) in momentum bins. A similar structure as in the analogue result obtained for K^+ (cf. Fig. 8.4) is observed. The peak position is found at a lower value of the momentum, qualitatively compatible with the expectation: In contrast to the K^+, neutral kaons do not

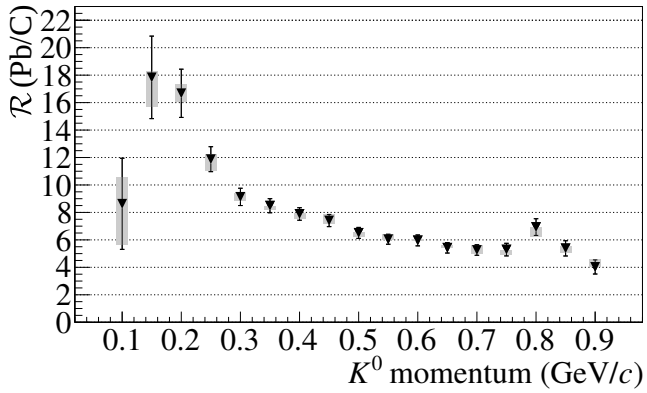

Figure 8.10: Ratio of the production cross-sections for K^0_S as defined in Eq. (8.21), shown as a function of the kaon momentum and obtained with a target cut $c_t = 4\,\text{mm}$. The error bars show the propagated statistical errors from the fits in momentum bins. The grey boxes represent the total observed variation when varying the vertex cut value c_t in steps of 1 mm in the range $c_t \in [1,7]\,\text{mm}$ (see the discussion in the text).

feel the additional push from the Coulomb potential of the nucleus.

In order to quantify the systematic uncertainty introduced by the MC model as described in Sec. 8.5.2, a comparison between results obtained with different values of c_t is performed: c_t is therefore varied in steps of 1 mm in the window $c_t \in [1,7]\,\text{mm}$, and the full range of variations observed in $\mathcal{R}$(Pb/C) is visualised by the grey boxes in Fig. 8.10. Since the choice of c_t directly affects the signal-to-background ratio in the spectra of the invariant mass, the variations also contain a contribution connected to the selection of the fit model (cf. Fig. 8.6). In addition, it has been already stated that MC model implicitly *contains* the assumption of a cancellation of acceptance effects: As c_t also directly represents a cut into the phase-space distribution of the observed K^0_S, it can thus be argued that the performed scan of the cut value is also – to some extent – sensitive to the validity of this assumption. Considering all of the above, the observed systematic effects appear small and increase the confidence in the assumptions that entered the analysis.

8.6 Summary of the analysis results

First, let us compare the two results obtained for $\mathcal{R}$(Pb/C) in Secs. 8.4 and 8.5: Both show a similar structure, compatible with the interpretation that the phase space at small momenta is depleted in the heavier system relative to the light system. This is in qualitative agreement with the considerations of Sec. 8.3.

In the direct comparison, two main differences can be observed: The ob-

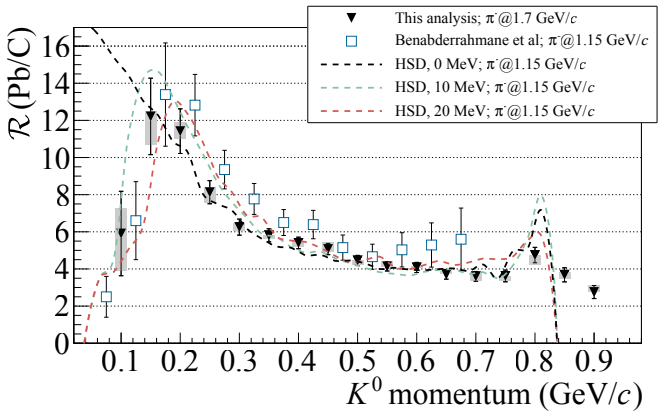

Figure 8.11: The result of Fig. 8.10 in comparison with the results from Ref. [82] and transport calculations performed at the associated beam momentum. The absolute value of $\mathcal{R}$ depends on the cross sections for kaon production at the given pion momentum. In order to allow a more direct comparison of the structural shape, the data of Fig. 8.10 have been scaled by an arbitrary factor. Only the statistical errors of the data set from Ref. [82] are drawn. The HSD calculations are discussed in the text.

served peak in the K^0 result is located at a lower momentum, as one would expect from the missing contribution of the Coulomb potential in that case. It is also more narrow than in the K^+ case. Whether this is a physical property of the result or has to be attributed to the increased uncertainty of the analysis method below $|\mathbf{p}| = 200\,\mathrm{MeV}/c$, remains an open question.

Secondly, the peak amplitude is significantly larger in the K^0 case, and also the general level of the ratio seems to be slightly elevated. An explanation for this larger excess of K^0 produced in the Pb nucleus when compared to the K^+ case might be the isospin dependence of the production cross sections (cf. Sec. 8.1.1) in correlation with the larger abundance of neutrons in the Pb system. Moreover, charge-exchange reactions in quasi-elastic scattering off nucleons of the sort

$$pK^0 \longleftrightarrow nK^+ \tag{8.23}$$

introduce a coupling between the two measurements. Since there are no experimental data available for the $\pi^- n \longrightarrow (K^0, K^+)$ cross sections, this hypothesis cannot directly be checked. The results need to be compared by means of transport calculations, incorporating the kaon re-scattering and absorption-cross sections. In that light, the two presented measurements can also be regarded as valuable input for these models. However, this evaluation is beyond the scope of this thesis.

The ratio $\mathcal{R}$(Pb/C) obtained for K^0_S can additionally be compared to earlier results, published by Benabderrahmane *et al.* (Fig. 3 of Ref. [82]). Using identical nuclear targets, these have also been obtained from data taken with

the FOPI spectrometer, however at a π^- momentum of 1.15 GeV/c. Figure 8.11 shows the direct comparison of the two collections of data. The structure of both is in very good agreement over the full momentum range. The position of the peak obtained from S339 data is slightly shifted towards smaller momenta in comparison. From a purely technical point of view, this is consistent with the fact that the momenta extracted from the TPC-combined analysis, as described in this thesis, tend to be systematically smaller than the ones obtained from the native FOPI feature extraction (see, for example, Fig. 6.9). A potential influence of the different beam momenta on the position of the peak has, yet again, to be checked in future transport calculations.

Results from former such calculations at 1.15 GeV/c π^- momentum, obtained within the Hadron-String Dynamics (HSD) model [96], are also shown in Fig. 8.11. These are also already contained in Ref. [82]. At the energies relevant for this measurement, HSD calculations are of the BUU type (cf. Sec. 8.3.1). Inside the model, kaons are propagated off-shell through the mean field of the nucleus, and the influence of the K-N potential is modelled as an effective, momentum-independent shift of the meson mass. The density dependence of the potential is described using a linear functional form, which is a good approximation recalling Fig. 8.1. Using this approximation, the values of the potential strength quoted in Fig. 8.11 correspond to the value at $\rho = \rho_0$. Within the predictions from HSD calculations, both measurements are clearly not compatible with a vanishing kaon-nucleon interaction.

In view of the different experimental setups and fundamentally different analysis techniques used for their extraction, the agreement between the results obtained by Benabderrahmane *et al.* and from S339 data in this thesis is remarkable. Having been obtained at different beam energies, the combined data set thus can be used to put further constraints on the parameters of transport models, and strengthen the understanding of kaon-nucleon interactions.

Chapter 9

Conclusion

In the first part of this work, the development of a TPC with GEM-based gas amplification and of the algorithms required for the reconstruction of its data has been documented. As proof of the detector principle, a large detector of this type has been constructed and installed in the FOPI spectrometer at GSI, where it participated in a two-weeks physics campaign (strangeness production in pion-induced reactions) in the year 2011. The obtained data have been used to i) characterise the performance of the detector and to ii) study signatures of kaon-nucleon interactions in a dedicated analysis.

The performance of the device has been found to fully meet or even exceed the expectations. With the GEM-TPC present in the FOPI setup, the tracking performance of the spectrometer could be significantly enhanced, especially along the beam direction (drift direction of the TPC): the track-to-track (vertex) resolution along this axis was improved by two orders of magnitude from $\sim 10\,\mathrm{cm}$ to below $1\,\mathrm{mm}$. As a direct consequence, the combined momentum resolution for forward tracks could be improved by $\sim 30\,\%$. The quantification of the specific energy loss ("$\mathrm{d}E/\mathrm{d}x$") performance of the GEM-TPC has received special attention, as local gain variations in multi-GEM stacks are a possible threat to the energy resolution. Making use of calibration data obtained from the reconstruction of ${}^{83m}_{36}\mathrm{Kr}$ decays, a detailed study of the $\mathrm{d}E/\mathrm{d}x$ performance has been conducted. It was found to be fully compatible with the expectations for classical, MWPC-based devices of similar size. The results of this study represent the first such measurement from collision data for a large-scale GEM-TPC, and have been published in 2014 [25].

The methods and the software employed in the physics-driven analysis of the data represent a completely new approach for FOPI. Since the GEM-TPC is the most central detector of the S339 setup, track finding is first performed stand-alone on TPC data, and the association of tracks across detector boundaries is thus anchored to the TPC. Instead of describing the identified tracks with a circle in the azimuthal plane, an adaptive, advanced variant of the Kalman Filter, the DAF, has been employed for the task of track fitting. In

doing so, the energy loss of the particles, the spatial variations of the magnetic field and a realistic model of the detector material are taken into account. Finally, a new strategy for the task of identifying particle species has been devised and implemented: In order to fully integrate the TPC into this task, a method based on a probabilistic description of the response of the different detector systems is used. In this way, the full set of information available for PID is correctly taken into account, as opposed to methods of particle selection via hard cuts in single spectra, which had been used in the past.

Using the data taken during the S339 experiment – obtained with a C and a Pb target –, K^+ and K^0 mesons are studied. The latter are reconstructed from the decay of their short-lived, weak eigenstate into two pions, $K^0_S \longrightarrow \pi^+\pi^-$. The invariant-mass spectrum of the $\pi^+\pi^-$ pairs shows a a clear signal from correctly identified K^0_S candidates. Owing to the advanced feature-extraction methods employed in the analysis and the contribution of the GEM-TPC to tracking, the absolute value and width of the measurement of the K^0 mass ($498.27 \pm 0.08\,\mathrm{MeV}/c$, width: $6.58 \pm 0.08\,\mathrm{MeV}/c$) could be improved significantly compared to the earlier results from FOPI. In the measured momentum spectra, signatures of a strangeness-related interaction with nucleons of both K^+ and K^0 could be identified. Specifically, a depletion of the low-momentum region of the phase space could be observed in the heavier nucleus, when comparing the data from the two different targets. This is in accordance with theoretical predictions from an effective, mean-field theory of this interaction, as well as with earlier experimental results obtained for K^0 with FOPI. When compared to transport calculations, the observed data are not compatible with a vanishing K-N potential.

Outlook

The excellent performance of the GEM-TPC for FOPI has raised the interest of the ALICE collaboration and sparked a new cooperation, and the decision was taken to realise the inevitable high-rate upgrade of the ALICE TPC with GEM technology. It will be exciting to see the world's largest TPC become the world's largest GEM-TPC, which will have to prevail under even more extreme experimental conditions at the LHC after its upgrade.

Concerning the analysis of the S339 data, the excellent agreement between the outcome from two different setups and two fundamentally different data reconstruction and analysis schemes, strengthens confidence in the past and present results. This is especially important in view of future contributions from the HADES experiment, which will – among other things – also investigate strangeness production in pion-induced reactions at similar energies. The combined information from past FOPI measurements, the analysis presented in this thesis and future results from HADES will help to further constrain free parameters of transport models and improve the understanding of the

kaon-nucleon interaction.

Own contributions

The author of this thesis has joined the group of Prof. Dr. Stephan Paul (E18, Physik Department, TUM) as a technical student in the year 2007, during the early phase of the GEM-TPC project and under the direct supervision of Prof. Dr. Bernhard Ketzer. The author's own contributions to the work presented in this thesis shall be once again explicitly listed. As stated before, the focus of the author's work has been lying on the development of detector simulations at first – which have not been discussed in this thesis –, and generally on software development during the later stages of the project.

Reconstruction software

Chapter 4 represents a complete overview over the current state of the feature-extraction software for the large FOPI GEM-TPC. FOPI data is embedded as external input into this scheme. The decision in favour of the comprehensive presentation of Chapter 4 was taken in view of the fact that no consistent documentation was available elsewhere. The development of the algorithms presented therein has been a collaborative effort of many, and can rarely be attributed to single persons. Whenever possible, it is mentioned in the text. The author has contributed directly to many of the described algorithms, and has been particularly involved in the development of software required for the combined feature extraction with FOPI data (e.g. track matching, extraction of $\mathrm{d}E/\mathrm{d}x$, parameter management and quality control, large-scale production). All presented evaluations of the algorithm and detector performance have been performed by the author, unless stated otherwise.

Online-monitoring and decoding for the FOPI TPC

The stand-alone software (cf. Sec. 3.4) used for online-monitoring of GEM-TPC data during operation has been designed and implemented by the author during the years 2010 and 2011. The software has been written in the C++ programming language, and consists of $\sim 28\,000$ lines of code.

Characterisation of the detector performance

With the exception of the analysis of the Kr-calibration data, all systematical studies of the performance of the GEM-TPC presented in Chapter 6 have been conducted by the author. In particular, an in-depth characterisation of the specific energy loss performance of the device has been performed (cf. Sec. 6.5) and published [25]. As a result of these studies, significant improvements of the reconstruction quality of the GEM-TPC data could be achieved. In the process, unforeseen problems with FOPI data have been revealed, some of them – unfortunately – still present at the time this thesis is written (cf. Chapter 5). These remaining issues will have to be resolved as part of the geometrical alignment procedure in the future.

Combined PID

The probabilistic scheme for PID, described in Chapter 7, has been designed and implemented by the author. It represents the first approach towards a combined treatment of PID-relevant data across different detector systems in FOPI.

Physics analysis

The extraction of kaon properties, as presented in Chapter 8, represents the author's contribution to the physics analysis of the S339 data set. Although a similar measurement has already been performed by the FOPI collaboration at a different beam energy [82], the results of Chapter 8 represent a completely independent analysis: The entire scheme for the extraction of physical properties and all required (scripting) code have been written from scratch. Only results from the TPC-combined feature extraction (cf. Chapter 4) – with the exception of the deliberate comparison made in the context of Fig. 8.4 – have been used in the process.

Publications

As part of the work underlying this thesis, two work packages have been published by the author: The first ([15], Appendix A) is based on the author's earlier work on detector simulations in the scope of the development for PANDA, specifically the simulation of space-charge accumulation in a GEM-TPC operated in a high-rate environment. During the analysis of the S339 data, the algorithms developed in that context have been used again to investigate the impact of field-cage imperfections of the FOPI GEM-TPC (the reader is referred to the short discussion of Sec. 6.1). As part of the necessary consolidation and extension of the software, the original results have been published by the author in 2013.

Secondly, the quantitative study of the $\mathrm{d}E/\mathrm{d}x$ performance of the FOPI TPC (cf. Sec. 6.5) has been published ([25], Appendix B) in 2014.

Appendix A: Journal publication on space-charge simulations

The following pages contain the author's published work on simulations of space-charge effects.

Nuclear Instruments and Methods in Physics Research A 719 (2013) 101–108

Contents lists available at SciVerse ScienceDirect

Nuclear Instruments and Methods in Physics Research A

journal homepage: www.elsevier.com/locate/nima

Simulation of space-charge effects in an ungated GEM-based TPC ☆

F.V. Böhmer *, M. Ball, S. Dørheim, C. Höppner, B. Ketzer, I. Konorov, S. Neubert, S. Paul, J. Rauch, M. Vandenbroucke

Technische Universität München, Physik Department E18, D-85748 Garching, Germany

ARTICLE INFO

Article history:
Received 18 September 2012
Received in revised form
20 March 2013
Accepted 4 April 2013
Available online 21 April 2013

Keywords:
Time Projection Chamber
Gas Electron Multiplier
Particle tracking
Ion backflow
Space charge
Drift distortions
Laser calibration

ABSTRACT

A fundamental limit to the application of Time Projection Chambers (TPCs) in high-rate experiments is the accumulation of slowly drifting ions in the active gas volume, which compromises the homogeneity of the drift field and hence the detector resolution. Conventionally, this problem is overcome by the use of ion-gating structures. This method, however, introduces large dead times and restricts trigger rates to a few hundred per second. The ion gate can be eliminated from the setup by the use of Gas Electron Multiplier (GEM) foils for gas amplification, which intrinsically suppress the backflow of ions. This makes the continuous operation of a TPC at high rates feasible.

In this work, Monte Carlo simulations of the buildup of ion space charge in a GEM-based TPC and the correction of the resulting drift distortions are discussed, based on realistic numbers for the ion backflow in a triple-GEM amplification stack. A TPC in the future $\overline{\text{P}}$ANDA experiment at FAIR serves as an example for the experimental environment. The simulations show that space charge densities up to 65 fC cm^{-3} are reached, leading to electron drift distortions of up to 10 mm. The application of a laser calibration system to correct these distortions is investigated. Based on full simulations of the detector physics and response, we show that it is possible to correct for the drift distortions and to maintain the good momentum resolution of the GEM-TPC.

1. Introduction

A Time Projection Chamber (TPC) [1] can be regarded as an almost ideal device for charged-particle tracking. A large number of 3-dimensional space points measured along a particle track (typ. 50–100) eases the task of pattern recognition in a dense environment and allows particle identification (PID) via the measurement of specific ionization. Large solid-angle coverage combined with very little material in the active part of the detector makes this device very attractive for applications in which high resolution is to be combined with small photon conversion probability and little multiple scattering. TPCs have been successfully used as large volume tracking devices in many particle physics experiments, e.g. PEP-4 [2], TOPAZ [3], DELPHI [4], ALEPH [5], NA49 [6], STAR [7], CERES [8] and ALICE [9].

In a TPC, electrons created by ionizing particles traversing the chamber are drifting over distances of the order of 1 m, before they undergo avalanche multiplication on a plane of proportional wires. The reconstruction of a track from the measured arrival point in space and time of the ionization electrons requires a precise knowledge of the drift of electrons and hence of the electric and magnetic fields in the chamber.

Electrons have drift velocities of the order of several cm μs^{-1} and are thus quickly removed from the drift volume. The drift velocity of ions, however, is three to four orders of magnitude smaller (see Table 1 for the values used for our simulations), leading to a slow buildup of space charge in the chamber. There are two principal sources of ions in a TPC:

- Gas ionization by fast charged particles traversing the drift volume: The created ions slowly drift towards the cathode end-plate of the TPC.
- Avalanche multiplication: During avalanche amplification, a large number of electron–ion pairs is created, given by the total gain G, which is typically of the order of 10^3–10^4. Without further measures, the ions created in the amplification process would move back into the drift volume and lead to significant distortions of the electric field.

The total amount of charge accumulated in the drift volume depends on the rate and momentum distribution of the incident particles, the properties of the gas, and the amount of ions from the avalanche region drifting back into the drift volume. To prevent avalanche ions from reaching the drift volume, TPCs are

☆This work has been supported by the 7th Framework Program of the EU, the German Bundesministerium für Bildung und Forschung and the DFG Cluster of Excellence "Origin and Structure of the Universe".

* Corresponding author. Tel.: +49 89 289 12592; fax: +49 89 289 12570.
E-mail address: felix.boehmer@tum.de (F.V. Böhmer).

0168-9002/$ - see front matter © 2013 Elsevier B.V. All rights reserved.
http://dx.doi.org/10.1016/j.nima.2013.04.020

Table 1
Parameters of the space charge simulation.

Event rate	2×10^7 s^{-1}
Beam momentum	$p_{\overline{p}} = 2.0$ GeV/c
Gas mixture	Ne/CO_2 (90/10)
Average energy per electron-ion pair	W_i=36.7 eV
Nominal drift field	**E**=(0,0,400 V cm^{-1})
Magnetic field	**B**=(0,0,2.0 T)
Nominal ion drift velocity	$u^+ = 1.766$ cm ms^{-1}
Electron mobility	$\mu^- = 6.828 \times 10^3$cm^2(Vs)$^{-1}$
Nominal electron drift velocity	$u^- = 2.731$ cm μ s^{-1}
Long. diffusion	229 μm cm$^{-1/2}$
Trans. diffusion	128 μm cm$^{-1/2}$
TPC dimensions (active volume)	r=(15.75,41.2) cm z=(−39.5,109.5) cm
Ion yield	$\epsilon = 4$

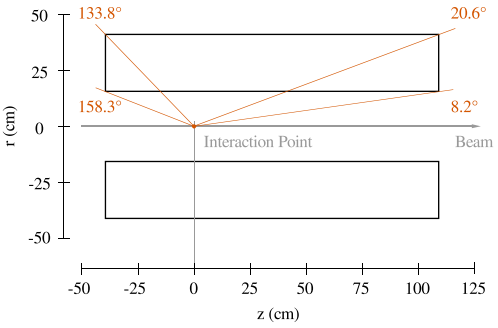

Fig. 1. Geometry and dimensions of the active part of the $\overline{\text{P}}$ANDA TPC (cross-section). In its final form, the field cage of the $\overline{\text{P}}$ANDA TPC was designed to be split into two identical and independent volumes of half-circular cross-section to make room for the target pipe which traverses the TPC vertically.

normally operated in a pulsed mode, where an electrostatic gate to the readout region is opened only when an interaction in the target has occurred, and is closed immediately thereafter [10]. The time needed to remove the ions as well as the switching time of the gate constitute dead times for the experiments, which limit the trigger rates to several hundred per second.

Modern particle physics experiments, in contrast, require high interaction and trigger rates and little or no dead time of the detector systems. In order to benefit from the advantages of a TPC in a high-rate experiment, one has to find other means of space charge suppression. As an alternative to ion gating, the usage of (GEMs) [11] for gas amplification has been proposed, since these devices feature an intrinsic suppression of the ion back-drift [12,13]. Operating a TPC at interaction rates which are large compared to the inverse drift time of electrons – which is of the order of 100 μs for typical drift distances of 1 m – means that several events will be overlapping in one drift frame. The TPC hence acts as an "analog track pipeline" with signals arriving continuously at the readout pads. Instead of an event-based, triggered readout, the appropriate readout mode of such a device is then a continuous electronic sampling of signals combined with an autonomous detection of hits, which are further processed based on their individual time stamps. The association of these hits to tracks and of tracks to distinct physics events ("event deconvolution") requires real-time tracking capabilities of the data acquisition system. The successful development of a continuously running TPC, though challenging, opens the possibility to benefit from the advantages of such a detector in future high-rate experiments.

Among other options, a GEM-based TPC was proposed as the central tracker of the $\overline{\text{P}}$ANDA (Antiproton Annihilations at Darmstadt) experiment [14] at the future international Facility for Antiproton and Ion Research (FAIR). $\overline{\text{P}}$ANDA will use an intense, cooled antiproton beam with momenta from 1.5 to 15 GeV/c impinging on different targets and will reach luminosities of up to 2×10^{32} cm^{-2} s^{-1}, resulting in a $\overline{p}p$ interaction rate up to 2×10^7 s^{-1}. The dimensions of the $\overline{\text{P}}$ANDA GEM-TPC are shown in Fig. 1. It consists of a cylindrical vessel with 150 cm length and an inner (outer) radius of 15.5 cm (41.5 cm) with GEM amplification at the upstream endcap [15], placed in a 2 T solenoidal magnetic field. Owing to the fixed-target geometry of the experiment, the interaction point is not located in the middle of cylinder axis, but shifted upstream. Detailed simulations of the TPC have shown the potential to provide excellent standalone pattern recognition and momentum resolution of the order of a few percent [16]. At typical event rates at $\overline{\text{P}}$ANDA about 4000 tracks are superimposed in the drift volume at any given time.

Track densities similar to this environment are expected for the ALICE TPC after an upgrade of the LHC, foreseen for the year 2018 [17]. At an expected luminosity for Pb–Pb collisions of 6×10^{27} cm^{-2} s^{-1}, a continuous readout of the TPC is required to make full use of the interaction rate of about 50×10^3 s^{-1}. This cannot be achieved with the present gated MWPC-based amplification system. A replacement by a triple-GEM amplification using large-size foils is currently under evaluation.

The ion leakage from a multi-GEM detector, however, is considerably larger than that from a closed gating grid, which is typically $< 10^{-4}$ [9]. It is therefore important to develop an understanding of the effects of residual space charge in a GEM-based, continuously running TPC. To this end, we have developed a computer simulation of space charge accumulation and drift distortions for such a device. The simulation is based on the following steps:

- transport particles from minimum bias physics events through the detector setup and calculate their energy loss;
- generate electron–ion pairs accordingly and propagate them through the detector including drift, diffusion, and avalanche amplification;
- model the drift of ions to obtain the spatial distribution of space charge;
- calculate the resulting electric field in the drift volume using finite element methods;
- solve the drift equation for electrons in electric and magnetic fields to get a map of drift distortions as a function of the point of generation;
- simulate a laser calibration system to measure the drift distortions.

In the present paper, the example of the $\overline{\text{P}}$ANDA TPC is used as a case study to investigate the distortions expected in a GEM-based TPC due to space charge effects. We focus on calculating the order of magnitude of distortions expected for a GEM-TPC in a high-rate environment and show that corrections are possible. We use an iterative numerical method to calculate the space charge distribution due to ionization and backdrifting ions, assuming an azimuthally symmetric problem. As such, the method is readily applicable to other TPCs with cylindrical geometry. In case the azimuthal symmetry is broken due to unexpected problems at the field cage or the amplification stage, the method can in principle be extended to three dimensions. In order to decrease computing time, also analytical solutions of the electric field due to an arbitrary charge distribution [18] could be plugged into our simulation framework. Section 2 describes the detector setup

and defines the parameters used in the simulations. In Section 3 we describe how the charge accumulation is modeled to derive a space charge distribution in the drift volume of the TPC. Section 4 details how drift distortions in the inhomogeneous drift fields are calculated. Values for expected drift distortions in the simulated $\overline{\text{P}}$ANDA environment are given. Finally, in Section 5 we demonstrate how the drift distortions can be measured and corrected by means of an array of ionizing laser beams.

2. Ion backflow in a GEM-based TPC

The Gas Electron Multiplier (GEM) [11] consists of a 50 μm thin insulating Polyimide foil with Cu-coated surfaces, typically 5 μm thick. The foil is perforated by photo-lithographic processing, forming a dense, regular pattern of (double-conical) holes. For standard GEM foils, the holes have an inner diameter of ~50 μm and a pitch of 140 μm. The small dimensions of the amplification structures lead to very large field strengths $\mathcal{O}(50\ \text{kV cm}^{-1})$ inside the holes of the GEM foil when a moderate voltage difference of typically 300–400 V is applied between the metal layers, sufficient for avalanche creation inside the GEM holes.

The dynamics of charge movement and avalanche creation inside the GEM holes are complicated. Fig. 2 shows a Garfield/Magboltz [19] simulation qualitatively explaining the suppression of ion backflow from the amplification region. Two electrons (light lines) are guided into the GEM hole by the drift field (here 250 V cm^{-1}), and produce avalanches by ionizing gas molecules (dots). The ions created in the avalanches (dark lines) closely follow the electric field lines because of their much smaller diffusion. Most of the ions are collected on the top side of the GEM foil, because the field inside the GEM hole is much higher than the field above the hole. Only a few ions drift back into the drift volume. The extraction of electrons from the hole is facilitated by a higher transfer field below the GEM (here 3.75 kV cm^{-1}). The electrons can then be transferred to another amplification stage or collected at the anode.

Typically three GEM foils are combined in a stack, leading to effective gains of the order of 10^3–10^4 and at the same time guaranteeing a stable operation without the occurrence of discharges [20]. The effective gain G_{eff} of the gas amplification system is given by the average number of electrons arriving at the readout anode N_{A}^- divided by the number of ionization electrons N_{I}^-:

$$G_{\text{eff}} = \frac{N_{\text{A}}^-}{N_{\text{I}}^-}. \tag{1}$$

Gas ionization produces an equal amount of electrons and ions, hence $N_{\text{I}}^- = N_{\text{I}}^+ \equiv N_{\text{I}}$. The effective gain G_{eff} differs from the intrinsic gas gain of the amplification stage, as it already includes losses due to limited electron collection or extraction efficiencies of the foils. These, as well as gain fluctuations, have not been explicitly simulated in the present work.

We define the ion backflow as[1]

$$IB = \frac{N_{\text{C}}^+}{N_{\text{A}}^-} \tag{2}$$

where N_{C}^+ denotes the number of positive ions arriving at the drift cathode. Note that this quantity also includes a contribution from ions created during the ionization process. Ion backflow values of $IB = 0.25\%$ have been reached experimentally in a magnetic field of 4 T in an Ar/CH_4/CO_2 (93/5/2) mixture [21].

A very convenient parameter to describe the ion backflow in the simulation is the ratio ϵ of the number of ions drifting back from the GEM amplification stage N_{G}^+ and the number of ionization electrons N_{I}, i.e. the ion yield in the amplification region per incoming electron:

$$\epsilon = \frac{N_{\text{G}}^+}{N_{\text{I}}} \tag{3}$$

Since the number of ions arriving at the drift cathode is given by the sum of ions from ionization and the ones from the amplification stage,

$$N_{\text{C}}^+ = N_{\text{I}} + N_{\text{G}}^+, \tag{4}$$

the two quantities ϵ and IB are linked by

$$IB = \frac{N_{\text{I}} + \epsilon N_{\text{I}}}{G_{\text{eff}} N_{\text{I}}} = \frac{1+\epsilon}{G_{\text{eff}}}. \tag{5}$$

The suppression factor η defines the efficiency of ion-backflow suppression in the GEM stack:

$$\eta = \frac{N_{\text{G}}^+}{N_{\text{A}}^-} = \frac{\epsilon N_{\text{I}}}{N_{\text{I}} G_{\text{eff}}} = \frac{\epsilon}{G_{\text{eff}}} \tag{6}$$

and thus

$$\epsilon = \eta G_{\text{eff}}. \tag{7}$$

As a rule of thumb, a suppression factor of $\eta \sim 1/G_{\text{eff}}$ is usually considered necessary in order to operate a TPC without gating grid.

The detector gas is a crucial parameter for the performance of a TPC [22]. In order to minimize multiple scattering and photon conversion, as well as space charge effects, a popular choice is a Ne/CO_2 (90/10) gas mixture [6,9], which combines low diffusion even at moderate magnetic fields, low ionization density, large ion mobility and high radiation length. The results presented in this paper are based on realistic values for the ion backflow of $IB = 0.25\%$ and the effective gain of $G_{\text{eff}} = 2000$, yielding $\epsilon = 4$ according to Eq. (5), i.e. four ions drifting back from the amplification stage per incoming electron. The full set of simulation parameters used for the presented results is summarized in Table 1.

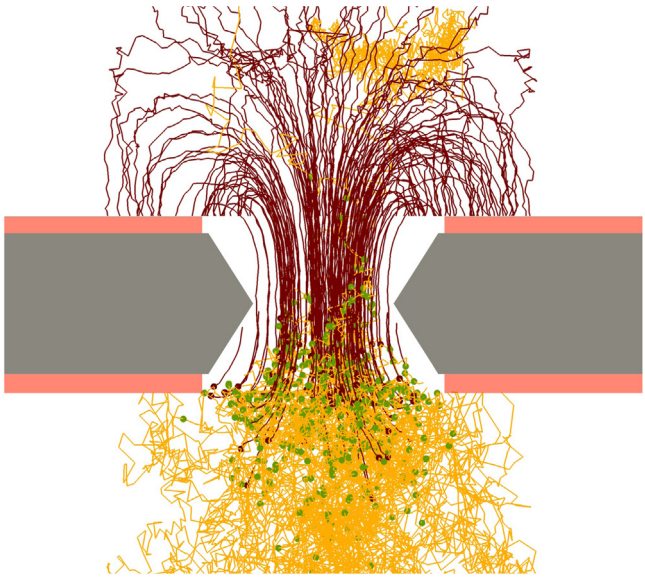

Fig. 2. Garfield/Magboltz simulation of charge dynamics of two arriving electrons in a GEM hole. Electron paths are shown as light lines, ion paths as dark lines. Spots mark places where ionization processes have occurred. The paths have been projected onto the cross-section plane.

[1] There appear different definitions of the term *ion backflow* in the literature. We choose this definition since it can be easily measured via the ratio of cathode to anode current.

3. Simulation of space charge buildup

3.1. Ionization charge creation

To model the spatial distribution of ionization charge in the TPC for the case of $\overline{\mathrm{P}}$ANDA, the Dual Parton Model (DPM) [23] Monte Carlo event generator is used to simulate antiproton–proton ($\bar{p}p$) annihilations at an incident $\bar{p}$ momentum of 2 GeV/c. The resulting phase space distribution of charged particles is shown in Fig. 3.

A large sample of these generated events is then passed through a GEANT [24] simulation of the detector geometry in order to calculate the energy loss of the particles in the TPC gas volume. For the simulations presented here we used GEANT3 with a simplified energy loss model as proposed in the ALICE TPC Technical Design Report [25] and experimentally verified in [26]. From the GEANT energy deposit $\Delta E(r,z,\phi)$ in a volume element dV around a point (r,z,ϕ) inside the TPC, summed up for a given number of simulated events N_{ev}, the number of ionization electrons/ions $N_{\mathrm{I}}(r,z,\phi)$ produced in this volume element is calculated using an average energy per electron–ion pair for the Ne/CO_2 (90/10) gas mixture of $W_{\mathrm{I}}=36.7$ eV [27,28]. Here, r, z and ϕ denote cylindrical coordinates, where the z-axis coincides with the symmetry axis of the TPC. The creation rate of ionization charge in dV is then

$$\dot{N}_{\mathrm{I}}(r,z,\phi,t)=\frac{\Delta E(r,z,\phi,t)/W_{\mathrm{I}}}{N_{\mathrm{ev}}}\cdot R(t) \tag{8}$$

with $R(t)$ being the event rate.

3.2. Model of space charge accumulation

In general, the charge density $\rho(r,z,\phi,t)$ at time t in a volume element dV centered around a point (r,z,ϕ) inside the TPC volume is given by

$$\rho(r,z,\phi,t)=\frac{e}{\mathrm{d}V}\cdot\int_0^t \dot{N}(r,z,\phi,t')\,\mathrm{d}t'. \tag{9}$$

Here $\dot{N}(r,z,\phi,t')$ is the net rate of ions entering/leaving the volume element dV in the time interval $[t',t'+\mathrm{d}t']$. $\dot{N}(r,z,\phi,t')$ includes both ions directly created in gas ionization processes, $\dot{N}_{\mathrm{I}}(r,z,\phi,t)$, as well as ions moving through the volume surface by drift and diffusion.

Solving Eq. (9) in principle requires perfect knowledge of the dynamics of charge creation and drift/diffusion inside the TPC volume. In order to arrive at a manageable, yet sufficiently realistic simulation model, the following assumptions are made:

1. Azimuthal symmetry: owing to the cylindrical geometry of the TPC, we treat the problem in azimuthal symmetry so that the resulting charge density map can be represented in the r–z-plane. For the special case of the $\overline{\mathrm{P}}$ANDA TPC, edge effects due to the splitting in two half cylinders are expected to be noticeable only within a distance of a few mm from the edges of the field cage and have thus been neglected.[2] Non-azimuthally symmetric field cages were also employed for the NA49 TPCs, where no distortions have been seen beyond the accuracy of the measurement of 50 μm, even in the immediate vicinity of the field cage [29].
2. Constant luminosity: we assume that $R(t)=\text{const.}$, i.e. the rate of charge created in gas ionization processes is constant on time scales of interest to us [$\mathcal{O}(10\,\mu\mathrm{s})$]: $\dot{N}_{\mathrm{I}}(r,z,t)=\dot{N}_{\mathrm{I}}(r,z)$.
3. Electrostatic forces between the ions are neglected: the ion drift proceeds along straight lines with constant velocity u^+.
4. The effect of diffusion on the motion of ions is neglected.

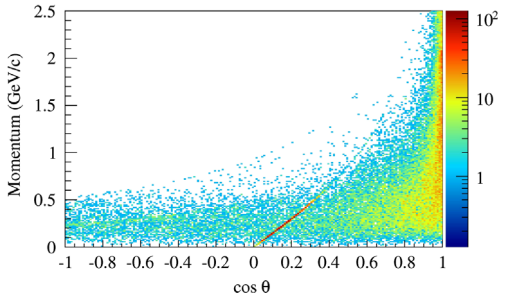

Fig. 3. Phase space distribution of primary particles in the laboratory frame produced with the DPM generator for $\bar{p}p$ collisions at 2.0 GeV/c beam momentum. The plot shows the absolute momentum versus the cosine of the polar angle of 10 000 produced events. The sharp band of recoil protons from elastic scattering processes dominates the bulk of charged pions and kaons that are created in annihilation reactions and inelastic scattering.

In addition, we move from the infinitesimal volume elements dV of Eq. (9) to macroscopic volumes $\Delta V(r_i,z_j)\equiv\Delta V^{ij}$ with constant bin widths $\Delta z=1.0$ cm and $\Delta r=0.98$ cm. Each such bin (i,j) then represents a ring-shaped volume in the TPC:

$$\Delta V^{ij}=\pi\cdot(r^2_{i,\mathrm{out}}-r^2_{i,\mathrm{in}})\cdot\Delta z_j, \tag{10}$$

where $r_{i,\mathrm{out}}=r_i+\frac{1}{2}\Delta r$ and $r_{i,\mathrm{in}}=r_i-\frac{1}{2}\Delta r$ are the outer and inner radius of bin (i,j), respectively. The integral in Eq. (9) can then be solved numerically by a discrete sum:

$$\rho(r,z,t)=\frac{e}{\Delta V^{ij}}\cdot\sum_{k=1}^{n}\dot{N}^{ijk}\,\Delta t\equiv\frac{e}{\Delta V^{ij}}\cdot N^{ijn} \tag{11}$$

with the time t given by the number of steps in time bins $t=n\cdot\Delta t$.

During each time step Δt, the ionization charge $\dot{N}^{ij}_{\mathrm{I}}\Delta t$ is newly created in bin (i,j) of the chamber. Now the backflow of ions from the amplification stage has to be included. As can be seen from Table 1, the drift velocity of electrons exceeds that of ions by several orders of magnitude. In order to calculate the ion space charge we can therefore assume instantaneous electron drift. As a consequence, a contribution proportional to the total amount of newly added gas ionization charge in the full TPC volume has to be added to the first bin in z ($j=1$) for each time bin Δt. The total number of ions added in each time step is therefore

$$N^{ij}_{\mathrm{I}}=\dot{N}^{ij}_{\mathrm{I}}\Delta t+\delta_{1,j}\epsilon\sum_{j'}\dot{N}^{ij'}_{\mathrm{I}}\,\Delta t \tag{12}$$

with $\delta_{i,j}$ being the Kronecker delta symbol.

As a last ingredient, the drift of ions has to be taken into account. For the geometry of the $\overline{\mathrm{P}}$ANDA TPC, where the readout anode is located at the upstream endcap of the chamber, the ion drift proceeds along the positive z direction towards the cathode endcap. We choose Δt to correspond to the time needed for an ion of drift velocity u^+ to travel the distance Δz. This allows us to include the ion drift in a time bin Δt simply by shifting the total charge by one bin in z. We therefore arrive at a recursive algorithm to calculate the space charge in the nth time step:

$$N^{ijn}=N^{ij}_{\mathrm{I}}+N^{i,j-1,n-1}. \tag{13}$$

From the equations above it is clear that an equilibrium space charge in time, $N^{ijn}=N^{ij,n-1}$, will be reached everywhere in the chamber as soon as the perturbation due to ion backflow reaches the cathode, i.e. for $t=z_{\mathrm{max}}/u^+$, where z_{max} is the maximum drift distance. Fig. 4 shows the space charge distributions calculated with this method after the first step in time (i.e. immediately after switching on the beam) and after reaching equilibrium. The input parameters to the simulation are given in Table 1. After the first

[2] It should also be mentioned here that the assumption of azimuthal symmetry breaks down in case one sector of a GEM stops to work. In such an extreme case the simulation would have to be done e.g. in slices of ϕ.

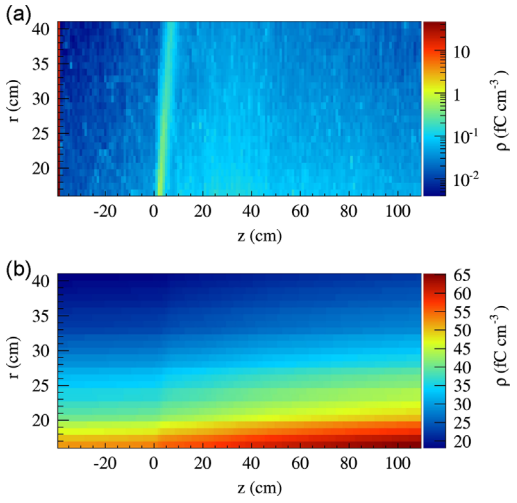

Fig. 4. Space charge density $\rho(z,r)$ in the $\overline{\text{P}}$ANDA TPC for 2×10^7 s^{-1} $\overline{p}p$ annihilations at beam momentum $p_{\overline{p}}=2.0$ GeV/c with ion yield $\epsilon=4$, using the recursive algorithm of Eq. (13). (a) After one step the distribution of ion charge from gas ionization processes is visible superimposed with the corresponding charge back-drifting from the amplification stage ("disk" of high charge density at $z=-40$ cm). The band of high primary ionization density at z~0 is caused by slow protons from hadronic elastic $\overline{p}p$−scattering. (b) Final equilibrium space charge density.

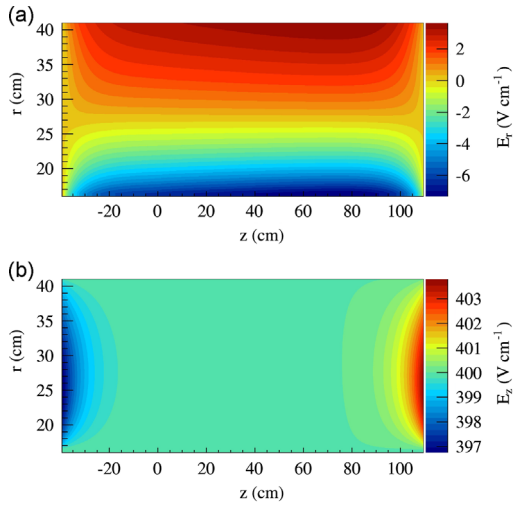

Fig. 5. Electric field caused by accumulated space charge in the $\overline{\text{P}}$ANDA TPC for 2×10^7 s^{-1} $\overline{p}p$ annihilations at beam momentum $p_{\overline{p}}=2.0$ GeV/c with ion yield $\epsilon=4$. (a) Radial component E_r, and (b) component along drift direction E_z superimposed with the nominal drift field $E_\text{d}=400$ V cm^{-1}.

step, Fig. 4a, the distribution of ions from direct gas ionization by charged particles from $\overline{p}p$ annihilations with a band at a polar angle close to 90° from elastic $\overline{p}p$−scattering is visible, together with the sheet of charge at $z\approx-40$ cm starting to drift back from the amplification region for this time bin. Due to the fixed target geometry of $\overline{\text{P}}$ANDA and the resulting forward boost of the scattered particles, the charge distribution is not symmetric in z around the interaction point. Fig. 4b shows the equilibrium space charge distribution which is reached after ions from the amplification stage have reached the cathode. The final space charge density varies between 20 and 65 fC cm^{-3}.

4. Drift distortions

4.1. Electric field due to space charge

From the charge-density distribution the electrostatic potential φ is computed by numerically solving Poisson's equation using the Finite Element Method [30] and assuming azimuthal symmetry. The software package Dolfin/FeniCs [31] is used to realize the finite element solver.

By calculating the gradient of the resulting potential we finally obtain the electric field **E** caused by the space charge. Due to the assumed ϕ−symmetry, the non-vanishing components of **E** are the r and z components. The drift field $E_\text{d}=400$ V cm^{-1} is oriented along the z direction and is superimposed onto the distortion field (see Fig. 5).

4.2. Electron drift offsets

To compute a map of the drift distortions as a function of the starting point of the drift, the equation of motion for electrons drifting in electric and magnetic fields (**E**, **B**):

$$m\frac{\mathrm{d}\mathbf{u}^-}{\mathrm{d}t}=e\mathbf{E}+e[\mathbf{u}^-\times\mathbf{B}]-K\mathbf{u}^- \tag{14}$$

is solved with a fourth order Runge–Kutta (RK) algorithm.[3] In Eq. (14) m is the electron mass, $\mathbf{u}^-$ is the macroscopic electron drift velocity, e is the electron charge and $K=e/\mu^-$ is a friction term modeling the microscopic stop-and-go motion of the drifting electron due to collisions with the gas components. The algorithm gives the electron drift velocity direction and magnitude for each point in space. The electric field **E** is the result of the steps described in Section 4.1 and shown in Fig. 5. Its variations are within 1% of the nominal field, justifying the assumption of a constant mobility μ^- and hence a constant friction term.[4] The magnetic field is chosen to be completely homogeneous (c.f. Table 1), matching our general assumption of azimuthal symmetry. Of course, a more realistic field map can be plugged into the algorithm.

The fact that the distorted drift field **E** has a non-zero component perpendicular to z leads to a displacement of drifting electrons compared to the ideal drift with constant velocity along z. Fig. 6 shows the radial and azimuthal components of this deviation at the readout plane as a function of the coordinates of the starting point of the drifting electron. It should be noted that although both **E** and **B** are assumed to exhibit cylindrical symmetry, there are nevertheless drift distortions perpendicular to the r–z-plane. This is due to the $\mathbf{E}\times\mathbf{B}$ term in the solution to Eq. (14). Distortions up to 0.8 cm in radial direction and 1 cm in azimuthal direction are observed for electrons originating from the region with highest track density in the forward region.

Similarly, the resulting distortions along the *nominal* drift direction (z) can be obtained from the difference in total travel time of the electrons (as calculated by the RK algorithm) in the distorted field configuration when compared to the ideal drift scenario. They are found to be one order of magnitude smaller than the displacements in the r–ϕ-plane and are shown in Fig. 7.

5. Measurement and correction of drift distortions

In order to correct track data for space charge effects, the resulting drift distortions have to be measured during the operation of the TPC. This can be achieved by creating a well defined pattern of electron sources in the TPC and analyze its image as

[3] When reading field values from maps with finite bin size, linear interpolation in between bin centers is applied.

[4] In the vicinity of ±5 V cm^{-1} of the nominal drift field, the **E**-dependent drift velocity recovered from the RK solution with constant friction term differs by less than 1‰ from the corresponding values obtained from Garfield/Magboltz [19].

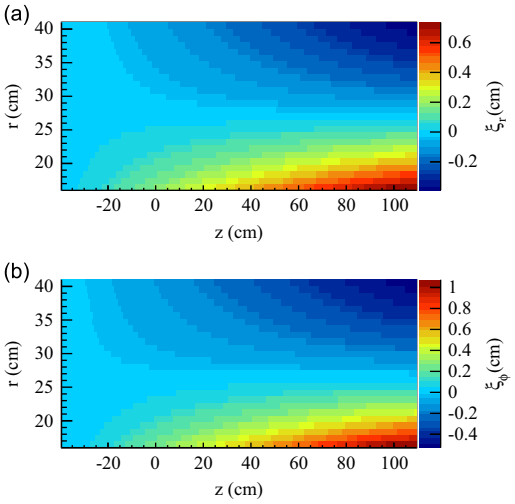

Fig. 6. Drift distortions ξ of electrons as obtained from Eq. (14) using the distorted **E**-field configuration (a) in radial and (b) in azimuthal direction. The graphs show the deviations from a straight line drift experienced by an electron which starts its drift at points (r,z) in the TPC.

measured by the detector. A comparison with the expected image directly yields the distortions. Straight line ionization tracks from UV lasers can provide such a pattern [32] and have already been used for calibration in other drift chambers (e.g. in STAR [33]). To assess the potential of this method in the case of an ungated TPC, we have simulated such a laser system.

5.1. Laser calibration system simulation

Having found the drift distortions in z direction to be small, we want to measure the distortions in the r–ϕ-plane as precisely as possible. Ideally, this can be done with laser tracks parallel to the drift direction/detector symmetry axis. We chose a grid of 6 laser beams aligned equidistantly in radial direction, where the innermost (outermost) laser is placed 0.5 cm away from the inner (outer) field cage wall. One such row of lasers is created every 20° in azimuthal direction. The laser beams are parameterized as straight line tracks with an average ionization density of 45 e^- cm^{-1} [33], and a Gaussian beam profile ($\sigma = 300$ μm).

In the simulation routines, the electrons created by the laser rays are then drifted to the readout anode, applying the calculated distortion map and taking into account the diffusion. The induced signals are calculated using GEM amplification and signal induction with a realistic response of hexagonal readout pads with an outer radius of 1.5 mm as designed for the $\overline{\text{P}}$ANDA TPC. In a last step, signals adjacent in space and time are combined to hits by a fully 3-dimensional clustering algorithm. A sample of such hit data as written out by the simulation framework is shown in Fig. 8.

5.2. Reconstruction of drift distortions

The reconstruction of the laser tracks is greatly simplified by the knowledge of the geometry (and the time, at which the laser grid has been illuminated): The hits are assigned to tracks by applying simple residual cuts, such that all hits inside a tube of reasonable radius (15 mm for the results presented) around the nominal track position are associated to the corresponding laser track. It is assured that each reconstructed hit is assigned to only one (the closest) track. For each hit, a residual vector is obtained in the plane perpendicular to the corresponding track.

In order to map out drift distortions as a function of the point of electron creation in the drift volume, the large amount of signal data from the laser calibration needs to be fitted, smoothed and

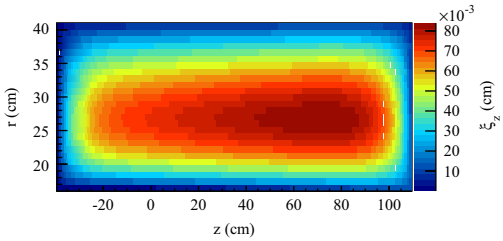

Fig. 7. Drift distortions ξ of electrons in nominal drift direction z. The values are extracted by multiplying the total travel time as obtained from solving Eq. (14) with the nominal drift velocity (c.f. Table 1) and subtracting the values for ideal drift. The zone of small deviations for large z can be understood in terms of compensating effects of the distortion field near cathode and anode (c.f. Fig. 5b).

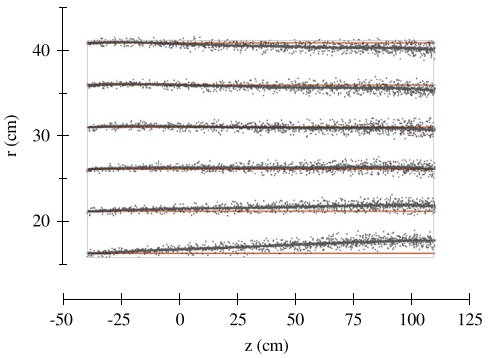

Fig. 8. Positions of TPC hits (after running of the clustering algorithm) from a laser event. The laser tracks are sketched as lines along the drift direction in the TPC. For better visibility, distortions have been scaled by a factor of 2 for this image. Note that only the *radial* component of the distortions can be seen in this projection.

parameterized. For this purpose we have implemented an algorithm for fitting of a bi-cubic spline surface $s(z,r)$ [34] to the measured residual data (c.f. Fig. 8). A two-dimensional mesh of $h \times k$ knots (λ_i, μ_j) over the data area (z,r) is chosen.[5] At each of these knots two cubic B-splines $M_i(z)$, $N_j(r)$ are attached, each of which has a fixed shape and spans over five mesh knots $\lambda_{i-4,\ldots,i}$ $(\mu_{j-4,\ldots,j})$. Coefficients γ_{ij} at every knot scale the B-splines:

$$s(z,r) = \sum_{i=1}^{h+4} \sum_{j=1}^{k+4} \gamma_{ij} M_i(z) N_j(r). \tag{15}$$

Assuming the underlying noise (mainly given by diffusion during drift) to be Gaussian, the surface fitting problem is equivalent to finding the set of coefficients γ_{ij} which minimize the sum of squared distances

$$S = \sum_{r=1}^{n_r} [s(z_r, r_r) - f_r]^2 \equiv \sum_{r=1}^{n_r} R_r^2 \tag{16}$$

to the residual data $f_r(z_r, r_r)$ (where $r = 1 \ldots n_r$). The corresponding matrix-equation ("normal equation") reads

$$\mathbf{A}^T \mathbf{A}\, \boldsymbol{\gamma} = \mathbf{A}^T \mathbf{f} \tag{17}$$

where $\mathbf{A}$ is an $n_r \times (h+4)(k+4)$−dimensional matrix containing the spline information, $\boldsymbol{\gamma}$ is the vector of knot coefficients with $(h+4)(k+4)$ elements and $\mathbf{f}$ is the vector containing the n_r measured residuals. Weighting of hits can be incorporated by introducing a weight matrix $\mathbf{W}$. Under the assumption of independent hit errors, $\mathbf{W}$ becomes diagonal, and instead of Eq. (16) one now has to

[5] In addition 4 knots on each side outside the data area are required to define the full set of B-splines.

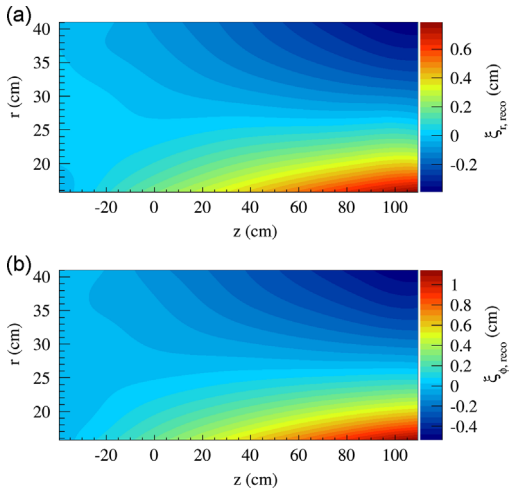

Fig. 9. Reconstructed drift distortions ξ in (a) radial direction and (b) azimuthal direction, based on one laser event (compared to Figs. 6a and b).

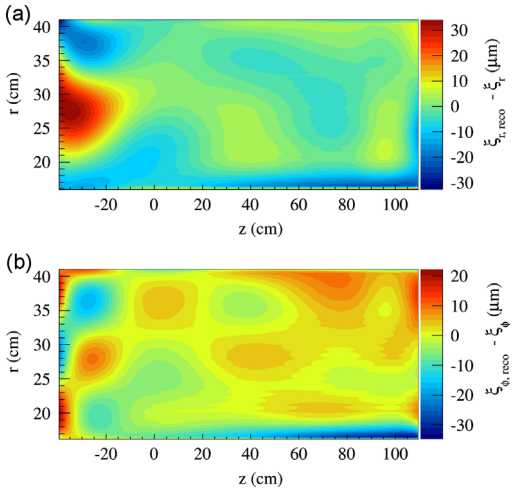

Fig. 10. Direct comparison of drift distortions as reconstructed with the Laser grid (spline fit) and original simulation input. Shown are the differences of the original (binned) deviation map and the fit evaluated at the bin center for the (a) radial and (b) azimuthal drift distortions. The underlying spline mesh structure is clearly visible.

minimize

$$S_{\mathrm{w}} = \sum_{r=1}^{n_r} \mathrm{W}_{rr} R_r^2. \tag{18}$$

Eq. (17) then reads

$$\mathbf{A}'^{T}\mathbf{A}'\,\boldsymbol{\gamma} = \mathbf{A}'^{T}\mathbf{f}', \tag{19}$$

where $\mathbf{A}' = \mathbf{wA}$, $\mathbf{f}' = \mathbf{wf}$, and $\mathrm{w}_{rr} = \sqrt{\mathrm{W}_{rr}}$. The weights for each hit are obtained from the covariance ellipsoid available after clustering, taking into account the orientation of the laser track. By setting the error to be large along the track direction, it is possible to work also with laser grids that are not optimized to the distortions topology.

The solution to Eq. (19) can be obtained by matrix inversion or, more stably, by QR-decomposition. Fig. 9 shows the least squares spline solution to the *reconstructed* residual data for both radial and azimuthal drift distortions. One laser event as described in Section 5.1 is used, resulting in ~35 000 reconstructed residuals. Typical fit times are of the order of 1 s on a single CPU desktop PC.

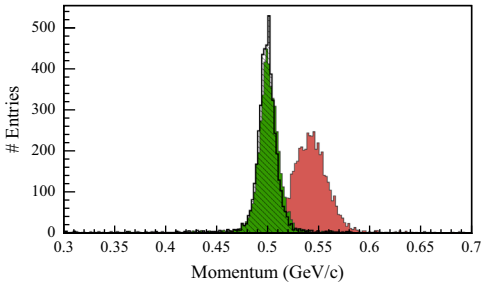

Fig. 11. Effect of drift distortions (and their correction) for π^+−tracks at 0.5 GeV/c momentum (primary and secondary GEANT tracks). Right peak: Uncorrected case. Left peak: Hit positions corrected with spline fit results. Shaded distribution: Simulation with no drift distortions present.

5.3. Quality of reconstructed distortion map

To be able to judge the quality of the result shown in Fig. 9, we compare the reconstructed distortion maps to our original drift distortion input (Fig. 6) in Fig. 10, which shows the distribution of differences between the reconstructed and the calculated distortion maps.

The choice of the number of spline-mesh knots $h \times k$ over the data area is very important for the procedure. On the one hand, a higher number of knots means higher overall fit precision, but performance suffers and also overfitting becomes an issue. A lower number of knots, on the other hand, results in a smoother result, but the fit might not be able to follow all the features of the data set sufficiently well. To a small extent, this cannot be avoided for a reasonable choice for the number of mesh knots. In general, we found $(h \times k) = 5 \times 3$ knots to be a balanced compromise.

In Fig. 10 the effect is indeed visible for a fit obtained with this number of mesh knots. However, the fit reproduces the original map with an accuracy better than 35 μm over the full r–z-plane, which is one order of magnitude below the expected single-hit resolution of the PANDA TPC. Hence, using a grid of laser beams, drift distortions in the TPC can be measured with a precision better than $\mathcal{O}(100\,\mu\mathrm{m})$, not taking into account the mechanical distortions of the calibration system.

5.4. Effect on track reconstruction

The most important question to be answered is of course the impact of space charge effects on track reconstruction. As explained in the previous sections, the steps required to obtain a model of space charge and study its possible effects and their correction are:

1. calculate space charge based on background events;
2. calculate the drift distortion map;
3. create one “laser event” consisting of the full laser beam mesh;
4. reconstruct the laser tracks and fit the data with a spline;
5. use this spline to correct for drift distortions.

In the running experiment, measurements of drift distortions have to be constantly updated, requiring steps 4 and 5 to be triggered on a timescale short enough to be able to resolve possible space charge fluctuations.

To study the effect of drift distortions on charged particle tracks, we simulated a test sample of 5000 pion tracks (π^+) at a momentum of 0.5 GeV/c, uniformly distributed scattering angle ($20^\circ \le \theta \le 133^\circ$, c.f. Fig. 1) and azimuthal angle ($0^\circ \le \phi \le 360^\circ$) in the PANDA TPC. Tracks are reconstructed using a Kalman-filter-based track fitting framework [35]. Fig. 11 visualizes the impact of uncorrected drift distortions on the momentum measurement compared to the ideal situation of a completely homogeneous

electrical field. Without correction, the distribution of reconstructed momenta is deformed and systematically shifted towards larger values by space charge effects. This can be understood within the scope of the preceding sections: Depending on its polar angle, a track is more or less affected by drift distortions (c.f. Fig. 6), leading to the broadening of the distribution. The asymmetric nature of the drift distortions with respect to the radial coordinate causes the measured curvature of the track to appear smaller than it actually was, leading to the shift to higher momenta.

Applying the correction derived from the laser system recovers the momentum reconstruction, with a resolution of $\sigma_p/p = 1.88\%$. For comparison, the distribution of reconstructed momenta for the ideal case without any space charge effects yielding a resolution of $\sigma_p/p = 1.65\%$ is shown as an outline in Fig. 11. The reconstructed mean changes from 5.01×10^{-1} GeV/c in the ideal case to 4.99×10^{-1} GeV/c.

It is important to point out that the drift distortions along the nominal drift direction as shown in Fig. 7 are fully present in the simulation, but — unlike the distortions in the r–ϕ-plane — they are *not corrected*. The fact that the momentum spectrum can be recovered with satisfying accuracy proves that the z-component of the drift distortions can be indeed neglected during correction.

6. Conclusions and outlook

In this paper we have presented detailed studies on space-charge buildup in a continuously operating GEM-TPC without a gating grid exposed to high interaction rates. We have presented a recursive algorithm to calculate the space charge accumulating in the drift region, starting from minimum bias physics events, and taking into account the primary ionization as well as the ions drifting back from the amplification region. The calculations are performed assuming azimuthal symmetry of the problem, i.e. for the case of a cylindrical detector. Assuming constant luminosity, an equilibrium space-charge distribution is reached after one full drift time of ions through the chamber. In the example of the environment of the future $\overline{\text{P}}$ANDA detector, ion space charges of up to 65 fC cm^{-3} are reached. The electric field resulting from this space charge is calculated using a finite element method to solve the Poisson equation. The drift of electrons in the full electric and magnetic field of the setup is calculated from the Langevin equation solved by a fourth order Runge–Kutta method. Drift-path distortions of $\mathcal{O}$(1 cm) are found for the $\overline{\text{P}}$ANDA environment, requiring corrections to be applied to the measured hit coordinates.

To this end, we have simulated a laser calibration system creating a regular grid of straight ionization tracks at known positions in the chamber. The geometry of the laser grid was optimized to yield an accurate measurement of the expected distortions, which are dominantly in radial and azimuthal direction for the $\overline{\text{P}}$ANDA case. In the case of azimuthal symmetry of the distortions, a two-dimensional spline fit to the measured residuals is sufficiently fast and accurate, reproducing distortions with a precision better than 100 μm, thus opening the possibility to be applied even in the online reconstruction software. This distortion map is then used to correct hits from charged particle tracks. Using Kalman-Filter-based track fitting we are able to reconstruct the momentum of tracks with a resolution very close to the ideal case of no distortions in the chamber.

The method to calculate the space charge effects and their correction presented in this paper is also applicable to the case of other TPCs with azimuthal symmetry, e.g. at STAR or ALICE. If one cannot exploit symmetry features, the method can in principle be extended to three dimensions, possibly making use of analytical solutions of the electric field instead of the numeric ones used in the present approach. For the reconstruction of the distortion map using laser tracks, a proper treatment of errors taking into account the grid geometry — as realized in the present work — is important to minimize systematic errors arising from projections of residuals. This allows the algorithm to be extended to make use of track information from other detectors instead of a fixed laser grid to measure the drift distortions.

References

[1] D.R. Nygren, J.N. Marx, Physics Today 31N10 (1978) 46.
[2] R.J. Madaras, et al., TPC/Two Gamma Collaboration, IEEE Transactions on Nuclear Science NS-30 (1983) 76.
[3] T. Kamae, et al., TOPAZ-TPC Group, Nuclear Instruments and Methods in Physics Research Section A 252 (1986) 423.
[4] C. Brand, et al., Nuclear Instruments and Methods in Physics Research Section A 283 (1989) 567.
[5] W.B. Atwood, et al., Nuclear Instruments and Methods in Physics Research Section A 306 (1991) 446.
[6] M. Fuchs, NA49 Collaboration, Nuclear Instruments and Methods in Physics Research Section A 367 (1995) 394.
[7] K.H. Ackermann, et al., STAR Collaboration, Nuclear Physics A 661 (1999) 681.
[8] D. Adamova, et al., CERES Collaboration, Nuclear Instruments and Methods in Physics Research Section A 593 (2008) 203 arXiv0802.1443.
[9] J. Alme, et al., Nuclear Instruments and Methods in Physics Research Section A 622 (2010) 316 arXiv1001.1950.
[10] W. Blum, W. Riegler, L. Rolandi, Particle Detection with Drift Chambers, 2nd ed., Springer-Verlag, Berlin, 2008.
[11] F. Sauli, Nuclear Instruments and Methods in Physics Research Section A 386 (1997) 531.
[12] F. Sauli, S. Kappler, L. Ropelewski, IEEE Transactions on Nuclear Science NS-50 (2003) 803.
[13] A. Bondar, et al., Nuclear Instruments and Methods in Physics Research Section A 496 (2003) 325 physics/0208017.
[14] M. Kotulla, et al., PANDA Collaboration, Technical progress report for PANDA: strong interaction studies with antiprotons, FAIR-ESAC/Pbar/Technical Progress Report, 2005.
[15] Q. Weitzel et al., 2007 IEEE Nuclear Science Symposium Conference Record, Piscataway, NJ, IEEE, 2007, pp. 227–233.
[16] GEM-TPC Collaboration, M. Ball, et al., Technical Design Study for the PANDA Time Projection Chamber, arXiv1207.0013 2012.
[17] L. Musa et al., ALICE Collaboration, CERN preprint CERN-LHCC-2012-012. LHCC-I-022, 2012.
[18] S. Rossegger, B. Schnizer, W. Riegler, Nuclear Instruments and Methods in Physics Research Section A 632 (2011) 52.
[19] R. Veenhof, Garfield - simulation of gaseous detectors, ⟨http://garfield.web.cern.ch⟩, 1984–2010.
[20] S. Bachmann, et al., Nuclear Instruments and Methods in Physics Research Section A 479 (2002) 294 CERN-EP-2000-151.
[21] S. Blatt, et al., Nuclear Physics B (Proceedings Supplements) 150C (2006) 155.
[22] R. Veenhof, Choosing a gas mixture for the ALICE TPC, ALICE-INT-2003-29, 2003.
[23] A. Capella, et al., Physics Reports 236 (1994) 225.
[24] R. Brun, F. Carminati, GEANT - detector description and simulation tool, CERN Program Library Long Writeup W5013, 1993, ⟨http://wwwasdoc.web.cern.ch/wwwasdoc/geant_html3/geantall.html⟩.
[25] The ALICE Collaboration, ALICE TPC Technical Design Report, CERN/LHCC 2000-001, ALICE TDR 7, 2000.
[26] P. Christiansen, et al., Nuclear Instruments and Methods in Physics Research Section A 609 (2009) 149.
[27] S. Biagi, Nuclear Instruments and Methods in Physics Research Section A 421 (1999) 234.
[28] R. Veenhof, Nuclear Instruments and Methods in Physics Research Section A 419 (1998) 726.
[29] A. Kuehmichel, NA49 Collaboration, Nuclear Instruments and Methods in Physics Research Section A 360 (1995) 52.
[30] H.G.R.Ch. Grossmann, Numerik Partieller Differentialgleichungen, 1st ed., Teubner, 1992.
[31] A. Logg, et al., DOLFIN Project, ⟨http://fenicsproject.org/⟩, 2009.
[32] H. Hilke, Nuclear Instruments and Methods in Physics Research Section A 252 (1986) 169.
[33] J. Abele, et al., Nuclear Instruments and Methods in Physics Research Section A 499 (2003) 692, The Relativistic Heavy Ion Collider Project: RHIC and its Detectors.
[34] J.G. Hayes, J. Halliday, IMA Journal of Applied Mathematics 14 (1974) 89.
[35] C. Höppner, et al., Nuclear Instruments and Methods in Physics Research Section A 620 (2010) 518 arXiv0911.1008.

Appendix B: Journal publication on the dE/dx evaluation

The following pages contain the author's published work on the evaluation of the dE/dx performance of the GEM-TPC in the S339 setup.

Nuclear Instruments and Methods in Physics Research A 737 (2014) 214–221

Contents lists available at ScienceDirect

Nuclear Instruments and Methods in Physics Research A

journal homepage: www.elsevier.com/locate/nima

First measurement of dE/dx with a GEM-based TPC ☆

F.V. Böhmer [a,*], M. Ball [a], S. Dørheim [a], K. Eckstein [a], A. Hönle [a], C. Höppner [a], B. Ketzer [a], I. Konorov [a], S. Neubert [a], S. Paul [a], J. Rauch [a], S. Uhl [a], M. Vandenbroucke [a,1], M. Berger [b], J.-C. Berger-Chen [b], F. Cusanno [b], L. Fabbietti [b], P. Gasik [b], R. Münzer [b], R. Arora [c], J. Frühauf [c], T. Hackler [c], J. Hehner [c], M. Kiš [c], V. Kleipa [c], J. Kunkel [c], N. Kurz [c], Y. Leifels [c], K. Peters [c], H. Risch [c], C.J. Schmidt [c], L. Schmitt [c], S. Schwab [c], D. Soyk [c], B. Voss [c], J. Weinert [c], R. Beck [d], D. Kaiser [d], M. Lang [d], R. Schmitz [d], D. Walther [d], P. Bühler [e], P. Müllner [e], J. Zmeskal [e], N. Herrmann [f]

[a] *Technische Universität München, Physik Department E18, D-85748 Garching, Germany*
[b] *Excellence Cluster Universe, Technische Universität München, D-85748 Garching, Germany*
[c] *GSI Helmholtzzentrum für Schwerionenforschung GmbH, D-64291 Darmstadt, Germany*
[d] *Helmholtz-Institut für Strahlen- und Kernphysik, D-53115 Bonn, Germany*
[e] *Stefan Meyer Institut für Subatomare Physik, 1090 Wien, Austria*
[f] *Universität Heidelberg, D-69120 Heidelberg, Germany*

ARTICLE INFO

Article history:
Received 29 June 2013
Received in revised form
7 September 2013
Accepted 22 October 2013
Available online 8 November 2013

Keywords:
Time projection chamber
Gas electron multiplier
Specific energy loss
Particle identification
Exponentially modified Gaussian
FOPI

ABSTRACT

In this work we present the first measurement of the specific energy loss (dE/dx) and an analysis of the resulting charged-particle identification (PID) capabilities of a large-scale TPC with GEM-based gas amplification. The data has been recorded inside the FOPI spectrometer at GSI, Germany, using reactions of 1.7 GeV/c pions impinging on a carbon target.

In the specific energy loss spectrum clear bands for pions, kaons, protons and deuterons are observed. The specific energy loss resolution is studied as a function of the total particle momentum and as a function of the track length. It is found to be $\sim 15\%$, consistent with expectations.

1. Introduction

Time Projection Chambers (TPCs) are widely used as central tracking detectors. Their low material budget and large solid angle coverage combined with particle identification (PID) capabilities through the measurement of the specific energy loss make them an ideal choice for many experiments.

On the downside, an important limitation of TPCs so far has been the necessity of gating structures. Their purpose is to prevent ions produced in the gas amplification stage – traditionally realized with Multi Wire Proportional Chambers (MWPCs) – from drifting back into the active volume, where they would lead to distortions of the drift field. As a consequence, trigger rates of experiments employing TPCs have been limited to the low kHz regime.

The application of Gas Electron Multipliers (GEMs) [1] as amplification stage promises to lift this limitation: the intrinsic ion-backflow suppression of GEM foils [2] will allow the operation of TPCs without gating techniques and the inevitable dead times they entail, thus opening the possibility of using TPCs as continuously running tracking devices even in high rate experiments.

Obviously, the traditional traits of MWPC-driven TPCs should not be compromised by the introduction of GEMs – most importantly the energy resolution, where gain fluctuations in (multi-) GEM systems will play a role. In this work, we present the first measurement of specific energy loss "dE/dx" for the purpose of PID with a triple-GEM-TPC for different particles, using reactions of 1.7 GeV/c pions impinging on a carbon target.

☆This work has been supported by the 7th Framework Program of the EU, the German Bundesministerium für Bildung und Forschung and the DFG Cluster of Excellence "Origin and Structure of the Universe".

* Corresponding author. Tel.: +49 89 289 12592; fax: +49 89 289 12570.
E-mail address: felix.boehmer@tum.de (F.V. Böhmer).
[1] Present address: Temple University, Philadelphia, PA 19122, USA.

0168-9002/$ - see front matter © 2013 Elsevier B.V. All rights reserved.
http://dx.doi.org/10.1016/j.nima.2013.10.094

2. Experimental setup in FOPI

In 2011 a GEM-based TPC (called the "FOPI GEM-TPC" from here on) was installed in the FOPI spectrometer for a dedicated 3-week physics campaign. FOPI is located at the GSI Helmholtzzentrum für Schwerionenforschung in Darmstadt, Germany and was originally constructed in 1990. A recent description of the entire spectrometer can be found in Ref. [3].

2.1. The GEM-TPC for FOPI

The FOPI GEM-TPC [4,5] was completed in the end of 2010. To date, it is the detector with the largest active volume of this kind. It features a stack of three GEMs as gas amplification stage with a gap of 2 mm in between the foils (cf. Fig. 12.3 of [5]). The potential differences over the three GEMs ΔU_{G1}, ΔU_{G2}, ΔU_{G3}, the voltage drops over the transfer gaps in between the foils ΔU_{T12}, ΔU_{T23} and the induction gap between the last foil and the readout plane ΔU_{I} are given in Table 1, along with the exact dimensions and the most important technical details of the detector. The cylindrical field cage has been designed to fit into the inner gap of the FOPI spectrometer (see Section 2.3).

A peculiarity of the FOPI GEM-TPC which is of special importance for the analysis presented in this work is the readout plane. It consists of 10,254 *hexagonally shaped* pickup pads with 3.0 mm outer diameter. Fig. 1 shows a section of the outer region of the readout plane in a close-up view.

2.2. Readout electronics

For signal readout the AFTER ASIC [6] was chosen, which has been originally developed for the T2K experiment [7]. It features a low-noise charge preamplifier and a 511 cell analog buffer per channel with adjustable sampling frequency and shaping time.

Table 1
Key parameters of the experimental setup.

Environment	
Beam	π^-, 1.7 GeV/c
Rate	$\sim 1.5 \times 10^4$ π^- s^{-1}
Target	C, 10 mm (2.6% λ_I)
Magnetic field	0.6 T Solenoid
Detector	
Drift length	727.8 mm
Inner ⌀	104.0 mm
Outer ⌀	308.0 mm
Drift gas	Ar/CO_2 (90/10), 1 atm
Drift field	234 V cm^{-1}
e^- drift velocity	16.5 μm ns^{-1}
Effective gain	$\sim 1 \times 10^3$
GEM parameters	50 μm thickness 140 μm pitch 70 μm hole ⌀
Gaps between foils/ last foil and readout	2 mm/ 4 mm
ΔU_{G1}, ΔU_{G2}, ΔU_{G3}	324 V, 296 V, 259 V
ΔU_{T12}, ΔU_{T23}, ΔU_{I}	604 V, 604 V, 1208 V
Readout	10,254 hex. pads
Electronics	
Sampling clock	15.55 MHz
Buffer time bins	511
Peaking time	116 ns
Dynamic range	120 fC (11-bit ADC)
Sensitivity	394 e^-/ADC channel
Mean noise σ_N	678 e^- (RMS: 126 e^-)
Input capacitance	13–16 pF per pad
Threshold	4.5σ_N (per channel)

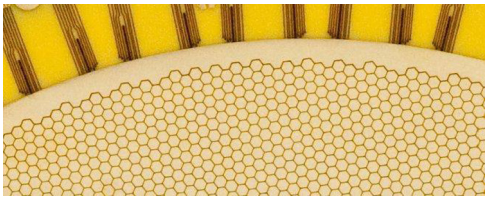

Fig. 1. Detail of the pad plane as installed in the GEM-TPC for FOPI. The 10,254 hexagonal pickup electrodes have an outer diameter of 3.0 mm.

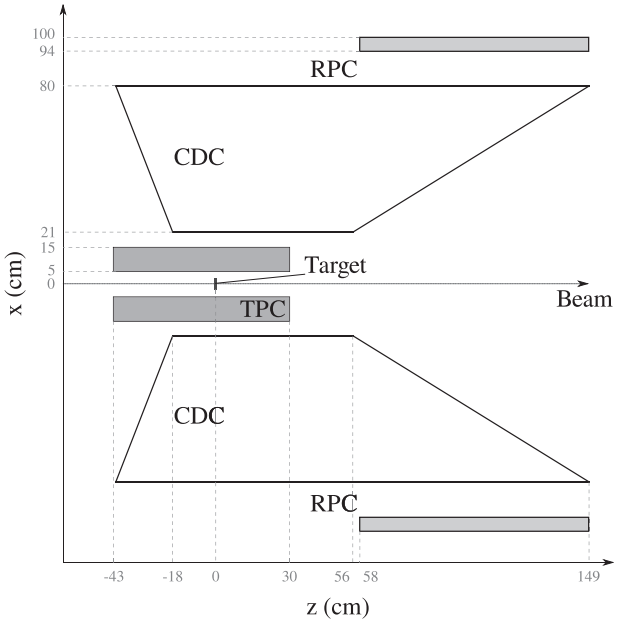

Fig. 2. Cross-section of the GEM-TPC + FOPI setup. Only the detectors relevant for this analysis are shown. The given dimensions are rounded values.

Each AFTER chip has 72 channels, of which 64 are connected to pads on the pad plane (4 additional, internal channels of the chip are used for common mode noise correction [8]). In total, 42 front-end cards equipped with 4 AFTER chips each have been connected via 11 ADC boards to read out all channels of the detection plane. The mean noise performance of the fully connected readout during data taking has been found to be $\sigma_N \sim 680\, e^-$ ENC per channel, calculated using the width of baseline fluctuations and the single-channel sensitivity. The input capacitance to the preamplifier was estimated to be between 13 and 16 pF per pad, dominated by the ASIC packaging and the trace lengths. Table 1 summarizes the settings and performance during data taking. More information about the readout electronics can be found in Refs. [5,8].

2.3. Physics campaign inside the FOPI spectrometer

For the analysis presented here, only the barrel detectors of FOPI are of interest. A sketch of the involved systems is shown in Fig. 2. The GEM-TPC surrounded the target, covering the full azimuthal angle and the polar angular region $26^\circ < \theta < 159^\circ$ for primary tracks reaching the outer wall of its volume.[2] The GEM-TPC in turn was placed inside FOPI's Central Drift Chamber (CDC), which covered the polar angle range $22^\circ < \theta < 122^\circ$ with respect to the target with its inner wall. The CDC offers a good spatial resolution of $\sigma_{x,y} \sim 300$ μm

[2] For the data presented here only a part of the physical drift length (approx. -24 cm $< z < +30$ cm in Fig. 2) has been read out due to the choice of the drift field, as summarized in Table 1.

in the azimuthal (xy-) plane, while the resolution along the beam direction (z) is considerably lower ($\sigma_z \sim 10$ cm).

The CDC was augmented by a time-of-flight system consisting of Resistive Plate Chamber (RPC) detectors, covering the forward region $32^\circ < \theta < 58^\circ$ [9]. It offered a time resolution below 70 ps during this experiment, allowing a very clean particle identification for associated tracks in the covered polar angle window (cf. Section 5.3).

2.4. Data sample

The data used in this analysis have been taken in June 2011 over a period of roughly 12 hours. During this time, 1.53×10^6 events have been recorded from reactions of 1.7 GeV/c π^- impinging on a carbon target of 10 mm thickness, containing 2.88×10^6 tracks reconstructed in the TPC. Of these, 1.77×10^6 tracks could be matched with the surrounding CDC and entered the analysis (cf. Section 3.3). The average track multiplicity in the TPC was 1.88. Fig. 3 shows the phase space distribution of all matched TPC–CDC tracks.

3. Track reconstruction

In this section we summarize the most important steps on the way from pad signals to particle-track feature extraction in the FOPI GEM-TPC system. Processing of the recorded data is done within the context of a custom software framework written and implemented in the C++ programming language. The code is based on the FairRoot [10] package developed at GSI, Germany. The ROOT framework [11] developed at CERN acts as the underlying code base and is used for data persistence and analysis purposes.

3.1. Gain calibration

The gain of the detector is measured and equalized by introducing radioactive ^{83m}Kr into the active volume, a widely used method for gas detectors. The well-known decay modes of ^{83m}Kr lead to spatially constrained ionization clusters (length scale $\mathcal{O}$(1 cm)) from a discrete energy spectrum in the range of $\sim$9 keV to $\sim$42 keV. Several dedicated measurements with Krypton in the active volume of the TPC have been performed during the physics campaign. As stated above, these data can be used to (i) calibrate the global effective detector gain and (ii) map out gain inhomogeneities across the amplification stage plane, allowing us to perform relative amplitude correction on pad level.

The absolute gain is obtained using the sensitivity of the readout chain, which was determined by injecting a known charge into the preamplifier of a single channel (cf. Table 1). With this sensitivity an analysis of the ^{83m}Kr spectra [12] yields a gain of $(1.0 \pm 0.1) \times 10^3$ for the dataset discussed here (analysis ongoing, publication in preparation), compatible with a gain measurement performed with a small detector with the same GEM configuration (the settings of the presented setup correspond to a voltage of 3240 V in Fig. 11.1 of [5]).

Using the same Krypton calibration data for relative corrections on pad level, the energy resolution observed in the ^{83m}Kr spectrum measurement can be improved by up to 25%, yielding a resolution of $\Delta E/E = 4.4\%$ for the main 41.55 keV peak [12]. Fig. 4 shows the obtained relative amplitude correction factors for all active pickup pads on the readout plane.

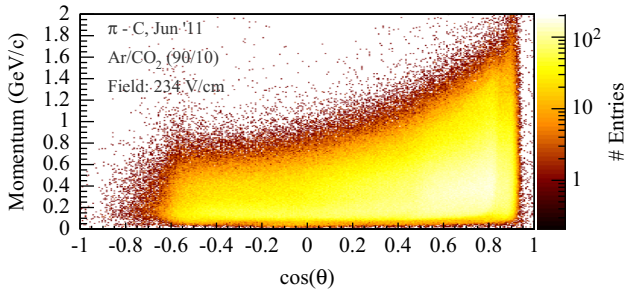

Fig. 3. Phase space distribution of all matched TPC–CDC tracks after performing a combined fit. θ is the scattering angle in the laboratory system.

3.2. TPC hits

In a truly 3-dimensional tracking detector like a TPC, it is necessary to clarify how a single measurement – a "detector hit" – is defined. There are two conceptual abstractions on the way from signals induced on the readout electrodes to feature extraction of physical particles.

First, the analog signals recorded on individual pickup electrodes of the pad plane are digitized by an ADC and then processed by a simple pulse shape analysis (PSA) algorithm. A set of adjacent ADC samples that is identified by the PSA to belong to one pulse is called a *pad hit*. Each pad hit k holds the following information: its total (integrated) amplitude a_k, a time stamp and the unique ID of the pickup pad it was recorded on. When pad hits overlap in time – most commonly caused by tracks going in forward direction – the PSA algorithm separates them at positions of local minima in the digitized amplitude spectrum. Currently – apart from gain calibration – no corrections on signal level like tail cancellation or reshaping are performed.

With the knowledge of the drift velocity in the chamber, we can map each pad hit into 3-dimensional GEM-TPC detector space via

$$(\text{time stamp},\ \text{padID}) \longrightarrow (u, v, w). \tag{1}$$

The drift velocity is currently taken from MAGBOLTZ [13] simulations for the correct environmental conditions and field strengths. The values have been checked against measurements obtained with single runs where the drift field and sampling settings allowed a direct analysis of the full physical drift length of the TPC and hence a straightforward extraction of the drift velocity. The agreement between these data points and simulations has been found to be accurate within the measurement errors.[3]

In a second step, the pad hits are combined into *clusters* in time and now also across pad boundaries. This step allows data reduction and offers an early possibility of noise suppression. To fully exploit the high level of symmetry of our detection plane (see Section 2.1) – and thus the absence of any preferred orientations or "pad rows" – this association is to be performed in the full 3-dimensional space (u, v, w). The search for clusters starts at local amplitude maxima and combines neighboring pad hits. Each cluster can finally be assigned a total amplitude, a center of gravity and a covariance ellipsoid describing its spatial uncertainty. Clusters are the objects that are passed to the tracking algorithms, but they are not used further for extracting the energy loss information (cf. Section 4).

3.3. Alignment & track matching

Track finding on the TPC side is performed standalone using an implementation of a conformal mapping method onto the so-called Riemann sphere [14]. The identified tracks are then fitted with a Kalman filter (using the GENFIT [15] track fitting framework).

[3] It is foreseen to include the drift velocity extraction in the alignment procedure as described in Section 3.3.

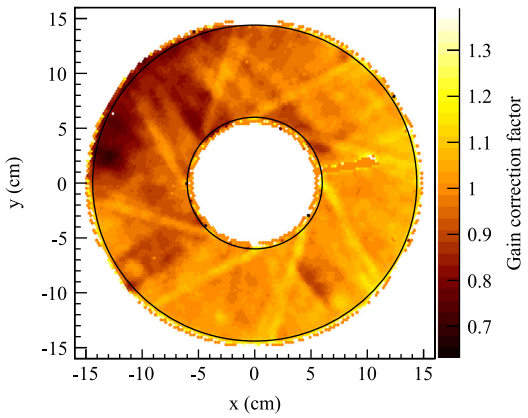

Fig. 4. Gain calibration factors for each pad extracted from the ^{83m}Kr calibration data as used in the analysis. The underlying distribution centered around 1 shows a RMS of 0.107. The solid black circles visualize a cut that is applied during extraction of energy loss information in order to exclude fringe effects in the current gain calibration data (cf. Section 4.3). The iris-shaped structures run along the physical segmentation of the GEM foils, and the region at $y \sim 0$ cm, $5\text{ cm} \lesssim x \lesssim 10$ cm belongs to a broken readout chip, where correction factors have been set to 1 by hand.

The obtained TPC tracks together with tracking data from the surrounding detectors can be used to geometrically align the GEM-TPC detector with respect to the FOPI spectrometer, which defines the global coordinate frame (x, y, z). In the scope of this work, alignment was performed using an iterative procedure working on TPC and CDC tracks, minimizing translational and rotational displacements of the TPC hits with respect to the FOPI coordinate frame.

Owing to the generally poor z-resolution ($\mathcal{O}(10\text{ cm})$) of the CDC, final matching of TPC and CDC tracks is realized using constraints exclusively in the r–ϕ-plane. We require (i) a relative azimuthal displacement of the outermost TPC hit and the innermost CDC hit within $\pm 15^\circ$, and at the same time (ii) a relative angular change of the tangents to both tracks at the matching point of less than $\pm 10^\circ$. Under these requirements, a matching efficiency of $\varepsilon > 99\%$ is observed, while ambiguities occur in less than 4% of the cases. Recalling the low track multiplicity (cf. Section 2.4), it should be noted that many of these ambiguous matches are related to track splitting issues during pattern recognition which are not resolved in the presented analysis. In case of such an ambiguity, we decide in favor of the better match based on the residual data. After a successful match, a complete refit of the combined TPC–CDC track using the GENFIT Kalman filter implementation is performed, taking into account material effects of the full combined TPC & FOPI setup.

4. Extraction of specific energy loss

For given gas parameters, the energy ΔE deposited by a charged particle when traveling a certain distance Δx through the detector gas fluctuates due to the statistical nature of the underlying scattering processes. For length scales Δx relevant for gas detectors, the ΔE are distributed asymmetrically, with a long tail towards high energy deposits. The distributions describing these fluctuations are called *straggling functions* $f(\Delta E; p, \Delta x)$. The mean value divided by the distance $\langle \Delta E \rangle / \Delta x$ follows the Bethe formula ($\mathrm{d}E/\mathrm{d}x$) and usually differs considerably from the most probable one (an extensive review on the topic can be found in Ref. [16]). The fact that both the mean and the most probable value depend on the particle type X for a given momentum can be exploited for the purpose of particle identification.

If the signal amplitude registered on the readout plane is proportional to the energy deposited in the detector gas by the traversing particle, the straggling distributions can in principle be measured for each particle track. In (large) gas detectors this is achieved by sampling the recorded hit amplitudes of a track over certain distances Δx_i. Usually, the Δx_i are defined by the track projection on given geometrical features of the detection plane, e.g. pad rows.

Exploiting the high level of symmetry of the pad plane in our case (cf. Section 2.1) requires a different approach: based on the matched and fitted tracks, we walk along the actual reconstructed particle trajectory in 3-dimensional space inside the TPC volume with a fixed step length[4] $\Delta x = 5$ mm. Starting at the first pad hit of the track, after each track segment Δx a plane P_i perpendicular to the track is constructed. The set of all amplitude-corrected pad hits Ω_i lying in between the two adjacent planes P_i, P_{i+1} is combined to make one measurement of $A_i/\Delta x$, where $A_i = \sum_{k \in \Omega_i} a_k$. An artistic view visualizing the procedure is shown in Fig. 5, the obtained stepping statistics for the choice $\Delta x = 5$ mm in Fig. 6.

4.1. Truncated mean

Due to the long tail of the straggling distributions $A_i/\Delta x$, their mean value is not a good estimator for the characteristic energy loss. More correctly one should use the most probable value $(A/\Delta x)_{\mathrm{mp}}$. Its extraction, however, requires the reconstruction of the underlying straggling function and becomes increasingly difficult for small N.

A robust and commonly used practice is that of extracting the *truncated mean* instead: by discarding a certain fraction t_{high} (t_{low}) of the largest (smallest) values of $A_i/\Delta x$ an attempt is made to symmetrize the distributions, aiming to move the mean $\langle A/\Delta x \rangle_{\mathrm{tr}}$ of the remaining, truncated distribution towards the most probable value and – most importantly – stabilize it in the process.

The choice for the newly introduced parameters t_{high}, t_{low} has to be optimized. This can be done in terms of the resulting specific energy loss resolution or other defining quantities (a short discussion follows in Section 6.3). We found $t_{\mathrm{low}} = 5\,\%$ and $t_{\mathrm{high}} = 25\%$ to be a good choice, i.e. retaining the interval 5–75% of all sorted pad hit amplitudes. With this choice of truncation limits we observe a minimal amount of fluctuation of the extracted truncated mean values, and thus an optimal $\langle A/\Delta x \rangle_{\mathrm{tr}}$ resolution. All results in the following have been produced using these values. It should be noted, however, that the $\langle A/\Delta x \rangle_{\mathrm{tr}}$ extracted in this way overestimate the most probable value of the straggling function.

4.2. Specific energy loss

It is common practice to call the measurement of amplitudes per travel distance described in the above sections just a measurement of "$\mathrm{d}E/\mathrm{d}x$". Under the assumption of perfectly linear readout electronics and that the truncated mean is indeed a valid estimator, the energy loss of a particle per traveled distance $\mathrm{d}E/\mathrm{d}x$ as described by the Bethe formula and the quantity $\langle A/\Delta x \rangle_{\mathrm{tr}}$ are equivalent up to a proportionality factor in good approximation, at least in the momentum range this analysis is concerned with. For the sake of conformity we adopt the common terminology and identify

$$\langle A/\Delta x \rangle_{\mathrm{tr}} \equiv \mathrm{d}E/\mathrm{d}x_{\mathrm{tr}} \tag{2}$$

for the remainder of this work. The distribution of the measured samples $A_i/\Delta x_i$ we call the $\mathrm{d}E/\mathrm{d}x$ distribution from here on.

[4] The first and last step along the particle trajectory has variable length. A discussion of the choice $\Delta x = 5$ mm can be found in Section 6.3.

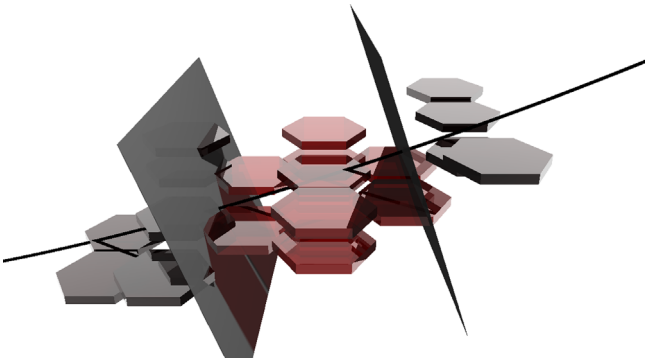

Fig. 5. On the stepping procedure explained in Section 4: the single pad hits are visualized as hexagons as defined by the readout plane. Their displacement out of this plane represents different hit times (or z coordinates). For the dE/dx sampling the full track fit is used (black helix), and only the pad center coordinates are considered when collecting pad hits in between planes perpendicular to the particle track. The pad hits selected in this way for one dE/dx sample appear highlighted.

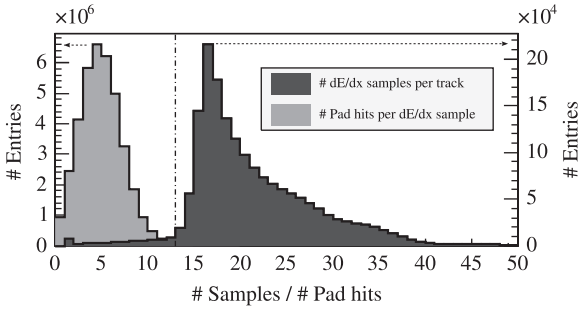

Fig. 6. Distribution of (right scale) the number N of extracted samples $A_i/\Delta x_i$ (or "dE/dx"; see Section 4.2) per track and (left scale) the number of *pad hits* per such measurement. The dashed vertical line marks a cut applied on N for the final analysis as given in Section 4.3.

4.3. Cuts applied

We complete the discussion of the more technical aspects of the analysis by summarizing the cuts we apply when extracting information on specific energy loss. In addition to the zero suppression during data taking (cf. Table 1) and the implied preselection made by requiring a successful match between TPC and CDC tracks, the following is required:

- The pad center must lie inside rings as shown in Fig. 4 ($6.0\,\text{cm} < r_{\text{pad}} < 14.0\,\text{cm}$) to be considered in d$E$/d$x$ extraction.
- The number of dE/dx samples per track N before truncation has to be at least 13 (cf. Fig. 6).

4.4. Energy loss spectrum

Fig. 7 shows the full spectrum of all obtained dE/dx_{tr} as a function of the measured particle momentum. Note that, while the value for energy loss is reconstructed from TPC data only as discussed above, the total particle momentum is extracted from the combined fit of the matched TPC–CDC track. Bands for different particle types (pions, kaons, protons and deuterons) are clearly visible.

5. Extraction of dE/dx_{tr} resolution

In order to quantify the relative widths of the bands, we subdivide the data of Fig. 7 along the momentum axis into slices

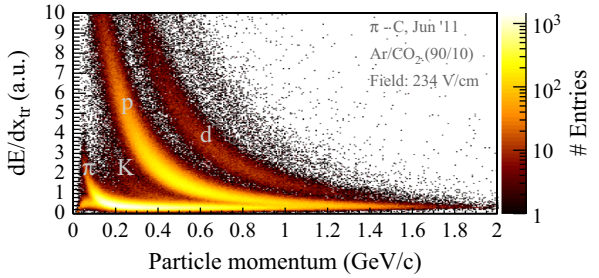

Fig. 7. Specific energy loss dE/dx_{tr} obtained with the truncated mean method (discarding the lowest 5% and the highest 25% of all amplitude-sorted samples) as a function of particle momentum. Both positively and negatively charged particles enter.

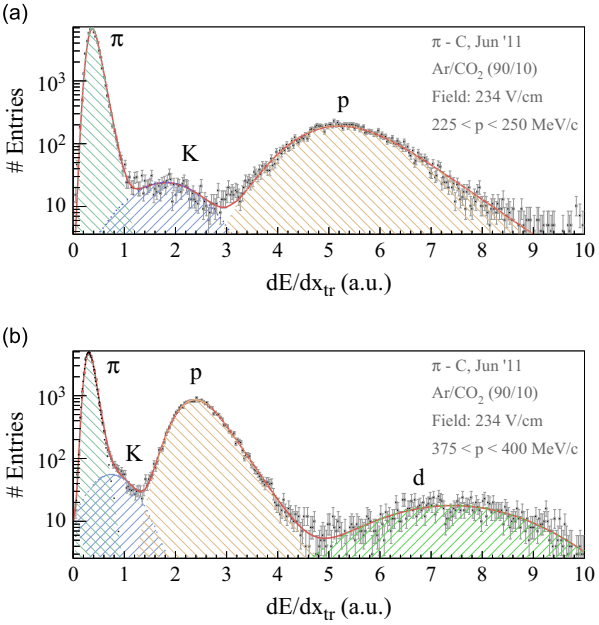

Fig. 8. Examples of dE/dx_{tr} spectra obtained when projecting out the data of Fig. 7 in slices of 25 MeV/c. The plots correspond to (a) $225 < p < 250\,\text{MeV}/c$ and (b) $375 < p < 400\,\text{MeV}/c$. The solid line shows the result of a (binned) maximum likelihood fit using the pdf of Eq. (3), the individual contributions of each particle type are drawn as shaded areas. None of the fit parameters have been constrained during the fit.

of fixed size. Fig. 8 shows two such slices, each obtained by projecting out the data from a 25 MeV/c momentum window onto the energy axis.

One remark concerning this slicing technique is in order: by mere projection along the momentum axis, an additional broadening of the resulting distributions occurs due to the slope of the dE/dx_{tr} bands. In principle, this could be avoided by linearizing one band at a time using a suitable Bethe parametrization. For small slice widths of 25 MeV/c we found only a marginal impact on peak widths (within error bars) using this technique, while the task of fitting the spectra – now describing the energy loss relative to one particle type – becomes more difficult. This led us to decide in favor of the simpler, more stable approach of using simple projections.

5.1. Fit function and treatment of asymmetries

The peaks shown in Fig. 8 have a dominant Gaussian component, but they also exhibit a tail towards higher values of specific energy loss. To properly capture this asymmetry, we choose the convolution $E(x;\tau) \otimes G(x;\mu,\sigma)$ of an exponential decay function $E(x;\tau)$ with decay constant τ and a Gaussian distribution $G(x;\mu,\sigma)$

with mean μ and RMS width σ as basic fit function. The resulting probability density function (pdf) has the analytical form

$$C_{\mathrm{EG}}(x;\mu,\sigma,\tau)=\frac{\tau}{2}\cdot\exp\left[\frac{\tau}{2}(2\mu+\tau\sigma^2-2x)\right]\cdot\mathrm{erfc}\left(\frac{\mu+\tau\sigma^2-x}{\sqrt{2}\sigma}\right), \tag{3}$$

where $\mathrm{erfc}(x;\mu,\sigma,\tau)$ is the complementary error function and x runs along the energy axis. The overall fit function is then a sum of multiple such pdfs, the exact number depending on the momentum range. Performing (binned) maximum likelihood fits using this fit function we found that all data features can be very accurately described (cf. Fig. 8 and A1 in Appendix).

5.2. Resolution expectation

For later reference, we want to introduce an expectation value for the specific energy loss resolution. Within the framework of the Photo-Absorption Ionization (PAI) model, Allison and Cobb [17] give an approximate parametrization of the expected resolution R (in % FWHM) of sampling gas detectors in Ar-based mixtures, based on experimental data:

$$R(N,\Delta x,P)=0.96\cdot N^{-0.43}\cdot(\Delta x\cdot P)^{-0.32}. \tag{4}$$

Here N is given by the number of energy loss measurements per track, Δx is the sampling step length (cm) and P is the gas pressure (atm).[5]

5.3. Monte Carlo study: peak shape

The sample size N of the experimental data taken into account by Allison and Cobb is typically $\mathcal{O}(10^2)$, so it is a priori not clear if Eq. (4) can be extrapolated to our scenario, where $N\sim 20$ (see Fig. 6).

Thus, before proceeding to the final results of the data analysis, it is worth taking a closer look at the peak shape. To be able to apply the available benchmark given by Eq. (4) to the results of this analysis, we have investigate the impact of the $\mathrm{d}E/\mathrm{d}x$ sample size N per track on the peak asymmetry in a data-driven Monte Carlo study.

Instead of generating artificial amplitude data, we use the excellent PID capabilities of the RPC detector of FOPI (cf. Section 2.3) to select only one particle type (protons) from the full dataset. Further constraining the selection to a narrow momentum and θ window yields a clean straggling distribution $f(\Delta E;\Delta x=5\ \mathrm{mm})$, which can be sufficiently well parametrized by a polynomial fit. This allows us to extrapolate to "track lengths" beyond the limits of the detector by sampling from this parametrization with variable sample size N. After extracting the truncated mean, the resulting $\mathrm{d}E/\mathrm{d}x_{\mathrm{tr}}$ spectra are fitted using Eq. (3).

Fig. 9 shows the results of this Monte Carlo analysis: plotted are (Gaussian) σ/μ of Eq. (3), FWHM/μ and the ratio of σ and the square root of the full variance $\mathrm{var}_C=\sigma^2-1/\tau^2$. The latter ratio is a direct measure of the peak asymmetry. For long tracks (large number of samples N) it slowly approaches unity, the limit of a perfectly Gaussian distribution after truncation. For small N, the probability of large amplitudes surviving the truncation grows, leading to an increased asymmetry.

The FWHM resolutions obtained within this Monte Carlo model – extrapolated from our data for small N – are systematically larger than the expectation given by Eq. (4) over the full range of simulated N. For large N the distributions of $\mathrm{d}E/\mathrm{d}x_{\mathrm{tr}}$ become increasingly symmetric. Already being close to a purely Gaussian spectrum

$$R_{\mathrm{G}}(N,\Delta x,P)=\frac{1}{2.35}\cdot R(N,\Delta x,P) \tag{5}$$

should then become a good approximation for σ/μ (lower solid line in Fig. 9). Interestingly, when comparing this to the Gaussian component of the fits from our data-driven model, both are in very good agreement, even in the low N regime. Apparently, the exponential component of the convolution as defined in Eq. (3) – governed by the single parameter τ – fully absorbs the peak asymmetry.

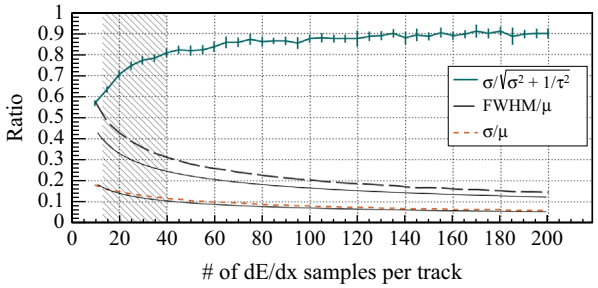

Fig. 9. Monte Carlo study: effect of the sample size (before truncation) of the specific energy loss measurement per track on the peak shape and the final resolution (after truncation). The solid lines follow the predictions of Eqs. (4) and (5). The shaded area marks the relevant range for the data analyzed in this work. The error bars represent the statistical uncertainties of the fit using the pdf as in Eq. (3) and are smaller than the line width for both σ/μ and FWHM/μ.

6. Results

With the fit function in place and found to be reasonable, we can now proceed to quantify the data of Fig. 7.

6.1. Resolution vs. track momentum

First, we complete the analysis in bins of the particle momentum. Motivated by statistical weight and energy range, we use the proton peak for the extraction of the relative width. Fig. 10 shows the $\mathrm{d}E/\mathrm{d}x_{\mathrm{tr}}$ resolution for protons, both in terms of purely Gaussian σ/μ and FWHM/μ. The resolution as obtained from the Gaussian component of Eq. (3) is found to be better than 20% throughout, reaching 14% for $p\sim 400$ MeV/c. For completeness, all fits used in the analysis can be found in Fig. A1 of Appendix.

A quantity that is a more direct measure for the PID capabilities of the detector is the actual separability of the $\mathrm{d}E/\mathrm{d}x_{\mathrm{tr}}$ distributions of different particle species, usually called *separation power*, that can be defined as

$$S_{\mathrm{AB}}=\frac{|\mu_{\mathrm{A}}-\mu_{\mathrm{B}}|}{\sigma_{\mathrm{AB}}} \tag{6}$$

for two particle types A, B. Here, σ_{AB} is the arithmetic average of the Gaussian sigmas of the two involved peaks. Fig. 11 shows the separation powers S_{pX} for protons and X = pions, kaons, deuterons as a function of the particle momentum.

In the symmetric form of Eq. (6) only the width of the Gaussian contribution enters, but from Section 5 we know that the asymmetry arising from the limited sample size is already significant in the case of the FOPI GEM-TPC data ($N\sim 20$). However, for performing particle identification during physics analysis, one aims to assign likelihoods for each particle based on the actual underlying probability distributions. These are parametrized very precisely for our data as has been demonstrated in Section 5.1. In this light the results of Fig. 11 are to be considered as a basic benchmark for comparison with data from other detectors, together with the evolution of the peak asymmetry as shown in Fig. 9.

[5] Actually, the exponent of N is -0.46 in the formula originally given in Ref. [17]. The choice of -0.43 is a common modification used to better describe resolutions obtained with a *truncated mean* analysis.

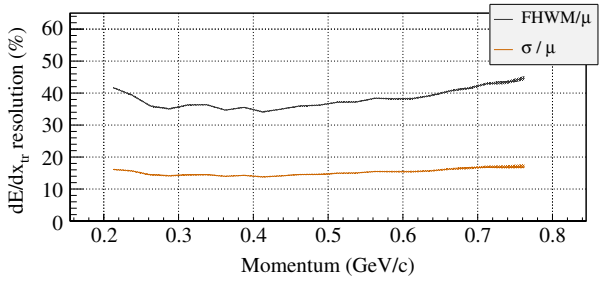

Fig. 10. Relative dE/dx_{tr} resolution for protons as obtained from fits with the pdf as in Eq. (3) in 25 MeV/c momentum bins. Both σ/μ for the Gaussian component of Eq. (3) and the FWHM/μ are shown. Statistical uncertainties are of the order of the line width and are visualized as shaded area.

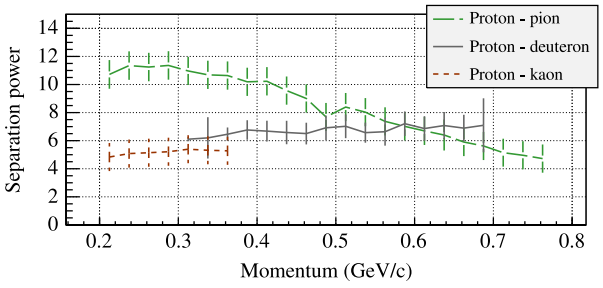

Fig. 11. Separation power S_{px} as defined in Eq. (6) with statistical errors.

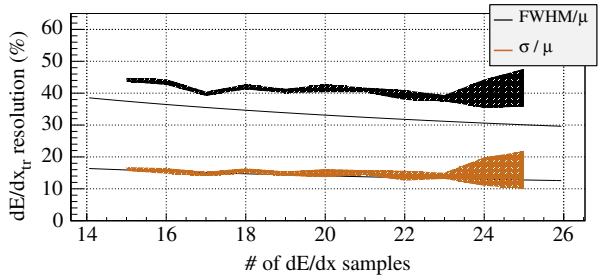

Fig. 12. dE/dx resolution as a function of the number of samples per track. The expectations given by Eqs. (4) and (5) are drawn as solid lines. Statistical uncertainties appear as shaded areas.

6.2. Resolution vs. track length

Returning to the expectations from Eqs. (4) and (5) – now for real data – we show the dE/dx_{tr} resolution as a function of the number of samples N in Fig. 12. Since we have to subdivide our dataset further with respect to N, statistical uncertainties become an issue and we have to restrict the analysis to a rather small range of $N \in [15, 25]$ (cf. Fig. 6).

Similar to the discussion of Section 5.3 it can be observed that σ/μ is in very good agreement with the expectation given by Eq. (5) (under the assumption of symmetric peak shapes).

6.3. Choice of truncation t and stepping Δx

The results shown so far have all been obtained with one choice of settings regarding the step length ($\Delta x = 5$ mm) during dE/dx sampling and the truncation (retaining all but the lowest 5% and the upper 25% of the amplitude-sorted samples) on track level. In this section we provide some motivation for these default settings.

Fig. 13 shows the final dE/dx_{tr} resolution as discussed in the preceding sections for a selection of different truncation and Δx settings. The situation is rather clear for the choice of the sampling stride length, where a distinct minimum is visible for $\Delta x = 5$ mm. The choice of the truncation setting is less straightforward: here we can identify a shallow minimum around the default settings, but the difference in between different choices is already of the order of the statistical uncertainties of the final resolutions.

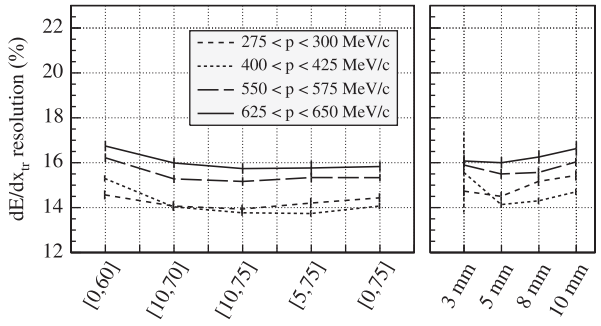

Fig. 13. Final dE/dx_{tr} resolution as a function of truncation settings (left) and choice of Δx (right) for a selection of momentum bins. The labels in the left plot specify the *retained* interval (%) of the amplitude-sorted $\Delta A_i/\Delta x_i$, the labels in the right plot mark different Δx settings (mm). Note that $\Delta x = 5$ mm has been used for the study of the influence of the truncation, which in turn has been set to the default settings [5,75] to study Δx.

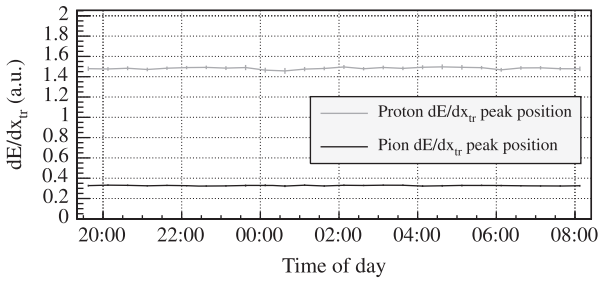

Fig. 14. Evolution over time of the specific energy loss peak position for pions and protons with $500 < p < 550$ MeV/c. Peak positions and errors are obtained from Gaussian χ^2 fits. Each data point corresponds to a 30 min time window.

The separation power as defined in Eq. (6) would in principle also be a good criterion for optimization. In view of the already ambiguous situation for the peak resolutions (recalling the uncertainties visible in Fig. 11) and the further complications arising from the involved asymmetries, however, it becomes clear that optimizing parameters with respect to the separation power is not possible given the size of our data sample.

6.4. Stability with time

For the data underlying the study presented in this work, the operating parameters have been kept constant (see Table 1). However, no corrections for variations of detector parameters (e.g. gain, drift field) or environmental conditions (temperature, pressure) over time are applied so far.

To study a possible impact on the presented results, we analyzed dE/dx_{tr} peak positions in selected momentum slices of Fig. 7 as a function of time. Fig. 14 shows this evolution as obtained from a Gaussian χ^2 fit to the pion and proton peak, respectively. Relative fluctuations around the mean values are smaller than 1% – compatible with zero given the magnitude of the statistical errors – and thus cannot be resolved.

We can conclude that the results presented in this work can already be regarded as a close-to-optimal benchmark of the dE/dx capabilities of the FOPI GEM-TPC.

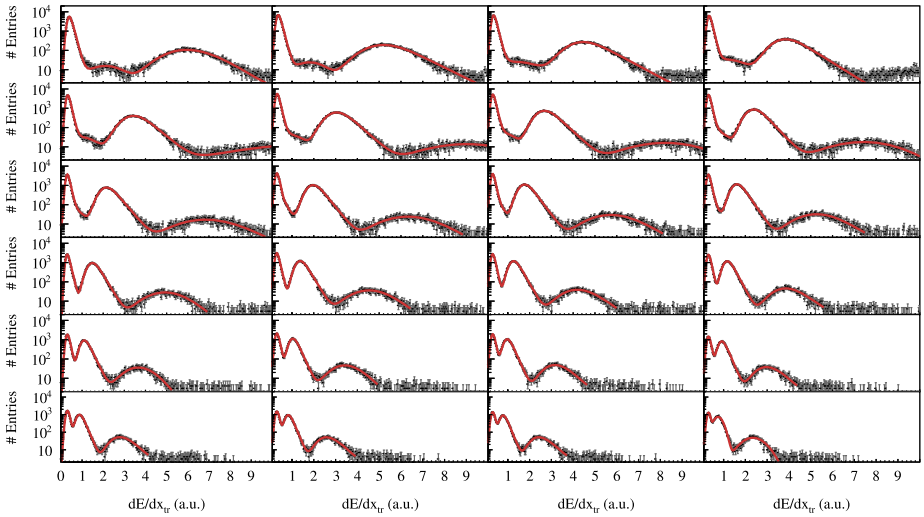

Fig. A1. Complete set of momentum slices with fits as used in the resolution analysis of Section 6.1. Each plot corresponds to a 25 MeV/c window, starting at 200 MeV/c < p < 225 MeV/c in the upper left, then continuing from left to right and top to bottom. The fit model is given by Eq. (3). The number of peaks included in the fit is dynamic: Kaons are fitted for the first 10 bins, deuterons are fitted from the 5th bin on. None of the fit parameters have been constrained.

7. Conclusions

In this work we have presented a detailed analysis of PID capabilities of a GEM-based TPC based on the measurement of specific energy loss of charged particles, using reactions of a pion beam with a carbon target. It is the first measurement of this kind with a GEM-TPC. Clear bands for different particle types in the specific energy loss spectrum can be identified.

We have demonstrated that – after the application of gain corrections on pad level – the dE/dx_{tr} resolution of the detector is 14–17% for the studied particle momentum range, very well compatible with the expectations for a truncated mean analysis [17]. For extraction of the relevant quantities we used a convoluted fit function to be able to correctly describe asymmetries caused by the comparatively short track lengths. From the point of view of performing particle identification for physics analysis, the precise description of the straggling peaks by the fit model given in Eq. (3) is a satisfying result in itself, as it allows us to safely assign particle type probabilities.

In addition, we have investigated the peak shape of the measured straggling distributions in a data-driven Monte Carlo study. We have characterized the extent of asymmetry of the final truncated mean distributions arising from the basic problem of sampling from long-tailed straggling functions with limited sample size for a wide range of track lengths. It became apparent that the asymmetry can be fully absorbed in the exponential component of the fit function, leaving the purely Gaussian sigma a good estimator for the resolution and compatible with expectations even for small track lengths.

Acknowledgments

We would like to thank the FOPI collaboration for their support during numerous test beams and the physics beam time with the GEM-TPC.

Appendix A. Fits from momentum based analysis

As supporting material, Fig. A1 shows all projections along the momentum axis as discussed in Section 5 including the fits.

References

[1] F. Sauli, Nucl. Instrum. Methods Phys. Res. A Accel. Spectrom. Detect. Assoc. Equip. 386 (1997) 531.
[2] F. Sauli, S. Kappler, L. Ropelewski, IEEE Trans. Nucl. Sci. NS-50 (2003) 803.
[3] M.S. Ryu, B. Hong, T.I. Kang, J. Korean Phys. Soc. 59 (2011) 1605.
[4] L. Fabbietti, et al., Nuclear Instrum. Methods Phys. Res. Sec. A Accel. Spectrom. Detect. Assoc. Equip. 628 (2011) 204.
[5] M. Ball, et al., ArXiv e-prints (2012), 1207.0013.
[6] P. Baron, et al., IEEE Trans. Nucl. Sci. NS-55 (2008) 1744.
[7] K. Abe, et al., Nucl. Instrum. Methods Phys. Res. A Accel. Spectrom. Detect. Assoc. Equip. 659 (2011) 106.
[8] S. Dørheim, J. Instrum. 7 (2012) C03011.
[9] M. Kiš, et al., Nucl. Instrum. Methods Phys. Res. A Accel. Spectrom. Detect. Assoc. Equip. 646 (2011) 27.
[10] M. Al-Turany, et al., J. Phys.: Conf. Ser. 396 (2012) 022001.
[11] R. Brun, F. Rademakers, Nucl. Instrum. Methods Phys. Res. A Accel. Spectrom. Detect. Assoc. Equip. 389 (1997) 81.
[12] B. Ketzer, Nucl. Instrum. Methods Phys. Res. A Accel. Spectrom. Detect. Assoc. Equip. 732 (2013) 237.
[13] S. Biagi, Nucl. Instrum. Methods Phys. Res. A Accel. Spectrom. Detect. Assoc. Equip. 283 (1989) 716.
[14] J. Rauch, J. Phys.: Conf. Ser. 396 (2012) 022042.
[15] C. Höppner, et al., Nucl. Instrum. Methods Phys. Res. A Accel. Spectrom. Detect. Assoc. Equip. 620 (2010) 518.
[16] H. Bichsel, Nucl. Instrum. Methods Phys. Res. A Accel. Spectrom. Detect. Assoc. Equip. 562 (2006) 154.
[17] W.W.M. Allison, J.H. Cobb, Ann. Rev. Nucl. Part. Sci. 30 (1980) 253.

List of Figures

List of Tables

Bibliography

[1] D.R. Nygren and J.N. Marx, Phys. Today 31N10 (1978) 46.
(Cited on page 5.)

[2] TPC/Two Gamma Collaboration, R.J. Madaras et al., IEEE Trans. Nucl. Sci. 30 (1983) 76.
(Cited on page 5.)

[3] TOPAZ-TPC group, T. Kamae et al., Nucl. Instr. Meth. A 252 (1986) 423.
(Cited on page 5.)

[4] C. Brand et al., Nucl. Instr. Meth. A 283 (1989) 567.
(Cited on page 5.)

[5] W.B. Atwood et al., Nucl. Instr. Meth. A 306 (1991) 446.
(Cited on page 5.)

[6] NA49 Collaboration, M. Fuchs, Nucl. Instr. Meth. A 367 (1995) 394.
(Cited on page 5.)

[7] STAR Collaboration, K.H. Ackermann et al., Nucl. Phys. A 661 (1999) 681.
(Cited on page 5.)

[8] CERES Collaboration, D. Adamova et al., Nucl. Instr. Meth. A 593 (2008) 203, 0802.1443.
(Cited on page 5.)

[9] J. Alme et al., Nucl. Instr. Meth. A 622 (2010) 316, 1001.1950.
(Cited on page 5.)

[10] F. Sauli, Nucl. Instr. Meth. A 386 (1997) 531.
(Cited on page 5.)

[11] W. Blum, W. Riegler and L. Rolandi, Particle Detection with Drift Chambers, 2 ed. (Springer-Verlag, Berlin, 2008).
(Cited on pages 7, 10, and 24.)

[12] B. Ketzer, Private communication, 2015.
(Cited on page 13.)

[13] R. Veenhof, Garfield - simulation of gaseous detectors, `http://garfield.web.cern.ch`, 1984-2010.
(Cited on page 13.)

[14] S. Biagi, Nucl. Instr. Meth. A 421 (1999) 234.
(Cited on pages 13 and 56.)

[15] F.V. Böhmer et al., Nucl. Instr. Meth. A 719 (2013) 101 .
(Cited on pages 13, 14, 60, 61, 93, and 158.)

[16] The ALICE Collaboration, CERN preprint CERN-LHCC-2013-020/ALICE-TDR-016 (2013).
(Cited on pages 14, 27, and 28.)

[17] The ALICE Collaboration, CERN preprint CERN-LHCC-2015-002/ALICE-TDR-016-ADD-1 (2015).
(Cited on pages 14 and 27.)

[18] J. Abele et al., Nucl. Inst. Meth. Section A 499 (2003) 692 .
(Cited on page 14.)

[19] J. Alme et al., Nucl. Instr. Meth. A 622 (2010) 316, 1001.1950.
(Cited on page 14.)

[20] C. Altunbas et al., Nucl. Instr. Meth. A 490 (2002) 177 .
(Cited on page 15.)

[21] B. Ketzer et al., Nucl. Phys. B125 (2003) 368.
(Cited on page 15.)

[22] B. Ketzer et al., Nucl. Inst. Meth. A A535 (2004) 314.
(Cited on page 15.)

[23] G. Mallot et al., Nucl. Instr. Meth. A 518 (2004) 121 , Frontier Detectors for Frontier Physics: Proceedin.
(Cited on pages 15 and 33.)

[24] L. Hallermann, Analysis of GEM Properties and Development of a GEM Support Structure for the ILD Time Projection Chamber, PhD thesis, DESY, 2010.
(Cited on page 15.)

[25] F.V. Böhmer et al., Nucl. Instr. Meth. A 737 (2014) 214.
(Cited on pages 15, 105, 111, 124, 153, 158, and 159.)

[26] H. Bichsel, Nucl. Instr. Meth. A 562 (2006) 154.
(Cited on pages 15, 22, 23, and 25.)

[27] H.A. Bethe, Ann. Phys. 5 (1930) 325.
(Cited on pages 17 and 20.)

[28] Particle Data Group, K. Olive et al., Chin.Phys. C38 (2014) 090001.
(Cited on pages 17, 21, 97, 135, 145, and 147.)

[29] M. Inokuti, Rev. Mod. Phys. 43 (1971) 297.
(Cited on page 19.)

[30] J. Lindhard and A.H. Sørensen, Phys. Rev. A 53 (1996) 2443.
(Cited on page 20.)

[31] B. Weaver and A. Westphal, Nucl. Instr. Meth. B 187 (2002) 285 .
(Cited on pages 20 and 21.)

[32] R. Sternheimer, M. Berger and S. Seltzer, Atomic Data and Nuclear Data Tables 30 (1984) 261 .
(Cited on pages 20 and 21.)

[33] W.W.M. Allison and J.H. Cobb, Annual Review of Nuclear and Particle Science 30 (1980) 253.
(Cited on pages 22, 107, and 108.)

[34] S. Agostinelli et al., Nucl. Instr. Meth. A 506 (2003) 250 .
(Cited on page 22.)

[35] L. Landau, J. Phys. USSR 8 (1944) 201.
(Cited on page 24.)

[36] L. Fabbietti et al., Nucl. Instr. Meth. A 628 (2011) 204 .
(Cited on pages 29 and 30.)

[37] M. Ball et al., Technical design study for the PANDA time projection chamber, 2012, arXiv:1207.0013.
(Cited on pages 29, 30, 31, 33, 93, 100, and 103.)

[38] B. Ketzer, Nucl. Instr. Meth. A 732 (2013) 237 , Vienna Conference on Instrumentation 2013.
(Cited on page 31.)

[39] Q. Weitzel et al., IEEE Nuclear Science Symposium, pp. 227–233, 2007.
(Cited on page 32.)

[40] M.E. Berger, SiLViO: Entwicklung eines auf Silizium basierenden Trigger und Tracking Systems, Master's thesis, Technische Universität München, 2009.
(Cited on page 33.)

[41] P. Baron et al., Nuclear Science, IEEE Transactions on 55 (2008) 1744.
(Cited on page 33.)

[42] K. Abe et al., Nucl. Instr. Meth. A 659 (2011) 106 .
(Cited on page 33.)

[43] M. Vandenbroucke, Development and Characterization of Micro-Pattern Gas Detectors for Intense Beams of Hadrons, PhD thesis, Université Pierre et Marie Curie / Technische Universität München, 2012.
(Cited on pages 33, 55, and 60.)

[44] I. Konorov et al., Nuclear Science Symposium Conference Record, 2001 IEEE, pp. 98–99, IEEE, 2001.
(Cited on page 33.)

[45] P. Abbon et al., Nucl. Instr. Meth. A 577 (2007) 455 .
(Cited on page 33.)

[46] S. Dørheim, Journal of Instrumentation 7 (2012) C03011.
(Cited on page 33.)

[47] J. Ritman, Nuclear Physics B - Proceedings Supplements 44 (1995) 708 .

(Cited on pages 34, 36, 38, and 39.)

[48] A. Gobbi et al., Nucl. Instr. Meth. A 324 (1993) 156 .
(Cited on page 34.)

[49] M.S. Ryu et al., J. Korean Phys.Soc. 59 (2010) 1605.
(Cited on page 34.)

[50] M. Merschmeyer, Production and flow of neutral strange particles in Ni+Ni collisions at 1.93 AGeV, PhD thesis, Universität Heidelberg, 2004.

(Cited on pages 37, 38, 41, and 47.)

[51] R. Schlesier, Erste Untersuchungen am Testsegment der CDC, Master's thesis, Universität Heidelberg, 1991.
(Cited on page 38.)

[52] M. Kiš et al., Nucl. Instr. Meth. A 646 (2011) 27 .
(Cited on page 38.)

[53] J. Frühauf, Trigger logic, `https://www-alt.gsi.de/informationen/wti/ee/elekt_entwicklung/trigger_detailed.pdf`, 2008.
(Cited on page 40.)

[54] B. Allardyce et al., Nuclear Physics A 209 (1973) 1 .
(Cited on page 42.)

[55] S. Dørheim, PhD thesis - *in preparation*, Technische Universität München, 2015/2016.
(Cited on pages 42, 77, 81, 82, and 90.)

[56] R. Brun and F. Rademakers, Nucl. Instr. Meth. A 389 (1997) 81 .
(Cited on pages 42 and 48.)

[57] V. Fine, QtROOT: Qt-based ROOT implementation for Unix and Windows, `http://root.bnl.gov/QtRoot/QtRoot.html`, 2010.
(Cited on page 43.)

[58] M. Al-Turany et al., Journal of Physics: Conference Series 396 (2012) 022001.
(Cited on page 48.)

[59] S. Neubert, A GEM-based TPC for PANDA - detector simulations and prototype design, Master's thesis, Technische Universität München, 2005.

(Cited on page 48.)

[60] C. Höppner et al., Nucl. Instr. Meth. A 620 (2010) 518 .
(Cited on pages 51, 62, and 65.)

[61] D. Kaiser, Steuerung und Überwachung einer Zeitprojektionskammer mit GEM-Auslese, PhD thesis, Universität Bonn, 2014.
(Cited on page 56.)

[62] R.O. Duda and P.E. Hart, Commun. ACM 15 (1972) 11.
(Cited on page 60.)

[63] P. Hough, Method and means for recognizing complex patterns, 1962, US Patent 3,069,654.
(Cited on page 60.)

[64] F.V. Böhmer, A High-Rate Time Projection Chamber for PANDA: Simulation Studies and GPU-based Track-Finding, Master's thesis, Technische Universität München, 2009.
(Cited on page 60.)

[65] J. Rauch, Journal of Physics: Conference Series 396 (2012) 022042.
(Cited on page 60.)

[66] J. Rauch and T. Schlüter, (2014), 1410.3698.
(Cited on page 63.)

[67] R.E. Kalman, Transactions of the ASME–Journal of Basic Engineering 82 (1960) 35.
(Cited on page 63.)

[68] CERN, GEANT - Detector description and simulation tool, CERN Program Library Long Write-up, W5013, 1993.
(Cited on page 66.)

[69] R. Frühwirth and A. Strandlie, Computer Physics Communications 120 (1999) 197 .
(Cited on pages 67 and 68.)

[70] S. Fleischmann, Track Reconstruction in the ATLAS Experiment – The Deterministic Annealing Filter, Master's thesis, Bergische Universität Wuppertal, 2006.
(Cited on page 67.)

[71] M. Ohlsson, C. Peterson and A.L. Yuille, Computer Physics Communications 71 (1992) 77 .
(Cited on page 69.)

[72] W. Waltenberger, IEEE Transactions on Nuclear Science 58 (2011) 434.
(Cited on page 69.)

[73] R. Frühwirth et al., Computer Physics Communications 96 (1996) 189 .
(Cited on page 70.)

[74] F. James and M. Winkler, MINUIT User's Guide, `http://seal.web.cern.ch/seal/documents/minuit/mnusersguide.pdf`, 2004.
(Cited on page 76.)

[75] V. Walbrecht, Untersuchung der Auflösung eines GEM-TPC Detektors, Bachelor's thesis, Technische Unviversität München, 2014.
(Cited on pages 80 and 93.)

[76] V. Eckardt et al., (2001), nucl-ex/0101013.
(Cited on page 101.)

[77] M.O. Krause, Phys. Rev. 140 (1965) A1845.
(Cited on page 101.)

[78] R. Schmitz, Energy calibration of a gem-tpc prototype with 83mkr, EXA 2011, edited by P. Bühler et al., pp. 329–331, Springer Netherlands, 2012.

(Cited on pages 102 and 103.)

[79] W. Verkerke and D. Kirkby, ArXiv Physics e-prints (2003), physics/0306116.
(Cited on page 125.)

[80] C. Fuchs, Progress in Particle and Nuclear Physics 56 (2006) 1 .
(Cited on pages 131, 136, 137, and 138.)

[81] C. Hartnack et al., Physics Reports 510 (2012) 119 , Strangeness production close to the threshold in protonnucleus and heavy-ion collisions.
(Cited on pages 131, 138, and 140.)

[82] M.L. Benabderrahmane et al., Phys. Rev. Lett. 102 (2009) 182501.
(Cited on pages 133, 139, 146, 151, 152, and 158.)

[83] V. Koch, International Journal of Modern Physics E 06 (1997) 203.
(Cited on pages 134 and 135.)

[84] M. Gell-Mann, R.J. Oakes and B. Renner, Phys. Rev. 175 (1968) 2195.
(Cited on page 135.)

[85] S. Klimt, M. Lutz and W. Weise, Physics Letters B 249 (1990) 386 .
(Cited on page 135.)

[86] G. Brown and M. Rho, Physics Reports 269 (1996) 333 .
(Cited on page 135.)

[87] M. Gell-Mann and M. Lévy, Il Nuovo Cimento 16 (1960) 705.
(Cited on page 135.)

[88] D. Kaplan and A. Nelson, Physics Letters B 175 (1986) 57 .
(Cited on page 136.)

[89] A.E. Nelson and D.B. Kaplan, Physics Letters B 192 (1987) 193 .
(Cited on page 136.)

[90] M. Büscher et al., The European Physical Journal A - Hadrons and Nuclei 22 (2004) 301.
(Cited on page 139.)

[91] H. Stöcker and W. Greiner, Physics Reports 137 (1986) 277.
(Cited on page 140.)

[92] J. Aichelin and H. Stöcker, Physics Letters B 176 (1986) 14.
(Cited on page 140.)

[93] S.A. Bass et al., Progress in Particle and Nuclear Physics 41 (1998) 255.
(Cited on page 140.)

[94] C. Hartnack et al., Phys.Rept. 510 (2012) 119, 1106.2083.
(Cited on page 140.)

[95] Y. Leifels, Private communication, 2015.
(Cited on page 144.)

[96] W. Ehehalt and W. Cassing, Nucl.Phys. A602 (1996) 449.
(Cited on page 152.)

Acknowledgements

First and foremost I want to thank my mentor Prof. Dr. Bernhard Ketzer for his support and guidance through all these years. His style of teaching has always been to encourage learning by setting valuable standards and by good example, never by imposing a certain way to do things. He has been an inspiration in terms of methodical, scientific work, and gave me the opportunity to grow as a person. It has been an honour to work with you, Bernhard! I also want to extend my gratitude to his wife, Marion, for her kind hospitality during the numerous scientific gatherings at her kitchen table in Bonn. I am deeply grateful to both of you for your support during complicated months.

I am also thankful to my advisor Prof. Dr. Stephan Paul for giving me the opportunity to work in a very special group of excellent scientists. Also he has always set an example by being open-minded, and through that encouraged his students to think outside of the box.
From Prof. Paul's group, I want to personally thank a few people that I have grown especially fond of, and who I will miss dearly: First of all I want to name Christian Höppner, who became a valuable part of my education and, more importantly, a friend. Your sunny disposition is missed tremendously! I also want to thank Sebastian Neubert, who has been an important influence during my first years in the group, and who has taught me some important life lessons. A very big heap of gratitude goes to Boris Grube for spending an incredible amount of time discussing my work with me, for his constructive criticism in the process, and for always keeping the supply lines for gummy bears open. You have been a great help! Thank you! His office mate Charly Bicker deserves to be honoured for his very unique sense of humour, and in general for being a great guy. I do hope we'll see each other again, maybe over a good steak? I want to thank Lingxin for her support, her puns and her warm smiles that always managed to cheer me up. My office mate for many years and former minion, Johannes Rauch, also deserves a big hug. The time with you in New York has been great! Keep rocking! I want send a warm goodbye to Sebastian Uhl, who is too smart for his own good, to Alex Austregesilo for not getting that last bet right, and to my office mate Wolfgang Schott, who is just amazing. Special thanks go to Markus Krämer and Karin Frank, who kept everything going.

I also want to thank my fellow PhD colleagues Martin Berger and Sverre

Dørheim for sticking up with me over the years. I wish you the best of luck in the remaining time of your PhD and all your future endeavours! During my work on the GEM-TPC project I also had the honour to meet the nice people of Prof. Dr. Laura Fabbietti's group, especially Chii Berger-Chen and Piotr Gasik: You are great! The same goes for Dr. Markus Ball, with whom I had the pleasure to have many delightful and interesting conversations over the years. I will never forget Seattle! And I also want to thank Francesco Cusanno for being a wonderful person. The memory of your kindness will stay with me. You have gone too early, and I wish I could have thanked you in person.

Last, but not least, I want to thank Dr. Yvonne Leifels, Prof. Norbert Herrmann and Victoria Zinyuk of the FOPI collaboration for their help during and after the S339 experiment. I am especially grateful for their enduring support over the last months in countless and fruitful discussions. I guess I have been quite persistent at times, but I have never taken your help for granted. Thank you!

Most importantly, though, I want to thank my friends and family: Being part of my "PhD life" must not have been easy. In fact, I know it wasn't. Thank you Jakob, Matthias, Constanze, parent #1, Christian, Lingxin, Steve, Hannes and parent #2. The order of your appearance has been drawn randomly using ROOT's `TRandom2` implementation.